

Université catholique de Louvain
École Polytechnique de Louvain
ICTEAM Institute

Metal electrode integration and Palladium nanoparticle functionalization on a miniaturized macroporous silicon chemiresistor

Gilles Scheen

Thesis presented for the degree of Ph.D. in Engineering Sciences

Jury members

Pr. Laurent Francis (Advisor)	UCL
Pr. Denis Flandre	UCL
Pr. Isabelle Huynen	UCL
Dr. Marc Debliquy	UMONS
Dr. Giuseppe Barillaro	University of Pisa

July 17, 2015

"Il est souvent nécessaire
d'entreprendre pour espérer
et de persévérer pour réussir."
(Gilbert Cesbron)

A mes parents
A Anaïs, Sian et ...
A mon Amour

Remerciements

Une thèse est avant tout un long voyage semé d'embûches et de moments de joie. Durant ce périple, j'ai eu l'occasion et la chance de croiser un grand nombre de visages. Certains m'ont aidé, d'autres m'ont souri. Certains m'ont motivé, d'autres m'ont éprouvé. Mais quoi qu'il en soit, de ce parcours, j'en tire une incroyable expérience, de formidables souvenirs et de nombreuses amitiés qui me suivront tout au long de ma vie.

La fin de ce chemin approche et avant de passer sur la route suivante, je me retourne pour dire merci à tous ceux qui ont emboité le pas sur une courte ou longue distance.

Commençons par l'instigateur, celui qui m'a lancé sur le chemin. Il m'a donné la carte, le matériel et m'a dit : « *Vas-y !*». Je remercie le Professeur Laurent Francis de m'avoir fait confiance (parfois aveuglément) tout au long de mon chemin et de m'avoir permis de vivre cette formidable aventure.

Ensuite, il y a ce couteau suisse qui ne vous quitte jamais et qui est là à chaque moment de votre parcours, surtout lors des tracés tumultueux. Il vous épaule, vous protège, vous soutient, vous rassure, ... Je ne remercierai jamais assez Margherita Bassu pour tout ce qu'elle a apporté à cette thèse, ainsi qu'à mon expérience et à mon moral. Pour toutes ses paroles, ses faits et ses rires, merci mille fois.

A l'arrivée, il y a ce petit groupe de personnes qui vous attend, chrono à la main pour vous donner votre résultat. Je remercie chaque membre de mon comité d'accompagnement et de jury : Le Professeur Denis Flandre pour sa perspicacité qui m'a guidé tout au long de ma recherche; Le Professeur Isabelle Huynen pour ses conseils et ses encouragements; Marc Debliquy pour son accueil, son aide, ses conseils et les bons moments; Giuseppe Barillaro dont les articles ont été le point de départ de ce travail de recherche.

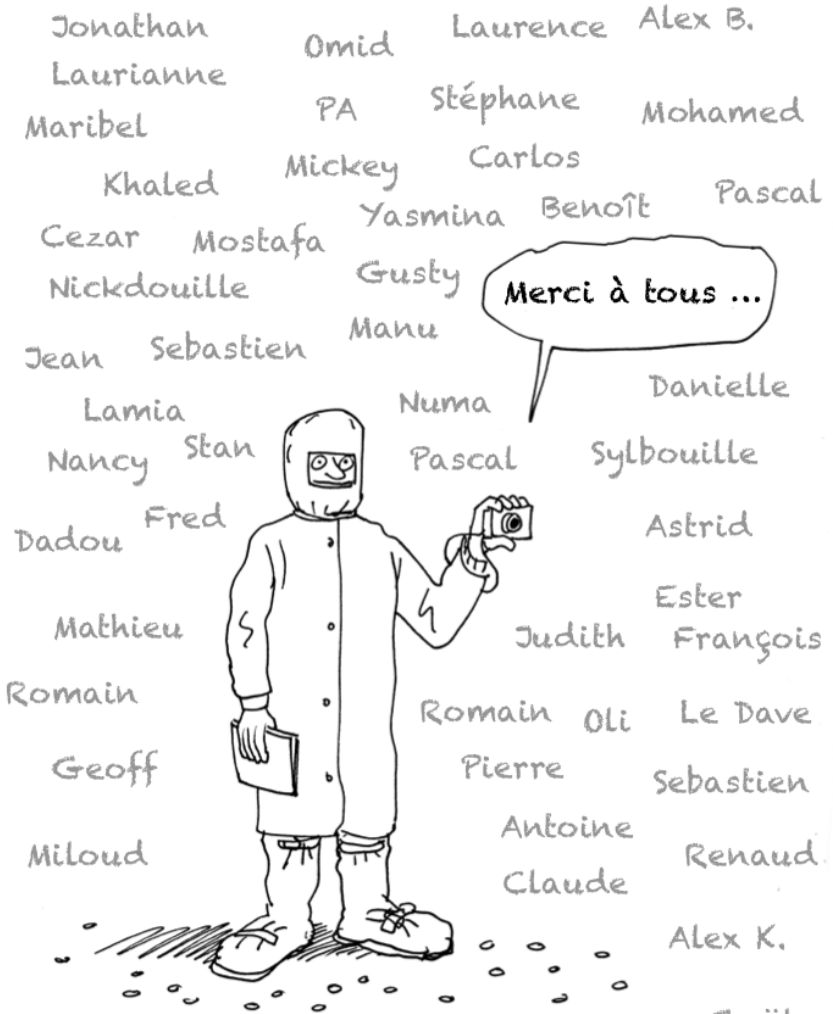
Un long voyage est fait de rencontres, de discussions et d'entraides avec les personnes croisées sur le chemin. Une vraie amitié s'est installée avec ces compagnons de route. J'aurais aimé avoir quelques mots pour chacun, je me contenterai de leur dire à tous : *merci merci merci* ...

Sur la route, la nuit tombante, il est temps de regagner le refuge pour un temps de détente et de repos. Ces gîtes d'étape sont des lieux de retrouvailles avec de vieilles connaissances. Les discussions nourries avec ces randonneurs d'un autre itinéraire sont de vrais instants de bonheur. Dans ces moments d'évasion, les pensées s'échappent le temps d'un bon verre tout en conversant de sujets éloignés du quotidien. Merci en particulier à Bubu et Sabine, Séba et Malou, mes jolis-parents, le G7, les Sterput et à tous les autres ...

Ils m'ont appris à marcher, ils m'ont donné la soif de découvrir et la persévérance de continuer. Sans eux, rien n'aurait été possible. Un merci colossal à mes parents à qui je dois une grande partie de mes réussites.

Enfin, dans toute aventure il faut de la volonté, du courage, de l'énergie, de la persévérance... Cette force, je l'ai tirée dans l'amour de ma Puce et de mes enfants. Je ne les remercierai jamais assez pour leur patience, leur aide, leurs encouragements, leurs coups de pied au *** affectueux, leur tendresse et leur amour. Sans eux, j'aurai rebroussé chemin à maintes reprises.

Un incommensurable merci à mon Amour qui a subit avec patience mon stress et mon indisponibilité. Son travail dans l'ombre a permis la réussite de cette thèse. Son immense soutien, son aide gigantesque et ses tendres encouragements m'ont particulièrement été indispensables dans les moments les plus difficiles. Merci de tout mon coeur à ma chérie de partager ma vie.



Jonathan Omid Laurence Alex B. Laurianne
Maribel PA Stéphane Mohamed
Khaled Mickey Carlos
Yasmina Benoît Pascal
Cezar Mostafa
Nickdouille Gusty
Manu
Jean Sebastien
Lamia Numa Danielle
Nancy Stan Pascal Sylbouille
Fred
Dadou Astrid
Ester
Mathieu Judith François
Romain
Romain Oli Le Dave
Geoff Pierre Sebastien
Antoine
Miloud Renaud
Claude
Alex K.

Adapté d'un dessin de J.Y. Duhoo

Benja Gaël
Nicolas André Wally
Brigitte Alex V. Vivi Isabelle
Guigui
Andra Guigui Giorgana
John
Christian Yann Magali
Katir Samuel
Xiaohui Aurore Christel
Céline MS
Petros Marie-Christine
Ferran Delphine
Et tous les autres ...

Abstract

Porous silicon has a particularly large surface area available in a limited volume, tens or hundreds of square meters in a cubic centimeter. This attractive property is used to concentrate a large number of surface reactions (such as physico-chemical adsorption of gases) in a small volume. With a simple and cheap fabrication, the porous silicon is an ideal candidate for gas sensing applications.

In this work, new gas sensor architecture in macroporous silicon is presented. The development of this new architecture, based on chemiresistor principle has led to several technological innovations. Three aspects were particularly studied:

1. Integration of miniaturized metal electrode on macroporous silicon to improve the sensitivity of measurement and to enable miniaturization of the sensor. The fabrication process has focused on standard microfabrication techniques to enables the transfer of the sensors to an industrial valorization.

2. A masking technique for localized formation of macroporous silicon to eliminate the mask underetching during the anodization of the porous silicon.

3. The functionalization by palladium nanoparticles of macroporous silicon with metal electrode integrated on the surface, to increase the sensitivity and selectivity of hydrogen sensing.

Contents

1 Introduction **3**
- 1.1 Gas sensors . . . 3
- 1.2 Thesis objectives . . . 10

2 Fabrication, applications and gas sensors **15**
- 2.1 Fabrication and mass transfert . . . 15
- 2.2 Application fields of porous silicon . . . 32
- 2.3 Porous silicon gas sensors . . . 41
- 2.4 Why to miniaturize electrodes? . . . 45
- 2.5 Techniques of metal electrode integration . . . 48

3 Macro-pSi : electrode integration and masking **59**
- 3.1 Introduction . . . 59
- 3.2 New metal electrode integration method . . . 60
- 3.3 Macroporous silicon masking . . . 107
- 3.4 Micrometric metal pattern . . . 123
- 3.5 Simulations of electronic behavior . . . 129
- 3.6 Chapter conclusions and perspectives . . . 144

4 Functionalization of metal-patterned macroporous Si **149**
- 4.1 Introduction . . . 149
- 4.2 Functionalization of pSi: Overview . . . 154
- 4.3 Materials and methods . . . 181
- 4.4 Results . . . 187
- 4.5 Discussions . . . 201
- 4.6 Conclusions on the comparison of functionalization methods 208
- 4.7 Basic characterization of miniaturized chemiresistor . . . 209
- 4.8 Chapter conclusions and perspectives . . . 213

5 Conclusions and outlook **217**

A Mass transfert theory **221**
- A.1 Expressions for Flux . . . 221
- A.2 The diffusion equation . . . 222
- A.3 The diffusion constants . . . 222

B Metallisation **227**

C Equivalent circuit of the microsensor **231**

D Corrosion kinetics **235**
D.1 Electrochemical corrosion 235
D.2 Polarization diagram and Tafel plot 236
D.3 Galvanic corrosion 237
D.4 Overpotential and polarization 244

E Redox potential **249**

F Finite element simulations **251**
F.1 Simulation of the electrode spacing impact on penetration depth of the electric current lines. 251
F.2 Simulation of the distribution of hole concentration and the hole curent density in Si crystallites 255
F.3 Simulation of the hole current density and the hole concentration under the mask 256
F.4 Simulation of the impact of surface charge on the concentration of charge carriers in the pore walls 259
F.5 Simulation of the response time of the measuring cell at H_2 diffusion 260

G Hydrogen sensors and their applications **263**
G.1 What is Hydrogen? And its safety issues. 263
G.2 Operating principles of H_2 sensors 268

H Matlab code for SEM pictures processing **281**

I Microsensor fabrication process **285**
I.1 Fabrication process 285
I.2 Gas sensor design 296

List of Acronyms

pSi	Porous silicon
LOD	Limit of detection
SCR	Space charge region
p-type Si	p-type silicon
MAE	Metal-assisted etching
macro-pSi	macroporous silicon
RTA	Rapid thermal annealing
LPCVD	Low pressure chemical deposition
PECVD	Plasma-enhanced chemical deposition
NPs	Nanoparticules
TMAH	Tetramethyl ammonium hydroxyde
RIE	Reactive ion etching (Plasma etching)
DRIE	Deep reactive ion etching (Plasma etching with passivation step alternance)
MAE	Metal assisted etching
SBH	Schottky barrier height

List of Symbols

ε_r	relative permittivity
ε_0	vacuum permittivity (8.854 10^{-12} F·m^{-1})
ρ	resistivity (Ω·m)
λ	mean free path (m)
Kn	Knudsen number (dimensionless)
k_B	Boltzmann's constant (J·K^{-1})
ϕ_{cin}	kinematic diameter of molecule (m)
T	temperature (K)
P	total pressure (Pa)
A	the effective Richardson constant
q	the electronic charge unit

Publications

Journals:

(1) Scheen, G.; Ziouche, K.; Bougrioua, Z.; Godts, P.; Leclercq, D.; Lasri, T. Simultaneous Fabrication of Superhydrophobic and Superhydrophilic Polyimide Surfaces with Low Hysteresis. In : *Langmuir*, 27(10), 6490-6495 (2011).

(2) Walewyns, T.; Scheen, G.; Tooten, E.; Dupuis, P.; Francis, L. A. Development of a Miniaturized Gas Ionization Sensor for Harsh Environments by Using Polyimide Spacer. In : *ECS Transactions*, 35(30), 119-128 (2011).

(3) André, N.; Rue, B.; Scheen, G.; Francis, L. A.; Flandre, D.; Raskin, J.-P. Ultra Low Power 3-D flow meter in monolithic SOI technology. In : *ECS Transactions*, 35(5), 319-324 (2011).

(4) Scheen, G.; Bassu, M.; Francis, L. A. Metal Electrodes Integration on Macroporous Silicon : Pores Distribution and Morphology. In: *Nanoscale research letters*, 7(1), 395 (2012).

(5) Bassu, M.; Scheen, G.; Francis, L. A. Thick Macroporous Silicon Membranes: Influence of the Masking Layer on the Underetching Characteristics. In: *Sensors and Actuators A*, 185, 66-72 (2012).

(6) Belaroussi, Y.; Belaroussi; M. T.; Scheen, G.; Ben Ali, K.; Raskin, J.-P. Porous Si substrate: A high-quality and cheap substrate for advanced RF applications. In: *Nano Studies*, 8, 45-52 (2013).

(7) André, N.; Rue, B.; Scheen, G.; Francis, L. A.; Flandre, D.; Raskin, J.-P. Out-of-plane MEMS-based mechanical airflow sensor co-integrated in SOI CMOS technology. In : *Sensors and Actuators A*, 206, 6774 (2014).

(8) Scheen, G.; Bassu, M.; Douchamps, A.; Zhang, C.; Debliquy, M.; Francis, L.A. Palladium nanoparticle deposition via precipitation: a new method to functionalize macroporous silicon. In : *Science and Technology of Advanced Materials*, 15, 065002 (2014)

(9) Bassu, M.; Scheen, G.; Debliquy, M.; Francis, L.A. One-Step Integration of Interdigitated Electrodes in Macroporous Silicon: A Matter of Interface. *(In Writing)*

Conference proceedings:

a. Moreno Hagelsieb, L.; André, N.; Scheen, G.; Grard, P.; Nizet, Y.; Tang, X.i T.; Bulteel, O.; Dupuis, P.; Francis, L.; Flandre, D.; Raskin, J.-P. Aluminium Oxide Based Sensors Integration for Medical and Health Monitoring Applications. *COMS'09* (Copenhagen (Denmark), 2009).

b. Walewyns, T.; Scheen, G.; Tooten, E.; Dupuis, P.; Francis, L. A. Development of a Miniaturized Gas Ionization Sensor for Harsh Environments by Using Polyimide Spacer. *219th ECS Meeting* (Montreal (Canada), 2011).

c. André, N.; Rue, Bertrand; Scheen, G.; Francis, L. A.; Flandre, D.; Raskin, J.-P. Ultra Low Power 3-D flow meter in monolithic SOI technology. *219th ECS Meeting* (Montreal (Canada), 2011).

d. Walewyns, T.; Scheen, G.; Tooten, E.; El Fissi, L.; Dupuis, P.; Francis, L. A. Fabrication of a miniaturized ionization gas sensor with polyimide spacer. *SPIE* (Prague (Czech Republic), 2011).

e. Walewyns, T.; Scheen, G.; Tooten, E.; Francis, L. Synthesis of patterned freestanding Nickel nanowires by using ion track-etched polyimide. *SPIE* (Prague, (Czech Republic), 2011).

f. Belaroussi, Y.; Slimane, A.; Belaroussi, M.T.; Trabelsi, M.; Scheen, G.; Ben Ali, K.; Raskin, J.-P. RF and Non-linearity characterization of porous silicon layer for RF-ICs. In : *Design & Test Symposium (IDT), 9th International* (Algiers, (Algeria), 2014).

Popular-scientific publication:

- Duhoo, J.-Y.; Scheen, G. La Microfabrication. In : *Le journal de Spirou, 3981* (2014).

CHAPTER 1
Introduction

Gases are omnipresent around us. Often colorless, sometimes odorless, their presence is sometimes forgotten. Nevertheless, gases have significant utility in many fields such as industry, health, safety or the environment. According to their physico-chemical properties, the gases can "carry", "heat", "modify", "mix", "clean", "etch", "push", "save", "kill" ... They can be dangerous because harmful to health or explosive.

To handle a gas, it is essential to detect it, to "smell" it. The gas sensors are the interfaces between the gases and us. They convert non-electrical physical or chemical quantities into signals more adequate to use. Generally, they translate the gas concentration into an electrical or optical signal. Gas sensors have become an essential element of process control and measurement systems in almost all the spheres of our life. The emerging applications of gas require improved performances and ever higher levels of miniaturization of gas sensors. However, this does not have to mean an increase of fabrication costs.

1.1 Gas sensors

1.1.1 What is a gas sensor?

A gas sensor is a device which detects the presence of one or more gases in a medium. The target gases are called analytes. A gas sensor is composed of several elements: the sensitive layer, one or more transducers and, generally, the processing electronics (figure 1.1). The output is generally a signal that is converted to human-readable display.

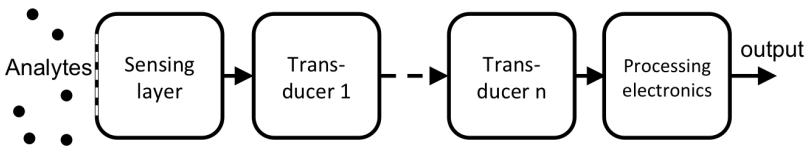


Figure 1.1: block diagram of a gas sensor

The *sensitive layer* is the part of the sensor undergoing a physical or chemical modification when submitted to the medium. This modification can be electro-magnetic (change in resistivity, electrical permittivity, magnetic permeability), optical (color, polarization, refractive index), thermal or mechanical (volume, internal constraint).

A *transducer* is a device that converts energy of one form into output energy of another. Different kinds of energies can be involved: electrical, mechanical, electromagnetic, chemical, optical, acoustic or thermal energy. The transducer translates the modification undergone by the sensitive layer in a measurable signal. The output of the transducer is usually an electrical signal that can be measured using suitable equipment.

Usually the *processing electronics* is placed downstream of the transducer to change the signal in order to be measured after if needed being amplified, or transformed into a signal less sensitive to noise. In some cases, this electronic processing transforms the analog signal of the transducer into a digital signal used by a computer or display.

1.1.2 Overview of basic characteristics of gas sensors

Gas sensors have different performances. In this section, some characteristics of gas sensors are presented to quantify performance [1]. These characteristics enable you to compare different sensors between them, but also to assess to which type of application the sensor is used.

The most commonly used features are:

1. concentration levels,
2. sensitivity,
3. selectivity,
4. response time,
5. recovery time,
6. signal to noise,
7. miniaturization.

Concentration levels

The concentration is the amount of a constituent divided by the total volume of a mixture. In a gas mixture, the concentration of the analyte gas is often measured as a mole ratio (the number of moles of the analyte gas divided by the number of moles of all gases in the mixture).

Concentration levels are typically measured in parts per million (ppm). Parts per billion (ppb), parts per trillion (ppt) and percent ... are also commonly used. All of these values represent the molar concentrations of the analyte within the sample of gas being tested.

Sensitivity

The sensitivity of the sensor indicates how much the sensor's output changes when the measured quantity changes. It characterizes the magnitude of a response to a particular analyte. Mathematically, it is defined as the slope of the output characteristic curve (DY/DX in figure 1.2). In the case of gas sensors, the sensitivity can be expressed as a ratio between some measurements of the response and the concentration of the analyte being delivered. Current per ppm, voltage per ppm, and resistance per ppm, for example, are all common measurements of gas sensor sensitivity. This parameter may be constant over the range of the sensor (linear response), or it may vary (nonlinear response) (figure 1.2). Generally, the sensitivity is considered as the most important characteristics of gas sensors.

Selectivity

Selectivity is the second most important characteristics of gas sensors. It determines the usefulness of the sensor for any given application. Selectivity can be defined as the ability of a sensor to respond primarily to only one species (analyte) in the presence of other species or a parameter of the environment (temperature, illumination level, pressure ...) (figure 1.2). For instance, gas sensors involving a semiconductor material as transducer are often sensitive to temperature. A change in environmental temperature causes a variation in the sensor response even though the concentration of the analyte is not changed. The sensor response is erroneous.

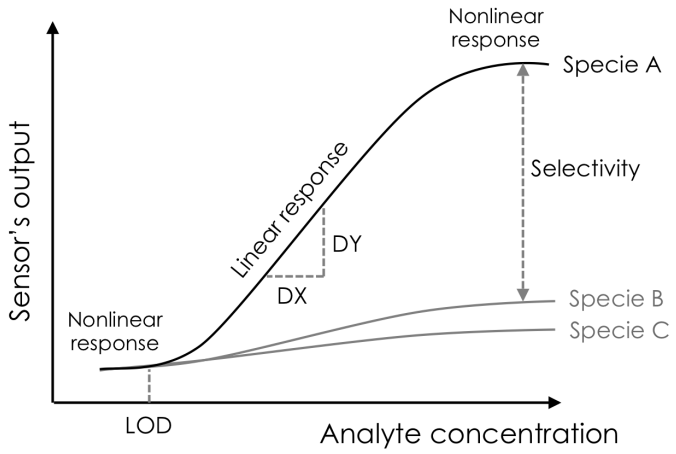


Figure 1.2: Diagram of a typical response of a physico-chemical sensor. Visualization of sensitivity, limit of detection, linearity and selectivity of the measurement.

Good selectivity is imperative in many applications. It is often impossible for a sensor to be completely selective versus all other species or all the environmental parameters. The list of necessary selectivity should be established to correctly select the appropriate sensor for a particular application.

There are four standard ways to increase the selectivity of gas detector: by physico-chemical properties, using a catalyst or a promoter to favor the transformation of the poorly-detectable gas in some other detectable product; by control of the temperature of the sensitive surface which allows both to circumvent the variation of the temperature, but also the variations resulting from the presence of humidity (by sufficiently heating the sensitive coating); by the use of specific surface additives, a material deposited on the transducer specifically absorbs or reacts with the gas of interest; and physically, by using a filter upstream of the sensitive layer. Two kinds of coatings have been used to increase the selectivity: The first consume non-target gas which must not reach the gas detector to avoid false detection; the second permits the passage of selected gases to the sensor [2].

A common technique is to place, in parallel, a sensitive sensor and a dummy sensor. This dummy sensor remains sensitive to temperature and humidity for example, but not to the target gas. By subtracting the response of the two sensors, the response to gas can be isolated and by eliminating the influence of temperature and humidity.

Response time

Sensors do not change the output state immediately when an input parameter change occurs. The interval time it takes the sensor to reach its new state is called the response time. The response time can be defined as the time required for a sensor output to change from its previous state to a final settled value. Generally, the response time is the time it takes to reach 90% of final output state. The response time is then called the T90 (figure 1.3).

Generally, the response time should be as short as possible so the user of the sensor is informed as soon as possible about the presence or absence of the analyte. The response time may be constant or vary with the magnitude of the response.

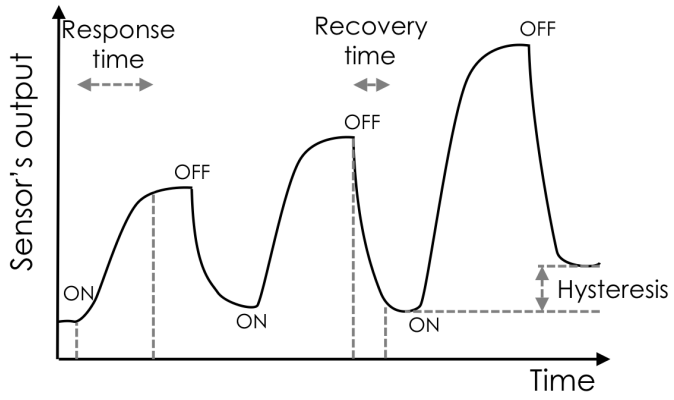


Figure 1.3: Diagram of a typical response of a physico-chemical sensor. Visualization of the response and recovery times and hysteresis. "on" and "off" respectively represent the moments at which the analyte is added or removed from the atmosphere around the sensor.

Reversibility, recovery time and hysteresis

The reversibility of a sensor is its ability to be used again after a measurement. Some sensors are single use. They can be used only once and they are no longer operational. In contrast, the other sensors can be used several times, sometimes even infinitely.

In the case of multiple use sensors, the sensor output does not instantly return to its original state because of the physical and chemical inertia in the sensor (chemical reaction, desorption, temperature change ... as a result of the measurement). The recovery time is the time that the sensor takes to return the value it had before the exposure to the analyte (figure 1.3). Usually, the recovery time is the time that the sensor takes to return to 10% of its initial state. It is then called the T10.

A sensor should be capable of following the changes of the input parameter regardless of what was measured before and the direction of the change is made. Hysteresis is the behavior of sensor dependent on the immediate history to which they have been subjected. Typically the final settling point is different when it is approached from above to when it is approached from below (figure 1.3). A large hysteresis can cause measurement errors. A large number of sensors often have low hysteresis in a certain range of measurement. Outside this range, hysteresis becomes too large to exploit the measure.

Signal to noise

Signal-to-noise ratio (often abbreviated SNR or S/N) is a factor of merit used to quantify how much a signal has been corrupted by noise. It is the measurement of useful signal strength relative to background noise and is defined as the ratio of signal power to the noise power, often expressed in decibels (figure 1.4).

Miniaturization

Miniaturization is the development of mechanical, optical or electronic devices with smaller and smaller scales. It is often regarded as the third industrial revolution after the invention of the steam engine and the discovery of electricity. Miniaturization was first applied to electronics with the advent of the transistor (1947) and then three years later integrated circuit.

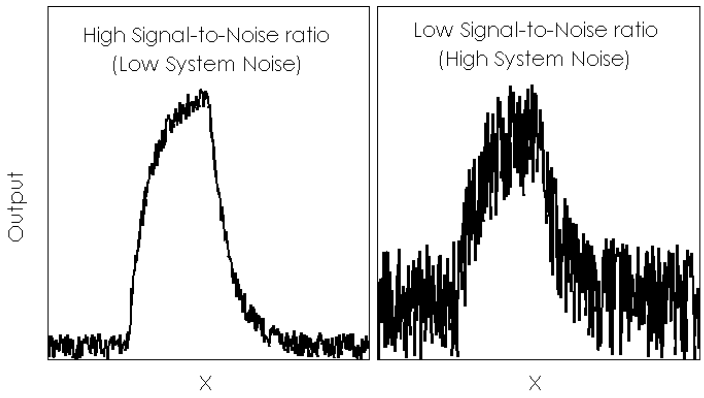


Figure 1.4: Schematic of a low noisy response (high SNR) and a high noisy response (low SNR).

Thereafter, in parallel with the further miniaturization of electronics, miniaturization of non-digital functions such as radio frequency communication devices, displays and sensors appeared. Very quickly, Micro Electro Mechanical Systems (MEMS) with microsensors of pressure, temperature, gas, light or movement were developed. Recently, microfluidics has integrated bio-chemical functions to achieve real labs on a chip.

The miniaturization of sensors has several advantages: reducing the occupied space thereby allowing the production of multi-sensory platform, reducing material consumption. Miniaturization is often associated with reducing the cost of production and energy consumption.

The sensor miniaturization is developed as much as possible using the standard microfabrication techniques. Indeed, microfabrication processes in the industry are often rigid. The commercialization of a new micro-device will come much faster if its development adapts to an existing manufacturing process in the industry rather than waiting for the industry to adapt to a new process.

1.2 Thesis objectives

Porous silicon (pSi) has a high surface to volume ratio corresponding to several tens or hundred square meters in one cubic centimeter. The surface reactions as the physico-chemical adsorption are widely abundant in a restricted volume. In addition, pSi presents a high chemical reactivity at room temperature. With its simple and cheap fabrication, pSi is an ideal candidate for gas sensing applications. The pore diameter of pSi is tunable from a few nanometers to several microns. Depending on their diameters (d), pores are classified into three categories: the micropores ($d < 2$ nm), mesopores (2 nm $< d <$ 50 nm) and macropores ($d >$ 50 nm). The large diameter of macropores increases diffusion kinetics of gases into pores and reduces response and recovery times of gas sensors. The diffusion of fluids inside the pores is also an interesting asset for macroporous silicon (macro-pSi) to facilitate the functionalization of its walls.

This thesis focuses on the first two elements of a hydrogen gas sensor (figure 1.1): the sensing layer and the transducer. Macro-pSi is poorly sensitive to hydrogen and has a very low selectivity towards other gases. It therefore requires a functionalization of the surface, in order to both enhance the sensitivity, and improve the selectivity. The palladium (Pd), sensitive and highly selective to hydrogen, is commonly used for hydrogen sensing applications.

The hydrogen sensor is based on the principle of the *chemiresistor*. The schematic view of the hydrogen chemiresistor based on porous silicon is shown in figure 1.5. The sensitive layer is composed of palladium nanoparticles and the macroporous silicon is used as a transducer. Nanoparticles and macroporous silicon form a Schottky junction and a charge region is created in the pore walls. An electric current applied to the porous layer moves across the walls of the macro-pSi.

In presence of hydrogen in the environment, hydrogen is absorbed in the palladium and diffuses to Pd/macroporous silicon interface. The presence of hydrogen modifies the electrical characteristics of the Schottky junctions interface. As macroporous silicon walls are thin, the width variation of the charge regions influences the applied electric current.

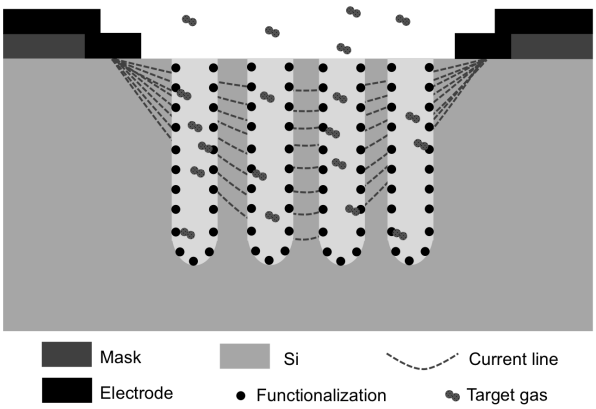


Figure 1.5: Schematic of cross-section view of a functionalized porous silicon chemiresistor.

The amount of hydrogen absorbed by the nanoparticles is proportional to the hydrogen concentration in the environment. Then, the measurement of the electric current variations enables to determine the concentration of hydrogen in the environment. The block diagram of the operating mode of the chemiresistor are shematized in figure 1.6.

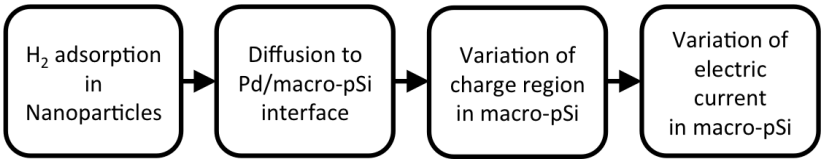


Figure 1.6: block diagram of our functionalized macro-pSi chemiresistor.

Figures 1.7d. and e. show the result of the electrochemical etching of metal patterned porous silicon (fabrication process is briefly detailled in figures 1.7a., b. and c.). No pretreatment was applied to the electrodes. The unmasked silicon initially patterned by metal electrode is porosified by an electrochemical etching. Two technological issues occur: the metal electrodes are delaminated (figure 1.7d.) and a wide underetching appears at the edge of the mask (figure 1.7e.).

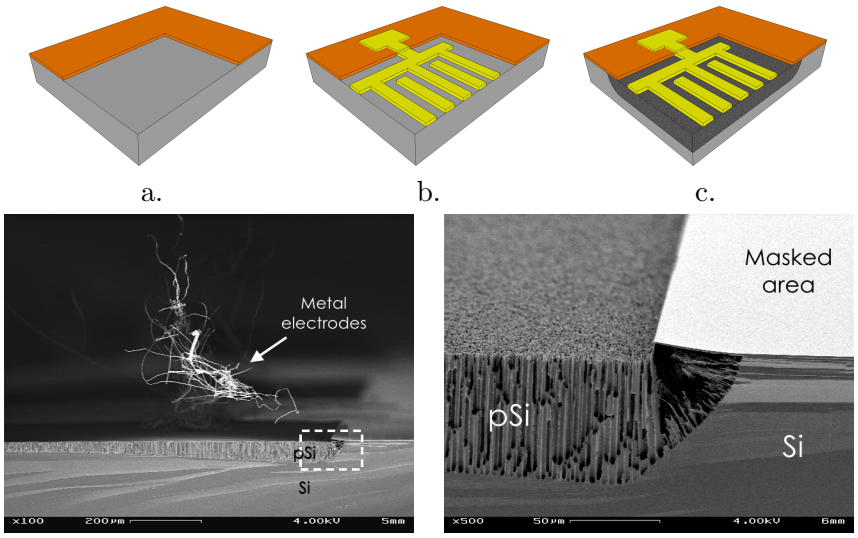


Figure 1.7: Brief schematization of the fabrication process of the electrochemical etching of metal patterned porous silicon. (a.) Mask patterning on the silicon surface. (b.) Metal electrode deposition. (c.) Electrochemical etching. SEM picture of (d.) cross-section of a chemiresistor fabricated. No pretreatment was applied to the electrodes. (e) Magnification of dotted rectangle. The metal electrodes are delaminated and a wide underetching appears at the edge of the mask.

To fix the issue of the delamination, the metal electrodes are commonly deposited on the macroporous silicon surface after the electrochemical etching with non-effective and non-standard techniques (presented in Chapter 2). At first, this is an obstacle to the industrialization of macroporous silicon-based sensors. Second, due to the high roughness of macroporous silicon, the design and the dimensions for the electrode pattern are not optimum to probe correctly the sensitive layer. As a result, the sensitivity measurement decreases and the SNR increases.

This thesis presents innovative solutions to the issues of metal electrode integration on macroporous silicon and to the issues of masking layer underetching (showed on figures 1.7). The functionalization of macroporous silicon is also discussed and a original effective technique is developped.

Three aspects are particularly studied:

1. The integration of miniaturized metal electrodes on macroporous silicon to improve the sensitivity of the measurement and to allow the chemiresistor miniaturization (see articles (4) and (9)). Standard microfabrication techniques are used to enable the transfer of the macroporous silicon based sensors to the industrial valorization.

2. Masking technique for the localized formation of macroporous silicon to eliminate the underetching of the masking layer (see article (5)).

3. Palladium nanoparticles functionalization of macroporous silicon patterned by metal electrodes to improve the performance in hydrogen sensing (see article (8)).

The Thesis is organized as follows:

Chapter 2 presents the fabrication and applications of porous silicon. Porosification by silicon electrochemical etching is particularly considered. We present a model describing the porosification process and the influence of the electrochemical etching parameters. Different models of mass transfer in porous media are compared to define the impact of the porous layer morphology on the gas kinetic. Then, a review of porous silicon-based gas sensor and of electrode integration techniques is shown. Finally, we show how the size and pattern of electrodes influence the distributions of electric current in a substrate composed of the sensitive and a non-sensitive layers. We show that the miniaturization of metal electrodes should improve the performance of gas sensors.

Chapter 3 presents a new approach to integrate miniaturized metal electrodes on porous silicon layer. The origin of the metal electrode delamination during the electrochemical etching was investigated. We propose a new method to prevent the electrode delamination. The electrode presence on the porous layer affects its morphology. This impact are detailed in this chapter. Then, selective anodization of patterned p-type silicon substrates to form thick macroporous silicon layers are interesting to fabricate a gas sensor. The influence of the electrical properties of the masking layer and the etching parameters on mask underetching is described. A solution to avoid under-etching the masking layer is presented.

Chapter 4 deals with the functionalization of the porous silicon to enhance its performance for gases sensing applications. In particular, we focus on the hydrogen sensing. We motivate the porous silicon functionalization for H_2-sensing applications. An overview on the hydrogen sensitivity of the Pd/Si system is reported. In particular, the mechanism and kinetics of palladium-hydrogen interaction, the impact on palladium/silicon junction and the palladium nanostructuration are discussed. A study of the two techniques of palladium nanoparticles deposition on the porous silicon walls is detailed. A comparison between the two techniques reveals the advantages and disadvantages of both techniques. The chapter concludes on some measurements of macroporous silicon-based sensors with and without palladium nanoparticles. The results show the performance improving thanks to the combination of the two new techniques developed in this thesis: the miniaturized electrode integration and the functionalization of macroporous silicon with palladium nanoparticles.

Finally, chapter 5 summarizes this thesis, takes stock of the results and introduces our future research prospects.

CHAPTER 2

Porous silicon: Fabrication, applications and gas sensors

Introduction

In this chapter, porous silicon and its fabrication method are at first presented. The theory of mass transfer in porous media is discussed to understand the kinetics of porous silicon based gas sensors. Then, porous silicon-based systems are introduced to present a large number of application fields of the material. A the state of the art of porous silicon based gas sensors are detailed. In final sections, we show the technological issues of current methods for patterning of the metal electrodes on the surface of porous silicon. Finally, we end this chapter by describing the motivation for the development of a new method of integration of metal electrodes on macroporous silicon.

2.1 Porous silicon: Fabrication and mass transfert

Porous silicon was discovered by accident in 1956 by Arthur Uhlir Jr. and Ingeborg Uhlir at Bell Labs in the US [3]. Initially, their research focused on the development of a new technique for polishing and shaping of surfaces of silicon and germanium by anodization. At the time, this discovery did not arouse interest and has not even been mentioned in the literature.

Despite the discovery of porous silicon in the 1950s, the scientific community had not been interested in porous silicon until the late 1980s when Leigh Canham (Defense Research Agency in England) thought that porous silicon could exhibit properties of quantum confinement [4]. The experiments led to successful results published in the 1990s. It has been shown that porous silicon is photo- and electroluminescent [5].

These discoveries stimulated the interest of the scientific community in the optical and electrical properties of porous silicon. The growing interest was evidenced in the number of published works concerning the properties and potential applications of porous silicon. The number of published works on porous silicon has grown steadily since 1990 (figure 2.1).

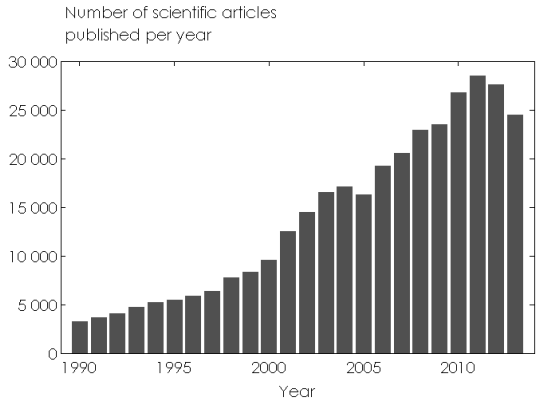


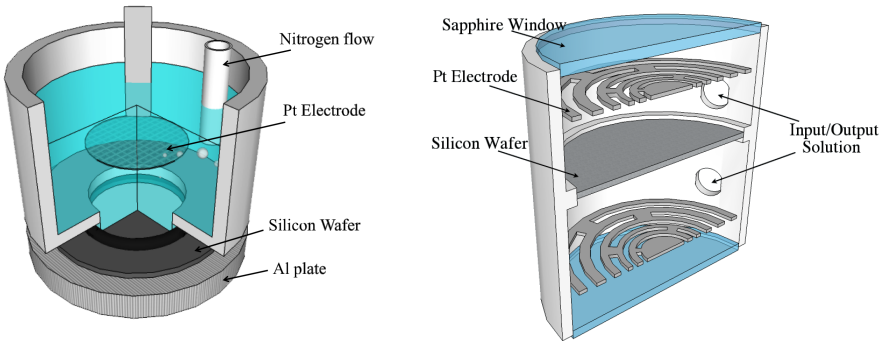
Figure 2.1: Number of scientific articles published by year. From data of Google Scholar (February 17, 2014).

2.1.1 Fabrication

Porous silicon can be fabricated using two main methods :

- Electrochemistry:
  - *Anodization* : Silicon in contact with an HF-containing electrolyte is etched under the application of an electric current [6, 7],
  - *Stain etching* : Silicon is etched under the action of spontaneous oxidation optionally enhanced by a catalyst and wet etching [8]. This method is also called *metal-assisted etching* (MAE).
- Dry etching: After applying a hard mask strewn with holes, porous silicon is anisotropically etched by plasma etching [9–11].

In this work porous silicon was fabricated by electrochemical anodization of silicon substrates. The anodization consists in the dissolution of silicon in HF-based electrolyte in the presence of an electric current. The etching is performed in a Teflon cell composed of one or two baths.



a. b.

Figure 2.2: Schematic images of anodization cells (a.) simple bath and (b.) double baths.

In a single bath cell (figure 2.2a.), the backside face of the silicon wafer is in contact with an electrode of copper or aluminum (anode). The etched surface is in contact with the electrolyte in which is immersed an electrode of platinum or gold. A double bath cell (figure 2.2b.) is composed of two baths separated by the silicon wafer. The two faces of the silicon wafer are in contact with an electrolyte (the same or different). Platinum or gold electrodes are immersed in each bath.

The porosification mechanism is still not fully understood. Several theories have been proposed [12]. Lehmann and Gösele [13] have proposed a model which is the most commonly accepted. The electrochemical reaction of dissolution of monocrystalline silicon is controlled by energy bonds involved. Without the application of the anodizing current, the silicon surface is inert in the HF solution. In the presence of the anodizing current, when a hole reaching the wafer surface, Si-H bonds are weakened and are substituted by stronger Si-F bonds (figure 2.3a.). The reaction is accompanied by the release of H_2 molecules in the electrolyte and electrons in silicon (figure 2.3c.).

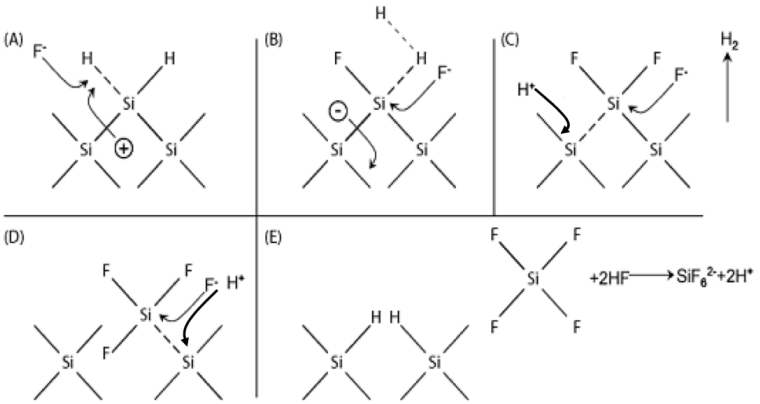


Figure 2.3: Dissolution mechanism of silicon anode in hydrofluoric acid (HF) associated with the porous silicon formation. Reproduced from reference [13]

Si-F bonds are more strongly polarized. Si-Si bonds are weakened and attacked by the electrolyte (figure 2.3d.). A SiF_4 molecule is released creating a gap in the substrate surface (figure 2.3e.). The surface modification results in a new local distribution of the electric field, with tip effect. The following reactions will take place preferentially to the bottom of created gaps favoring pore formation.

Pore walls are passivated by weakly polarized Si-H bonds. Because of the inhomogeneity of the electric field distribution, a space charge region (SCR) is created at the interface silicon/electrolyte on the pores walls. The SCR prevents lateral etching and accentuate the anisotropic etching of the pores (figure 2.4).

The thickness of this SCR depends on the current density and the doping of the substrate. It is thin for highly doped Si, while it is thick (a few tens of nanometers to several microns) for lightly doped Si. In p-type silicon, a pore wall is composed of two SCR. The thickness of the pore walls is two times the thickness of the SCR. In n-type silicon, holes, which initiate the dissolution, are minority carriers, and consequently their concentration is very low in pore walls which can be larger than two times the SCR thickness.

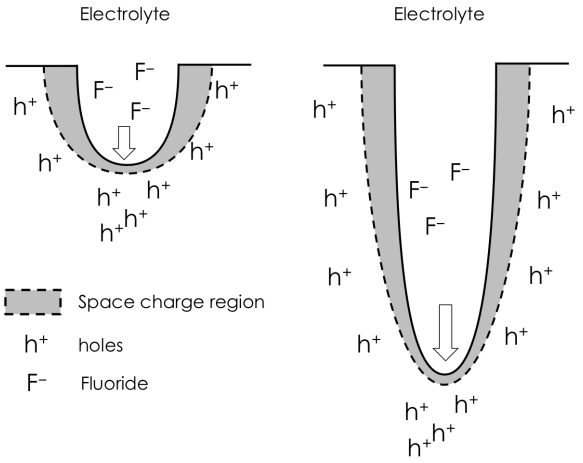


Figure 2.4: Growth of a pore. The space charge region tends to passivate the pore walls which promotes the the etching at the tip of the pore.

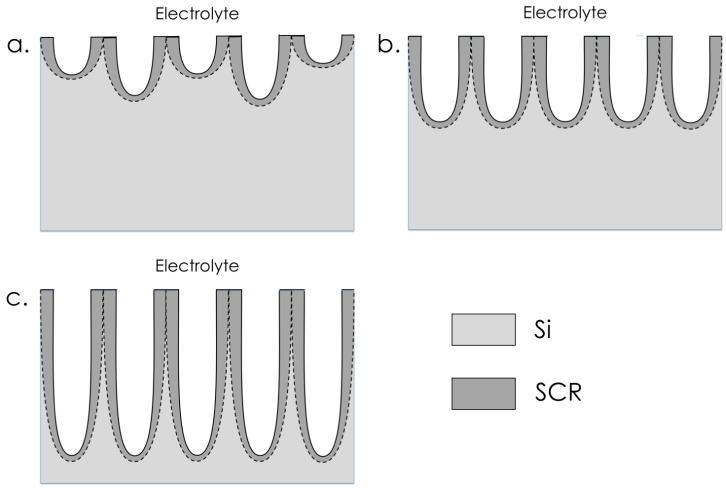


Figure 2.5: Mechanism of pore formation. Random pore initiation on the Si surface (a.), formation of SCR and directional growth of pores (b.), and dissolution advance only at the pore tips (c.).

The pore growth is performed in two phases: nucleation and growth. During the nucleation phase, the pores are initiated randomly at the silicon surface (figure 2.5a.). Then, the formation of the double SCR between pores promotes directional etching (figure 2.5b.). Finally, the etching occurs mainly at pore tips (figure 2.5c.).

To describe porous solids, five parameters are commonly used:

- *Porosity (P):* gives the ratio between the porous volume (V_{pores}) and the total volume of the porous structure (V_{total}), usually expressed in %,

$$P = \frac{V_{pores}}{V_{total}} \tag{2.1}$$

  However, determine V_{pores} and V_{total} is difficult to achieve. Gravimetric measurement is more convenient and is performed by weighing the sample before etching (m_1), after etching (m_2), and finally after chemical dissolution of the porous layer (m_3) [14].The volume of the pores is assumed to be equal to the volume of silicon that is removed during the electrochemical etching, which is related to the mass of the wafer before (m_1) and after (m_2) etching:

$$V_{pores} = \frac{m_1 - m_2}{\rho_{Si}} \tag{2.2}$$

  where ρ_{Si} is the density of elemental silicon. The total apparent volume of the porous film (including voids) can be determined from the mass of the wafer before etching (m_1) and the mass of the wafer after the porous layer has been removed (m_3):

$$V_{total} = \frac{m_1 - m_3}{\rho_{Si}} \tag{2.3}$$

  Applying Equations 2.2 and 2.3 to 2.1 yields Equation [14]:

$$P = \frac{m_1 - m_2}{m_1 - m_3} \tag{2.4}$$

- *Specific surface area:* is the area within the porous structure, reduced to its weight or volume, expressed in m^2/g or m^2/cm^3,

- *Pore diameter:* is the size of pore opening. Crystallites sizes are generally related to this parameter.

- *Pore distribution :* is the distribution of pores in the silicon surface (orderly, random, the pore density per unit area ...)
- *Thickness:* is the thickness of the porous layer.
- *Roughness* is a measure of the texture of a surface. It is quantified by the deviations in the direction of the normal vector of a real surface from its ideal form. There are different definitions of this parameter.
- *Tortuosity*, in the fluid mechanics of porous media, is the ratio of the length of a streamline (a flow line or path in pores) between two points to the straight-line distance between those points. It is the quality or state of being tortuous.
- *Thickness of pore wall* is the thickness of the silicon crystallite that separates two pores.

A classification of sizes of pore diameter (d) has been established dividing porous materials in : nanoporous (d $<$ 2 nm), mesoporous (2 nm $<$ d $<$ 50 nm) and macroporous (d $>$ 50 nm) [7].

2.1.1.1 Anodizing parameters

The electrochemical etching of silicon is strongly influenced by the anodizing parameters such as doping and orientation of the substrate, current density, hydrofluoric acid concentration and electrolyte composition.

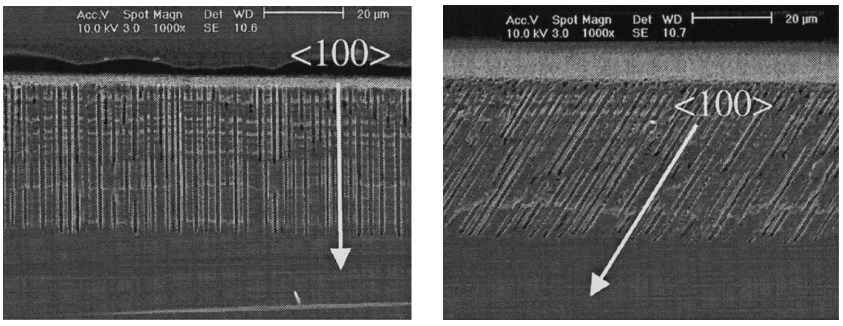
Substrate doping The substrate doping greatly influences the morphology of the porous layer (the pore diameter, the wall thickness, etching direction ...). The pore diameter may vary between about 1 nm to 10 μm. The other etching parameters also have a great influence on the morphology of the porous layer, which is why it is difficult to classify the type of porous silicon as a function of doping silicon. However, it is still possible to present the main trends [15]:

- moderately doped p-Si ($l0^{15}$-$l0^{18}$ cm^{-3}) : Pores are extremely small ranging typically from 1 to 10 nm.
- heavily doped materials, p^+-Si and n^+-Si ($> l0^{19}$ cm^{-3}) : Pores have diameters typically ranging from 10 to 100 nm.

- non-heavily doped n-Si ($< 10^{18}$ cm^{-3}) : Pores have a wide range of possible diameters from 10 nm to 10 μm.

- lowly doped p-Si ($< 10^{15}$ cm^{-3}) : two distinct distributions of pore diameters: large pores with a distribution of diameters in the order of μm and small pores on the order of nm.

Substrate orientation The morphology of microporous silicon is a sponge-like [7]. The pores of larger diameter (mainly macropores) appear straight and aligned. Macropores etching follows preferred crystalline directions <100> and <113> [16–18]. Depending on the wafer orientation, the pores have a vertical or oblique direction (figure 2.6).



a. b.

Figure 2.6: SEM picture of cross-sectional view of macroporous layer on p-type Si. The wafer orientation is (a.) <1 0 0> and (b.) <5 5 12>. Reproduced from reference [17]

Current density and anodization time The anodizing current density (J, mA/cm^2) is an essential parameter that affects the morphology of porous silicon. For a given concentration of hydrofluoric acid, the porosity and the etching rate increase with current density.

As mentioned in the Lehmann and Gösele model, a SCR is present at the interface between the silicon and the electrolyte. The interface can be assimilated to a Schottky contact. The SCR thickness essentially depends on the substrate doping.

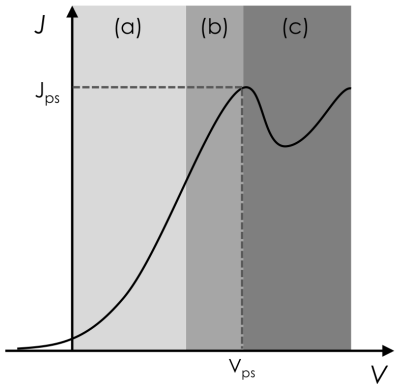


Figure 2.7: Reaction regions under anodic polarization: Porous silicon region (a); Transition region (b); Electropolishing region (c).

The figure 2.7 shows a typical J-V characteristic of a silicon anode. The curve has a peak (J_{etch}) dividing etching into two regimes (figure 2.8):

- Electro-porosification: For current density lower than J_{etch}, the anodic etching is limited by the supply of electric charges in the substrate and not by the diffusion of F^- ions in the electrolyte. The holes, few in number preferentially accumulate at the bottom of the pores under the action of the higher local electric field. The etching is essentially located at the pore tip. When the voltage increases, more and more holes pass through the depleted zone resulting in an increase of the current density. A wider pore surface is etched and the lateral etching becomes more important leading to an increase of the porosity.

- Electropolishing: For a current density of greater than J_{etch}, ion diffusion limits the anodic etching. The holes are distributed over the entire surface. F^- ions are attracted preferentially to surface defects in the action of the tip effect of the electric field and the surface is polished.

The boundary between these two regimes depends on the ion diffusion parameters: temperature and HF concentration.

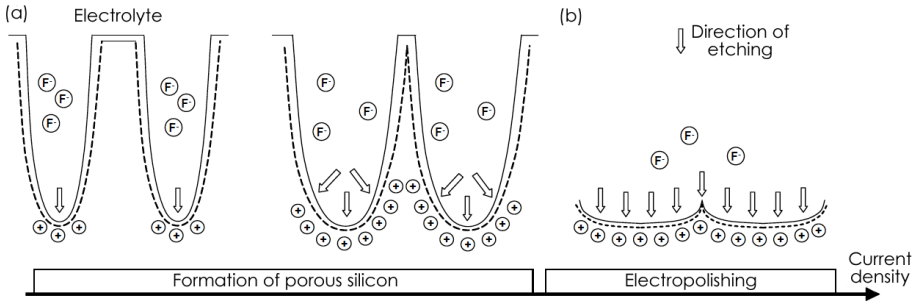


Figure 2.8: Schematic cross-sectional view of the pores. (a) The pore diameter increases with the current density. (b) When the current density exceeds J_{etch}, the pore coalescence causes the surface polishing. Reproduced and adapted from reference [19]

By modifying the current density over time during anodization, the pore diameter varies resulting in complex structures fabrication [20] (figure 2.9). If the increase of the current density over time is quite abrupt, etching changes from the electro-porosification regime to electropolishing regime and a cavity is formed under the porous layer. The porous membrane is released [21].

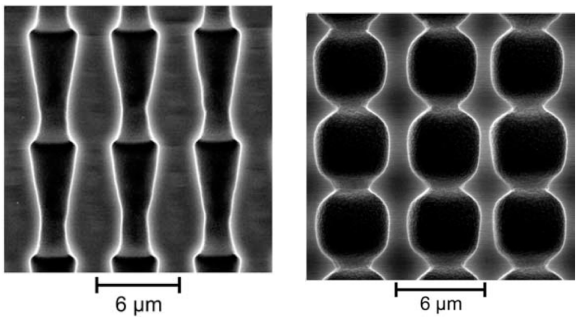


Figure 2.9: SEM picture of the cross-section of a regular array of macropore with variable diameter. The pore diameter varies depending on the depth. Reproduced from reference [20]

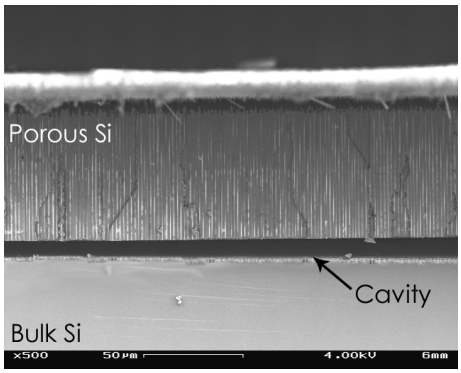


Figure 2.10: SEM picture of cross section view of macroporous membrane released by electropolishing. After the porosification of the membrane, the current density is abruptly increased and the etching is in the electropolishing regime to form a cavity under the porous membrane.

Electrolyte composition The electrolyte is composed in particular of hydrofluoric acid initially diluted in water. In contact with the electrolyte, the potential silicon native oxide is etched leaving bare silicon. Silicon is a hydrophobic material, a solution composed of HF and water does not fit fully into initiate pores. Also, during silicon dissolution, hydrogen bubbles formed are sticking to the surface and increase the inhomogeneity of the etching. These two problems are minimized by adding a wetting agent. The most commonly used are dimethylformamide (DMF), dimethyl sulfoxide (DMSO), ethanol, iso-propanol ...

The addition of a wetting agent also modifies the impact of doping of the substrate on the pore diameter for an HF concentration and a current density given.

2.1.1.2 Conclusions

The parameters described above have a large impact on the morphology of porous silicon. By controlling each of them, it is possible to achieve pore diameters ranging from a few nanometers to several microns and a range of porosity extending from 0 to more than 80 %. Well controlling these parameters is essential for optimizing devices incorporating a porous silicon layer.

2.1.2 Mass transfer in porous media

This section is intended to give an overview of different flow regimes depending on the dominant morphology of a porous medium. The knowledge of the relationship between flow and pore size is critical in choosing the type of porous silicon used for gas sensors. We begin by presenting the possible flows in porous media. Then we compare the dominant flows to optimize the pore diameter.

2.1.2.1 Diffusion regimes

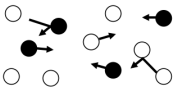
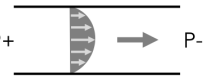
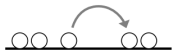
Model	Schema	Flow type
Molecular diffusion		Majority of collisions between molecules Kn << 1
Poiseuille flow		Flow by ∇P
Knudsen diffusion		Majority of collisions between molecules and walls Kn >> 1
Surface diffusion		Diffusion by "jumps" in absorbed phase

Figure 2.11: The main flows possible within a porous medium. Inspired from [22]

Mass transfer can be achieved by different flow. Molecular diffusion, Knudsen's diffusion, surface diffusion or Poisseuille flow (convective mechanism) are the main flows used to describe the mass transfer in porous media. (figure 2.11) [22].

We exclude Poisseuille flow since the flow is not forced into pores by an imposed pressure gradient on either side of the porous layer.

These models describe the transfer of material at different levels of porosity (macroscopic, mesoscopic and microscopic) by the introduction of diffusion coefficients. This diffusion coefficients depend on the different transfer mechanisms in a conventional diffusion law of mass under the effect of a concentration gradient.

The relative importance of molecular and Knudsen's diffusions depend on the dimensionless *Knudsen number* (Kn) comparing the mean free path of the molecule (λ) and the pore diameter (d_{pore}):

$$\lambda = \frac{k_B}{\pi\sqrt{2}\phi_{cin}^2}\frac{T}{P} \tag{2.5}$$

and

$$\mathrm{Kn} = \frac{\lambda}{d_{pore}} \tag{2.6}$$

where k_B is Boltzmann's constant (J/K), ϕ_{cin} is the kinematic diameter of a molecule (m), T is the temperature (K) and P is the total pressure (Pa).

It is then possible to study the influence of the pressure, temperature and pore diameter on λ and Kn to identify the regions of material diffusion (figure 2.12).

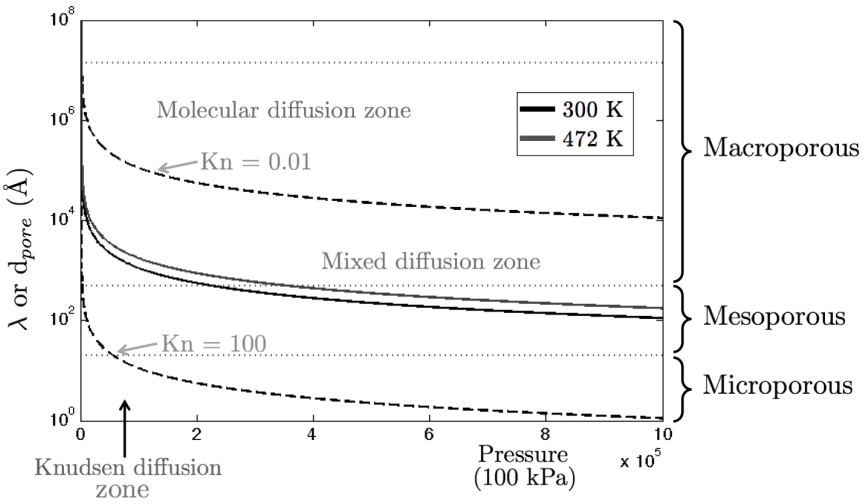


Figure 2.12: Mean free path for pure hydrogen gas and different diffusion regimes.

When the average pore diameter is greater than the mean free path of the molecule, Knudsen's constant is $\ll 1$, and the resistance of the

mass transfer is mainly due to intermolecular collisions. The movement of molecules is a pure molecular diffusion. In this case, the relative contribution of the Poiseuille flow regime depends on the pressure gradient between the two sides of the porous membrane. This is usually small and negligible.

Conversely, when the average pore diameter is less than or of the same order of magnitude as the size of the molecule (for example, in microporous), the Knudsen's constant is $\gg 1$ and the resistance of the mass transfer is mainly due to collisions molecule-walls, which is the Knudsen's diffusion similar to the ballistic transport of the molecules in the pores.

It appears that:

- Knudsen's diffusion is the dominant diffusion microporous materials especially for low pressure,
- molecular diffusion is dominant for macroporous pores especially at high pressure,
- temperature has a negligible influence on the choice of diffusion model,
- there is a very important area of operation where both Knudsen's and molecular diffusion are considered (mixed diffusion).

Note also that it may be added to the gaseous diffusion phase (Knudsen's and molecular diffusions), the influence of diffusion within the absorbed phase to the surface of the solid, due to the local difference concentration. This is the surface diffusion.

Diffusion coefficients comparison

The mass transfer theory in porous media is presented in Appendix A. In the gas sensing by a porous material, it is more advantageous to maximize the diffusion rate in the pores so that the gas is quickly in contact with the entire pore surface. The high diffusion rate is reflected in the equation A.3 (Appendix A) by a high diffusion coefficient. Since the expression of the diffusion coefficient varies depending on the diffusion

regime, we present in this section the comparison of diffusion coefficient for molecular diffusion and Knudsen's diffusion. The calculations of molecular and Knudsen's diffusion coefficients are presented in Appendix A.

Figure 2.13 shows the evolution of molecular diffusion coefficient and Knudsen's diffusion coefficient as a function of pore diameter. The evolution of Knudsen's number (Kn) is also shown to delineate the different diffusion regimes.

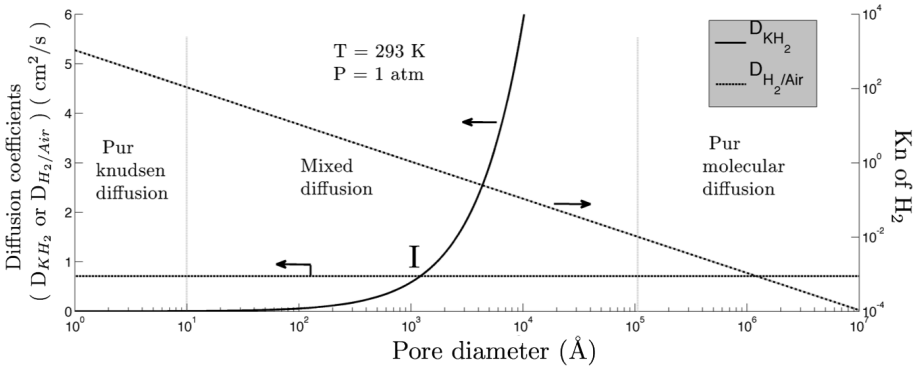


Figure 2.13: Comparison of the molecular diffusion coefficient ($D_{H_2/Air}$) and Knudsen's diffusion coefficient (D_{KH_2}) as a function of pore diameter and the various diffusion regimes for dihydrogen ($T = 293$ K and $P = 1$ atm). Point I is the equivalence point between the two diffusion coefficients (Kn = 1).

For pore diameters below 1 nm, the mass transfer is a pure diffusion of Knudsen (Kn $\geq$ 100). The mean free path of the molecules is significantly greater than the diameter of the pores and their movement is limited by the shock with the pore walls. Only Knudsen's diffusion coefficient (D_{KH_2}) is taken into account and its value is less than 10^{-2} cm^2/s. It greatly varies depending on the pore diameter and is proportional to $T^{1/2}$.

Conversely, the dihydrogen diffusion in pores whose diameter is greater than 10 μm is a pure molecular diffusion (Kn $\leq$ 0.01). In this case the mass transfer is limited by the shock of molecules between them. Only

the molecular diffusion coefficient ($D_{H_2/Air}$) is to be considered. It varies mainly depending on the pressure P and is proportional to $T^{3/2}$. Conversely, it does not depend on the pore diameter.

In the porous layer whose pore diameter is in the range from 1 nm to 10 μm, diffusion is mixed. Molecular diffusion and Knudsen's diffusion co-exist. For small pore diameters, the diffusion is mainly limited by Knudsen's diffusion coefficient. This increases to the point I (figure 2.13) where both diffusion coefficients are equivalent ($D_{KH_2} = D_{H_2/Air}$ en Kn = 1). For pore diameters greater than the point I mass transfer is limited by molecular diffusion.

In reality, mass transfer does not change suddenly from Knudsen's diffusion to molecular diffusion near to the point I on figure 2.13. A "resistance in series" approach enables us to consider the two diffusion regimes simultaneously introducing an effective diffusion coefficient (D_{eA}) of species A in B [23]:

$$\frac{1}{D_{eA}} = \frac{1 - \alpha y_A}{D_{AB}} + \frac{1}{D_{KA}} \tag{2.7}$$

where y_A is the mole fraction of species A in the mixture and

$$\alpha = 1 + \frac{N_B}{N_A} \tag{2.8}$$

In the case where species A is very low in concentration compared with the species B (y_A is close to zero), equation 2.7 reduces to

$$\frac{1}{D_{eA}} = \frac{1}{D_{AB}} + \frac{1}{D_{KA}} \tag{2.9}$$

According to the latter relationship, diffusion is limited by the lower diffusion coefficient.

The effective diffusion coefficient is established on a diffusion in a non-porous volume. It remains valid in a porous material with cylindrical pores and properly aligned and parallel. Much of the porous material does not have the morphology and pores of various diameters are twisted and interconnected with one another and the path for the diffusion of the gas molecule within the pores is "tortuous". In these cases the diffusion coefficient is corrected by the factor τ, the *tortuosity* [23, 24]:

$$D'_{eA} = \frac{1}{\tau} D_{eA} \tag{2.10}$$

where

$$\tau = \left(\frac{L_e}{L_p} \right)^2 \tag{2.11}$$

where L_e is the tortuous flow path through the medium and L_p is the physical length of the porous medium.

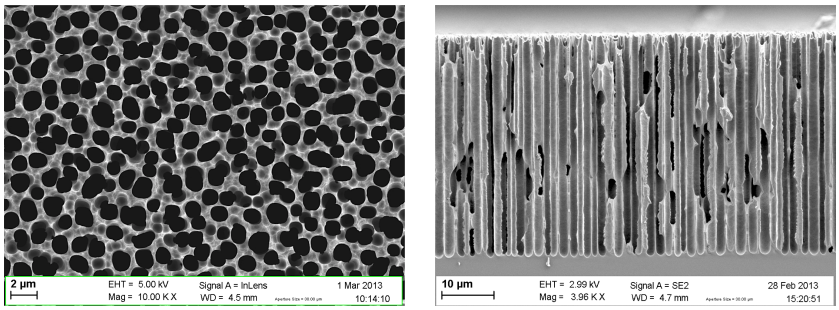
The tortuosity, τ, is the ratio between the length of the path actually runs through by the molecules and the path length if the pores were straight and aligned. τ is generally determined experimentally.

Depending on the pore diameter (d) of the porous layer, the tortuosity varies as:

- The microporous silicon ($d < 2$ nm) has a sponge-like structure, so $\tau >> 1$.
- The mesoporous silicon (2 nm $< d <$ 50 nm) has a sponge-like structure for low porosities ($\tau >> 1$). More the porosity increases, more aligned the pore [25] are and $\tau \geqslant 1$.
- The macroporous silicon ($d >$ 50 nm) shows a straight and aligned pore structure and $\tau \simeq 1$.

To conclude, at constant temperature and constant pressure, a large pore diameter increases the diffusion rate of hydrogen molecules in porous media. Indeed, in Knudsen's diffusion, the pore diameter being less than the mean free path, molecules collide more frequently, which impede their progress within the pore. For the rapid diffusion of molecules in the porous layer, it is advantageous to increase the pore diameter beyond 100 nm (for H_2 in air at $T = 293$ K and $P = 1$ atm). Also, the morphology of the pores should be straight and aligned and the tortuosity of the pores (τ) the closest to 1.

The macroporous silicon has ideal characteristics for increasing the diffusion rate. Using of an electrolyte composed from HF:H_2O:DMF (1:1:8), it is possible to produce a porous p-type silicon with standard-doping (10 - 20 Ω cm) with a pore diameter ≈ 1.4 μm and having a straight and aligned cylindrical morphology (figure 2.14).



a. b.

Figure 2.14: SEM picture of the (a.) top view and (b.) cross-section view of macroporous silicon formed on p-type silicon, with a standard doping (10 - 20 Ω cm).

2.2 Application fields of porous silicon

pSi thanks to its remarkable properties such as large surface area, simple fabrication methods, poor thermal conductivity and optical properties is used in a variety of different applications. This section provides a non-exhaustive list of applications for pSi. I list them divided into two parts : on the one hand, applications for micro- and mesoporous silicon, and applications for macroporous silicon, on the other. This differentiation is not strict. Some applications usually intended for microporous silicon are carried out with macroporous silicon and inversely.

Micro- and mesoporous silicon applications

• **Thermal insulation** : pSi has a thermal conductivity several orders of magnitude smaller than bulk silicon (21 to 2.3 $W(m \cdot K)^{-1}$) for mesoporous compared to 149 $W(m \cdot K)^{-1}$ for bulk silicon) [26,27]. This property was one of the first to be exploited in the fabrication of new microsystems. After porosification, a standard process can be performed on the wafer (figure 2.15). The porous layer provides thermal insulation between the device and the bulk substrate [28]. To improve the thermal insulation, the porous structure can be released. In this way the air cavity under the porous layer and the porous layer itself form a double thermal insulation [29]. Due to the issue of electrode integration, this type of structure is only possible on a micro- or mesoporous layer, but not on a macroporous layer.

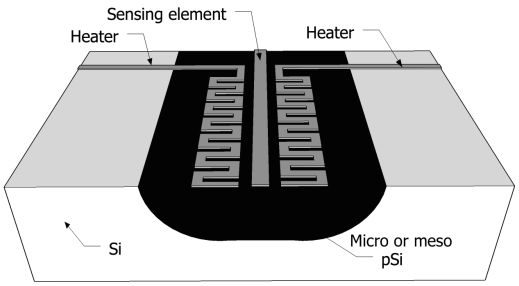


Figure 2.15: The porous layer thermally insulates the heaters and the substrate. Heat dissipation is reduced. The electrical power used by the heaters to heat sensitive components is largely lowered. This type of structure is only possible on a micro- or mesoporous layer.

• **Sacrificial layer**: In microfabrication, freestanding systems, such as beams or membranes, are built using a sacrificial layer. In this process, the suspended part is constructed and structured on a sacrificial layer, which is then selectively removed. The etching of the sacrificial layer creates a cavity under the structural parts (figure 2.16). It is important not to damage the structural layer by removing the sacrificial layer. Usually, chemically different materials are used for the sacrificial layer and the device allowing thus the selective etching. The use of a sacrificial layer enables to avoid double-sided lithography and often difficult and delicate backside etchings.

pSi as a sacrificial layer provides several advantages [30]. First, pSi is easy, fast and cheap to implement. Second, pSi allows achieving thick layers (several tens of microns and more), which is generally not possible with other materials traditionally used as a sacrificial layer. Third, by applying the appropriate, the shape of the porous layer can be well controlled. In addition, the chemicals used to produce and etch it can be CMOS-compatible.

The selective etching can be done in various ways. The commonest technique is are the pSi etching by highly diluted alkaline solutions, especially KOH (17 μm/min [31]) and TMAH [32], sodium hydroxide (NaOH) [33] or HF [34].

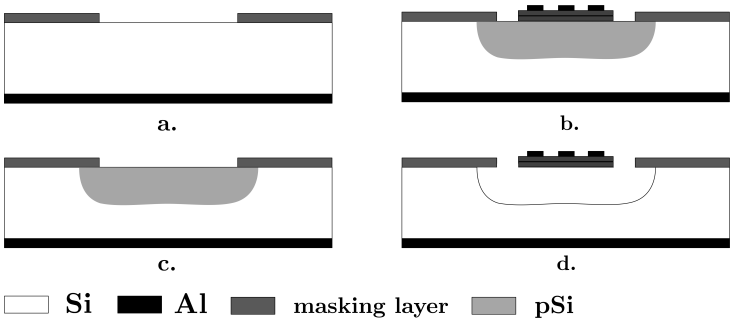


Figure 2.16: The process sequence for freestanding systems with sacrificial layer technology. (a.) metal deposition on backside, masking layer deposition and patterning; (b.) pSi formation; (c.) system layer deposition and patterning; (d.) pSi dissolution to release the system.

• **Optical and photonic layers**: The discovery of luminescence in the visible spectrum of pSi by Canham LT in 1990 [4] revealed the potential of pSi. Before this discovery, pSi has not generated much interest in the scientific community. Luminescence is the light emission following the excitation of electrons by an electric current (Electroluminescence [5]) or an illuminance (Photoluminescence [35]). Using the same material for optical and electronic co-integrate on the same chip is a crucial economic issue for the microelectronics industry. However, efficiency are currently too low for porous silicon to compete with III-V material.

Luminescence depends on the porosity of the porous layer but also the compound located in the interstices. This property has been extensively studied to achieve a multitude of devices for the detection of several compounds. When a compound penetrates into the porous layer, a shift of the spectral response of luminescence appears which causes a color change or a photoluminescence extinction of the porous layer [36,37] (figure 2.17). This shift is directly related to the compound. The distinction between different compounds is possible making selective detection. This principle enables the detection of gaseous or liquid compound [38] and biological compound [39–42].

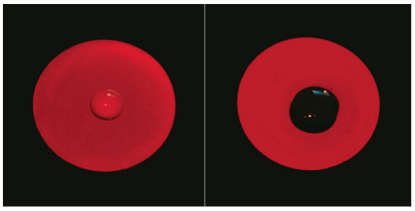


Figure 2.17: The images show two silicon chips that have circles of luminescent porous Si etched into them, photographed under ultraviolet light illumination. Liquid drops are deposited on the surface of the porous silicon sample. The drop on the left is pure water, the one on the right is 40% ethanol in water. Pure water does not infiltrate the hydrophobic, hydrogen-terminated porous Si surface, whereas the ethanol solution infiltrates the pores and quenches photoluminescence. Reproduced from reference [37].

The structure of pSi is also used as a "photon trap" or the antireflection properties in photovoltaic applications [43, 44] (figure 2.18). Bragg reflectors [45] and Fabry-Perot filters [46] have been realized by modulating the pSi porosity. This modulation is achieved by varying the etching parameters. These structures are also used in sensing applications [47].

Photonic microstructures based on nanoporous silicon as microcavities [48] or photonic waveguides were also fabricated [49]. Using the micromachining techniques described in the previous section, macroporous silicon has been also used to produce photonic crystals [50–52].

• **Energy storage and conversion :** Portable electronic devices require a power source to operate. To achieve higher levels of miniaturisation, the dimension of the power source should be reduced, and possibly the ability to stoke energy increased. The large surface area available in pSi offers a great potential to store large amounts of electrical energy [53–56] (figure 2.19) and makes pSi a good candidate for the next generations of batteries.

Another possible application of porous silicon is the storage of chemical energy for fuel cells or engine. Hydrogen is a clean fuel often mentioned as the energy source of the future.

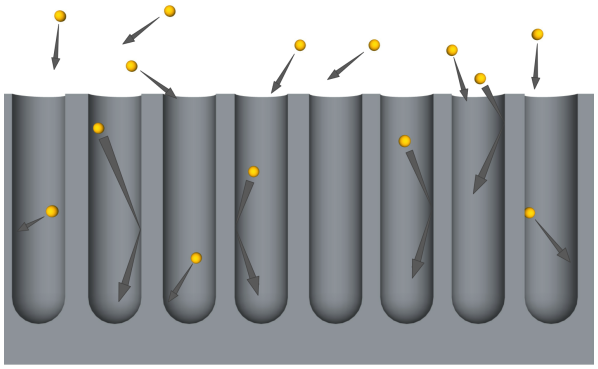
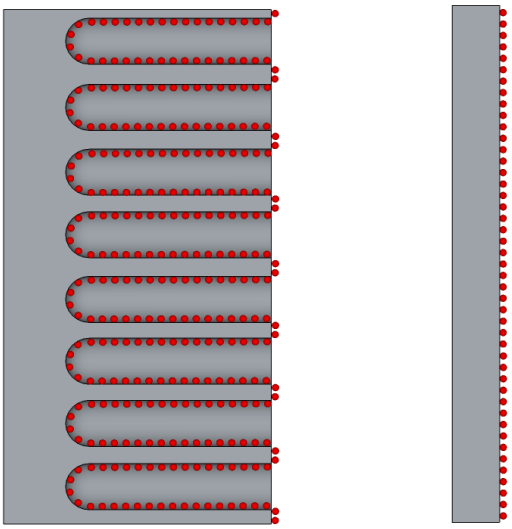


Figure 2.18: The pSi is used as "photons trap". Photons (shown schematically by balls) enter in the pores and undergo multiple reflections from the pore walls. Depending on the porosity, a high percentage of photons are absorbed in the porous layer.



a. b.

Figure 2.19: Electrical charges (represented by small spheres) are stored on the silicon surface. The higher surface of pSi (a.) in comparison with a flat silicon surface (b.) allows the storing of higher number of charges.

However, hydrogen is an explosive gas (particularly dangerous even when the concentration exceed values relatively low (4%)). Therefore, devices capable of storing large amounts of this gas are essential to its widespread use. Due to the large amount of surface area per unit volume of material in pSi, large amounts of gas such as hydrogen can be adsorbed and stored. He *et al.* [57] have made nanoporous silicon layers which can absorb 4.73 10^{-5} mol/gram.

In a fuel cell, the energy obtained making react hydrogen and oxygen is directly converted into electric energy. Fuel cells offer a significant advantage over traditional combusting-based thermal energy conversion, because they provide efficiencies of electrical power supply in the range of 35 to 55%, causing very low level of pollutant emission [58]. The high porosity of pSi and the very large surface-to-volume ratio ensures proton conductivity comparable to that of polymeric membranes such as Nafion® [59, 60].

Macroporous silicon applications

• **Filtration and chemical micro-reactors**: filtration is the action to separate certain components from a medium by letting pass these through a filter (figure 2.20). The medium may be a liquid [61] or a gaseous mixture [62, 63]. Filtration is also used to separate biological components [64]. For example, Striemer *et al.* [65] fabricated a porous silicon membrane capable of retaining proteins while permitting the transport of small molecules at rates an order of magnitude faster than existing materials or separate differently sized proteins under physiological conditions.

Porous membranes functionalized with catalytic materials, are transformed into chemical micro-reactors. The gas that flows through the membrane, reacts during the transit time and modified gas exits the membrane. For example for resistive gas sensors, it is an advantage to convert carbon monoxide (CO) in non-detectable carbon dioxide (CO_2) to enhance the selectivity to other gas molecules. [66].

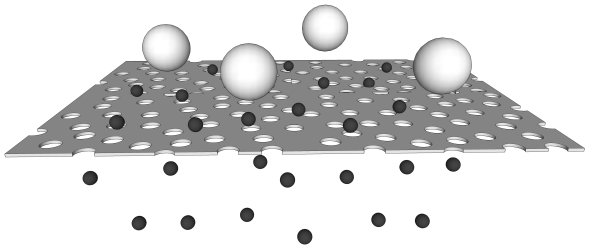


Figure 2.20: Species that have dimensions smaller than the pore size pass through the porous membrane. Other species are stopped.

• **Electrochemical micromachining of Silicon (ECM)**: This technique enables the fabrication of microstructures (suspended or not) with a high aspect ratio. The fabrication of microstructures and microsystems by ECM technology is carried out according to the following main technological steps [67], which are sketched in figure 2.21. The starting material is n-type silicon, of orientation (100), with a thin silicon dioxide layer on top. The pattern of the microstructure to be fabricated is defined on the SiO_2 layer by standard lithography, and buffered HF (BHF) etching (figure 2.21a), replicated (seed-point formation) into the silicon surface by potassium hydroxide (KOH) etching through the silicon dioxide mask (figure 2.21b), and finally grooved into the bulk material with an initial anisotropic phase (figure 2.21c), used to etch the seed pattern deep into the substrate and create high-aspect-ratio microstructures, and a final isotropic phase (figure 2.21d), used to release part of the etched microstructures from the substrate and, eventually, yield them to be freestanding. A further thermal oxidation step can also be performed to grow a 100 nm-thick conformal silicon dioxide layer (figure 2.21e), to be used as an insulation layer, on which a metal contact for actuation and/or sensing can be deposited by quasi-conformal metal sputtering (figure 2.21f).

This process has allowed the fabrication of a variety of complex MEMS structures (figures 2.22) such as suspended masses (for accelerometer) [68] or microgrippers [67]. It has the advantages of high flexibility and low cost.

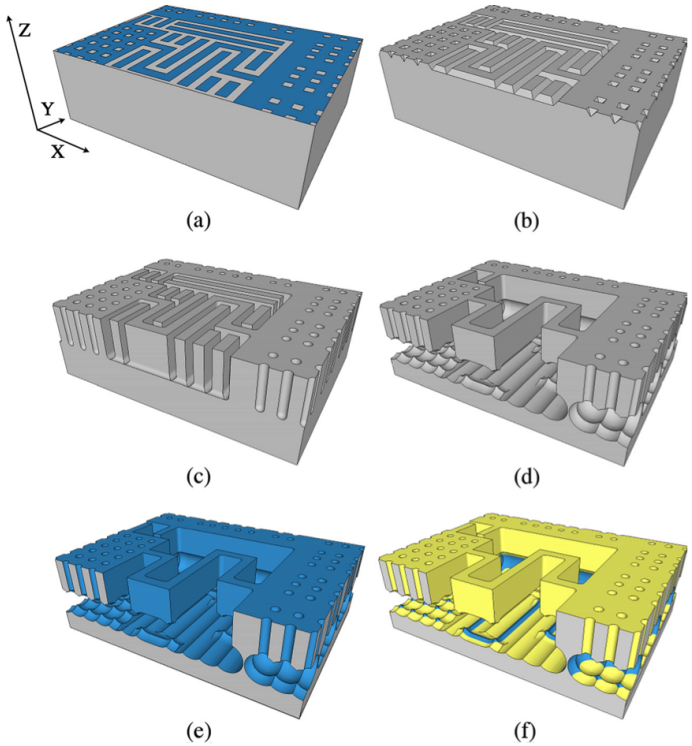
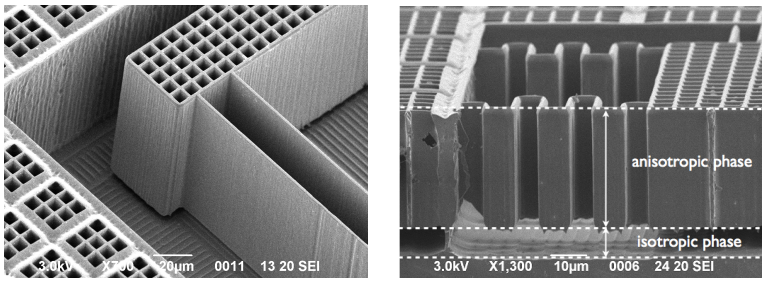


Figure 2.21: The main technological steps for the fabrication of microstructures and microsystems by ECM technology: (a) definition of the microstructure layout on the silicon dioxide layer, which is on top of the silicon substrate; (b) replication of the microstructure layout into the silicon surface by KOH etching (pore seed-point formation); (c) anisotropic electrochemical etching step to create a high aspect ratio structure; (d) isotropic electrochemical etching to release the structure from the substrate; (e) oxidation of the silicon to be used as an insulation layer; (f) metal deposition for electrical actuation and/or sensing. Reproduced from reference [67]

• **Electrical sensing layer :** pSi (micro-, meso- and macroporous) is used in many sensing applications. pSi is used in various manners as sensitive layer. Measurands targeted by pSi are very diverse and can be chemical, physical and biological. To report an exhaustive list of all the applications would be very long and unnecessary. In this work, only the commonest sensing applications are mentioned. An entire section will be dedicated to the state of the art of porous silicon based gas sensors.



a. b.

Figure 2.22: Complex MEMS suspended structures performed by ECM process. (a.) Tilted view and (b.) cross-section view. Reproduced from reference [67].

When a stress is applied to a porous silicon layer, the electrical conductivity varies. Energy bands of silicon nano-crystallites are altered by this stress [69]. The piezoresistive coefficient of a quantum confined structure is more than that of the bulk structure [70]. Kolokolov *et al.* [71] propose that the hole energy and the hole conduction mass suffer a larger shift on application of stress compared to that in the bulk Si.

The electrical conductivity of pSi varies also with illumination. pSi-based photodiodes were carried out for photodetector applications [72–75]. Abd Rahim *et al.* [76] developed photodetector exhibits lower dark (two orders of magnitude) and higher photocurrent compared to a conventional Si device and exhibits 158 times higher gain compared to the conventional Si device at 2.5 V.

Biology and medicine are two fields of applications that resort increasingly micro and nanotechnology to detect small amounts of bioparticles in a mixture. A common example is the detection of bacteria in the blood (due to sepsis). Micro and nanotechnologies can achieve more accurate, faster and less expensive diagnostics. These benefits are extremely important in the field of health. The demonstrated biocompatibility of pSi has attracted the attention of researchers in the biosensing field. Many of the applications of pSi as biosensor are addressed to the detection and sensing of complex biomolecules [77]. The target analytes are DNA [78–81], glucose [82], bacteria [81, 83–85], viruses [86], catechol [87], triglycerides [88], penicillin [89], etc.

2.3 Porous silicon gas sensors

The operating principle of a porous silicon sensor is based on the variation of the physico-chemical properties of the porous layer in the presence of the analyte [90]. The electrical and optical measurements are the two major principles of operation. For electrical measurement, adsorption and/or condensation of specific gas species on porous silicon material modify electrical properties of porous layer as dielectric constant, conductivity ... and can be quantitative monitored by the measurement of variation of different parameters (e.g. capacitance, current, resistance) as a function of the gas concentration. For optical measurement, the interaction of specific gas species with porous silicon material modifies optical properties of porous layer as refractive index, radiative recombination processes ... and can be quantitative monitored by the measurement of variation of different parameters (e.g. photoluminescence spectrum, reflected, transmitted, and diffracted optical power) as a function of the gas concentration.

Barillaro [90] listed ten main architectures: (i) five for the electrical domain (capacitor, Schottky-like diode, resistor, FET-like transistor, and junction-like diode) and five for the optical domain (single layer, waveguide, Bragg mirror, resonant cavity, and rugate filter). In this work, we are primarily concerned with electrical measurements. We invite the reader interested in the optical measures to consult the reference [90].

Capacitor architecture involves placing two electrodes on the porous layer (figure 2.23a.) [91–94] (figure ...) or an electrode on the porous layer and the other on the wafer backside (figure 2.23b.) [95, 96] and monitor the change in the capacitance-voltage plot (C-V) and a shift of the flat band voltage proportional due to presence of analytes species (figure 2.24). Following the same idea, Archer *et al.* [97] developed a pSi sensor where contacts are evaporated onto the backside of a Si wafer.

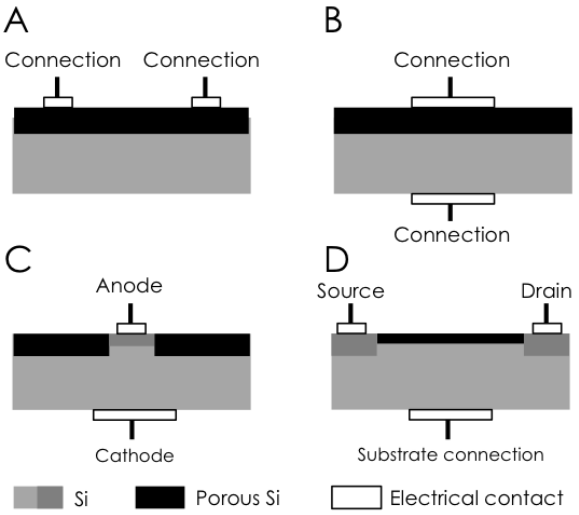


Figure 2.23: Schema of different gas sensor structures based on porous silicon.

Schottky-like diode architecture is formed by contacting a metal and a semiconductor. The electrical contact is nonlinear. The Fermi level of the semiconductor is curved to align with the Fermi level of the metal forming a potential barrier for a quantity equal to the difference between work functions of the two materials (the Schottky barrier height). The potential barrier depends on the target gas concentration in the gas mixing. Indeed, gas molecules adsorbed on the surface of the porous silicon diffuse through the metal film to the metal/porous silicon interface. At the interface, the gas molecule form a dipole layer, which changes the work function of the metal, and thus the height of the Schottky barrier [98]. This change in the barrier height is proportional to the number of absorbed molecules that diffuse into the metal, and thus is proportional to the concentration of gas. This change in the height of the Schottky barrier causes a change in the current-voltage characteristics (IV) (figure 2.24). Two structures exist: two electrodes on the porous layer (figure 2.23a.) [99,100] or an electrode on the porous layer and the other on the wafer backside (figure 2.23b.) [101–106] or on the front side but outside the porous surface [107].

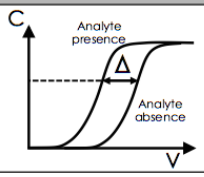
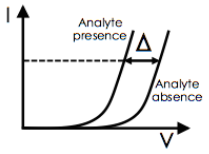
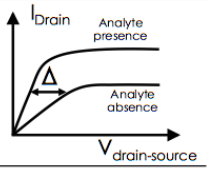
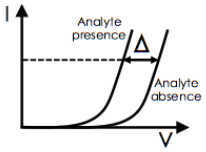
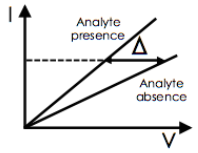
Sensor architecture	Physical parameter	Sensed quantity	
Capacitor	Dielectric constant	Capacitance	
Schottky-like diode	Energy barrier / Conductivity	Current	
FET-like transistor	Conductivity / Dielectric constant	Current / Impedance	
Junction-like diode	Energy barrier / Conductivity	Current	
Resistor	Conductivity	Resistance	

Figure 2.24: The main architectures of gas sensor based on porous silicon and the measured physical parameter. The last column gives a schematic of the measurement.

FET-like transistor architecture uses a field effect transistor (FET). Porous silicon layer is used as the gate (figure 2.23d.). As for the Schottky-like diode architecture, the absorbed gas molecules diffuse to the porous Si/Si interface altering the band bending of junction and a change of free carrier concentration in the silicon channel directly below the porous sensing layer, which influences the conductivity between the source and the drain (figure 2.24) [97, 108–114]. A second gate is sometimes placed on the back side to carry out a feedback loop.

Junction-like diode architecture consists of a crystalline p^+-n silicon diode is surrounded by a porous layer (figure 2.23c.). Adsorption of molecules in the porous material modifies the electrical properties of the p^+-n diode interface and in turn the diode current (figure 2.24) [115–117].

Resistor architecture operates on the measurement of the resistance variation of the porous silicon layer (figure 2.24). Resistor architecture sensor uses the principle that the electrical properties of porous silicon change when it is exposed to gas. Three structures exist: two electrodes on the porous layer (figure 2.23a.) [91, 118–136]; an electrode on the porous layer and the other on the wafer backside (figure 2.23b.) [137]; two electrodes on the porous layer backside [138]. In these structures, silicon substrate is inactive in gas detection. Furthermore, since it is much more conductive than porous layer, it can be a source of problems or noise in the measurement. An alternative to remove the silicon substrate, is to release the porous membrane and to place the freestanding membrane on an alumina substrate patterned by interdigitated electrodes [139, 140].

Bare porous silicon is used for the detection of humidity, organic vapors (alcohol, ether, aromatic and chlorinated hydrocarbon, etc.), and some gas as NO_x, Cl_2, Br_2 [7, 38]. Furthermore, pSi has been explored for electrical sensing of some organic solvents and molecules in liquid phase like acetone, benzene, toluene, acetonitrile, ethanol, chloroform, methanol, 1-propanol [97, 141]. However, the pSi sensitivity to all these various components gives a poorly selective measurement. The functionalization of the porous silicon (e.g., oxidation, hydrosilylation, carbonization, metalliza- tion, etc.) increases the sensitivity and selectivity, but also can render pSi sensitive and selective to other gases like CO_x, NH_3 [126], O_2, H_2, HCl, SO_2, H_2S, PH_3 ... Au_xO, Pd, $TiO_{2-x}N$ and SnO_2 are example of functionalization achieved [38]. Functionalization is studied in more detail in the chapter 4.

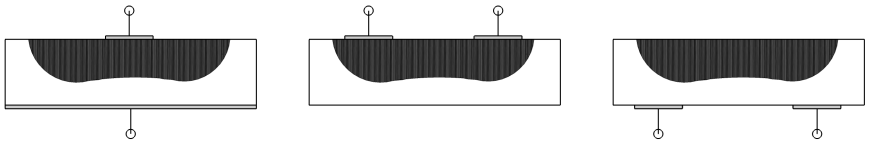
2.4 Why to miniaturize electrodes?

In the detection by resistive measurement, the sensitive layer is probed by an electric current. The electrical potential is imposed and electric current is measured or the current is applied and the electric potential is measured. These measurements are generally carried between the electrodes integrated into sensitive layer. The layout, size and disposition of electrodes can drastically influence the quality of the measurement.

The design of a new device must take in consideration the impact of the electrode position on the measurement quality. Also, it is essential to identify the area of the sensing layer probed by the electrodes. Indeed, a thick layer is useless if the sensing region probed by the electrodes is superficial. Conversely, electrodes placed in unsuitable locations probe also out of the sensing layer which may decrease the sensitivity or be a source of noise in the measurement.

One of the greatest properties of porous silicon as sensitive layer is its high surface to volume ratio. This morphology is very interesting for sensitive applications of surface reaction (as adsorption ...) since a large number of reaction sites are concentrated in a small volume. To take advantage of this property, the volume of porous silicon must be correctly probed. A too deep penetration of the electric current lines induces a measurement of nonporous silicon far from the volume of sensitive layer. Conversely, a penetration too superficial of the electric current lines does not draw the advantage of the sensitive layer volume.

The penetration depth depends largely on the positioning of the electrodes. Usually, two geometries are commonly used : the transverse and longitudinal geometries. In transverse geometry, electrical contacts are coated onto the sensitive layer and the backside of the wafer [142] (figure 2.25a.). The electric current is parallel to the thickness direction of sensitive layer. In contrast, in longitudinal geometry, both electrical contacts are coated on both sides of the sensitive layer [143–146] (figure 2.25b.). A third geometry (backside geometry) was also performed in which both electrical contacts are coated on the backside of the wafer [97] (figure 2.25c.).



a. b. c.

Figure 2.25: Patterns of three positions of the electrodes relative to the sensitive layer. (a.) Transverse geometry: electrical contacts are coated onto the sensitive layer and the backside of the wafer. (b.) Longitudinal geometry : electrical contacts are coated on the sensitive layer. (c.) Backside geometry: electrical contacts are coated on the backside of the wafer.

Transverse and Backside geometries (figure 2.25a. and c.) require that the electric current crosses the nonporous silicon. The sensitive layer is usually much thinner than the nonporous layer, a large part of electric current is not involved in the probing of the sensitive layer. The sensitivity of the measurement decreases. Furthermore, the electric current out of the sensitive layer is subject to changes in electrical properties of the nonporous silicon, which can be a source of noise in the measurement. Longitudinal geometry tends to concentrates the electric current in the sensitive layer volume.

First, let's consider an isotropic sensitive material. The Appendix F.1 presents the simulation of the variation of penetration depth of electric current in a wafer depending on the electrodes spacing. For this study, we arbitrarily set the thickness of the sensitive layer to 50 μm. This thickness is in the order of magnitude of that used in the literature of macroporous silicon-based gas sensors [120, 141, 147–151]. The results show that micrometric dimensions for the width and spacing of the electrodes are necessary to concentrate the electric current lines in the volume of an isotropic sensitive layer.

In the particular case of the macroporous silicon and its large and straight pores, the electrical properties of the sensitive layer are not isotropic. Three cases are possible : the current flows only in the sensitive layer (figure 2.26a.), only in the bulk substrate (figure 2.26b.) or both.

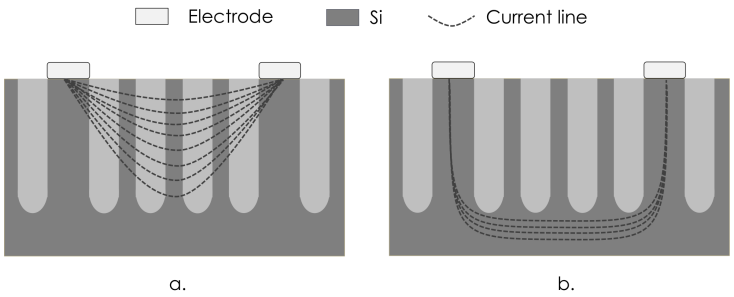


Figure 2.26: Depending on the properties of the sensitive layer, two paths are possible for the electric current (a.) The electric current passes through the walls of the porous layer or (b.) the electric current passes through the thickness of the porous layer then it passes under the porous layer and again passes through the thickness of the porous layer.

In the case where the electric current is able to pass through the walls of the porous layer indifferently in all directions, the conclusions of the simulations in Appendix F.1 remain relevant: micrometric dimensions for the width and spacing of the electrodes are necessary to concentrate the electric current lines in the volume of the sensitive layer.

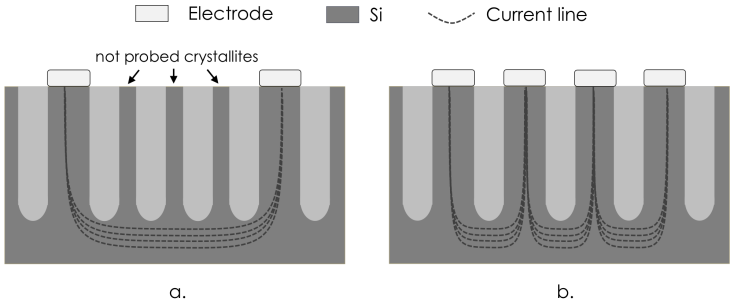


Figure 2.27: Schematic view of the cross-section of the porous silicon when the electric current passes under the porous layer. (a.) When the electrodes are widely spaced, silicon crystallites between the electrodes are not involved in the measurement. (b.) Reduce the electrode spacing maximizes the number of crystallites involved in the measurement.

Now, let's consider the anisotropy of the macroporous silicon layer. We assume that the resistivity in the thickness direction is lower than the resistivity in the width direction of the porous layer. If this difference is so high, the current injected from an electrode crosses the entire thickness of the porous layer, then it passes under the porous layer to the next crystallite with another electrode on top and it crosses again the porous layer thickness to reach the electrode (figure 2.27a.). In this configuration, the crystallites located in the space between the electrodes are not involved in the measurement. In this case, the spacing between the electrodes must be decreased to maximize crystallites numbers involved in the measurement (figure 2.27b.). This is achieved by using a micrometric pattern for the width and spacing of the electrodes.

To conclude, there are different geometries to place the electrodes around a sensitive layer. Placing two electrodes on the sensitive layer is the best geometry to minimize the passage of electric current in the nonporous silicon layer, as this part of the current is not involved in the measurement. However, we have shown that decreasing the electrode spacing shorter than the thickness of sensitive layer minimizes the part of electric current that cross the bulk substrate. In the particular case of anisotropic sensitive material as the macroporous silicon, two electrical paths are possible. We have shown that in both cases, a micrometric pattern of electrodes is required to maximize the concentration of electric current in or near the volume of the macroporous silicon, thereby increasing the quality of the measurement.

2.5 Techniques of metal electrode integration on macro-pSi

In silicon microtechnologies, the electrodes are generally made of metal and are usually obtained by patterning metal layers evaporated or deposited on the substrate surface. This deposition is carried out after the porosification of the macroporous layer. Indeed, the presence of the electrodes during the porosification involves several problematic reactions we discuss in the next chapter.

Due to the high macroporous silicon surface roughness (figure 2.28), the patterning of electrodes with few microns dimensions is a challenge. First, the standard photoresist on the macroporous layer does not spread

out uniformly [152]. Then, during the metal deposition, the metal is deposited in the portion above the porous layer, and partially into the pores. This problem does not ensure good continuity within the electrode length.

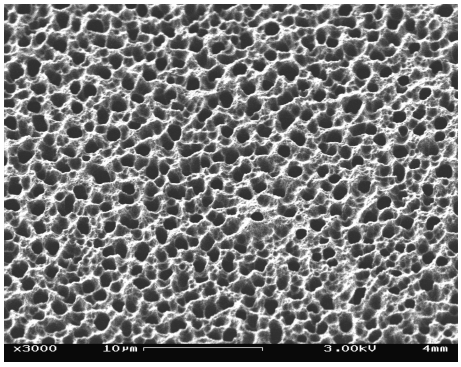
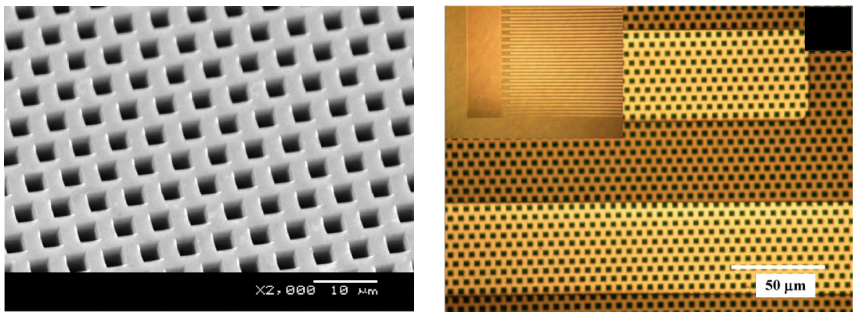


Figure 2.28: SEM picture of the roughness of the macroporous silicon.

The surface roughness can be reduced by pre-patterning by photolithography and KOH etching to define the nucleation spots of the pores. During anodization, the current is attracted from the tip formed by KOH etching and pores grown in keeping the pattern of photolithography. By this technique, Wang *et al.* [152] realized ordered macro-pSi array on which metal electrodes are deposited by lift-off. The standard resins are too liquid and could not form a compact layer on top of the porous layer. Therefore, AZP4330 (Clariant Corporation) is used for the lithography and deposited by spin-coating with a low speed (1000 rpm).

Archer *et al.* [80, 97] propose an alternative approach by placing the electrodes on the backside face of the sample. This technique enables a electrode patterning by standard photolithography and reach a submicroscopic resolution. However, the disadvantage of this geometry is that a large part of the electric current lines flows through the bulk silicon, do not participate in the detection. Furthermore, to promote the passage of the current lines in the porous layer, the electrodes must have a large area to avoid the concentration of the electric field near the electrodes.



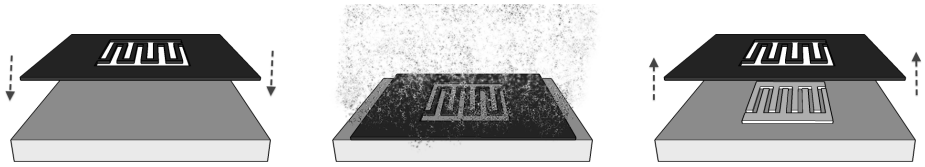
a. b.

Figure 2.29: (a) Tilted SEM image of an ordered macroporous silicon with square pores (1 μm in diameter); (b) a microscope image of the Al electrodes on top of the macropPi deposited by lift-off; the inset is a view of the interdigitated electrodes of the sensor. Reproduced and modified from reference [152]

The simplest technique consists in the deposition of a conductive paste, i.e. silver paste, on macroporous silicon [142]. This conductive paste can be deposited either manually or by inkjet. A similar technique is to glue metal pads on the macroporous silicon [60]. These techniques lack accuracy or are not versatile. Moreover, their implementation in a standard process is difficult.

Two other similar techniques are commonly used to integrate the metal electrodes to macroporous silicon: shadow mask (or stencil) technique [82, 153–155] and screen printing [141, 150, 156–158].

The shadow mask technique consists in machining the pattern of the metal layer in a high temperature resistant stencil (usually made of metal or plastic). The stencil is then applied to the porosified substrate (figure 2.30a.). A standard metal deposition technique (E-beam evaporator or sputtering deposition) is used. During the deposition, the metal crosses the stencil in the open areas thus respecting the pattern (figure 2.30b.). After depositing the stencil is removed from the sample (figure 2.30c.).



a. b. c.

Figure 2.30: Shadow mask technique: (a.) the stencil is applied to the sample. (b.) the metal deposition is performed. The metal traverses the stencil only at the open areas. (c.) the stencil is removed from the sample leaving the metal pattern on the sample surface.

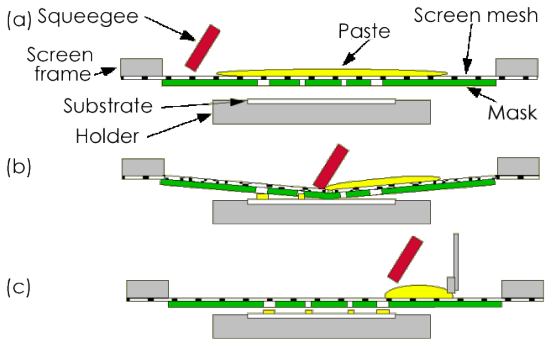


Figure 2.31: A screen-printing process allows the deposition of a material in paste form on a substrate. (a) A stencil is positioned above the substrate. A paste is applied to the mask. (b) A squeegee is used to force the passage of the paste through the stencil openings. (c) The paste on the substrate has the same pattern as the stencil. Reproduced and modified from reference [159].

The screen printing is also a very similar technique using a stencil to deposit a material in paste form on the substrate [85]. The openings in the stencil correspond to the pattern of the deposited layer. The stencil is placed above the substrate surface and the paste is applied on the stencil (figure 2.31a.). Then a squeegee is moved across the screen stencil, forcing the paste to pass into the stencil openings and be deposited on the substrate (figure 2.31b.). The stencil can be flexible and not in contact with the substrate. The pressure of the squeegee makes contact

locally the stencil and the substrate to prevent smudging, but also limit the pressure of squeegee on the substrate. Stencils can be realized in a photoresist and structured by standard photolithography to improve the resolution of the stencil. An advantage of this technique is it does not require a vacuum deposition, which makes it fast and cheap.

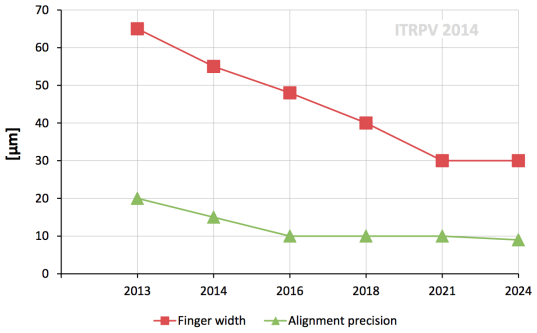


Figure 2.32: Predicted trend of ITRPV for alignment accuracy and finger width in screen-printing. Reproduced from http://www.itrpv.net (July 30, 2014).

However, the shadow mask and screen-printing techniques have several disadvantages. First, the micro-machining is much more restrictive in resolution and aspect ratio limit than the standard lithography. Indeed, it is exceedingly difficult to make micrometric IDE formed from electrodes with few microns in width, several hundreds of microns of length and spaced by few microns. This type of geometry is quite achievable with standard photolithography. Second, the alignment between the stencil and the sample is a complicated step and often not precise. It is very difficult to achieve the same resolution as the one obtained by standard photolithography. International Technology Roadmap for Photovoltaic (ITRPV) predicted in 2014 the trend for alignment accuracy and finger width in screen-printing (figure 2.32). The limitations of 30 μm for the resolution and 10 μm for the alignment are predicted for the next decade. These limitations are similar for shadow mask technique [160]. Finally, it is necessary to have a stencil by sample while a mask is sufficient for a large number of samples in standard photolithography. Figures 2.33 show some examples of macro-pSi-based sensors in the literature.

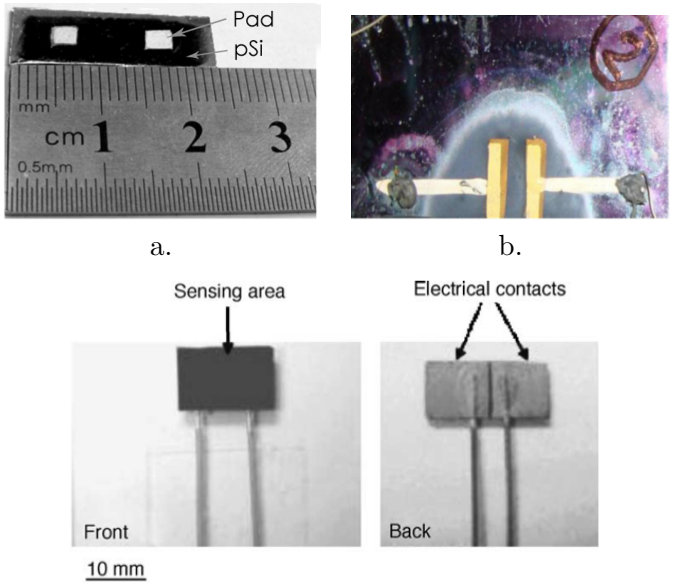


Figure 2.33: Some examples of macro-pSi-based sensors in the literature. Electrodes are deposited by (a.) stencil technique (Reproduced from reference [148]), (b.) screen-printing (Reproduced from reference [150]) and (c.) backside electrodes (Reproduced from reference [97]).

The deposition of freestanding pSi membrane on isolating substrate with interdigited contacts is another possible technique [139]. The porous layer is formed in a silicon substrate (figure 2.34b.) and is separated from it by abruptly increasing the current density at the end of the formation of the porous layer (figure 2.34c.). The freestanding porous membrane is collected and deposited on an insulating support (e.g. an alumina substrate) containing electrodes (figure 2.34d.).

This technique enables the microscopic electrode geometries and so miniaturize the sensor. However, the necessity to collect the freestanding porous membrane into the electrolyte and deposited it on the support renders difficult the integration of this process into a mass production of pSi-based sensors. Moreover, it is not obvious to ensure good contact between the electrodes on the support and the porous membrane.

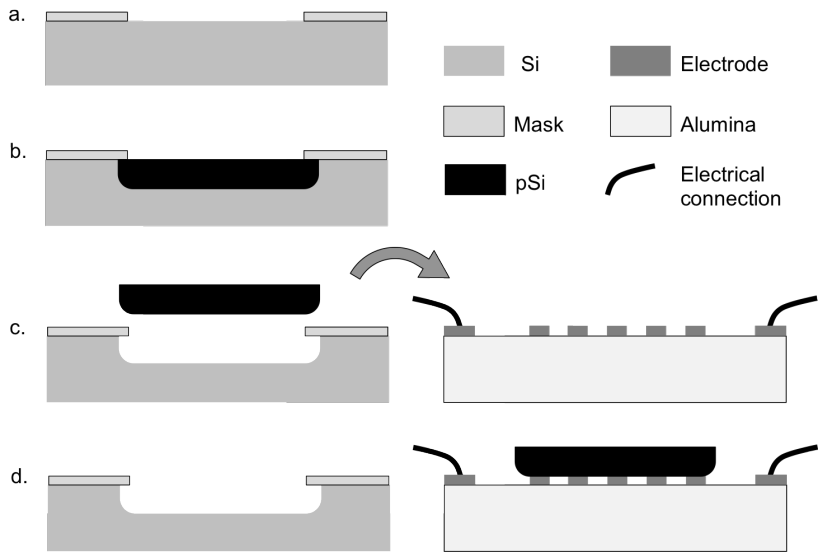


Figure 2.34: Process to put a freestanding pSi membrane on isolating substrate with interdigited contacts. (a.) A silicon wafer is patterned by a mask; (b.) The porous layer is formed by anodization; (c.) The porous layer is separated from the substrate by increasing the current abruptly after porosification (electropolishing); (d.) The freestanding porous membrane is collected and deposited on an isolating substrate with interdigited contacts.

Techniques	**Performances**			**Some examples**				
	Resolution	Alignment		Electrodes (μm)			Sensor size	Ref.
	(μm)	(μm)		Width	Length	Spacing	(mm)	
Shadow mask technique	± 30	± 10		1000	n/a	500	10 × 10	[154]
				3000	3000	8000	18 x 5	[153]
				1000	3000	1000	20 x 20	[155]
				2000	2000	9000	24 x 8	[148]
Screen-printing	± 30	± 10		1000	3000	1000	∼ 10 × 10	[141]
				1000	2000	1000	∼ 10 x 10	[150]
Backside electrodes	PL limit	PL limit		n/a	n/a	700	7 × 4	[97]
Pads gluing		± 30	± 30	n/a	n/a	n/a	3 × 3	[60]
Free-standing membrane	PL limit	PL limit		n/a	n/a	150	3 × 3	[139]
Our work	PL limit	PL limit		2	2	2	0.9 × 0.9	

Table 2.1: Summary of limitations according to the electrodes integration technique and some examples of dimensions of macro-pSi-based sensors listed in the literature. "PL limit" means limitations are give by photolithography limits.

Conclusions and motivation

Porous silicon has high flexibility in its morphology, which confers him interesting thermal, optical, electrical, mechanical ... properties. With a fabrication process, commonly a simple and inexpensive electrochemical etching, porous silicon is a versatile material used in a large number of domain. We presented a non-exhaustive list of the most common applications: thermal insulation, optical and photonic devices, microfluidics, micromachining ...

Porous silicon is a great sensitive layer in gas detection applications. Indeed, with its morphology, porous silicon has a big volume density of available surface area. This quality concentrates a large number of surface reactions (e.g. adsorption, absorption, surface conduction ...) in a reduced volume. Since its semiconductor properties are influenced by these surface reactions, the porous silicon is an effective transducer for converting a gas partial pressure in a modification of the electronic properties of the porous layer and thus allows the gases detection.

By the analytical study of the mass transfer in a porous matrix, we show that fluid diffusion rate increases with the pore diameter. The mean free path of gas (e.g. hydrogen) is large. A large pore diameter, as in the macroporous silicon, increases the penetration rate of the gases in the pores. The macroporous silicon also enables a better diffusion of liquid in its pores. This characteristic is essential for the pore wall fonctionnalization with wet process. Indeed, the liquid must penetrate homogeneously in all of porous matrix.

We explained the impact of the dimensions and pitch of the electrodes on the quality of the measurement. Indeed, wide spaced electrodes promotes the passage of electric current in non porous silicon, far away from the porous layer. This part of the electric current is not involved in the measurement. By decreasing the dimensions and spacing of electrodes, the electric current is concentrate in or in the vicinity of the porous layer. This phenomenon is expected to increase the sensitivity and signal to noise ratio of the measurement. To maximize this phenomenon, micrometric sizes are needed for both the width of the electrodes that for their spacing.

Porous silicon-based gas sensors are not the only application that requires the metal electrode integration on the porous surface. All fields of application cited in this chapter may require the metal pattern as electrodes or for other uses.

Although some techniques of metal pattern integration exist on micro- and mesoporous silicon, they are not or difficult to apply on macroporous silicon. Indeed, the macroporous silicon has a high roughness and wide discontinuities in the surface. Standard techniques of electrode patterning (such as photolithography, the lift-off ...) are not practical and/or ineffective on the macroporous silicon. Other techniques such as shadow masking or screen printing have significant restrictions on the electrode size. Table 2.1 lists the dimensions of pSi-based gas sensors obtained with techniques in the literature and the dimensions of the sensor developed in this thesis[1]. The techniques used in literature are: (i) limited in resolution (and therefore do not allow microsize electrodes), (ii) inaccurate in the alignment resolution between the different layers and (iii) do not enable miniaturization of the device. Moreover, they are not standard in microfabrication, which make it an obstacle in the industrialization valorization of the devices.

Due of these reasons, it is necessary to develop a new method of integration of microsize pattern of metal electrodes on a macroporous silicon with (i) high performance in term of dimension resolution and alignment resolution, (ii) a large flexibility in the design of electrodes (iii) a simple and cheap process and (iv) involvement only standard microfabrication techniques.

[1]Several articles in the literature do not mention the dimensions of their sensor. However, we assume that the dimensions listed in the Table 2.1 correctly reflect the dimension limitations of different techniques of electrode integration on macro-pSi

CHAPTER 3

Macroporous silicon : electrode integration and masking

3.1 Introduction

The complete process of fabrication of a miniaturized chemiresistor based on macroporous silicon is detailed in Appendix I (page 285). In this chapter we describe the studies conducted to understand and to provide solutions to technological barriers in this fabrication process.

In the first section, we present an original method of metal electrode integration on the porous silicon. This method uses efficient and standard techniques (e.g. photolithography and lift-off) to pattern the microsize electrodes on the silicon surface before electrochemical etching. It enables a high flexibility in the electrode design. Electrode dimensions never reached by the usual techniques of electrode integration on macroporous silicon have been achieved (see previous chapter).

The pattern presence on the silicon surface during the electrochemical etching disturbs pore growth and affects the morphology of the porous layer. In our fabrication process, two patterns are present during the etching: the masking layer and the electrodes. However, their impact on porous layer morphology are different. In the two next sections, we describe separately the impact of both patterns on the growth of the macroporous layer.

The presence of a masking layer during the electrochemical etching results usually in a problematic significant mask overetching. We detail the study of the causes and the morphology of the onveretching. With computer simulations, we provide an explanation of phenomena and we propose solutions to the issue. This study enables us to propose process rules to eliminate mask overetching issues.

The electrodes act locally as narrow masks. However, they do not generate the same overetching as the masking layer. With their width similar to the pore diameter, they affect differently the growth of pores. In contrast to the overetching of the masking layer which will tend to release a large part of it, the electrochemical etching near the electrodes tend to preserve the silicon under the electrodes. We study this phenomenon. With the results of this study, we suggest design rules of electrodes that would increase the quality of the measurement in a gas detection application.

The electrode pattern dimensions and the electric current density strongly influence the pore wall thickness. In the last section of this chapter, we study the impact of the pore wall thickness on the electrical behavior in the macroporous silicon. We show that the thickness and the oxidation state of the pore walls influence strongly on the distribution of the charge carriers flowing through the pore walls and then on its electrical behavior. With the results of others sections, we seek to connect the electrical behavior of macroporous silicon to the parameters of the electrochemical etching and metal pattern dimensions.

Finally, through all observations in this chapter, we recommand a simple fabrication process of a miniaturized chemiresistor based on macroporous silicon.

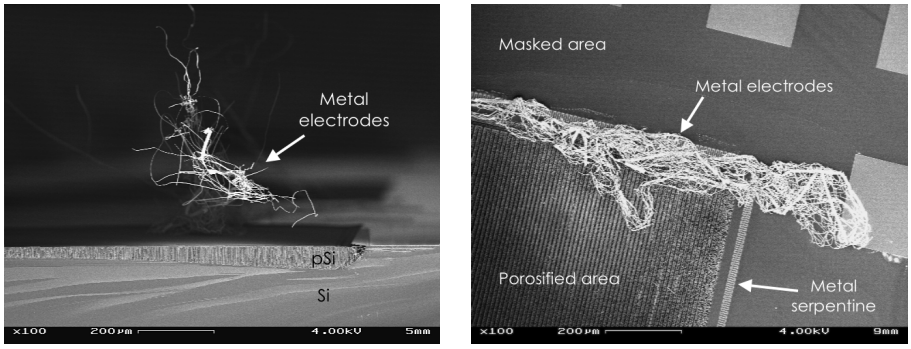
3.2 New metal electrode integration method on the macroporous silicon surface

This section presents an original method to integrate metal electrodes before sample porosification with only microfabrication standard techniques. This method eliminates the problem of surface roughness because the steps for the metal patterning are performed on the flat surface of silicon before electrochemical etching. In this way, larger flexibility and micrometric dimensions are possible to the electrode design.

This section uses several notions of the electrochemistry domain. We invite the reader not-familiarized with this scientific field to read the summary of these notions in Appendix D (on page 235).

3.2.1 Metal assisted etching

A silicon substrate partially covered by a metal and immersed in an electrolyte composed of HF and an oxidative agent, undergoes electroless etching or *galvanic corrosion*. The silicon in contact with metal layer is dissolved in the electrolyte. If corrosion is rapid, the metal sinks into the Si substrate, generating pores in the Si substrate. The pore cross-section have the same shape as the metal pattern [161]. This technique, called *metal-assisted etching* (MAE), is used in Si micromachining to fabricate high aspect ratio structures and pSi layer without requiring an external power source. In a MAE process, a noble metal is used as it would not etch in HF-based electrolyte.



a. b.

Figure 3.1: SEM picture of (a.) cross-section and (b.) top views of sensors after the first test of porosification of silicon with metal electrodes integrated. No pretreatment was applied to the electrodes. Porosification is performed in HF:H2O:DMF (1:1:8) electrolyte under a current density of 17.5 mA/cm^2 during 25 min.

Figures 3.1 show the result of electrochemical etching of a silicon substrate patterned by metal electrode composed of an adhesion layer of 5 nm titanium and 100 nm gold. No pretreatment was applied to the electrodes. The metal layer adheres very well on the masked area (a 100 nm layer of silicon nitride between the metal layer and the silicon substrate). In contrast, metal electrodes directly in contact with the silicon have all been delaminated. In our case, the corrosion is not fast enough and the metal is delaminating from the silicon surface.

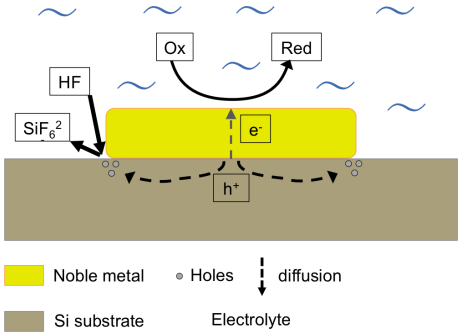


Figure 3.2: Scheme of metal assisted-etching procedure. Inspired from reference [161]

The metal acts as a catalyst and becomes an insulated micro-cathode. A reduction reaction of an oxidizer present in the electrolyte takes place at the metal/electrolyte interface (figure 3.2). The presence of the metal increases the rate of reaction. The reduction reaction generates an excess of holes which are then injected into the Si substrate in contact with the metal. Accordingly, the Si atoms under the metal are oxidized due to the hole injection and dissolved by HF [161].

During anodizing the porous silicon, the hole current imposed by the external source flows from the backside of the Si wafer towards the electrolyte. Nevertheless, the MAE current circulates from the electrolyte to the Si wafer. During the growth of pores, the pore walls are depleted (see section 2.1.1 on page 16). The hole current imposed by the external source does not pass through in pore walls, but by the tip of the pores. The metal electrode is on a Si part electrically insulated from the silicon substrate. Locally, the hole current flows in the opposite direction of the applied external electric potential source (figure 3.3).

Two-dimensional simulations of hole current in Si crystallites covered by metal electrodes during electrochemical etching were performed using COMSOL Multiphysics©. Figure 3.4 show the distribution of hole concentration in the silicon (color map) and the hole current density at the silicon interface of silicon (at vertical edges only) (red arrows).

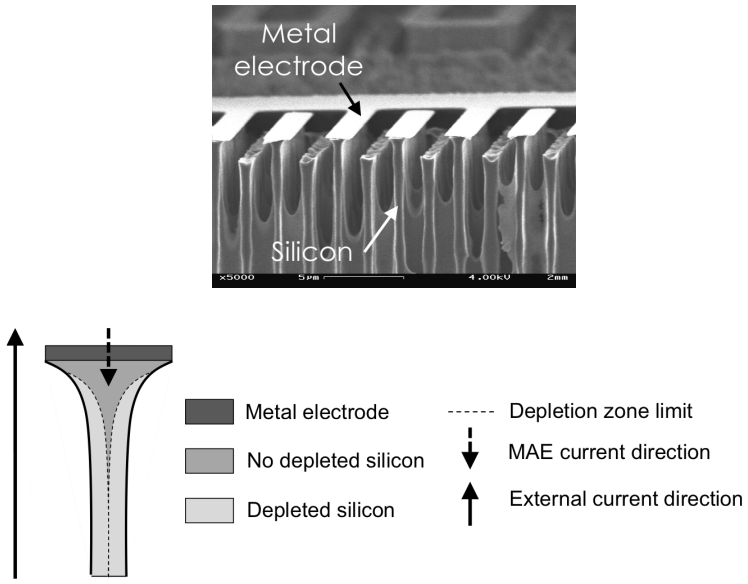


Figure 3.3: (Up) SEM picture of cross-section view of the Si crystallites under the metal electrodes (5 nm-Ti/150 nm-Au on a thin plasma oxide). (Down) Schematic of Si crystallites and the directions of electric currents. The electric current produced by the phenomenon of MAE is opposite to the applied external electric current source direction.

The Si crystallites were modeled by rectangles of 1 μm in width and 5 μm in height. This width is justified by the fact that we observe Si crystallites widths comparable to 1 μm. The height of 5 μm is justified by the desire to simulate the distribution of the hole concentration during the electrochemical etching. To avoid more complex simulation, crystallites not covered by metal electrodes have been neglected. Parameters and information about the simulations are presented in Appendix F.2 (page 255).

On the figure 3.4, Si crystallites are depleted except near the metal electrodes which inject a hole current arising from the reduction reaction at the metal/electrolyte interface. When holes are injected into the silicon, they head along the Si crystallites edges. The hole current is higher close to the metal electrodes and decreases strongly with distance from the electrodes. The etching is therefore larger directly under the electrodes, which causes the underetching and electrode delamination.

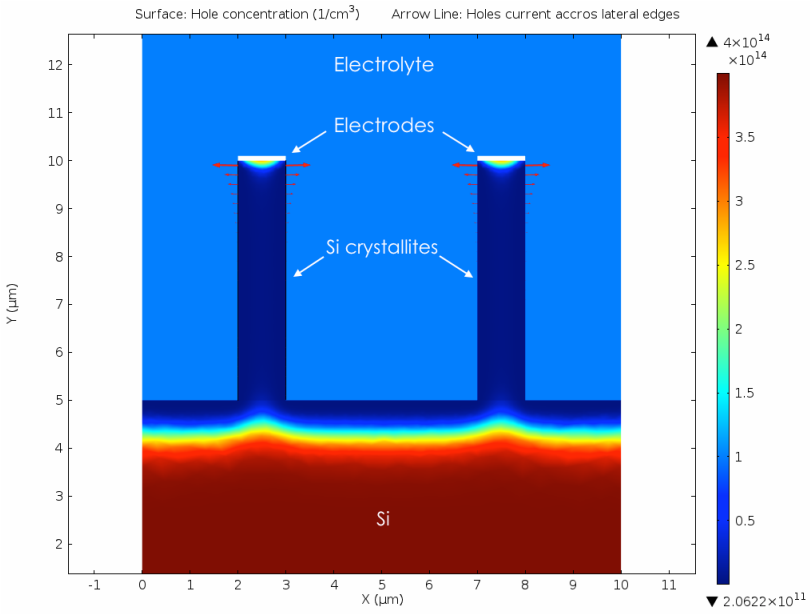


Figure 3.4: 2D finite elements simulation of hole concentration in silicon (color map) and the hole current density at the silicon interface of silicon (at vertical edges only) (red arrows). The Si crystallites are depleted except near the metal electrodes which inject a hole current arising from the reduction reaction at the metal/electrolyte interface.

Parameters that most influence the metal-assisted etching process are the metal nature, the electrolyte composition and the electrical and crystallographic properties of the silicon substrate [161] :

- **Metal nature** influences the etching rate in a MAE process. Indeed, each metal has a different catalytic activity and increases differently the reduction reaction in the electrolyte. This is mainly caused by the notion of exchange current detailed in Appendix D. The kinetics of the redox reactions at the metal/electrolyte interface depends largely on the metal nature. For example, the rate of hydrogen evolution, widely used as a cathodic reaction in the MAE process, varies by several orders of magnitude depending on the immersed metal nature in the electrolyte. It is *activation polarization* of corrosion.

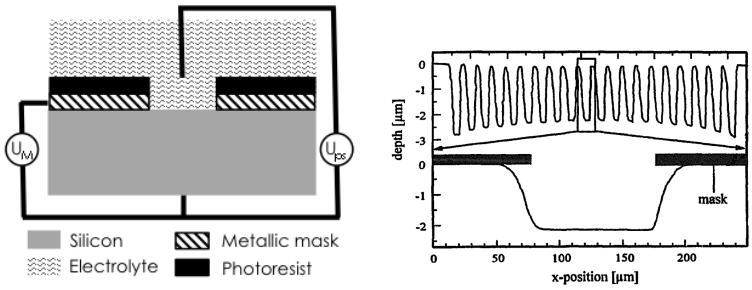
The metal nature also influences how the holes are injected into the silicon. Each metal has a different work function, which influences the electrical behavior of metal/silicon contact. The easier the electrical charges cross the contact, the faster the MAE process is. Conversely, more resistive contact slows down the MAE process.

It is important to note that the metal in contact with the electrolyte is not necessarily the same as the metal in contact with the silicon. A metallic multilayer enables to adjust independently the two aforementioned effects. The limitation of corrosion by modifying the electrical path between the anode and the cathode is called the *ohmic polarization*.

- **Electrolyte composition** plays an important role in MAE process. It determines the possible reduction reactions in contact with the metal. The nature and concentration of the oxidizer are crucial in the reduction reaction rate and thus in the hole generation. The diffusion of etching reactants to the metal/silicon interface is also determined by the electrolyte composition and its ability to wet the walls of the pores, which will change the morphology of the etching. It is a *concentration polarization* of corrosion. The hole generation rate not only influences the etching rate but also the morphology of the etched structure. Indeed, in the case of a large quantity of holes injected into the silicon, a part of them is not consumed directly near the metal layer. They diffuse to the uncovered area by metal and generate a porous layer at this location [161].

- **Properties of the silicon substrate and etching conditions :** Like for an electrochemical etching with an external current source (see section 2.1.1 on page 16), doping, resistivity and crystal orientation of silicon wafer are key parameters in a MAE process. In some cases, other etching parameters may be important as temperature or illumination (mainly for n-type Si etching)

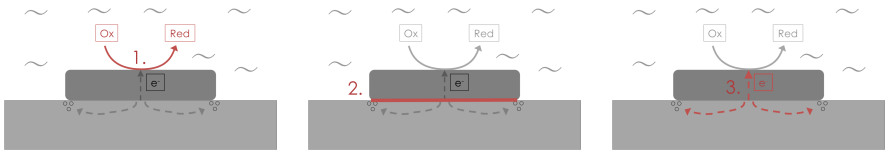
Krüger *et al.* [162] presented an alternative approach to counter the underetching caused by the MAE by using a biased metal masking layer. The metal masking layer was insulated from the electrolyte by a photoresist layer on top of the metal. During anodization, the current density through the interface substrate-metal layer was twice the anodization current density (figure 3.5). However, this technique does not prevent a strong overetching of the mask layer to occur, which would result in the narrow metal electrodes delamination.



a. b.

Figure 3.5: (a.) The technique of active mask is to use a biased metal masking layer. (b.) Results of the electrochemical etching. A strong underetching is present. (a.) Inspired and (b.) reproduced from [162].

3.2.2 Solutions to improve the electrodes adhesion during the electrochemical etching



a. b. c.

Figure 3.6: Schematic view of three modified elements to minimize parasitic MAE etching : (a.) decreasing of the reduction reactions at the metal surface, (b.) reducing the hole injection from electrodes to silicon and (c.) Changing of current direction in the galvanic cell.

With the aim of integrating metal electrodes to silicon before porosification, it is essential to limit the MAE process. We varied different elements of the MAE process to minimize this parasitic etching (figure 3.6) :

a. **Decreasing of the reduction reactions at the metal surface :** Two factors must be taken into account in the reduction reaction at the electrode surface : (i) the catalytic activity of metal and (ii) the concentrations of the reducible species in the electrolyte (or electrolyte composition).

b. **Reducing the hole injection from electrodes to silicon :** Reducing the hole injection from electrodes to silicon is done by modifying the electrical path between the cathode and the anode. The nature of the metal in contact with Si and the oxidation state of the metal/Si interface have a significant impact on the electrical behavior of the metal/silicon contact.

c. **Galvanic protection by a sacrificial anode :** In a galvanic cell, the anode undergoes dissolution because its redox potential is more negative. A sacrificial anode is a metal whose redox potential is below that of the material to be protected (silicon in this case). The sacrificial anode attracts more electric charges and it undergoes dissolution instead of silicon.

These alterations are described below.

Catalytic activity of metal

The catalytic activity is not identical for all metals. Some metals better promote the reduction reaction of the oxidant. Assuming that the cathode reaction is the only hydrogen evolution, it is possible to compare the rates of catalysis relative to the metal nature. Indeed, the catalytic rate is proportional to the exchange current of the hydrogen evolution on the metal. Various metals commonly used in microelectronics and HF-resistant (Au, Cr, Ni) were tested. Pt and Pd were not tested because their catalytic activity of hydrogen evolution is very high [163]. Despite slight differences in the delamination rate were observed, they are not significant. This indifference could be explained by the fact that the MAE process rate is not limited by the catalytic reaction rate, but probably by the rate of hole injection from the metal to the silicon. Ohmic polarization is higher than the activation polarization.

Electrolyte composition

Some components of the electrolyte are oxidizing agents which are liable to undergo a reduction in contact with the metal catalyst. These reduction reactions are half reactions of galvanic couple formed with the dissolution of silicon. They provide holes to the Si oxidation. Let us consider in more detail the composition of the electrolyte and the possible reduction reactions in it.

The electrolyte used for macropores generation in p-type silicon (10-20 Ω.cm) is a mixture of HF and N,N-dimethylformamide (DMF) (HF:H_2O:DMF = 1:1:8). DMF is not stable in the presence of acids like HF and is, thus, partly hydrolyzed back into formic acid and dimethylamine [164] (figure 3.7).

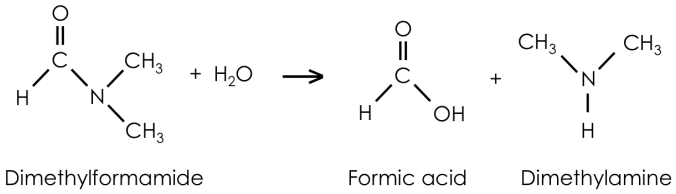


Figure 3.7: Dimethylformamide hydrolysis reaction

DMF hydrolysis consumes the water molecule. Water concentration in the electrolyte decreases. The reaction is exothermic and the solution temperature increases. Solution pH and conductivity were measured after the cooling of the solution at room temperature. A pH of 4 and a conductivity of 2 mS/m were measured. The hydrolysis of the DMF is not limited to the preparation moment. As a consequence, the properties of the solution were observed to change over time to reach a threshold value. Formic acid and dimethylamine are thus predominant impurities in DMF and they are respectively weakly acidic and weakly basic respectively; therefore, partial ionization does occur [165] :

$$\underbrace{HCOOH}_{\text{formic acid}} + \underbrace{(CH_3)_2NH}_{\text{dimethylamine}} \rightleftarrows HCCO^- + (CH_3)_2NH_2^+ \qquad (3.1)$$

that which results in a buffered solution entirely consumed by HF. Moreover, increasing the ion concentration increases the electrical conductivity of the electrolyte. A 20-day-old solution stored in a closed bottle was measured with a pH of 6 and a conductivity of 30 mS/m, indicating that a bigger fraction of the DMF was hydrolyzed.

There are several possible reduction reactions in our acidic electrolyte. We present below a non-exhaustive list, but incorporating the most plausible :

Hydrogen evolution

$$2H^+ \longrightarrow H_2(g) + 2h^+ \qquad E^0 = 0.00V_{SHE} \qquad (3.2)$$

Reduction of dissolved oxygen

$$O_{2(g)} + 4H^+ \longrightarrow 2H_2O + 4h^+ \qquad E^0 = 1.23V_{SHE} \tag{3.3}$$

Reduction of formic acid

$$HCOOH_{(aq)} + 2H^+ \longrightarrow HCHO_{(aq)} + H_2O + 2h^+ \quad E^0 = -0.03V_{SHE} \tag{3.4}$$

These three reduction reactions require free protons in solution to take place. Since the hydrolysis of DMF led to increased pH and thus a reduction of the proton concentration, the three reduction reactions are disadvantaged in an electrolyte which DMF is highly decomposed.

Metal/silicon interface

Another original approach for reducing the MAE process is to limit the injection of holes in silicon. This limitation is done by modifying the electrical path between the cathode and the anode.

Metal in contact with a semiconductor forms a potential barrier called *Schottky barrier*. Metal-semiconductor junctions can either be rectifier (Schottky diode) or non-rectifier (ohmic contact).

In general, for p-type silicon (p-type Si), non-rectifying behavior occurs in the case where the work function of the metal (Φ_m) is higher than that of the p-type Si (Φ_s) (figure 3.8a.). In this case, the energy bands in the p-type Si curve upward near the contact. A hole accumulation zone appears. The holes pass through the metal/p-type Si interface quasi indifferently in either direction. The contact resistance is generally low.

In the case of a rectifier contact, the work function of metal (Φ_m) is lower than that of the p-type Si (Φ_s). The energy bands curve downwards near contact generating a depletion region at this location. A depletion zone of holes appears (figure 3.8b.).

The first-order theory of the formation of a Schottky barrier is the view attributed to Walter Schottky and Sir Neville Mott [166]. The Schottky-Mott theory proposes that Schottky barrier height (SBH, Φ_B) between a metal with a work function of Φ_m and a p-type Si with an electron affinity of χ_{Si} and an energy gap of E_g is given by (q is the elementary charge):

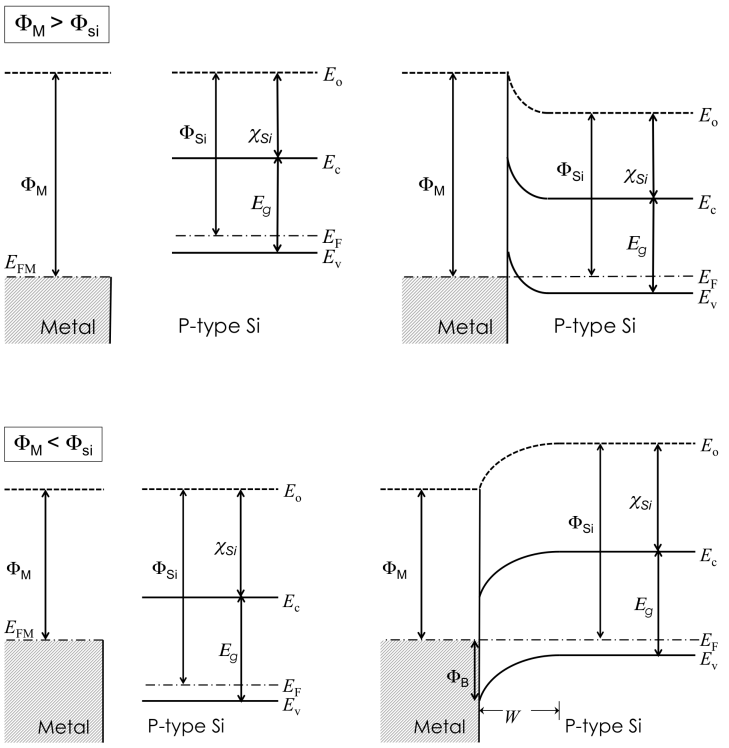


Figure 3.8: Energy band diagram of a metal/p-type Si contact when (up) $\Phi_m > \Phi_s$ and (down) $\Phi_m < \Phi_s$.

$$\Phi_B = \frac{E_g}{q} + \chi_{Si} - \Phi_m \tag{3.5}$$

When the rectifier contact is biased is positively biased (the highest potential is applied to the p-type Si), the holes in the top of the valence band in the p-type Si are attracted to the contact. They then collide with the potential barrier. Only the most energetic of them are able to cross this region. As the electric potential increases, the band bending decreases. The potential barrier decreases. A larger number of holes are able to pass through the contact. The current then increases exponentially.

When the rectifier contact is reverse biased (the highest potential is applied to the metal), the holes in the metal close to the interface, are attracted to the semiconductor. However, they collide with the potential barrier created by the semiconductor gap. Only a part of the most energetic holes is able to cross this barrier (they form the leakage current). Even when the electric potential increases, the potential barrier remains constant. The leakage current is almost constant when the electric potential increases. There are exceptions to this ideal behavior. At high reverse potential and for high semiconductor doping level, a breakdown phenomenon may appear mainly due to the tunnel effect [167].

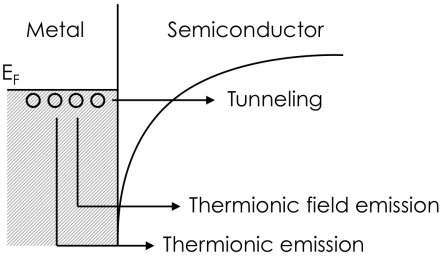


Figure 3.9: Schematic representation of the different transport mechanisms of current in the energy diagram of the metal/p-type semiconductor contacts in reverse mode.

In a MAE process on a p-type Si wafer, the holes, generated by the reduction reaction, are injected from the metal to silicon. The metal/silicon contact is therefore reverse biased. The hole current is a leakage current. Three distinctly different transport mechanisms co-exist in the leakage current [168] : the diffusion of carriers from the semiconductor into the metal, thermionic emission of carriers across the Schottky barrier and quantum-mechanical tunneling through the barrier. The diffusion theory assumes that the driving force is distributed over the length of the depletion layer. The thermionic emission theory postulates that only energetic carriers, those, which have an energy equal to or larger than the potential barrier at the metal/Si interface, contribute to the current flow. Quantum-mechanical tunneling through the barrier takes into account the wave-nature of the electrons, allowing them to penetrate through thin barriers. In a given junction, a combination of all three mechanisms could exist. However, typically one of them

limits the current, making it the dominant mechanism. In reverse bias contact, we do not take into account the diffusive transport as it only relates transport in the depletion region in the semiconductor and not at the potential barrier. The combination of transport mechanisms by thermionic emission and tunneling gives thermionic field emission (figure 3.9).

Due to the relatively small SBH in silicon Schottky contact and to the large depletion region (low p-type doping), the thermionic emission component is dominant. The leakage current (J_R) for the silicon Schottky contact can be obtained by using the thermionic emission theory [167].

$$J_R = AT^2 \mathrm{e}^{-(q\Phi_B/k_BT)} \tag{3.6}$$

where A is the effective Richardson constant, T is temperature (K), q is the electronic charge unit and k_B is the Boltzmann constant. The leakage current depends primarily on the SBH[1]. To decrease it, the potential barrier should be increased. Two ways to change the SBH were studied :

1. First, the nature of the metal in contact with the silicon changes the SBH [169]. Indeed, the work function of each metal is different. This causes different bands curvatures (figure 3.8a.). The nature of the metal in contact with the silicon can change the behavior of the rectifier contact.

2. Second, chemical preparation of sample before the metallization also plays an essential role in the behavior of the metal/silicon contact. Modifying the oxidation state of the Si surface is a common technique to modify the electrical behavior of the contact [170].

We propose to achieve MIS (Metal-Insulator-Semiconductor) contacts where the insulator is very thin. Despite the presence of an insulator, electric current can pass through the contact by the tunnel effect (for an insulation thickness of a few nanometers). The flow of electric current is no longer governed mainly by the laws of the thermionic emission (as in a conventional metal-semiconductor contact), but also by the laws of the tunnel effect to cross the insulating layer [171–174].

[1]Generally, the SBH in the direction metal-silicon is slightly lower than the SBH in direction silicon-metal due to image charges. This phenomenon does not affect our reasoning and we neglect it.

In the presence of an interfacial layer, equation 3.6 remains valid with the tunneling probability, an additional exponential factor dependent on interface layer parameters :

$$J_R = AT^2 \mathrm{e}^{-(a\delta(\chi)^{1/2})} \mathrm{e}^{-(q\Phi_B/k_BT)} \tag{3.7}$$

where $a = \frac{4\pi}{h}(2m^*)^{\frac{1}{2}}$ is a constant that depends on effective hole mass (m^*), χ is the effective barrier height presented by the thin interfacial layer and δ is the thickness of the interfacial layer. If the interface layer is extremely thin then it is transparent to holes and $\mathrm{e}^{-(a\delta(\chi)^{1/2})} \approx 1$.

However, it is useful to keep in mind that the metal electrode integration to the pSi is used primarily to measure the variation of the electric current passing through the porous layer. It is therefore necessary that the current easily flows through the electrical contacts. The rectifier behavior of contacts prevents a correct measurement of the variation. We present in Appendix C (page 231) the reasons why it is necessary to suppress the rectifier behavior of electrical contacts before the use of metal electrodes in their measurement applications.

To summarize, during the anodization of silicon, the contacts must act as rectifier to minimize the impact of MAE process. By cons, during the measurement of the final sensor, rectifier behavior must decrease or eliminate to optimize the measurement of the porous silicon resistivity and not the contact resistance.

The behavior of the rectifier contact can be suppressed by carrying out a rapid thermal annealing (RTA) to the sample [175] (figure 3.10a.). This technique enables to heat the sample at high temperature (several hundred degrees Celsius) in a short time (from tens of seconds to a few minutes). RTA technique promotes the chemical reactions, requiring high temperatures, between the metal and the silicon (silicidation) but limiting the diffusion of the metal in the silicon. In our case, the RTA technique allows the metal to diffuse just through the thin insulator layer and create a silicide with silicon below of the contact (figure 3.10b.).

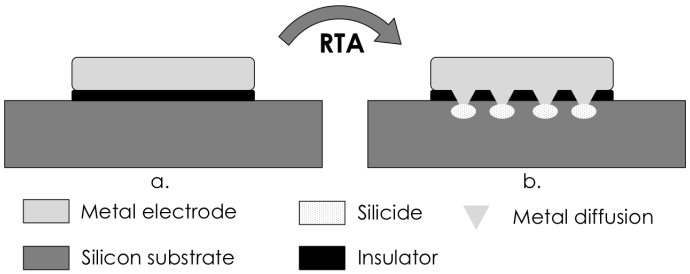


Figure 3.10: With the RTA technique, the metal diffuses through the thin insulating layer and reacts with silicon to create a silicide.

Creating an electrical insulator at the metal/silicon interface is done by deposition, growth or chemical treatment of silicon. We cite a few examples, but this list is not exhaustive. The natural oxidation of silicon exposed to air and humidity is a simple method to grow a native oxide on silicon. The thickness and quality of this oxide depend mainly on the temperature and humidity in an atmosphere which is difficult to control. The oxidation of the silicon can be well controlled by thermal growth at high temperature [172], by plasma [176–179] or by wet chemical [180] or anodic [181, 182] oxidation. The deposition of an insulating polymer between the metal and the silicon was also studied [183]. A plasma [173] or chemical [180] pretreatment of silicon before the metal deposition is enough to change the electrical behavior of the contact metal/semiconductor.

The impact of the presence of a native oxide and an oxide generated by plasma to the interface metal/silicon was studied as part of this work. Although thermal oxidation is a well-controlled technique, the thermal oxide has not been considered. A thermal oxide is dense and is a diffusion barrier for metal. The MIS contact with a thermal oxide is difficult to destroy by rapid thermal annealing (RTA) technique [175]. As the nature of the metal in contact with the silicon also influences the rectifier behavior of the contact, three metals are considered : aluminum, titanium and chromium. These three metals are standard adhesion promoter layers in microfabrication and their presence at the noble metal/silicon interface is essential to ensure good adhesion of the contact on the substrate.

Galvanic protection by sacrificial anode:

The electrolyte/metal/silicon system is similar to a galvanic cell wherein oxidation-reduction reactions take place. At the anode, the Si substrate is oxidized and dissolved. There are numerous models proposed for the dissolution process of Si (anode reaction), which can be catalogued into three groups [161] :

(RI) Direct dissolution of Si in tetravalent state

$$Si(s) + 4HF + 4h^+ \longrightarrow SiF_4 + 4H^+ \qquad E^0 = N.D. \tag{3.8}$$

$$SiF_4 + 2HF \longrightarrow H_2SiF_6 \tag{3.9}$$

(RII) Direct dissolution of Si in divalent state

$$Si(s) + 4HF_2^- + 2h^+ \longrightarrow SiF_6^{2-} + 2HF + H_2(g) \quad E^0 = -1.20V_{SHE} \tag{3.10}$$

(RIII) Si oxide formation followed by dissolution of oxide

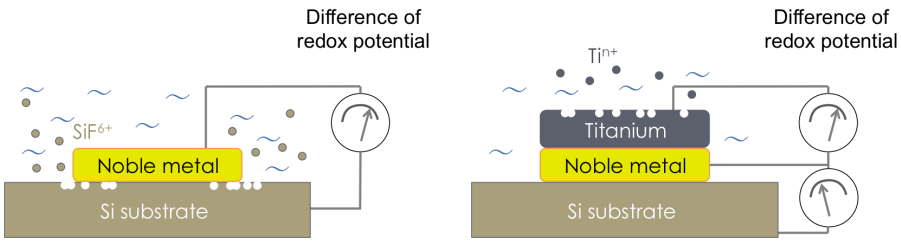
$$Si(s) + 2H_2O + 4h^+ \longrightarrow SiO_2 + 4H^+ \qquad E^0 = -0.86V_{SHE} \tag{3.11}$$

$$SiO_2 + 6HF \longrightarrow H_2SiF_6 + 2H_2O \tag{3.12}$$

Models RII and RIII differ in whether Si oxide is formed at the surface of the Si substrate before the dissolution of Si, and whether H_2 is generated accompanying the dissolution of Si. Gas evolution was observed during the process, but it is unclear whether it comes from the Si dissolution at the anode or the reduction reaction (hydrogen evolution) at the cathode. It is possible that two or three models occur simultaneously. The question remains open due to the difficulty in the in situ exploration of the surface state and the uncertainty in an ex-situ study of the Si surface state [161].

To prevent the dissolution of silicon, reactions 3.8, 3.10 and 3.11 should be limited. Silicon is a strong reducing agent, which means that its redox potential is very negative (E^0_{Si} = -0.86 to -1.20 V_{SHE}). To limit the silicon dissolution, the oxidation reaction must be done on a chemical species with a redox potential lower than that of silicon. In this way, the corrosion potential (E_{corr}) is forced to be in the cathodic domain of the silicon which preserves it of its dissolution.

Table E.1 in appendix E (on page 249) shows the redox potential of the metals commonly used in microfabrication and redox potential of the possible reactions in the electrolyte.



a. b.

Figure 3.11: Schematic representation of the contact as a galvanic cell (a.) without and (b.) with a Ti sacrificial layer. Without the Ti layer, the silicon is corroded near the noble metal. In the presence of the Ti layer, galvanic corrosion occurs preferentially on Ti because it has a redox potential lower than the silicon.

Aluminum and titanium are the only two elements that have a redox potential lower than silicon (E^0_{Al} = -1.60 V_{SHE} and E^0_{Ti} = -1.68 V_{SHE}). The use of these metals as the sacrificial layer makes it possible to limit the reaction of silicon dissolution under the electrodes. The galvanic cell is formed between the noble metal and the sacrificial layer and not with the silicon (figure 3.11). The electric current flows to the sacrificial layer which is etched instead of silicon. Titanium on top of noble metal electrodes is used as a sacrificial layer during the releasing step of silicon-based MEMS in a HF solution to prevent deterioration of the exposed silicon with HF. Liu *et al.* [184] show that the addition of a sacrificial layer is not sufficient to avoid the MAE process. They add a layer of photoresist on top of the sacrificial layer. However, this method is not readily achievable in our case because of the presence of DMF in our electrolyte. Indeed, DMF is a solvent for the standard photoresist which would dissolve rapidly during electro-etching.

3.2.3 Materials and method

Substrates preparation

The impact in Si corrosion of the electrolyte composition, the presence of an insulating layer at the metal/silicon interface, metal nature in contact with the silicon and the presence of a sacrificial layer have been studied. Numerous combinations of those four factors were performed to measure their effects on reducing the MAE process.

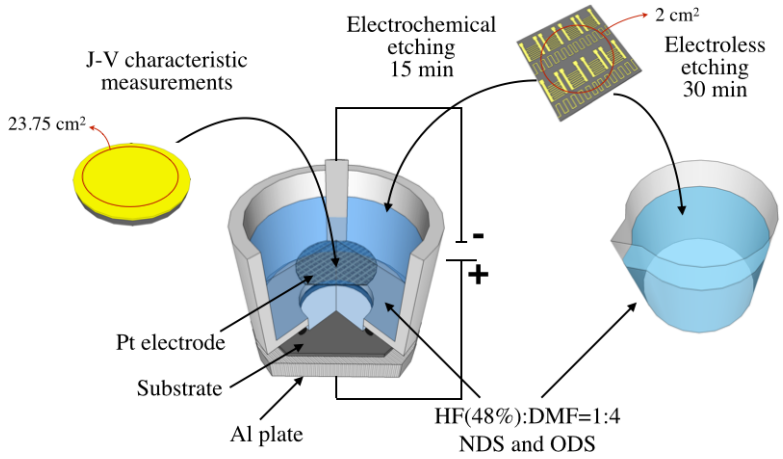


Figure 3.12: Schematic diagram of the experimental procedure. Fully metalized wafer were used for the measurement of J-V characteristics. Patterned samples were used for both electrochemical and electroless etching experiments.

As schematized in figure 3.12, two kinds of substrates were used in this work : Metal patterned Si substrates for the etching (electrochemical and electroless) experiments, and completely metal covered Si substrates for the J-V characteristic measurements.

p-type silicon wafers (10-20 Ω·cm, ⟨100⟩-orientation) are cleaned in a piranha solution, followed by a solution of HF (2%) to etch the oxide layer. The metal pattern was transferred on the silicon surface by a standard lift-off process. The pattern consisted of interdigitated electrodes with different pitch and width, alternate by serpentine spring structures and larger pads.

The oxidation state of the surface was changed using three procedures for the preparation of the samples to the metal evaporation:

Buffered HF (BHF) etching was performed on the wafer in order to obtain hydrogen terminated and oxide free Si surface. On samples patterned for the lift-off process this step was performed after the lithography. The samples as prepared were placed on the evaporator chamber, where the vacuum was suddenly reached in order to avoid the contact with air and the native silicon dioxide formation.

A native oxide layer was let to growth on the silicon surface exposing the samples to the air for more than 24 h at ambient temperature of 21°C and 40 ± 10 %RH. The thickness of the oxide layers was estimated around 1.8 nm by ellipsometry.

Room temperature plasma oxidation was performed in a barrel chamber for 90 s at 150 W at the pressure 0.5 and 1 mTorr in order to increase the quality of the thin oxide layer. Ultra thin silicon oxide layers with surface roughness and properties comparable to thermal oxide can be obtained using this method [179]. The thickness of the oxide layers so obtained were estimated around 2.3 nm by ellipsometry. For the preparation of metal patterned Si samples, the plasma oxidation was performed before the lithography.

Metal Evaporation was performed in a dual e-beam evaporator (e-gun Vacotec). The pressure was below 4×10^{-7} Torr at the start of the evaporation. The electrodes are composed of a multilayer metal. The metal nature constituting electrodes has an impact on the process MAE. Au and Ni have relatively low catalytic activity for hydrogen evolution and are resistant to HF. Moreover, they do not oxidize easily in air (for a good electrical contact with the external circuit) and they are common in microfabrication. The nature of the adhesive layer in direct contact with the silicon and the presence of a sacrificial layer above the electrodes will change widely MAE process. Several compositions of the metallic multilayer were deposited. The reasons for this variation in the composition of metallic multilayer are related to RTA annealing and are explained in Appendix B on page 227. The first metal multilayer consists of a 5 nm thick adhesion layer of Ti, Cr, or Al and a 100 nm

thick Au layer, each evaporated at a rate of 0.1 nm/s. This multilayer enables to determine the influence of the metal nature in contact with the silicon (the adhesion layer is this case) on MAE process. The second metal multilayer consists of a 5 nm thick adhesion layer of Ti, a 30 nm thick Pt layer and a 150 nm thick Ni layer evaporated at a rate respectively of 0.1 nm/s (Ti and Pt) and 0.5 nm/s (Ni). The third metal multilayer is composed of the same layers as the second metal multilayer completed by a 100 nm thick Ti layer as sacrificial layer. The second and third multilayer are used to determine the impact of the presence of the sacrificial layer on the MAE process.

We prepared and used in total 26 different types of samples. In Table 3.1 are reported the label assigned to the different samples, and their main characteristics. The results obtained with PNOx and UnNOx samples will not be shown and discussed as no substantial differences were observed in between them and PBE and UnBE samples.

Electrolytes

Mixtures of HF, water and N,N-Dimethylformamide (DMF) were used as electrolytes. Solutions with the following composition were prepared : HF(48%):DMF = 1:4. In the following we will refer to these solutions as NDS. As the electrolyte composition changes over time due to the hydrolysis of DMF (see section 3.2.2 on page 67) and the composition affect the MAE process, a 20 days old solution (referred in the following as ODS) was prepared. Both old (ODS) and new (NDS) solutions were used in the experiments.

Electrochemical Etching

The metal patterned samples were electrochemically etched to form a macroporous silicon layer. The area of the sample exposed to the electrolyte was about 2 cm^2 and had a circular shape. All the experiments were carried out at room temperature, and the solution was stirred with a rotating propeller to avoid inhomogeneities due to the gas accumulation on the surface. A platinum grid placed at 1 cm from the sample was used as cathode, while the anode was the silicon substrate. A 200 nm thick aluminum layer was evaporated on the wafer back side and annealed at 432 °C for 30 min in reducing atmosphere.

Table 3.1: This table shows the label assigned to samples used in the experiments. As an example, the label UnBETi and PBETi indicate respectively an un-patterned and a patterned sample which surface was etched with BHF before the metal evaporation with a 5 nm thick Ti layer as adhesion layer and on the top a 100 nm thick Au layer. As a second example, the label UnPOxnoSL and UnPOxSL indicate an un-patterned sample which surface was oxidized by plasma before the metal evaporation with a 5 nm thick Ti layer as adhesion layer, a 30 nm thick Pt layer and 150 nm thick Ni layer respectively without and with a 100 nm thick Ti layer as sacrificial layer (SL).

Sample Label		Interface	Metal Layers (tickness in nm)
Un / P BE	Ti	H terminated SiO_2 free surface	Ti(5) - Au(100)
	Cr		Cr(5) - Au(100)
	Al		Al(5) - Au(100)
Un / P NOx	Ti	Native SiO_2	Ti(5) - Au(100)
	Cr		Cr(5) - Au(100)
	Al		Al(5) - Au(100)
Un / P POx	Ti	RT Plasma SiO_2	Ti(5) - Au(100)
	Cr		Cr(5) - Au(100)
	Al		Al(5) - Au(100)
Un / P BE	noSl	H terminated SiO_2 free surface	Ti(5) - Pt(30) - Ni(150)
	Sl		Ti(5) - Pt(30) - Ni(150) - Ti(100)
Un / P POx	noSl	RT Plasma SiO_2	Ti(5) - Pt(30) - Ni(150)
	Sl		Ti(5) - Pt(30) - Ni(150) - Ti(100)

An electrical contact was made by placing an aluminum plate in direct contact with it (figure 3.12). The macroporous silicon layer was formed by setting the etching current density J_{etch} at 17.5 mA/cm^2. This value is smaller than the critical value J_{ps}=182 mA/cm^2 at which the silicon surface is polished. Two anodization times were used to make two thicknesses of porous silicon : 15 and 25 min. A potentiostat (Princeton Applied Research, Ametek, VersaSTAT 3) was used to apply the anodization voltage corresponding to the given current value between the silicon sample and the electrolyte. No reference electrode was used to perform the anodization. The results are shown via cross tilted scanning electron microscopy (SEM) views of the porosified samples. A LEO 982 field emission scanning electron microscope (LEO Electron Microscopy Inc., Thornwood, New York) was used to perform the SEM analysis.

Polarization curves and Evans diagrams

The fully metal covered wafers were placed on the electrochemical cell with the front side in contact with the electrolyte. The area of the sample exposed to the electrolyte was 23.75 cm^2 and had a circular shape. The solution was mechanically stirred with a rotating propeller. The electric contact with the back side surface was guaranteed by a 200 nm thick Al layer previously evaporated. Polarization diagram was performed using a Source Meter Unit (Keithley 2636A) in the different HF/DMF solutions, from −2.00 to +2.00 V at a (scan rate of 50 mV/s), and resulted in an log(i_{tot})-V plot dividing the measured current I_{tot} by the area of the exposed sample surface (i_{tot} is current density). No reference electrode was used to perform the measurements. For each sample, the Evans diagram was plotted by combining log(i_{tot})-V plots of each constituents of galavanic cell (metal and bare silicon). The diagram of Evans is used to calculate the corrosion current density (i_{corr}) proportional to corrosion rate in the galvanic cell (see Appendix D). Evans diagrams are plotted with V on the abscissa and the log(i_{tot}) on the ordinate. The anodic and cathodic curve branches are respectively placed on the left and right. To facilitate the distinction between the different corrosion potentials, E_{corr}, we adopt the notation resumed in table 3.2.

Notation	Corrosion potential measured on ...
$E_{corr(Si)}$	bare Si samples.
$E_{corr(M)}$	fully coated metal samples.
$E_{corr(M/Si)}$	partially covered metal samples. (not measured experimentally)

Table 3.2: Notation of different corrosion potentials. $E_{corr(M/Si)}$ is not measured experimentally but deduced from diagrams Evans.

Electroless Etching

The electroless etching experiments were performed by immersion of the metal patterned samples in a beaker containing 10 ml of NDS for 30 minutes. No agitation is used, leaving the solution static. The results are shown via top SEM views of the samples. A LEO 982 field emission scanning electron microscope (LEO Electron Microscopy Inc., Thornwood, New York) was used to perform the SEM analysis.

3.2.4 Results

Metal/silicon interface impacts

The following electro-etchings were all performed with an anodization time of 15 min.

Figures 3.13 show SEM cross-sectional tilted views of macroporous layers formed on Ti/Au patterned samples. Figures 3.13(a.) and (b.) show PBETi samples etched respectively with NDS and ODS. No substantial differences were observed between samples etched with NDS and ODS.

Nevertheless, the differences appear with the patterning geometry, a 15 μm in with long Au strip in figure 3.13(a.), and a 3 μm in width serpentine structure in figure 3.13(b.). In both cases the metal was stripped away during the etching and only the distribution of the pores enables to recognize the patterned areas. Metal patterns smaller than 5 μm in width result in the formation of thick pore walls. The wider patterns result in porous areas with pores of smaller depth delimitated by thicker walls in correspondence of the pattern edges.

The presence of a thin RT plasma oxide at the interface between the metal layer and the silicon surface drastically changes the results. Figures 3.13 (c.) and (d.) show the cross-section views of samples PPOxTi etched respectively with NDS and ODS electrolytes. Figure 3.13(c.) shows a sample patterned with interdigitated electrodes 2 μm wide with a pitch of 5 μm. The metal layer was not stripped during the etching, and resisted to the following rinsing and drying of the samples. The sample cleaving necessary to obtain a cross-sectional view of the samples emphasizes the poor adhesion of the metal. Figure 3.13 (d.) shows as samples etched with ODS solution exhibit a better metal adhesion, the 3 μm wide serpentine structure is integral after the cleaving and the metal layer follow the silicon cross-section profile.

Similar results were obtained with samples PBECr and PPOxCr. Figures 3.14 shown cross-sectional tilted views of PBECr sample (figure 3.14(a.) and (b.)) and PPOxCr sample (figure 3.14(c.) and (d.)) respectively etched with NDS (a. and c.) and ODS (b. and d.).

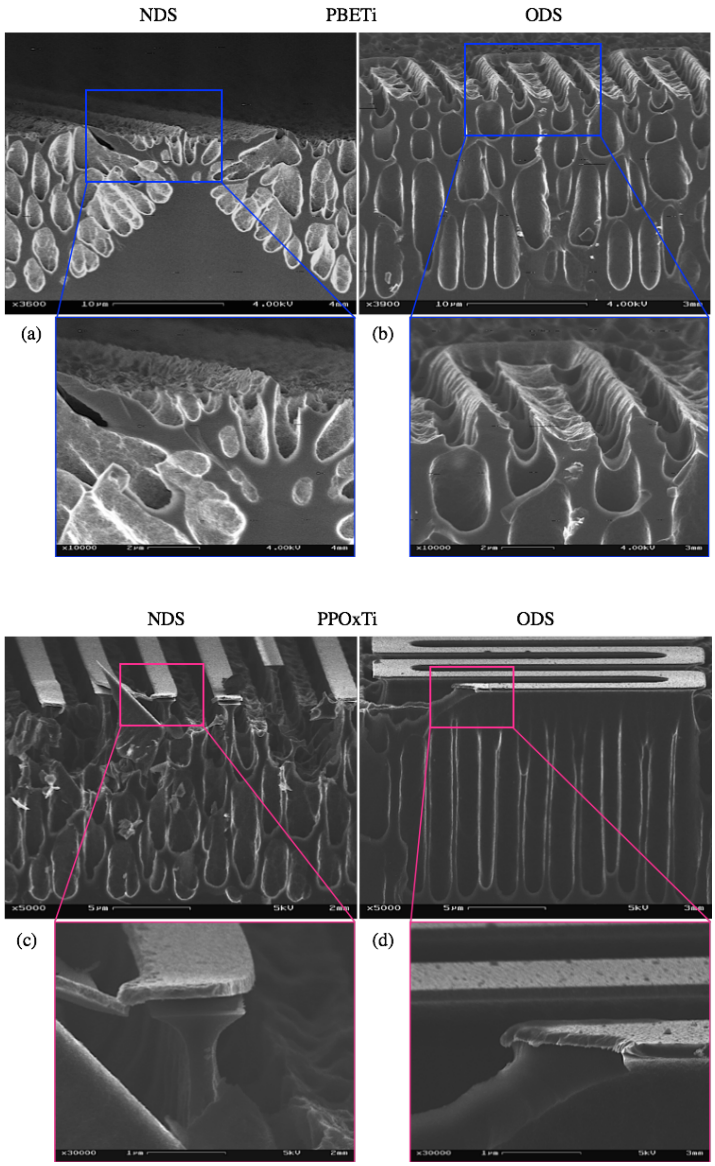


Figure 3.13: SEM cross-sectional tilted view of porosified samples previously patterned with Ti/Au layers. (a.) and (b.) show PBETi samples respectively etched in NDS, and ODS. (c.) and (d.) show PPOxTi samples respectively etched in NDS, and ODS.

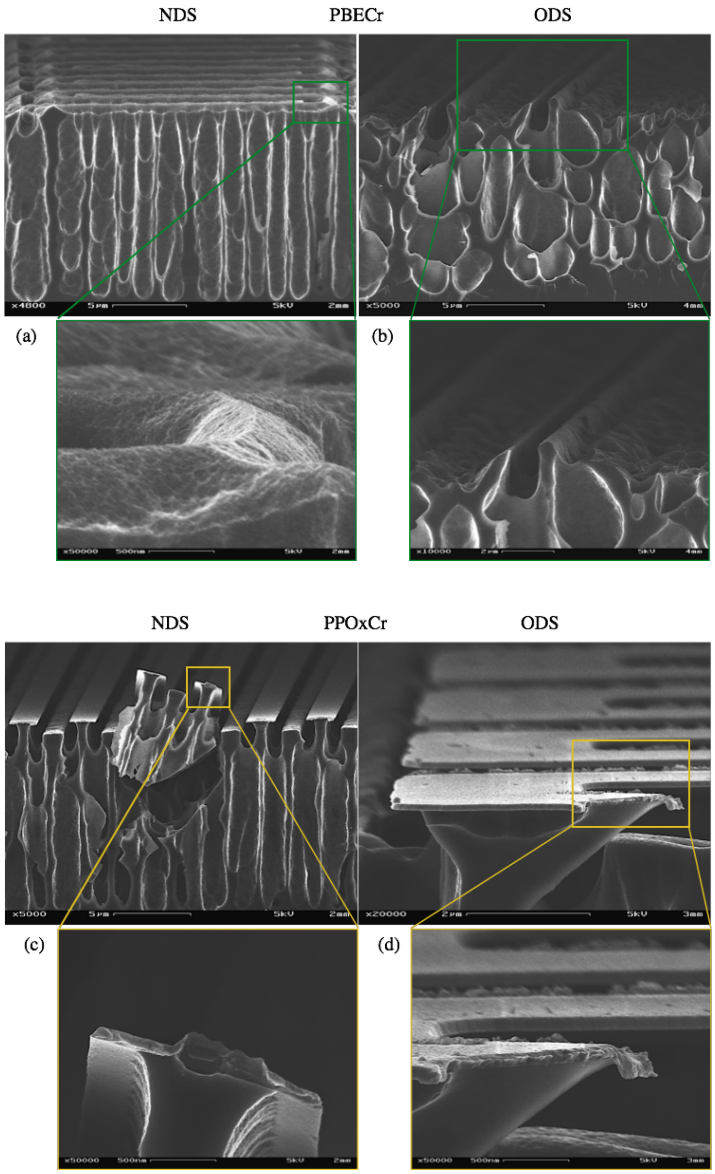


Figure 3.14: SEM cross-sectional tilted view of porosified samples previously patterned with Cr/Au layers. (a.) and (b.) show PBECr samples respectively etched in NDS, and ODS. (c.) and (d.) show PPOxCr samples respectively etched in NDS, and ODS.

The etching of PBECr samples resulted in the stripping of the metal during the etching, and no substantial differences were observed between the samples etched with NDS and ODS. The top surface of the samples is smoother than in PBETi samples, as is possible to observe in figure 3.14(a.) in which is shown samples previously patterned with a 3 μm wide serpentine structure. Moreover, the depth of the pores that grow after the metal stripping in correspondence of pattern features wider than 5 μm is higher that in PBETi samples. In figure 3.14(b.) is shown a portion of sample patterned with interdigitated electrodes 8 μm wide with a pitch of 2 μm. Parallel thick walls are in correspondence of the metal pattern edges. The depth of the pores inside these areas is almost the same than outside the patterned area. This suggests that in samples PBECr the Au layer is stripped away in a smaller time than in samples PBETi.

Also in this case the RT plasma oxide changes the scenario and the etching of samples PPOxCr did not result in the metal stripping. The metal resists to both rinsing and drying, and either in samples etched with NDS solutions the metal seems to be strongly adherent to the surface. Figure 3.14(c.) shows a sample patterned with interdigitated electrodes 2 μm wide with 5 μm pitch etched with NDS. The metal was not stripped away in the sample cleaving, and a broken part is anchored to the substrate by means of the metal layer itself. An underetching in correspondence of the edges of the metal pattern edges, that causes the complete exposition of the metal layer is observed for all pattern features, and also for samples etched with ODS (figure 3.14(d.)). This does not affect the strength of the adhesion, but reduces the contact area between silicon and metal, that for electrodes of small dimensions can be considerable.

As shown in figure 3.15(a.) and (b.) also the etching of samples PBEAl in both NDS and ODS electrolytes resulted in the stripping of the metal after few minutes of etching. Figure 3.15(a.) shows clearly the stripped metal pattern consisting of 2 μm wide interdigitated electrodes with pitch of 8 μm. Interestingly the gap between the top of the previously masked area and the macroporous layer is bigger than what observed with samples PBETi, and PBECr. This gap results from the nucleation phase of the macropores. Before the macropores distribution is established, the electro-etching requires a nucleation phase during which a mixed layer between nanopores and macropores exists.

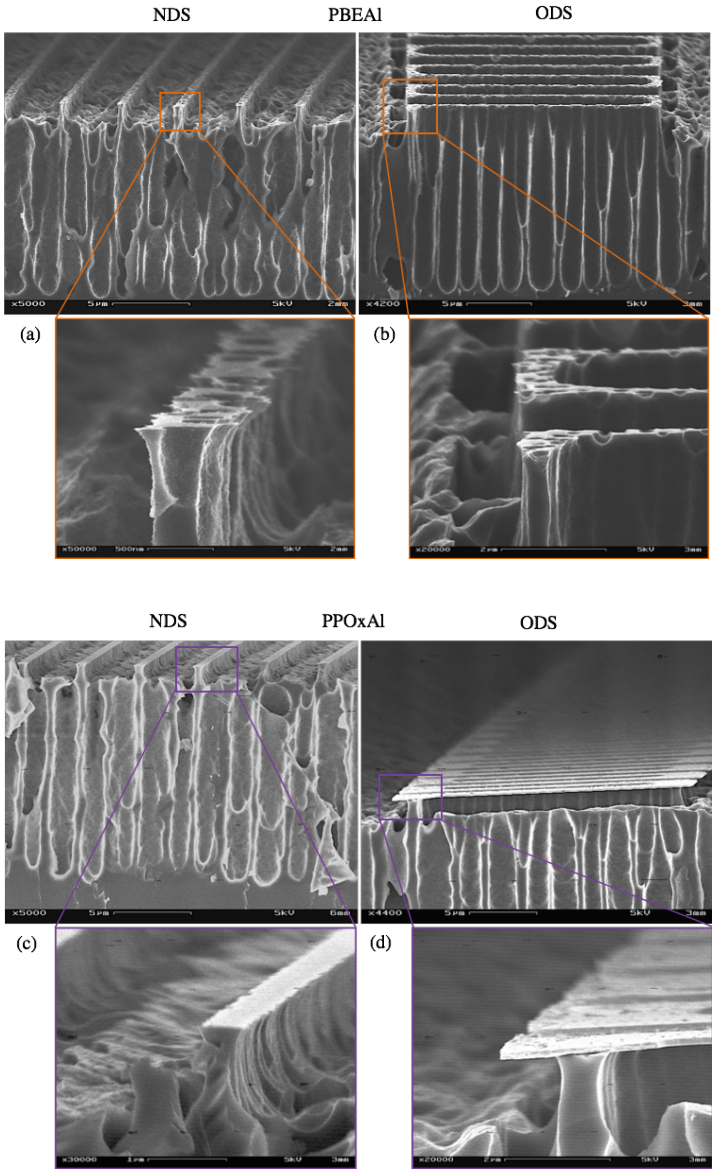


Figure 3.15: SEM cross-sectional tilted view of porosified samples previously patterned with Al/Au layers. (a.) and (b.) show PBEAl samples respectively etched in NDS, and ODS. (c.) and (d.) show PPOxAl samples respectively etched in NDS, and ODS.

This layer is completely dissolved in the first minutes of etching. A height difference appears between the porous zones and masked areas. Moreover, macropores of around 500 nm in depth are present in these smaller areas.

We also observe that the dimension of these areas is smaller than the metal pattern size. The same behavior was observed for samples etched with ODS solution. In figure 3.15(b.) is shown a portion of sample patterned with a serpentine structure. Also note the profile differences of the structures here shown from the structure of a similar portion of a PBETi sample shown in figure 3.13(b.) (except that the cleavage was not done with the same orientation according to the sample). The overall morphology of these structures, suggest that the formation of the small macropores on the previously patterned areas happen before the metal stripping. Apart from the pores, the surface is flat, which suggests that the pores are formed when the metal is still in contact with the silicon. This hypothesis is somehow confirmed by the results of the electroless etching shown below. However, it is difficult to determine the path of reactants and products of porosification reaction. Several hypotheses have been formulated in the literature [161]: (i) the reactants and products pass under the electrodes through the interstices in the metal/silicon junction; (ii) the reactants and products pass through the grain boundaries and/or pinholes in the metal layer.

Differently from what observed with PPOxTi and PPOxCr, the etching of samples PPOxAl in NDS electrolytes resulted in the stripping of the metal layer. Figure 3.15(c.) shows a portion of sample patterned with interdigitated electrodes 2 μm wide with a 8 μm pitch. The resulting structure is similar to what observed for samples PBEAl, the only difference are the small macropores on the top of the patterned areas that in this case are not observed. Figure 3.15(d.) shows a portion of a PPOxAl sample patterned with a 3 μm wide serpentine structure and etched with ODS. Here, the metal was not stripped during the etching, but the picture show the weakness of the metal adhesion. This picture also shows how large is the mask undercutting resulting in very thin silicon structures in correspondence in the metal pattern.

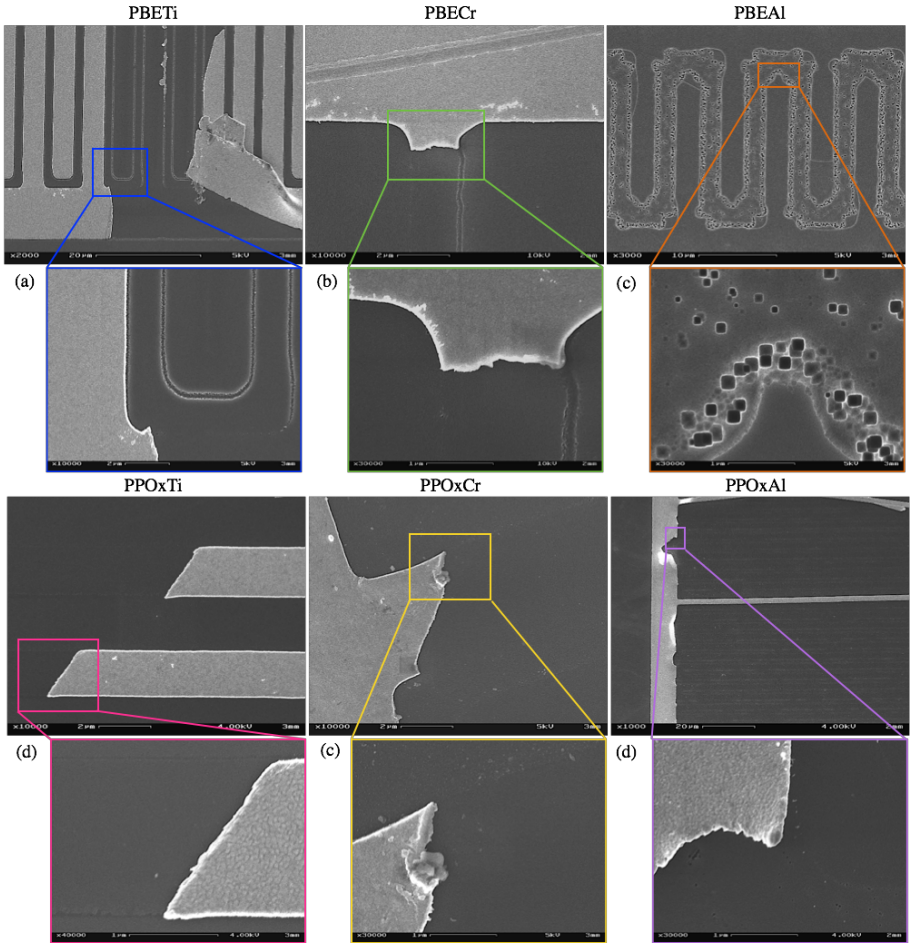


Figure 3.16: SEM top view of the metal patterned samples with and without plasma oxide at the interface metal/silicon after 30 min of immersion in NDS.

In figure 3.16 are shown SEM top views of portions of patterned samples electroless etched as described in the experimental section with NDS. Electroless etching is performed by a simple immersion of the samples for 30 min in a NDS. A dependency of the etching behavior on the adhesion promoter and on the oxidation state of the silicon surface is here also observed.

Even if all samples undergo to the metal stripping do to the etching of silicon beneath, in samples PBETi, PBECr, and PBEAl the etching appears to be faster and deeper.

Again PBETi and PBECr samples behave in a similar way. Figure 3.16(a.) shows a portion of PBETi sample patterned with interdigitated electrodes 4 μm wide with a pitch of 2 μm. The etching is faster at the edges of the metal strips, the silicon is etched deeper.

This kind of behavior is not observed on all electrode edges, most probably because of the different profile of the metal edges. As the metal pattern was transferred on the silicon wafers by lift-off process, the roughness and the profile at the edges depend strongly on the angle at which was placed the wafer during the metal evaporation and on the position of the structures on the wafer. The asymmetry on the metal shape affects the electrochemical etching, as an example in the figure 3.16(b.). The pore walls on the right are taller than on the left. The etching does not involve only the edges but go forward until to cause the metal stripping.

Again the scenario changes when PBEAl samples are etched. Figure 3.16(c) shows the SEM top view of a portion of samples patterned with a 3 μm wide serpentine. The silicon is here etched deeper than in samples PBETi and PBECr, and macropores that can reach the diameter of around 200 nm are distributed on the patterned surface, with a higher density close to the edges.

For a 30 minutes immersion in the electrolyte, the presence of the thin RT plasma oxide does not avoid the metal assisted etching of the silicon beneath the metal layer and the metal stripping during the rinsing of the samples. Even if the etching seems to be faster in PPOxAl samples and more metal is stripped, no fundamental differences were observed in the etching behavior.

In order to analyze the surface topography caused by MAE process, we performed AFM measurements on Si surfaces after electroless etching and consequent metal stripping. Figures 3.17(a.) and (b.) show the surface morphology of PBETi portions patterned respectively with 2 μm wide and pitch interdigitated electrodes, and with a 20 μm wide strip.

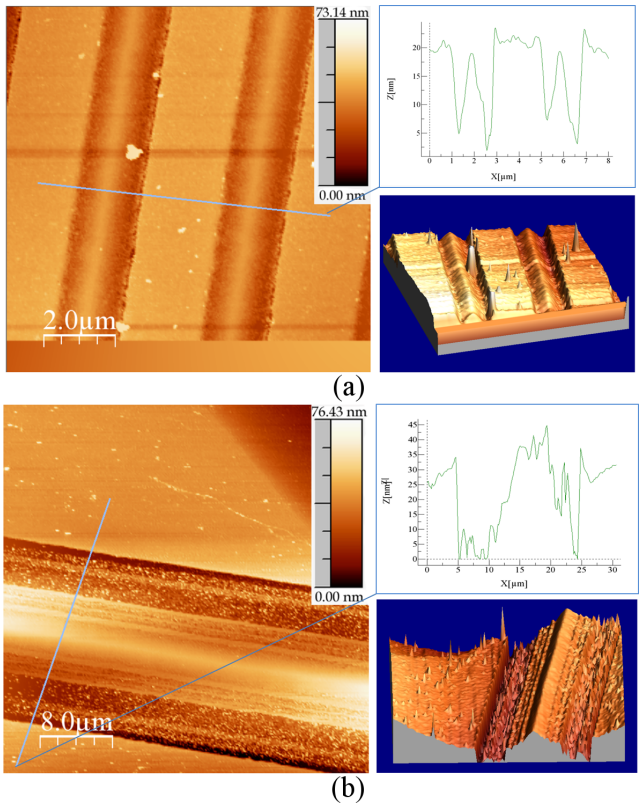


Figure 3.17: AFM 2D and 3D images of the surface of a PbbbeTi sample after electroless etching. Both sets of electrodes 2 μm wide (a.), and 20 μm wide (b.) were delaminated after 30 min of electroless etching with NDS.

The profile shape of the etched surface suggests that the etching starts at the edges of the metal strips and it propagates toward the center of the metal strip causing the delamination of the electrodes. This profile is typically that of an underetching. Etching takes place mainly at the metal/silicon/electrolyte interface. This interface, initially at the edges of the electrode, moves gradually as the underetching progresses towards the center of the electrode.

Nevertheless, etching continues at the edges of the electrodes. Thus the etching under electrode edges is deeper than under electrode center.

This explains why the narrower electrodes are faster delaminated than large electrodes (figure 3.18). Moreover, the etching depth is higher in the case of large electrodes. One possible explanation is that the holes generated by the center of the electrode diffuse into the silicon towards the edges of the electrodes (figure 3.18).

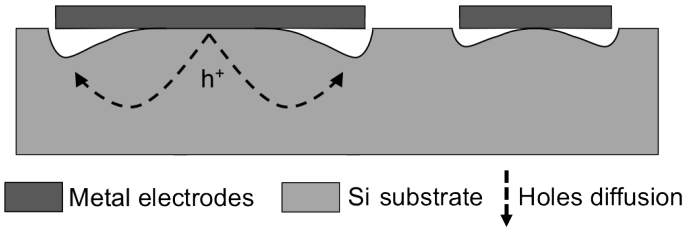


Figure 3.18: Diagram of a cross-section view of the underetching under a narrow and a wide electrodes. In the case of the wider electrodes, the holes generated by the center of the electrode diffuse into the silicon towards the edges of the electrodes and underetching is deeper.

The profile showed in the 3D images is very similar to that observed in the SEM images of electrochemically etched samples (figure 3.13(a.) and (b.)) at the metal pattern position, even if scales in the z direction are different.

The analysis of Evans diagrams of silicon/metal/electrolyte systems allows highlighting the parameters that influence the silicon corrosion. The diagram of Evans is used to calculate the corrosion current density (i_{corr}) proportional to corrosion rate in the galvanic cell (see Appendix D). Indeed, JV characteristics of the cathode (fully metallized sample) and the anode (bare silicon) separately measured, are plotted on the same graph. The intersection between the cathodic branch of the fully metallized sample and the anodic branch of the bare silicon provides information on the corrosion current (i_{corr}) proportional to corrosion rate.

At first, let's observe Evans diagrams of a bare silicon sample in contact with NDS and ODS (figure 3.19).

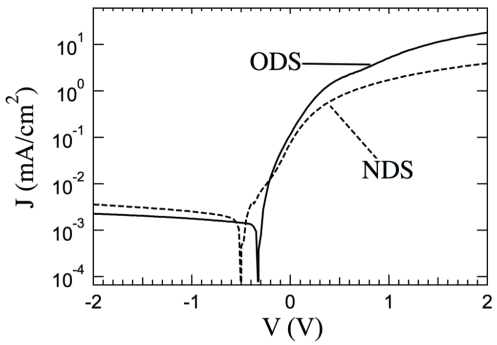


Figure 3.19: Evans diagrams of bare Si samples in NDS and ODS.

With both electrolytes, the electrical behavior obtained is similar to those of a Schottky diode. The mixed potential between hydrogen evolution on silicon surface (cathodic branch) and silicon dissolution (anodic branch), $E_{corr(Si)}$, is negative for both electrolytes, with a more negative value measured for NDS. At more negative potential (cathodic branch), hydrogen evolution is favored. The reaction rate increases relatively linearly with the potential. The corrosion current (i_{corr}) can be estimated by measuring the intersection of the tangents to the two branches of the curve and is of the order of 2×10^{-3} mA/cm^2. This value corresponds to the values in literature [185]. The corrosion current is somewhat higher for NDS. This is consistent with the fact that there is a difference in electro-etching achieved in NDS and ODS, although these differences were not significant. The difference in hydrogen ion concentration in the two solutions is a possible explanation of the variation of the corrosion current. Indeed, the hydrogen ion concentration in ODS is lower (higher pH) due to the DMF hydrolysis (see section 3.2.2). This low concentration in the bulk solution decreases the reactants supply to hydrogen evolution reaction and thus decreases the corrosion current. The galvanic system undergoes a concentration polarization.

In anodic branch, the hole concentration at the surface increases. Anodic dissolution occurs and the current increases exponentially with the increasing potential. The critical current J_{ps} was measured at potential V_{ps} higher than 2 V. A higher value of V_{ps} was measured with NDS electrolytes probably because of the lower conductivity of the solution (2 mS/m instead of 30 mS/m for ODS).

The anodic branch consists of two domains (two different slopes) separated by a transition zone. In the first area (for lower potential) surface reactions control the rate of charge flow in the system. Corrosion undergoes an activation polarization. In the second domain, the current becomes large and the charge transfer in the electrolyte limits the current. Corrosion undergoes a concentration polarization. In the transition zone, the corrosion shifts from activation to concentration control.

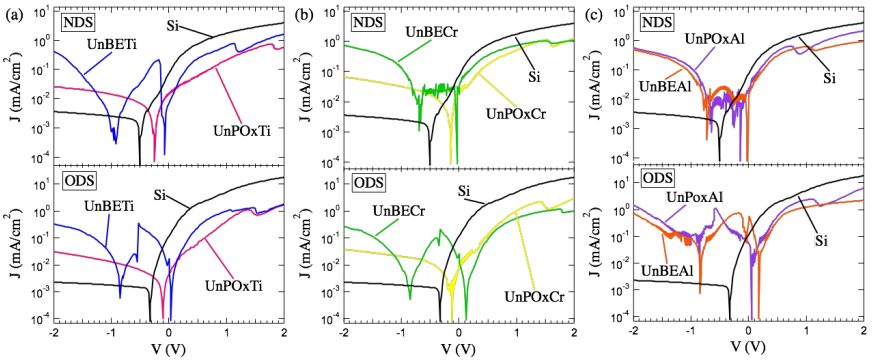


Figure 3.20: Evans diagrams of Si samples in NDS and ODS with and without Au coating. (a.) Comparison of J-V curves of Si samples with J-V curves of samples covered with Ti/Au layers (UnBETi and UnPOxTi) in NDS (top) and ODS (bottom); (b.) Comparison of J-V curves of Si samples with J-V curves of Si samples covered with Cr/Au layers (UnBECr and UnPOxCr) in NDS (top) and ODS (bottom); (c) Comparison of J-V curves of Si samples with J-V curves of samples covered with Al/Au layers (UnBEAl and UnPOxAl) in NDS (top) and ODS (bottom).

Figures 3.20 show the Evans diagrams of Si samples with and without metal coating. On top and bottom are respectively shown the characteristics measured using NDS and ODS as electrolytes. As a reminder, the metal coated samples have also different oxidation state at the metal/semiconductor interface. In this way, the measurement takes into account the charge transfer at the electrolyte/metal interface (cathode), but also the electrical path that connects this interface and silicon (anode). The measurement thus incorporates the ohmic polarization. Evans diagrams in figure 3.20 include both the anode (bare Si curve) and the cathode combined with the electrical path between anode and cathode. In this way, all the galvanic cell is considered.

With metal covered samples, $\log(i_{tot})$-V curves strongly depend on the surface state (presence or not of the interfacial oxide). They depend also on the metal used as adhesion promoter. In all curves, the corrosion potential of metal, $E_{corr(M)}$, is higher than the corrosion potential of bare silicon $E_{corr(Si)}$. When silicon and metal are both in contact with the electrolyte, the corrosion potential of the whole galvanic cell, $E_{corr(M/Si)}$, lies between these two measured corrosion potentials ($E_{corr(Si)} < E_{corr(M/Si)} < E_{corr(M)}$). The silicon acts as an anode and the redox reactions on the metal acts as a cathode. Galvanic corrosion of silicon is observed.

The anodic branches exhibit similar behavior independently of the adhesion layer used or the oxidation state of the metal/silicon interface. Near 1.5 V, a drop in the value of the current appears. We attribute this to the oxidation of the gold surface. Figure 3.21 is Pourbaix diagram for gold. A passivation zone exists above about 1.5 V relative to the pH of NDS and ODS. In this zone, the stable state is gold(III) hydroxyde ($Au(OH)_3$) which is an electrical insulator. The variation of the position of this peak can be simultaneously attributed to several reasons. First, a two-electrode measurement taking into account the potential drop in the electrolyte bulk (higher in NDS because it is more resistive) and the potential drop at the counter-electrode. Second, the Pourbaix diagram in figure 3.21 is valid for a specific solution and it is different for our electrolytes.

Cathodic branches have very different behavior according to both the used adhesion layer and the presence of RT plasma oxide at the interface.

Samples without RT plasma oxide at the interface (UnBE samples), independently of the adhesion promoter used, show a high current and a poorly rectifier behavior. For all samples the current does not grow monotonically as the potential is made negative, a drop of the current is observed for potential slightly higher than -1 V. The voltage at which occurs the drop, and the trend followed by the current changes depending on the sample, and on the electrolyte used (NDS or ODS). For UnBECr in NDS, and UnBEAl in both NDS and ODS, as the potential is made negative the current oscillates around a constant value and abruptly decrease. After few mV the current starts then to increase monotonically.

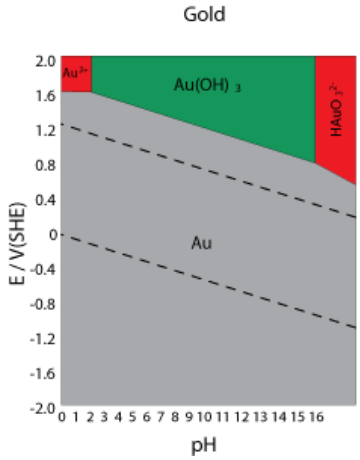


Figure 3.21: Pourbaix diagram of gold in aqueous solution. Reproduced from DoITPoMS, University of Cambridge (http://www.doitpoms.ac.uk/tlplib/pourbaix/pourbaix_example.php, August 22, 2014)

For samples UnBETi in both NDS and ODS, and UnBECr and UnBEAl in ODS, the drop of the current is less abrupt. As the potential is made negative, the current start to increase until around 500 mV and decrease again after that. This not monotonic trend followed by the current at potentials lower than $E_{corr(M)}$ is probably due to some transition phenomena that happen at the interface.

Characteristics of samples with RT POx at the interface show a bigger dependency on the metal used as adhesion promoter. The samples UnPOxTi and UnPOxCr have a rectifier behavior similar to bare silicon, although the asymmetry of the curves is less pronounced. Cathodic branchs present a relatively linear dependence of the electric potential with a current value of an order of magnitude higher than that measured on the bare silicon. In addition, unlike the sample without RT POx, cathodic branchs present no drop.

The characteristics of samples UnPOxAl are instead very similar to that of UnBEAl samples, with a shift in the $E_{corr(M)}$ smaller for UnPOxAl samples.

Impact of sacrificial layer presence

Figures 3.22 show SEM cross-sectional tilted views of macroporous layers formed on Ti/Pt/Ni patterned samples (without Ti sacrificial layer). Figures 3.22(a.) and (b.) showed PBEnoSL samples etched respectively with NDS and ODS. No significant difference was observed between the previous samples and thereof. The morphology is more acute in the sample etched in NDS compared to the one etched in ODS, suggesting that delamination was faster in the first sample.

In the presence of the oxide interface (figure 3.22(c.) and (d.)), the scenario is between a sample patterned by Ti/Au or Cr/Au layer and a sample patterned by Al/Au layer. Indeed, when etching in NDS, the metal layer is delaminated as in PPOxAl samples. However, the morphology suggests that delamination occurred at the end of the etching (possibly even during the rinse step). Conversely, when etching in ODS, the metal is still present on Si surface and adhesion seems good. Unlike other samples PPOx etched in ODS, the silicon layer below the electrode has the same width as the metal layer not leaving free the back surface of the electrodes.

Figures 3.23 show SEM cross-sectional tilted views of macroporous layers formed on Ti/Pt/Ni/Ti(SL) patterned samples. Figures 3.23(a.) and (b.) showed PBESL samples etched respectively in NDS and ODS. As with all other samples, the metal layer is delaminated for etching in NDS. By cons, when etching in ODS, part of the electrodes are always present on Si. In all other samples PBE, no electrode has resisted to delamination. It shows the reduction of MAE process due to the presence of the Ti sacrificial layer.

For etching the sample PPOxSL (figures 3.23(c.) and (d.)) in NDS and ODS, the metal electrodes still adhere effectively to the Si surface. In figures 3.23(d.), one Si crystalite is broken and it is retained by the metal electrode, which suggests an excellent adhesion. As for the sample PPOxnoSL, Si layer under the metal has the same width as the metal electrode. The MAE process is non-existent or very low to be detectable.

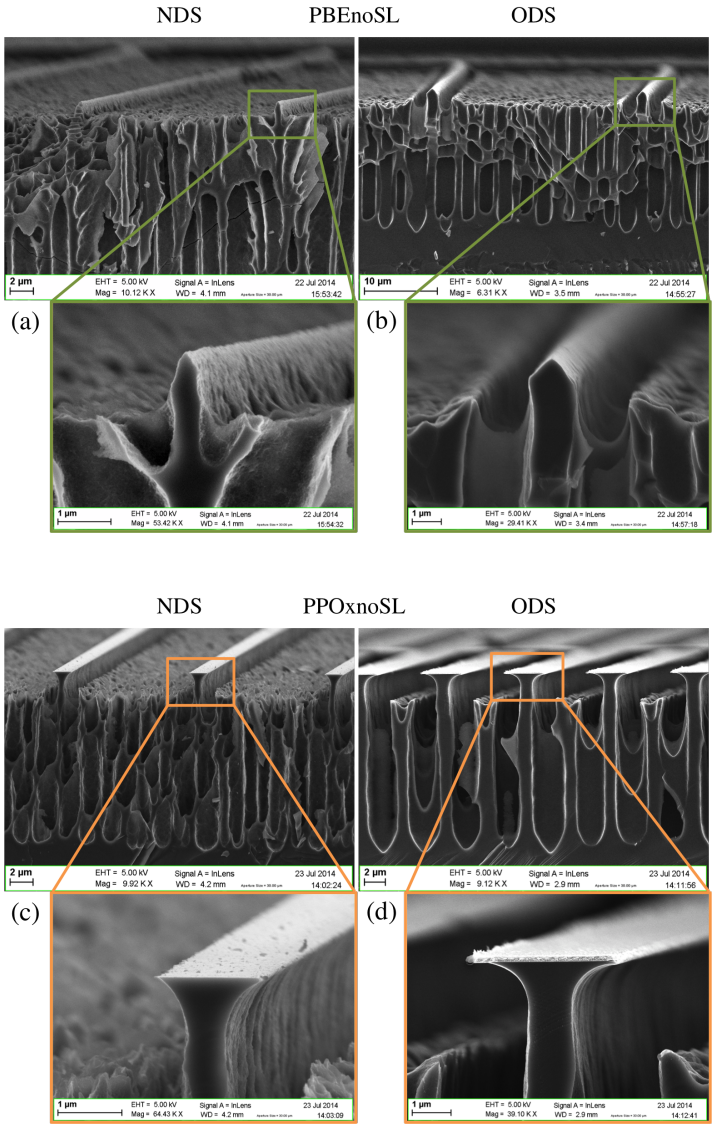


Figure 3.22: SEM cross-sectional tilted view of porosified samples previously patterned with Ti/Pt/Ni layers (without Ti sacrificial layer). (a.) and (b.) show PBEnoSL samples respectively etched in NDS, and ODS. (c.) and (d.) show PPOxnoSL samples respectively etched in NDS, and ODS.

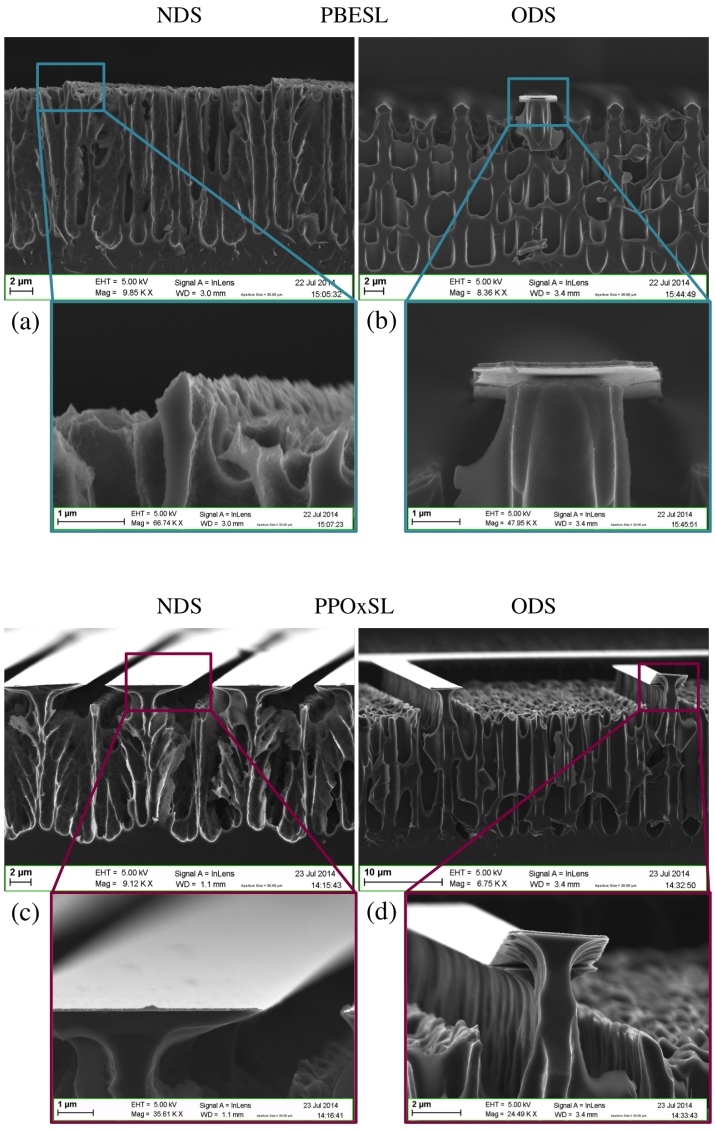


Figure 3.23: SEM cross-sectional tilted view of porosified samples previously patterned with Ti/Pt/Ni/Ti layers (with Ti sacrificial layer). (a.) and (b.) show PBESL samples respectively etched in NDS, and ODS. (c.) and (d.) show PPOxSL samples respectively etched in NDS, and ODS.

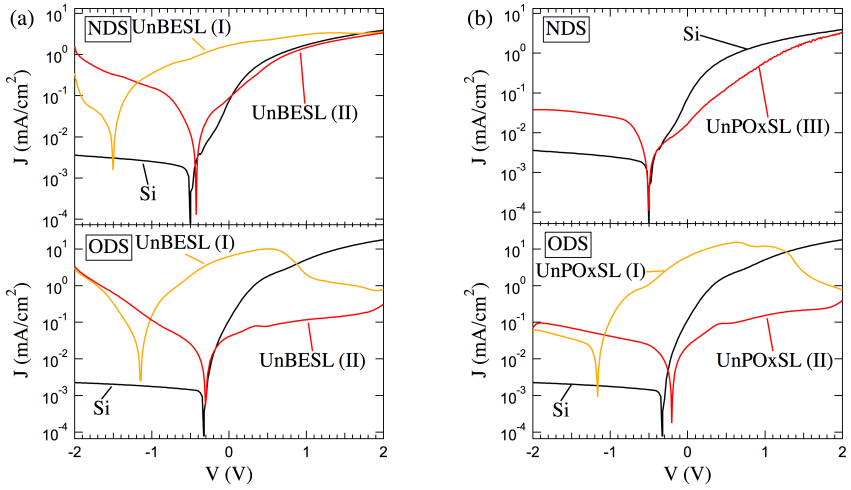


Figure 3.24: Evans diagrams of Si samples in NDS and ODS with and without metallic multilayer (including sacrificial layer (SL)) coating (Ti/Pt/Ni/Ti(SL)). (a.) Comparison of J-V curves of Si samples with J-V curves of samples covered metallic multilayer without RT POx (UnBESL) in NDS (top) and ODS (bottom); (b.) Comparison of J-V curves of Si samples with J-V curves of samples covered metallic multilayer with RT POx (UnPOxSL) in NDS (top) and ODS (bottom). The roman numeral in parenthesis (I, II and III) represents the order in which the measurements were made on the same sample.

Figures 3.24 show the Evans diagrams of Si samples with and without metal coating. On top and bottom are respectively shown the characteristics measured using NDS and ODS as electrolyte. Figure 3.24(a) compares J-V curves of Si samples with J-V curves of samples covered metallic multilayer with sacrificial layer but without RT POx (UnBESL); figure 3.24(b) compare J-V curves of Si samples with J-V curves of samples covered metallic multilayer with sacrificial layer and with RT POx (UnPOxSL).

Unlike measurements on gold samples, the J-V curves evolve drastically between the first measurement and the next. Then, the following measurements are broadly similar. To visualize this, the order in which the measurements were made is distinguished by the roman numeral in figure 3.24.

At the first measurement, $E_{corr(M)}$ of fully covered metal sample is more negative than $E_{corr(Si)}$ of bare Si sample. This observation can be made on samples with and without RT POx (UnBESL and UnPOxSL). For etching in ODS, in the anodic branch, the current increases monotonically to approximately 750 mV. At this point a drop in current density appears.

During the following measurements, $E_{corr(M)}$ shifts in the vicinity of $E_{corr(Si)}$ and the anodic current density is substantially lower than in the first measurement. In the presence of RT POx at the metal/Si interface, the rectifier behavior reappears, but it is less significant than for the samples metallized with Au.

3.2.5 Discussions

Table 3.3: $E_{corr(M/Si)}$ and i_{corr} values of all samples, calculated at the intersections of curves of bare Si samples and fully metal coated samples.

Samples	NDS		ODS	
	$E_{corr(M/Si)}$ (V)	i_{corr} (mA/cm^2)	$E_{corr(M/Si)}$ (V)	i_{corr} (mA/cm^2)
UnBETi	-0.137	0.021	-0.124	0.037
UnPOxTi	-0.362	0.004	-0.274	0.003
UnBECr	-0.100	0.029	-0.100	0.047
UnPOxCr	-0.276	0.008	-0.259	0.004
UnBEAl	-0.250	0.013	0.074	0.205
UnPOxAl	-0.175	0.016	-0.050	0.076

Table 3.3 lists corrosion potential ($E_{corr(M/Si)}$) and the corrosion current density (i_{corr}) calculated at the intersections of curves of bare silicon samples and fully metal coated samples (on figures 3.20). These two parameters are respectively the equilibrium potential and the internal corrosion current of the galvanic system composed of the electrolyte, the metal and silicon when all three are in contact with each other. This situation is similar to that of metal electrodes on the Si surface during the anodization of porous silicon. Corrosion current density (i_{corr}) is therefore proportional to the rate of electrode delamination during anodizing. Figure 3.25 graphically shows the difference in value of the corrosion current density.

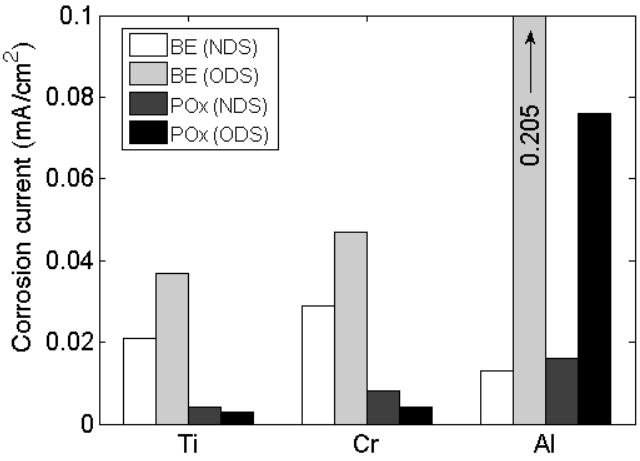


Figure 3.25: Graphical representation of the differences between the corrosion current density.

It is important to keep in mind that the i_{corr} values listed in the table 3.3 are given for an anode and a cathode having the same area. These values were measured on fully metallized samples. For metal electrodes patterned samples, the cathode surface (metal) is smaller than that of the anode (silicon). This difference in surfaces has an impact on the corrosion current. However, the i_{corr} values in the table 3.3 enable to compare qualitatively the MAE process on the different samples.

Samples without oxide interface

Without the oxide interface (samples BE), the metal electrodes were delaminated during the 15 min of electro-etching on all samples, independent of the adhesion layer and the electrolyte used (figures 3.13a.-b., 3.14a.-b. and 3.15a.-b.). During electroless etching experiments, the surfaces previously covered by metal electrodes showed high markings in etching (figure 3.16). The calculated i_{corr} values of these samples (for Cr and Ti) are about an order of magnitude higher than for RT POx samples. Si corrosion is faster on samples without RT POx. The corrosion is rapid enough to cause delamination of the electrodes during the 15 min of electro-etching.

For samples with aluminum as an adhesion layer (BEAl), i_{corr} is very high. In contrast, i_{corr} of the same sample in NDS has a relatively low value. We believe that the calculated i_{corr} is distorted by the presence of very noisy zone in UnBEAl curve. The intersection of the curves should be in a higher current. We correlate this high corrosion current with the observation of macropores in the areas previously covered by the metal. So far this is the first time that macropores are fabricated by metal assisted etching of silicon in HF based electrolytes. We think the corrosion current is large enough so that the MAE is in the regime of macropores formation unlike MAE made with other metals which are in the regime of micro and mesopores formation.

Other possible reason for the occurrence of macropores is the presence of aluminum. However, these reasonings are hypothetical and should be subject to further study:

1. The work function of aluminum ($\Phi_{m,Al} = 4.05$ to 4.25 eV) is lower than that of other metals ($\Phi_{m,Ti} = 4.33$ eV and $\Phi_{m,Cr} = 4.5$ eV), which generates a higher potential barrier (see equation 3.5 on page 70). The holes that have enough energy to pass over the potential barrier by thermionic effect, are injected deeper into the valence band of silicon. They have high energy. These highly energetic holes could have the ability to ionize silicon differently. Silicon undergoes a different dissolution compared to cases of less energetic holes injected by the Ti/Si or Cr/Si junction.

2. Still due to this low work function of the aluminum, the band curvature is larger at the Al/Si junction compared to the case of Ti/ Si and Cr/Si junctions. If this curvature is too large, the holes in the metal can pass through and not above the potential barrier (by tunnel effect). The tunnel current through the Al/Si junction is higher than the thermionic current which crosses the Ti/Si and Cr/Si junctions.

3. Aluminum is known to interact with the silicon. Si readily diffuses into aluminum and Al takes the initial place of the diffused Si. The aluminum then acts as p^+-doping for Si which increases electrical conductivity of the Al/Si junction.

It is not clear whether one hypothesis or a combination of several of them describe reality. A more in-depth study should be investigating to understand the phenomena involved.

Samples with oxide interface

In the presence of the oxide interface (samples POx), the metal electrodes were not delaminated during the 15 min of electro-etching on all samples, independent of the adhesion layer and the electrolyte used (figures 3.13c.-d., 3.14c.-d. and 3.15d.), except the sample with the aluminum adhesion layer etched in NDS (figure 3.15c.). During electroless etching experiments, the surfaces previously covered by metal electrodes showed very weak markings in etching (figure 3.16). The calculated i_{corr} values of these samples are low compared to BE samples (except the sample with the aluminum adhesion layer etched in ODS).

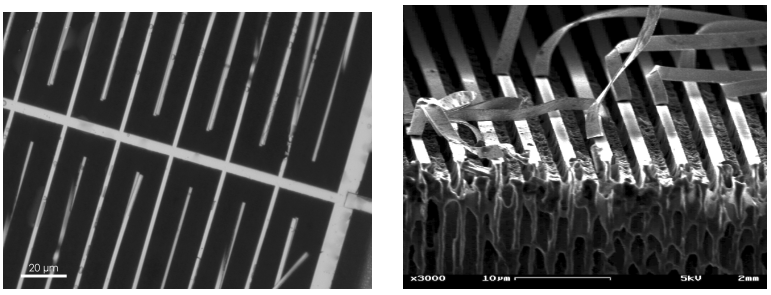
The presence of a thin oxide at the metal/semiconductor interface enhances the rectifier behavior of the contact and adds a resistance to the charge transfer through the interface (due to the tunneling current through junction). The curves of samples UnPOxTi and UnPOxCr exhibit this type of behavior. The Schottky like behavior of samples with RT POx could be imputed to both the good insulating properties of the oxide layer and to the high density of fixed charges (always positive) at the interface Si/SiO_2 [186]. Thin oxide layers have been observed to affect the behavior of Schottky contact giving rise to a lowering of the barrier for n-type Si and an increase of the barrier for p-type Si [187,188]. RT plasma oxidation has been proved to be suitable for the growth of high quality oxides with fixed charge higher than what obtained with the high temperature thermal oxidation [176, 179]. Nevertheless the small thickness (2.3 nm estimated by ellipsometry), this layer can dramatically affect the junction behavior.

By this rectifying behavior, the electrical path, between the anode and cathode, imposes the behavior at galvanic system which undergoes a significant ohmic polarization. The RT POx oxide layer avoids the formation of a good galvanic couple between Si and Au, therefore a slow down of the metal assisted etching of the silicon. The metal patterns resist to delamination during a 15 min electrochemical etching. The corrosion is limited by the passage of electric charges in the MIS junction.

The different behavior of the UnPOxAl samples shows how the adhesion promoter itself plays an important role in determining the junction behavior. The different behavior of samples UnPOxAl is most probably to be addressed to the interaction of the Al layer with the SiO_2 layer.

Aluminum is known for generating spiking through the SiO_2 and Si layers. Al undergoes a chemical reaction with the SiO_2 layer producing Si which introduces active centers for trapping electrons in the oxide layer [189]. The new amorphous layer resulting from this reaction can be as thick as the SiO_2 layer [190]. As a result the behavior of samples UnPOxAl and UnBEAl is very similar, and the Au layer can actively catalyze the Si etching thus causing the delamination of the metal strips.

The best electrode adhesion was obtained with the sample PPOxCr etched in ODS (figure 3.14). Let us consider the result of the electrodes adhesion to the substrate for a longer time etching.



a. b.

Figure 3.26: SEM pictures of a sample PPOxCr after 25 min of etching in ODS. (a.) Optical microscope picture of top view of IDE with 2 μm wide electrodes spaced of 10 μm. The narrow electrodes begin to delaminate from silicon. (b.) SEM picture of cross-section of 2 μm wide electrodes spaced of 2 μm. Cleavage of the sample caused delamination of electrodes poorly adherent to silicon.

Figures 3.26 show the result of anodization of the same samples for 25 min in ODS. Narrow electrodes (2 μm) begin to become detached from the silicon surface. Upon cleavage of the sample, the electrodes delaminate causing by their weak adhesion to silicon (figure 3.26). Although the presence RT plasma oxide at the metal/electrode interface and the nature of metal as adhesion layer have significantly increased the cohesion of the electrodes during anodizing, the time of the electro-etching remains limited within 25 min. Depending on the applied current density during the anodization, the maximum thickness of the porous layer is limited from 25 to 40 μm.

Impact of sacrificial layer presence

Adding a Ti sacrificial layer is another method to counter the problem of MAE process. Without the oxide interface (samples PBESL), the metal electrodes were delaminated during the 15 min of electro-etching in both electrolytes, but some electrodes resisted delamination during etching in ODS (figures 3.23a.-b.). However, contact between the metal layer and silicon is very limited.

In the presence of the oxide interface (samples PPOxSL), the metal electrodes were not delaminated during the 15 min of electro-etching in both electrolytes (figures 3.23c.-d.). The adhesion between the metal and silicon seems very good. An underetching of the electrodes, leaving free the bottom face of the electrode as in the cases Ti/Au or Cr/Au, has not occurred.

In the presence of the sacrificial layer, titanium polarization curves showed a very different behavior than those shown so far (figure 3.24). Indeed, during the first pass, $E_{corr(M)}$ is more negative than $E_{corr(Si)}$. Silicon has a cathodic behavior and Ti as the anode. In this configuration, the Ti undergoes anodization (dissolution) and silicon is preserved. However, the titanium layer is thin (100 nm thick). We attribute that the drop in the current density in the anodic branch of Ti results from the fact that the Ti layer is completely etched. Therefore, the following measures provide a different and stable behavior and $E_{corr(M)}$ shifts to the higher potential. The presence of the titanium layer as a sacrificial layer enables preserve the silicon from MAE process as long as it remains Ti.

3.2.6 Conclusions of the integration of electrode on the macroporous silicon surface.

In this study, we investigated two methods to counter the undesirable underetching of metal electrodes during electro-etching. The first method was to add a thin plasma oxide at the metal/Si interface. This oxide limits the flow of electrical charges between metal and silcium. The MAE process is then limited, which reduces the rate of electrode delamination. The second method is to add a sacrificial layer above the electrodes. This sacrificial layer is preferentially etched in place of Si.

The only addition of a sacrificial layer of Ti or oxide of the metal/Si interface is insufficient to avoid electrode delamination during a long electro-etching (over 15 min). It's necessary to combine both methods.

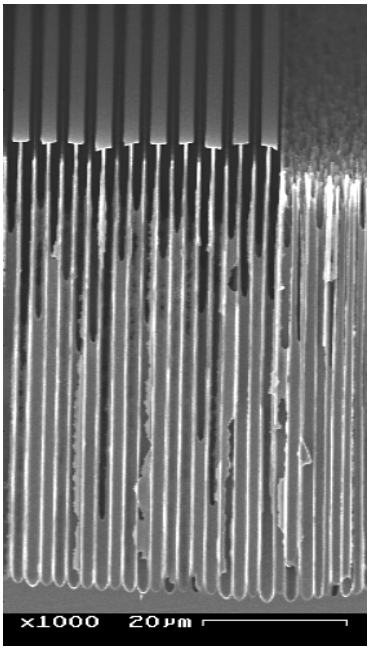


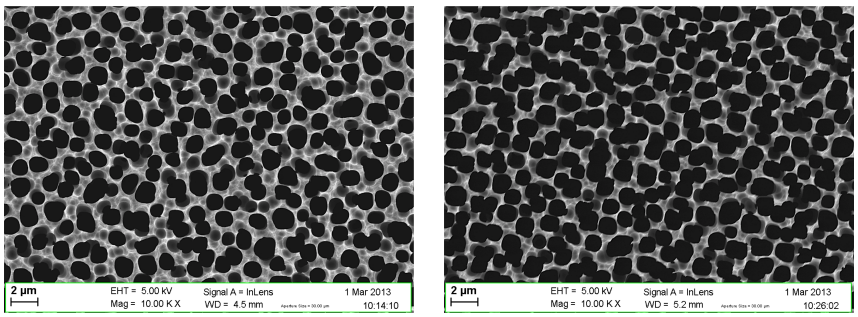
Figure 3.27: SEM pictures of tilted view of a PPOxSL sample after 45 min of electroetching in ODS with a current density of 17.5 mA/cm^2. The porous layer has a thickness of 72 μm.

Figure 3.27 shows the results of an electro-etching 45 min on a sample combining both methods. All electrodes are present on the surface of silcium. The underetching of the electrodes was greatly reduced by the combination of the two methods, thereby achieving a thick layer of porous silicon (more than 70 μm, depending on the applied current density).

3.3 Macroporous silicon masking

Introduction

In absence of masking pattern on surface, the arrangement of the pores is made randomly. Indeed, the current density is uniformly distributed over the entire surface of the sample (except for the periphery). In an electrolyte compound of HF:H_2O:DMF (1:1:8), the pore diameter is in the range from 1 to 2 μm (figure 3.28a.).

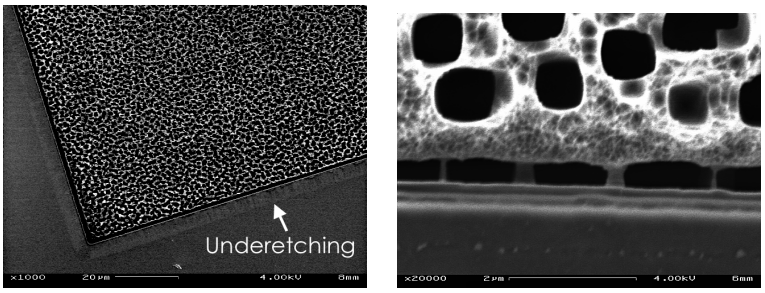


a. b.

Figure 3.28: SEM picture of top-view of marcroporous silicon made in a electrolyte composed by HF and DMF with a current density of (a.) 25% of J_{ps} and (b.) 50% of J_{ps}

By increasing the current density, the morphology of the pores is modified. Figures 3.28a. and b. respectively show the top view of porous layers made with a current equivalent to 25% and 50% of J_{ps}. The pore density is pretty the same for both current density. At the highest current density, the thickness of pore wall decreases and most pores coalesce with their neighbors.

The masking is a technique frequently used to achieve a local anodization of surface. This technique consists in depositing and patterning a layer of material resistant to (electro-)chemical etching by the electrolyte. In this way, the etching is done only at the opening of the mask. This method has been used with success for micro and mesoporous silicon in a number of applications, as for example bulk micromachining [191] and local thermal insulation [192].

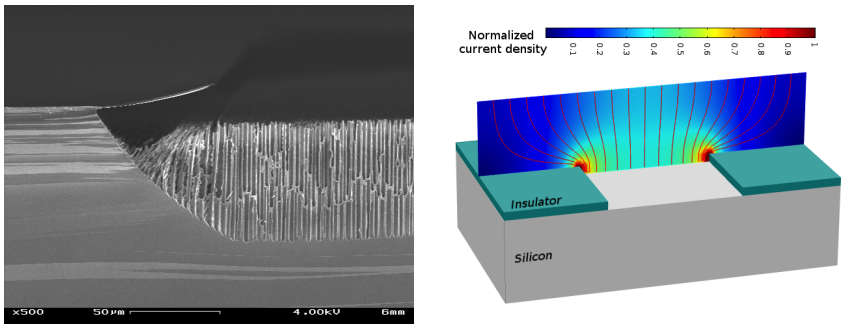


a. b.

Figure 3.29: (a.) SEM picture of top view of a porosified surface patterned by a mask. The image contrast was deliberately accentuated to bring up by transparency the underetching under the mask. (b.) Zoom on the edge of mask and the porosified area.

Figure 3.29a. shows the top view of macroporous silicon surface patterned by a mask. The lighter band in the mask surrounding the porous surface is due to the underetching under the mask (since electro-etching is an isotropic etching). The pores adjacent the mask have a diameter greater and the pore walls are much thinner than the rest of the porous surface (figure 3.29b.).

Figure 3.30a. shows a cross-section view of the mask edge and its underetching. The silicon under the mask is totally etched and the released mask bends due of its internal stresses. The porosity increases from the porous layer to the underetching below the mask. By getting closer to the mask, the porosity increases until the coalescence of pores and a total underetching. This phenomenon can be explained by the concentration of electric current on the edges of the mask (figure 3.30b.). The high current density at the edge of the mask locally increases the pore diameter (as on picture 3.29b.). The dilution of fluorine ions in this location is also involved in this local increase in the porosity. Indeed, the renewal of consumed ions in the porous layer becomes more difficult because access is narrower than anywhere else in the porous layer. The ratio of ions F^- decreases and current density increases in this location. J_{ps} decreases locally and the electrochemical etching approaches the electropolishing regime.



a. b.

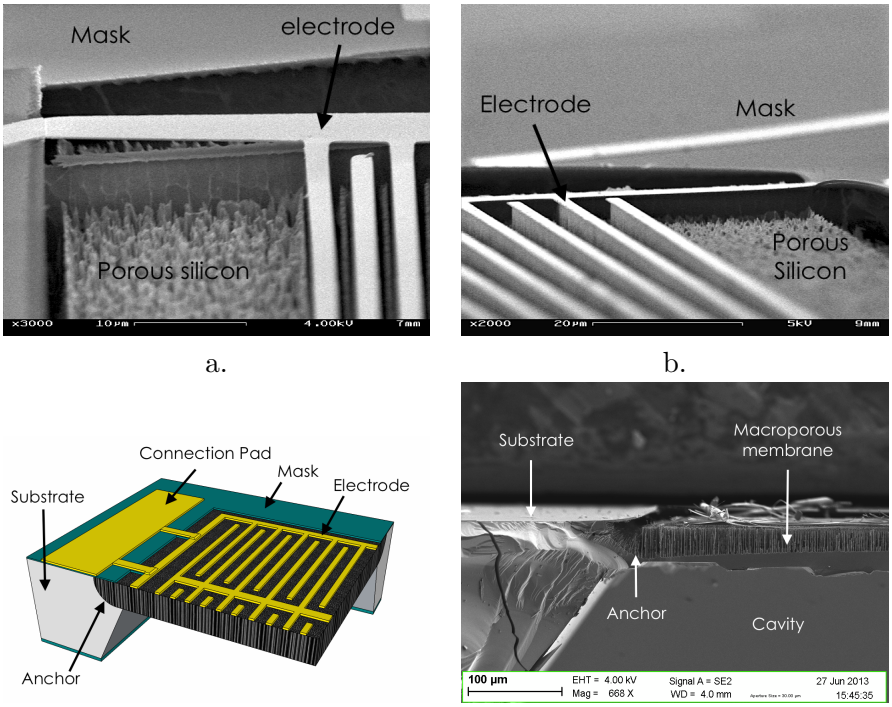
Figure 3.30: (a.) SEM picture of a cross-section view of a porous surface patterned by a mask. The silicon under the mask is totally etched and the released mask bends due of its internal stress. The porosity increases from the porous layer to the underetching below the mask. (b.) Simulation of current density distribution during anodization. The shading represents the current density and the streamlines shows the current lines. (The simulation parameters in Appendix F.3)

However, this geometric reason is not sufficient to fully explain the phenomenon of mask underetching. Indeed, the following study shows that some masks with the same dimensions (pattern and thickness) but made in different materials do not cause the same level of underetching. The properties of the material constituting the mask also has an impact on the underetching.

This significant mask underetching is an important technological issue in the fabrication process of chemiresistor:

1. The electrical path between the contact pads on the mask and the electrodes on the porous silicon is broken. Due to underetching, the edges of the mask are released and curve with the internal stresses. This mask bend tend to delaminate or break the electrical path between the electrodes and the contact pads (figure 3.31a. and b.).

2. In an architecture of chemiresistor on released porous membrane, the anchors between the membrane and the substrate are destroyed (figure 3.31c. and d.). The membrane is not attached to the substrate and is freestanding in the electrolyte.



a. b. c. d.

Figure 3.31: (a.) SEM picture of delaminated electrodes due to the mask bending. (b.) The mask bending tend to break the electrode. (c. and d.) The mask underetching destroys the anchor between the porous membrane and the substrate. (c.) 3D schema of an architecture of chemiresistor on released porous membrane. (d.) Magnification on the anchor destroyed by mask underetching. In this sample, the porous membrane remains attached to the substrate by a unwanted non-porous layer under the membrane.

The mask underetching does not involve the same phenomena causing of metal electrode delamination discussed in a previous section. Unlike the underetching involved in the delamination of metal electrodes, the mask underetching is not produced by the phenomenon of metal-assisted etching since the masking material is mostly an electrical insulator and not a catalyst for reduction reaction such as metal.

To resolve these issues, a study of the effect of the masking layer properties on the characteristics of the mask underetching is necessary to minimize their side effects. This study is performed for a formation of a thick macroporous layer on patterned p-type silicon substrates.

3.3.1 Materials and methods

For this study, several materials typically found in the semiconductor industry have been experimented as masking layers. Different thickness are tested :

- **LPCVD silicon nitride**
  (Si_3N_4) 100 nm, 500 nm, and 1000 nm thick layers are deposited respectively on the surface of three silicon wafers at 800°C by a low pressure chemical vapor deposition process (LPCVD) in a vertical furnace (Koyo, Japan). Standard photolithography is used to pattern the surface. After the lithography the LPCVD-Si_3N_4 layer is etched by Reactive Ion Etching (RIE) with CHF_3. Silicon nitride can be used as masking material for macroporous formation although not HF resistant. In the HF/DMF/H_2O mixture it is etched at an approximate rate of 0.4 nm/min, allowing etching 250 min long with a 100 nm thick masking layer.

- **Resist**
  A 1.3μm thick AZ6612 positive photoresist (PR) is deposited on two silicon wafers by spin-coating at 4000 rpm, and subsequently patterning by photolithography. To improve the adhesion of the PR with silicon a HMDS (MicroChemicals) layer is previously deposited on the surface. The two wafers are plasma etched with O_2 gas in order to obtain respectively 500 and 1000 nm thick PR layers. A 5 μm thick AZ6632-PR is spin-coated on the surface of a 500 nm thick previously patterned LPCVD-Si_3N_4 layer. To obtain this thickness, three layers of $AZ6632 - PR$ is spin-coated successively at 1000 rpm. The PR layer is patterned by lithography aligning the mask with the silicon nitride layer. To increase the resistance of the PR to the etching solution, the wafers are baked at 130°C for 30 min just before the electrochemical etching.

- **Polyimide**
  Polyimide (PI2525, Dupont) is spin coated at 2500 and 5000 rpm on the surface of two silicon wafers to obtain after a backing at 200°C (30 min in air) and 350°C (60 min in nitrogen atmosphere), respectively 5 μm and 11 μm thick polyimide (PI) layers. A 200 nm thick silicon nitride layer is deposited on the surface by Plasma-Enhanced Chemical Vapor Deposition (PECVD) in a plasma reactor (Oxford Plasmalab 100). A standard photolithography and plasma etching with CHF_3 gas are used to pattern the silicon nitride layer. Plasma etching in O_2 gas is used to etch isotropically the polyimide on the silicon nitride opened windows. A subsequent wet etching in BHF was used to etch the silicon nitride.

- **Metal**
  The metal mask consists of 150 nm of gold (Au) on 5 nm of titanium (Ti) as adhesion layer. We used Au for the metal mask because of its resistance to HF. To pattern the metal layer a lift-off process is used. The metal is evaporated in a dual e-beam evaporator (e-gun Vacotec).

The electrochemical etching is performed on p-type Si wafers (10 - 20 Ω cm, $\langle 100 \rangle -$orientation). A mixture of HF and N,N-dimethylformamide (DMF) (HF (48%):DMF:H_2O = 1:2:2) is used as electrolyte. A nitrogen flow is used to stir the solution and avoid inhomogeneities. All experiments are done at room temperature. Etching is performed in a single bath cell presented in section 2.1. Macroporous silicon layers are formed keeping constant the etching current density J_{etch} at a value lower than the critical current density J_{ps} = 182 mA/cm^2 at which the silicon surface electropolishing is produced.

3.3.2 Experimental results

- **LPCVD-Si_3N_4**

Figure 3.32 shows a SEM cross-sectional image of a macro-pSi layer formed in a silicon substrate patterned with a 100 nm thick LPCVD-Si_3N_4 (J_{etch} = 26 mA/cm^2, t_{etch} = 5 min). The growth of macropores is composed of two phases the nucleation phase and the stable macropores growth phase. A schematic drawing of the nucleation and growth phase are shown in figure 3.32.

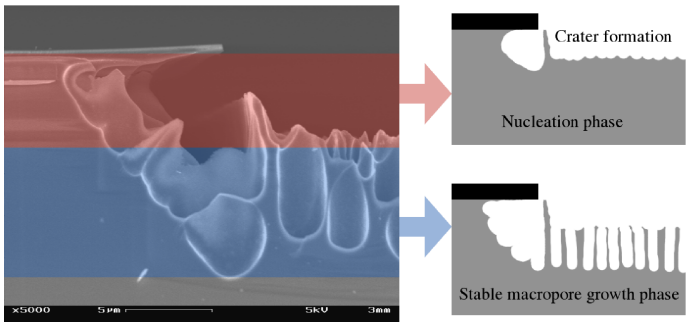


Figure 3.32: SEM cross-sectional image and schematic drawing of the nucleation and growth phase. The MPS layer is formed on a silicon substrate patterned with a 100 nm thick LPCVD-Si_3N_4 (J_{etch} = 26 mA/cm^2, t_{etch} = 5 min). The thickness of the pores in the unmasked area is $\backsim$ 5 μm, no pores are present under the mask edges. In the nucleation phase the formation of a crater, and the over-etching at the mask corners, are followed by the macropores nucleation.

The plane surface etching starts with a roughening, followed by formation of shallow pores with a higher density than pores in the stable phase. A number of these pores vanish before stable growth conditions are reached, leading to almost uniform etching of the surface. The duration of the nucleation phase and the thickness of the uniformly etched layer depend among others on the substrate doping concentration [193]. Due to nucleation phase, a crater separating the mask layer and the macropores in the non-covered areas is formed.

The nucleation phase even produces an over-etching at the mask corners. Nucleation centers are created under the mask edges, as well as inside the photolithographically defined regions. It is in fact not possible to observe the formation of pores under the mask edges after 5 min of etching. Increasing the etching time to 25 min, a 22 μm thick MPS layer is formed in the unmasked area, and the macropores grow even under the mask edges (Fig. 3.33(a.)). These pores grow in the direction of the current lines and not in the $\langle 100 \rangle$ -direction, like in the unmasked areas, causing a isotropically distributed mask underetching. A very thin layer of silicon separate the first horizontally placed macropores and the LPCVD-Si_3N_4 layer.

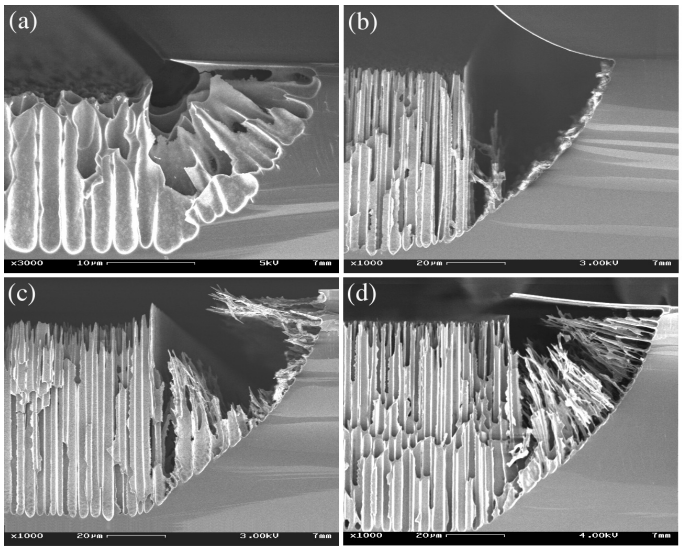


Figure 3.33: SEM cross-sectional view of MPS layers formed on silicon substrates patterned with LPCVD-Si_3N_4 100 nm thick (a.) and (b.), 500 nm thick (c), 1000 nm thick (d). The MPS layer in (a) was formed keeping the current density J_{etch} constant at the value of 26 mA/cm^2, while for other samples the current density was 91 mA/cm^2. The smaller current density result in a thinner MPS layer and no over-etching under the mask edges.

The etching rate for MPS formation in p-type silicon depends on J_{etch}, thus to obtain the formation of very thick macroporous membranes it is preferable to use high current densities to avoid long etching time. As shown in Fig. 3.33(b) increasing J_{etch} to 91 mA/cm^2 a 70 μm thick MPS layer was formed in 25 min. The drawback of using higher etching current densities, is to cause a double regime etching : macropores formation in the unmasked areas; electropolishing under the mask edges (over-etching). Experiments using thicker LPCVD-Si_3N_4 masking layers, 500 nm (Fig. 3.33(c)) and 1000 nm (Fig. 3.33(d)), are performed. The amount of volume involved in the electropolishing regime was observed to be dependent on the LPCVD-Si_3N_4 mask thickness, and to be higher for thinner mask layers, highlighting a dependence of the phenomenon on the capacitive effect bigger for thinner masking layers.

- **Resist**

As the deposition of thicker silicon nitride layers requires long deposition times and increase the process costs, it is preferable to use materials with smaller permittivity. Photoresist can be used instead of Si_3N_4 to reduce both the permittivity and the process cost. In figure 3.34(a) and (b) cross sectional views of MPS layers formed using as mask PR-AZ6612 respectively 500 nm and 1000 nm thick are shown. The over-etching is avoided, confirming the validity of capacitive effect hypothesis. Unfortunately, in this case the masking layer losses the adhesion to the silicon substrate after few minutes of etching, as highlighted by the presence of pores which started to grow on the masked silicon surface.

In order to exploit the positive effect of the smaller permittivity of PR and the good adhesion of the silicon nitride to the silicon, we used as mask a bi-layer constituted of 5 μm thick PR-AZ6632 on a 500 nm thick LPCVD-Si_3N_4. Figure 3.34(c) shows the cross sectional view of the resulting MPS layer, the PR is stripped with acetone to enable a better SEM imaging. The LPCVD-Si_3N_4 layer was broken during the PR stripping. The over-etching observed with the 500 nm thick LPCVD-Si_3N_4 layer is avoided. However, due to the thin silicon layer separating the horizontally placed pores and the mask layers, the silicon nitride on the underetching area was broken during the PR stripping.

When comparing to the sample with only resist in the undercutting area, a bigger porosity (smaller dimension of the silicon crystallites) is observed. This suggests that the resist layer lost the adhesion with the silicon nitride layer before the end of the etching, and that the etching characteristics are partly determined by the capacitive influence of the silicon nitride layer, and not of the double layer.

- **Polyimide**

Figure 3.34(d) shows the cross sectional view of a MPS layer formed using as mask material a $5\mu m$ thick polyimide (PI) layer. PI is a low cost organic material with $\varepsilon_r \approx 4$. Even with PI the challenging issue is the adhesion with the silicon after few minutes of etching. The PI layer in the sample cutting caused the crystallites breakage. The loss of adhesion of the PR and PI with the silicon is principally due to the presence of DMF in the electrolyte.

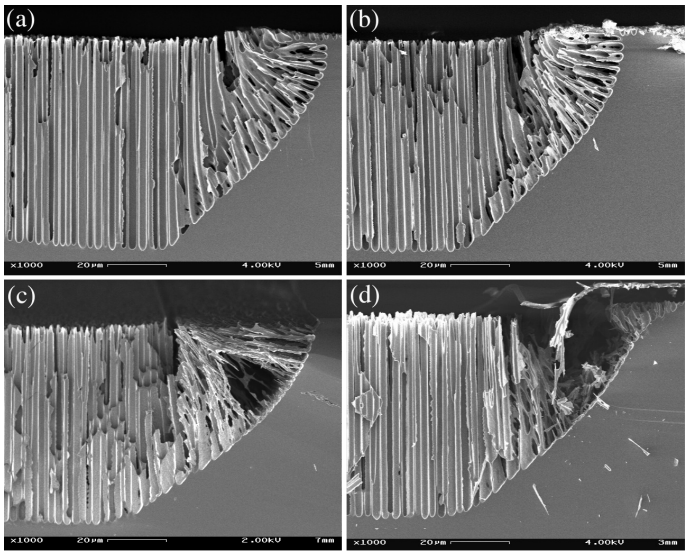


Figure 3.34: SEM cross-sectional view of MPS layers formed on silicon substrates patterned with PR-AZ6621 500 (a) and 1000 nm thick (b), bilayer PR-AZ6632 (5 μm) on LPCVD-Si_3N_4 (500 nm) (c), and PI 5.5 μm thick (d) (J_{etch} = 91 mA/cm^2, t_{etch} = 25 min). The resist layer is striped by acetone etching prior the SEM imaging of the sample to avoid the distortion due to charging. The LPCVD-Si_3N_4 in (c) is broken and removed during the resist stripping.

- **Metal**

Using an HF resistant metal as Au to pattern the silicon substrate, both over-etching and adhesion issues are resolved. Figure 3.35 shows the cross sectional view of a MPS layer formed using as mask a bi-layer 5nm-Ti/100nm-Au. Even if the mask underetching is still present, no over-etching is present. The horizontally placed macropores are separated from the mask layer by a silicon layer thicker to respect the one present in samples etched at lower current density using silicon nitride as mask. Due to the conducting nature of the masking layer, a fraction of the current from the bulk silicon can flow through the metal to the electrolyte. The charge accumulation that causes the over-etching is avoided, and thus a thicker silicon layer separating mask and pores is allowed.

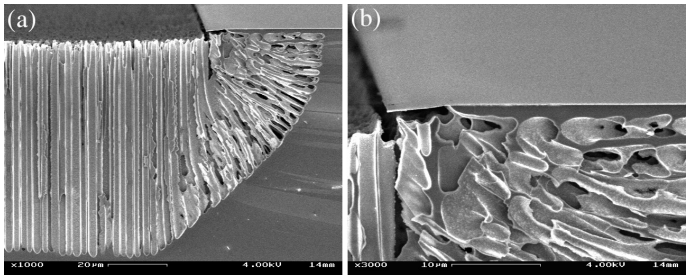


Figure 3.35: SEM cross-sectional view of a MPS layer formed on a silicon substrate patterned with a bi-layer consisting in 150 nm of Au and 5 nm of Ti (J_{etch} = 91 mA/cm^2, t$_{etch}$ = 25 min).

3.3.3 Simulation results

Two-dimensional (2D) simulations of the interface silicon/mask/electrolyte were performed using Comsol Multiphysics© (COMSOL AB, Sweden) to better understand the behavior of the underetching experimentally observed. As the dissolution of silicon proceed upon provision of hole carriers, we focused our attention on the hole current density and hole concentration distribution on the cross-section of the masked p-type silicon in contact with the electrolyte for different masking materials and thicknesses. To model the electrolyte/mask/silicon interface behavior, we considered a Schottky contact at the front side of a p-type wafer (10^{15} at/cm^3) with a bias of 1 V applied on the conductor border at 30 μm from the semiconductor surface. Systems with Si_3N_4, PR, PI, and Au as masking material are simulated. The relative permittivities (ε_r) assumed for different materials are shown in Table 3.4. Details on simulation parameters are presented in Appendix F.3.

masking material	ε_r
Si_3N_4	9.7
PR	2.9
PI	4
Au	/

Table 3.4: Relative permittivity assumed for different materials.

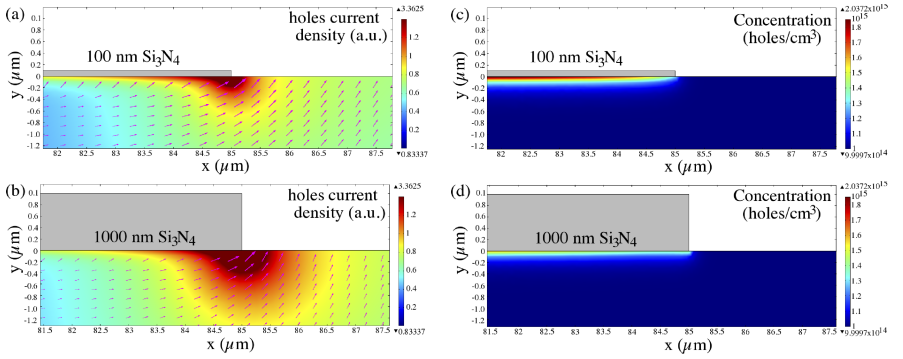


Figure 3.36: Simulated cross section of the masked structure, for 100 nm and 1000 nm thick Si_3N_4. In (a) and (b) the arrows show the hole flux velocity and the shading represents the holes current density. In (c) and (d) the shading represents holes concentration distribution. The masked area extends from x = 35 μm to x = 85 μm.

Figure 3.33 shows the simulated cross-section of the masked structure for 100 nm and 1000 nm thick Si_3N_4 masking layers. In figure 3.33(a) and (b) the arrows show the holes flux velocity and the shading represents the hole current density. In figure 3.33(c) and (d) the shading represents the hole concentration distribution. The hole current density is systematically higher close to the mask corner than in other parts of the semiconductor. This is a direct consequence of the hole carrier convergence in this region due to the local enhancement of the electric field. The higher current density on this area explains the over-etching at the mask corner observed on all the samples, even for the sample with metallic mask. As highlighted by the flux velocity arrows, the carriers tend to move toward the mask surface with higher velocity in case of thinner mask layer. Consequently, a higher hole current density and hole concentration are observed in proximity of the 100 nm Si_3N_4 layer surface. As the holes tend to move towards the masking layer, the holes accumulate under the mask, causing a large hole concentration in this area.

The simulation with other masking materials gave analog results, confirming the capacitive influence in the carrier accumulation under the mask. The 2D simulations are limited to describe the initial stage of the etching, and the working hypothesis are simplified to respect the reality

i.e. the modeling of the electrolyte as perfect conductor. Nevertheless, the simulation results agree with the experimental results, and confirm that carrier accumulation is the dominating phenomenon in determining the underetching behavior.

3.3.4 Discussion

When the silicon surface is patterned with a masking layer the discontinuity on the surface characteristics is reflected in an inhomogeneity of the current lines that are no more perpendicular to the surface in the close proximity of the masking edges. In this case the current density is not uniform over the whole surface. This leads to a large underetching below the mask edges that depends on etching conditions and mask layer characteristics.

We did some observations from the results presented in the previous section:

- For a given material, the underetching is more important for a thinner mask.
- For the same thickness of the mask, the underetching is more important for a material having a high relative permittivity.
- The underetching is non-existent for a metal mask passing the electric current.

In fact, if the mask is a dielectric material, the capacitive influence plays an important role on the hole carriers convergence at the interface with the masking layer, as confirmed by the 2D simulation of the silicon/mask/electrolyte interface.

The mask acts as a dielectric layer separating two electrodes (silicon and the electrolyte). Approximating that set by a capacitor formed by two parallel plates, it is possible to determine the influence of the parameters of the mask on the surface charge (Q, h^+/m^2):

$$Q = V.C = V.\frac{\varepsilon_r.\varepsilon_0}{t} \tag{3.13}$$

where V is the applied electric potential, C is the surface capacitance (C/m^2) of silicon/mask/electrolyte system, ε_r is the relative permittivity of the mask, ε_0 is the vacuum permittivity and t is the mask thickness.

For a fixed electrical potential, the surface charge (Q) increases with the surface capacitance (C). The accumulation of electric charge under the mask is higher for thin masks and for mask materials with a relative permittivity (ε_r) high (For example silicon nitride). The combination of high etching current and high capacitive effect of the mask layer cause a double regime etching : macropores formation in the unmasked area; electropolishing and over-etching under the mask edges.

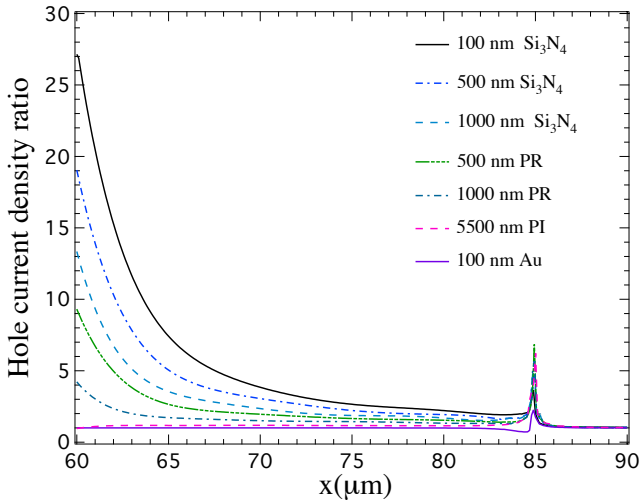


Figure 3.37: Calculated holes current density ratio (J_{1nm} /$J_{1\mu m}$) between 1 nm and 1 μm in depth from the mask surface as a function of the x dimension of the simulated surface.

To evaluate the impact of the mask thickness and permittivity, figure 3.37 shows, starting from the simulated cross sections, the hole current density ratio (J_{1nm} /$J_{1\mu m}$) from 1 nm to 1 μm in depth from the mask surface, and figure 3.38 shows the hole concentration at 1 nm in depth, for different materials and thicknesses. Hole current density in proximity of the masking layer is larger in case of thinner high permittivity mask layers. This highlights the trend for the current to concentrate under the mask layer because of the higher capacitive influence. On the contrary, for 5.5 μm thick PI ($\varepsilon_r = 4$), except of the limited area in proximity of the mask corner, there are no relevant differences between the hole current density at 1 nm and at 1 μm from the mask.

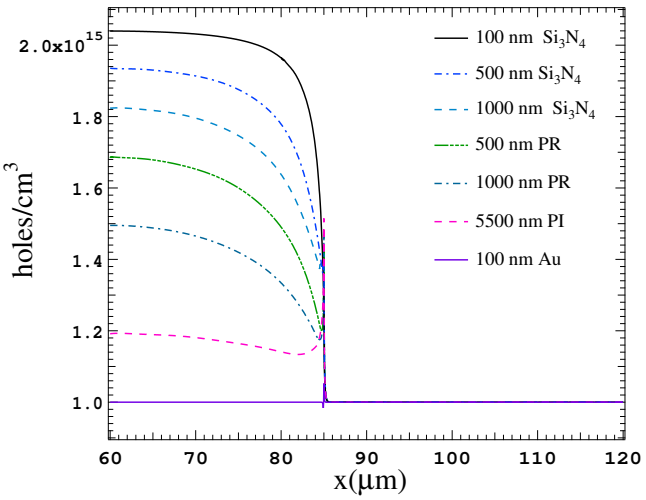
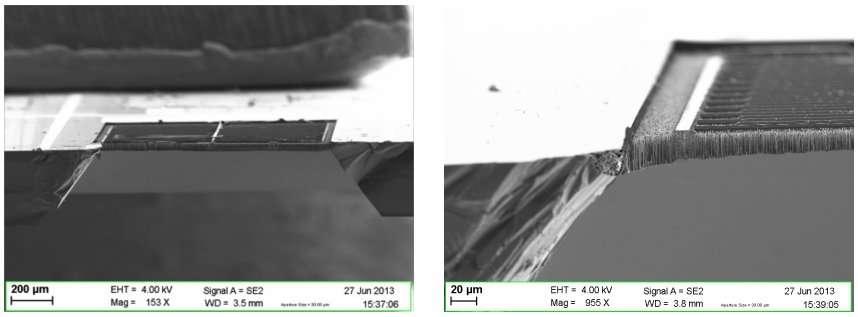


Figure 3.38: Calculated holes concentration as a function of the x dimension of the simulated surface.

This is a consequence of the combined effect of the high thickness and low permittivity of these layers. The behavior of the hole current density ratio and the hole concentration under the mask suits the experimental results. In case of metal masking layer, no hole accumulation under the mask is observed. The holes can go into the electrolyte trough the metal. The underetching is not avoided for metal layers, but the possibility for the holes to go through the metal on the electrolyte is reflected in the presence of a thicker silicon layer separating the pores and the mask layer (Fig. 3.35).

3.3.5 Conclusions of macroporous silicon masking

We have shown that the mask undercutting can be influenced by the masking layer properties. When silicon nitride was used as masking layer the undercutting for small current densities was characterized by the presence of macropores grazing the mask layer. Increasing the current density the undercutting was transformed in overetching. A decrease of the overetching was observed increasing the layer thickness. This behavior was attributed to a capacitive influence of the masking layer. A first confirmation of this hypothesis was given by the experimental results obtained by using mask materials with smaller permittivity (photoresist, polyimide).



a. b.

Figure 3.39: SEM pictures of (a.) cross-section view of macroporous silicon released membrane. (b.) Magnification on an anchor. SEM pictures are taken on two different membranes.

However, these materials do not have good adhesion to silicon (independantly of the electrochemical etching), which makes them difficult to use as a mask. 2D simulations of the interface silicon/mask/electrolyte confirmed that carrier accumulation under the mask is the dominating phenomenon leading to the under mask overetching for materials with higher permittivity and smaller thickness (as silicon nitride).

An alternative approach to eliminate the accumulation of charges under the mask is to use a electric conductive mask. Using HF resistant metal layers, as gold, were demonstrated to be a solution to overetching. In our fabrication process, the second use of the mask is to insulate the contact pads and the non-porous silicon. A metal mask does not allow electrically insulating the connection pads of the substrate.

Therefore, we recommend applying a lower current density to prevent underetching. By decreasing the electric current density and by increasing the thickness of the silicon nitride mask (up to 250 nm), we have achieved a macroporous silicon released membrane with the electrode pattern (figures 3.39a.). Figure 3.39b. shows that the porosity under the mask does not cause an overetching of the mask. Anchors are preserved and the membrane is held to the substrate.

3.4 Micrometric metal pattern: Impact on pore distribution and morphology

Now, we consider the morphology of the porous layer in the presence of a mask with similar dimensions of the pore diameter (a few microns). As part of this work, this type of masking is achieved by the interdigited electrodes (IDE) of the sensor studied in this thesis.

In the previous section, since the electrochemical etching is highly isotropic, the presence of wide mask leads to an underetching of similar width to the thickness of the porous layer, several tens of microns. Hence why the electrodes of a few microns wide are not totally underetched? How does the growth of pores between electrodes spaced by a few microns? Is the pore distribution disturbed by the periodicity of the IDE? What is the impact of the electrode dimensions and pitch on the morphology of the porous layer? What are the optimum electrode dimensions?

The following study provides answers to these questions. We show that the presence of electrodes drastically disrupts the morphology and distribution of pores, which should have an impact on the quality of the measurement. Computer simulations show and enable to understand the phenomena involved. Finally, we end up giving advice to optimize electrode design in order to maximize the quality of the measurement.

Materials and method

Metal interdigitated electrodes were patterned on the surface of p-type silicon substrates (10 - 20 $\Omega\times$cm, $\langle 100 \rangle$ orientation) using standard lift-off. The metal deposition is carried out by a dual e-beam evaporator after RT plasma oxidation to avoid delamination of the metal layer (see section 3.2). The electrodes consist of 1400-μm long ribbons (5-nm thick Ti and 100-nm thick Au). Three geometries (widths and spacings, WS) were tested on the same sample (listed in Table 3.5).

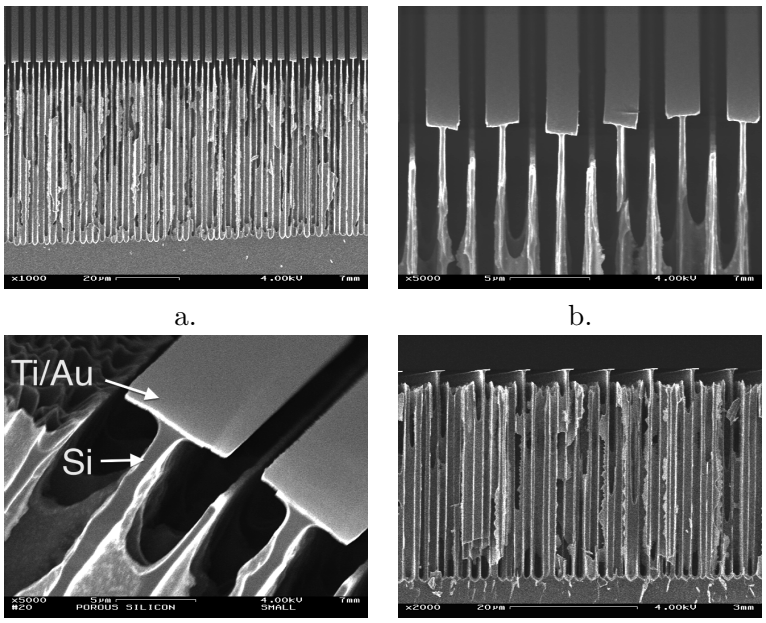
The prepared samples were then electrochemically etched to form the macroporous silicon layer in the single bath anodizing cell (section 2.1) by using a partly hydrolyzed mixture of HF and N,N-dimethylformamide (DMF) (HF (48%):DMF = 1:4). A 200-nm thick aluminum layer was evaporated on the wafer back side for contact with the aluminum electrode of the anodizing cell.

	width (μm)	**spacing** (μm)
WS1	2	2
WS2	5	2
WS3	2	5

Table 3.5: Widths and spacings of interdigitated electrodes.

The current densities (J_{etch}) used to achieve porosification are kept at a value lower than the critical current density $J_{ps} = 182$ mA/cm^2 at which the silicon surface electropolishing is produced.

Results and discussion



a. b. c. d.

Figure 3.40: SEM picture of cross-sectional tilted view of a macroporous layer grown on Ti/Au patterned silicon substrates. Geometry WS1 (a. and b.), geometry WS2 (c.) and geometry WS3 (d.). The current density is set at the constant value of 91 mA/cm^2 for 25 min.

Figures 3.40 show the SEM cross-sectional tilted view of Ti/Au prepatterned samples (geometry WS1 (a. and b.), geometry WS2 (c.) and geometry WS3 (d.)) etched used a current density at the constant value 91 mA/cm2 for 25 min.

The pore distribution is affected by the presence of the Ti/Au mask. More specifically, the pores tend to grow in proximity of the metal edges. As a consequence, the pores grow with a random distribution in the direction parallel to the metal strips, and they grow with a regular spacing in the transverse direction. The depth and the high roughness of the top surface of this wall are due to the nucleation phase in which the initiation of the pore growth follows an almost-uniform etching of the surface. The dimension of this wall, as well as the pore diameter, depends on the applied current density.

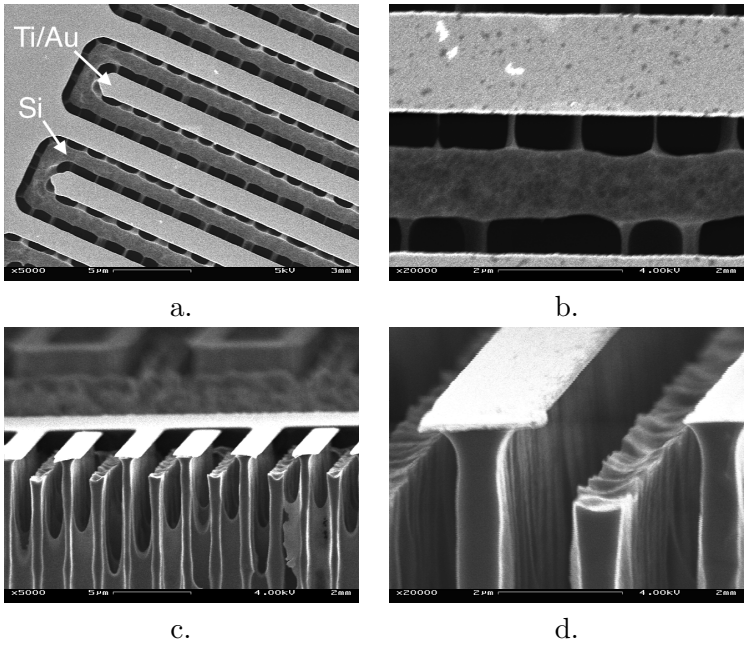


Figure 3.41: SEM picture of a macroporous layer grown on Ti/Au patterned silicon substrates. Top (a. and b.) and cross-sectional tilted views (c. and d.) of the macroporous layer with geometry WS1. The current density is set at the constant value of 26 mA/cm^2.

Figures 3.41 show the top and cross- sectional SEM views of a macroporous silicon layer with metal electrodes of WS1 geometry. The etching current density is set at the constant value of 26 mA/cm^2 for 25 min. Both walls, the one sustaining the metal layer and the one between the electrodes, are larger with respect to the samples shown in figures 3.40 because of the smaller etching current. On the contrary, the thinner perpendicular wall separating the pores does not show a strong dependence on the applied etching current.

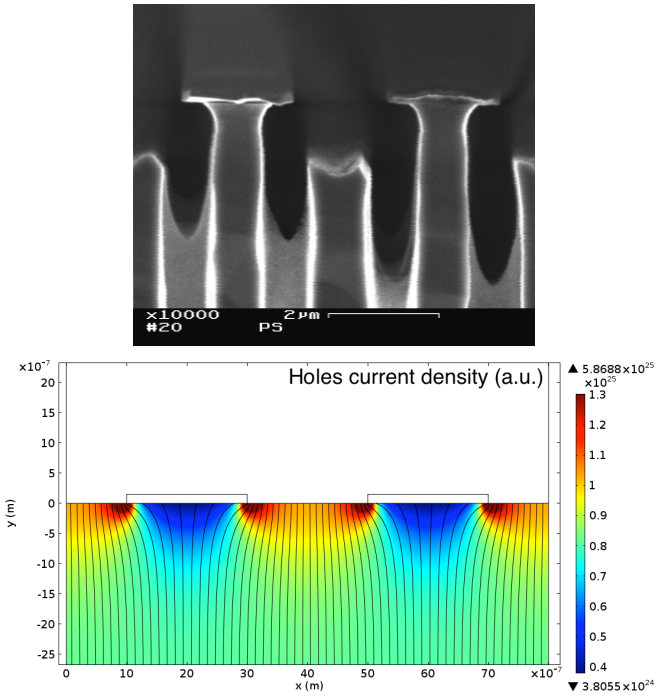


Figure 3.42: Comparison of experimental and simulation results for the WS1 geometry. (UP) Cross-sectional tilted views of the macroporous layer. The current density is set at the constant value of 26 mA/cm^2. (DOWN)The COMSOL-simulated cross-section. The shading represents the holes current density; the streamlines, the hole flux streamlines.

Two-dimensional simulations of the interface silicon/mask/electrolyte were performed using COMSOL Multiphysics© (COMSOL AB, Stockholm, Sweden) to better understand the etching behavior of how the

metal pattern geometry affects the macroporous layer morphology. To model the electrolyte/mask/silicon interface behavior, we considered a semiconductor/metal contact at the front side of a p-type wafer (10^{15} at./cm^3) with a bias of -1 V applied on the conductor border at 30 μm from the semiconductor surface.

Figure 3.42b. shows the simulated cross-section of a metal pattern with geometry WS1. Hole current density (shading) and hole flux streamlines are shown. The flux streamlines follow the electric field lines. The simulation results show that, in the initial stage of the etching, the current density is higher at the metal electrode edges and converges with the field lines towards the metal strip corners.

A direct consequence of the current density distribution is the experimentally observed growth of the pores in proximity of the mask edges. Even if during the nucleation phase pores start to grow in all the unmasked area, the pores on the corners of the mask are privileged by the higher current density that leads to a bigger growth rate. In case of smaller pitches, this behavior is reflected in the formation of the middle walls because the space between the metal strips is not sufficient to support the formation of another pore (figure 3.42a.).

We also observe a lower concentration of holes under the electrodes with respect to the rest of silicon (at least an order of magnitude) (blue zone). This low concentration area has the same shape as the crystallites under the electrodes after the electrochemical etching (figure 3.42b.). This low concentration disadvantages the etching in this area, which is preserved. Thus the pores preferentially grow downwards and the crystallite under the electrode is maintained. The electrode is not fully under-etched.

In case of bigger spacing between the metal strips, the formation of the thicker middle wall is avoided. Figures 3.43 show the SEM cross-sectional tilted view (a. and b.) and the simulated cross-section for a Ti/Au prepatterned surface with geometry WS3 (c.). As visible in these figures, the pores on the middle go further the nucleation phase. The higher current at the mask edges in the initial stage of the etching is reflected in a bigger nucleation and pore depth and a bigger pore diameter.

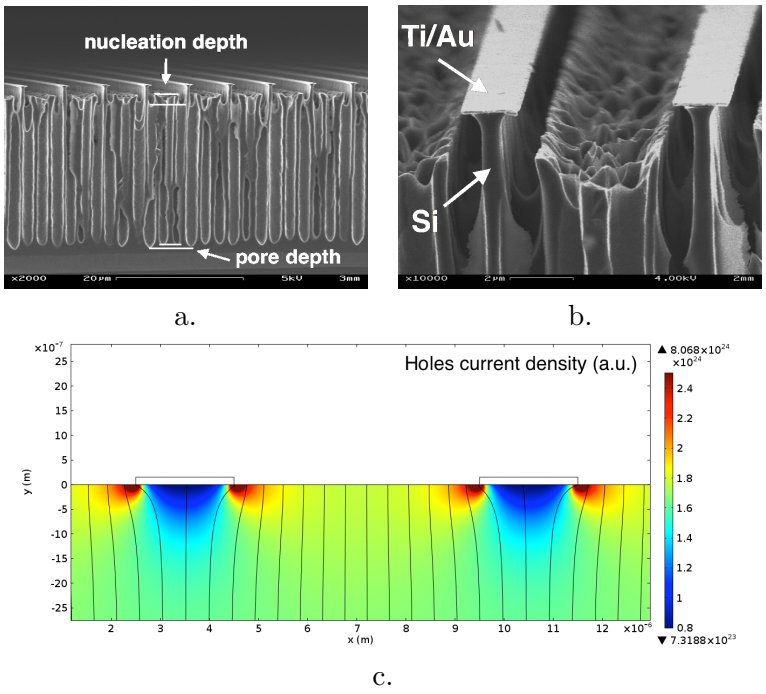


Figure 3.43: Comparison of experimental and simulation results for the WS3 geometry. SEM cross-sectional views of the macroporous layer (a and b). COMSOL-simulated cross-section (c).

A difference between the thickness of the pore walls at proximity of the electrodes and the thickness of the other pore walls exists. Again, inhomogeneity of the current density is at the origin of the results. In fact, the electric current density is higher near the electrodes, which increases the pore diameter and decreases the thickness of the pore walls. This difference in wall thickness is likely to play an important role in the involvement of the various pore walls in measurment in gas sensing applications. We assume that the thinner walls have a higher impact than the thicker walls. In this way, it is necessary to maximize the number of fine pore walls and thus reduce the pitch between the pores. By cons, the electrode width not seems to occur in the thickness of the pore walls. We suggest to decrease the width of the electrodes to increase the porosified surface area.

3.4.1 Conclusions of the micrometric pattern impact

The pore distribution and morphology are affected by the presence of the micrometric metal pattern. Pores grow faster in close proximity of the metal strip edges, leading to the formation of walls in the middle of the uncovered area for small pitches. The influence of the electrode presence attracts the electric current lines in their vicinity and the surface center between the electrodes does not undergo the electrochemical etching. The pores follow the periodicity of the electrodes in the direction perpendicular to them. By cons, their growth remains random in the parallel direction.

For larges pitches ($\geqslant 5$ μm), the surface area between electrodes are normally porosified with wider pores in close proximity of the metal strip edges. The experimental results were in agreement with the COMSOL simulation results that showed a current density distribution influenced by the enhanced electric field at the metal edges.

The pore walls near the electrodes is thinner than the pore walls in the center of the area between electrodes. We assume that the thin walls will have more impact in the measurement in gas detection application. So it is necessary to reduce the pitch of the electrodes. Therefore, we recommend an electrode pitch of 2 μm, which should be more efficient than the pitch of 5 μm.

3.5 Simulations of electronic behavior in macroporous silicon

3.5.1 Space charge region modulation model

The exact mechanisms related to the sensing of pSi towards various gases are still subjects of serious and diverse discussions. Erson et al. [94] suggested that it is due to condensation of the gas in the pores which changes the effective permittivity of the porous silicon. The permittivity is mixed one between that of porous silicon and that of trapped gas. Also, the formation of a condensed film can also introduce a parallel ionic conductivity on the walls of the pores.

However, Ben-Chorin et al. [194] showed the limits of this mechanism as the enhancement of the conductivity starts well below the condensa-

tion conditions in air. They propose that the absorbed molecules cause charge redistribution inside the pSi crystallites. It thus affects the depletion of carriers, which is one of the reasons for the high resistivity of the material. As the charge transport is possible by their thermal activation, small changes in the activation energy resulting in great changes on the conductivity of pSi.

Stievenard and Deresmas [102] have proposed an interesting 2D model related to pSi in the form of a silicon wall (crystallite) being sandwiched by two neighboring pores (figure 3.44). The pore surface is slightly oxidized (native oxide) and associated interface states due to contamination, crystal defects, the ambient humidity and the surface roughness. This interface states have a density σ (cm^{-2}) and is called *surface charge density*. The associated electric field E is given by

$$E = \frac{\sigma}{\varepsilon_0 \varepsilon_r} \tag{3.14}$$

where ε_r is the dielectric constant of silicon. The trapped charges at the interface SiO_2/pSi form a space charge region (SCR) by the action of the electric field over a distance W in the silicon crystallite. If d is the crystallite width, then there is a central channel of width d_{eff} = (d - 2W) in which the carriers can move when a potential is applied on the junction (figure 3.44). The depletion width, W, is proportional to the interface states and hence silicon oxide concentration. However, they observed increment of conductivity with the exposure to molecules with non-zero dipolar moment, which they associated with the gas passivation on the dangling bonds and decreasing W, hence increasing the channel width for increased conductivity. On the contrary, there is no effect for gases which have a zero dipolar moment.

This phenomenon is the basis of the transduction by the porous layer in our microsensors. Indeed, adsorbed molecules change the space charge region or depletion layer of the Si crystallites and change their electrical conductivity. In lightly doped Si small changes in the surface charge produce a large change in the width of the space charge region.

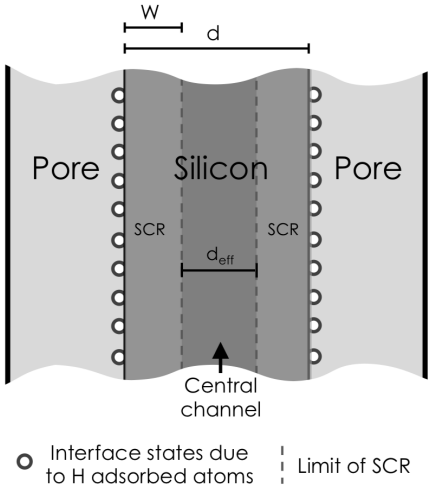


Figure 3.44: Schematic representation of a Si crystallites between two pores. In the crystallites, the central channel where the electrical current flows, is surrounded by SCR.

To analyze the impact of surface charge density on central channel width, d_{eff}, we propose a simple model based on charge balance between positive surface charge and negative space charge in the depleted region (initial doping of silicon is p-type). Figure 3.44 schematically illustrates the cross-section of a Si crystallite with physical width d, length L, height h, positive surface-charge density σ (cm^{-2}), and dopant concentration N_a (cm^{-3}). The effective central channel width, d_{eff} is less than the crystallite width, d. The positive surface charge should be balanced by the negative space charge in the depletion region to satisfy charge neutrality

$$\int_S \sigma \, dS = \int_V N_a \, dV \tag{3.15}$$

If we assume uniform surface charge density and depletion charge density, equation 3.15 simplifies to

$$\sigma \, L \, h = N_a \, L \, h \, (d - d_{eff}) \tag{3.16}$$

and then

$$d_{eff} = d - \frac{\sigma}{N_a} \tag{3.17}$$

From the equation 3.17:

- The central channel width decreases linearly with increasing the surface charge density.
- More doping is low, the higher is the impact of the change in surface charge density on the variation of the channel width.
- To have a conducting central channel, the minimum crystallite width is given by

$$d_{min} = \frac{\sigma}{N_a} \tag{3.18}$$

Consider surface charges only from the native oxide of the pore walls. In the literature, it is known that the typical value of σ is between 5×10^{10} and 3×10^{12} cm^{-2}. The doping level, N_a, of the wafers used in this work is between 2×10^{14} and 5×10^{14} cm^{-3}. Then, the minimum crystallite width should be between 2 to 5 μm.

Figures 3.40 and 3.41, we observed crystallites widths well below the calculated values. The crystallites in the electrodes of Figure 3.41 have a width of about 700 nm while the crystallites perpendicular to the edge of the electrodes have a width of about 100 to 200 nm. We can certainly assume that the crystallites are depleted of holes.

Figures 3.45 and 3.46 schow the top views of a metal patterned macroporous layer with a zoom on the thin perpendicular walls separating the pores.

3.5.2 Simulations

The silicon surface is not the same chemical and physical composition as the bulk silicon, causing the formation of a charge layer on the silicon surface [195]. The surface charge distribution arises from the trapping of carriers at the surface of semiconductor. There are different important types of surface traps: First, due to the broken periodicity of the crystal lattice at the surface, allowed surface states in forbidden gap can be found. Second, the surface chemisorption process in general requires a charge transfer from the volume to the surface of semiconductor (e.g. oxidation process). Third, an adsorbed layer or impurities on the silicon surface (e.g. water vapor [196]). As a result, the carrier concentration in space-charge region is different from the bulk concentration [197].

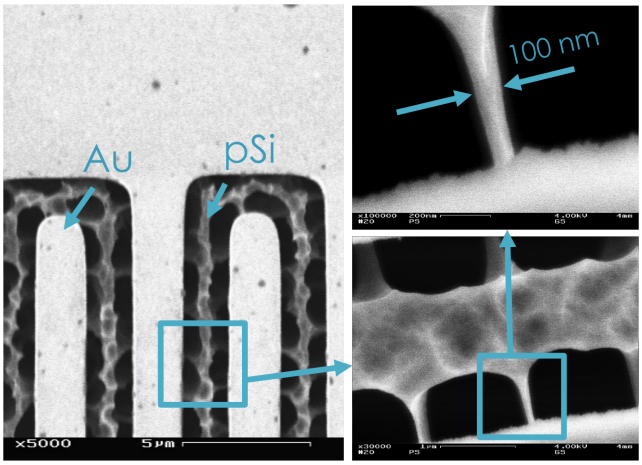


Figure 3.45: Top views of a metal patterned macroporous layer (2 μm-width electrodes spaced of 2 μm) grown with a current density of 26 mA/cm^2 (20% of J_{ps}) for 25 min. The thin perpendicular walls separating the pores have a thickness about 100 nm.

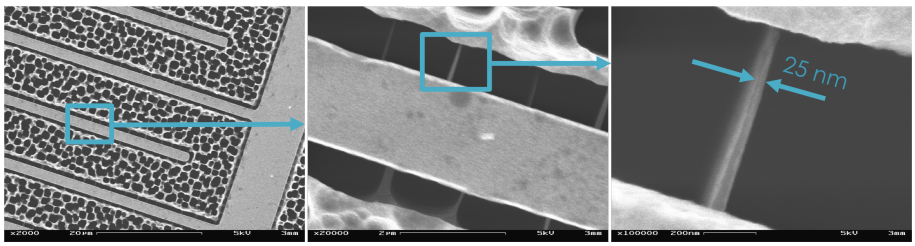


Figure 3.46: Top views of a metal patterned macroporous layer (2 μm-width electrodes spaced of 8 μm) grown with a current density of 91 mA/cm^2 (70% of J_{ps}) for 25 min. The thin perpendicular walls separating the pores have a thickness about 25 nm.

In reference [198], it is illustrated that a large positive charge can be formed on the surface of a p-type semiconductor, causing an n-type inversion layer near the surface. Brown [199] measured the conductance of an n-type surface channel on the surface of p-type semiconductor. For oxide process, the effects of oxidation conditions, silicon orientation, annealing treatments, oxide thickness ... have a impact on surface-state charge density which then is in a range of 10^{10}-10^{12} cm^{-2} [200].

Table 3.6: Surface charge density values on the silicon surface for various oxidation processes

Oxidation process	**Surface charge density** (10^{12}/cm^2)	**Ref.**
Native oxide	< 0.01 - > 1.5	[201]
Dry thermal oxide (950 - 1200 °C)	0.02 - 0.42	[200]
Wet thermal oxide (950 - 1200 °C)	0.08 - 0.34	[200]
Wet-chemical oxide	0.08 - 0.34	[202]
Piranha cleaning (120 °C)	5	[203]
HNO3(65%) (60 °C)	8	[203]
Deonized H_2O (80 °C)	0.1 - 1.5	[202, 203]

Table 3.7: parameters used in numerical simulation of the concentration of charge carriers in the pore walls.

Parameters	**Values**
Doping type	p-type
Doping level	2×10^{14} cm^{-3}
Oxide thickness	1.7 nm

Table 3.6 lists the values in literature of surface charge density present on the oxidized silicon surface for various oxidation processes.

We conducted numerical simulations to characterize the impact of surface charge on the concentration of charge carriers in the pore walls. Numerical simulations were performed using the Atlas software (Silvaco, inc., USA) and Comsol. The parameters used are listed in Table 3.5.2 and simulations are presented in Appendix F.4.

Figure 3.47 shows the geometry used in the simulation. The symmetry is exploited to simulate only 4 half-pores between two metal electrodes (yellow). The pore surfaces (blue) are oxidized and the surface charge density is a parameter of the simulation. A potential difference of 1 V is applied between the electrodes. The electrode/silicon is considered as an ideal ohmic contact.

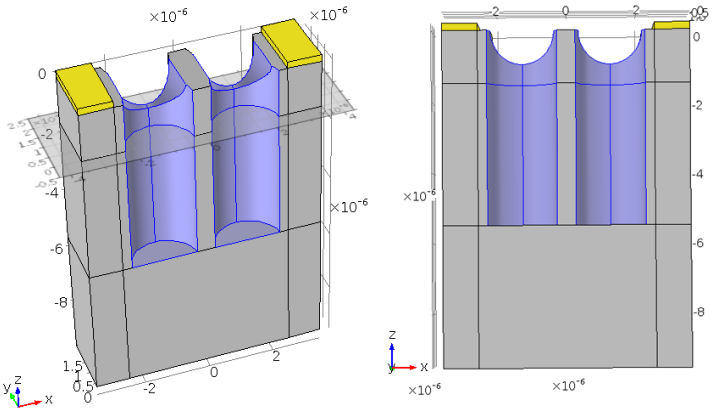


Figure 3.47: 3D geometry used in numerical simulations. The geometry consists of 4 half-pores between two metal electrodes (yellow). The pore surfaces (blue) are oxidized and present a surface charge density.

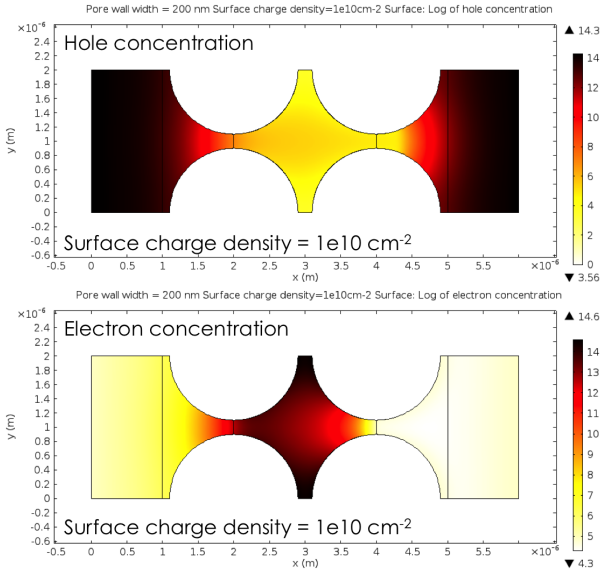


Figure 3.48: 2D simulation of distribution of the concentration of (up) holes and (down) electrons for a surface charge density of 10^{10} cm^{-2}. The pore wall thikness is 200 nm.

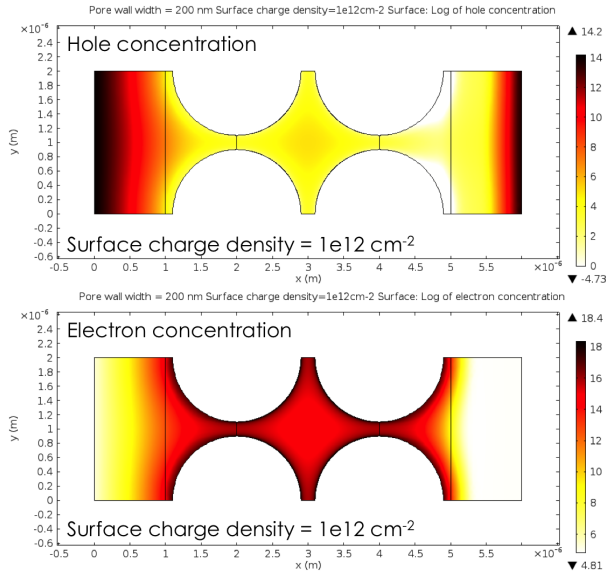


Figure 3.49: 2D simulation of distribution of the concentration of (up) holes and (down) electrons for a surface charge density of 10^{12} cm^{-2}. The width of pore wall is 200 nm.

First, we conducted 2D simulations of the cross-section shown by the gray transparent plane in figure 3.47 for a 200nm-thick pore wall. Figure 3.48 and 3.49 show the distribution of the concentration of holes and electrons when the surface charge density is, respectively, 10^{10} and 10^{12} cm^{-2}. The results show a significant variation in the distribution of the concentration of charge carriers depending on the surface charge density. There is a threshold beyond which appears a strong inversion of charge carriers type in the pore walls initially p-type, then forming an n-type channel with high levels of concentrations.

Figures 3.50 show the total current density distribution for surface charge density, respectively (UP) 10^{10} and (DOWN) 10^{12} cm^{-2}. For a surface charge density of 10^{10} cm^{-2}, the electric current density is relatively uniform over the cross section of the pore walls (the electric current density varies depending on the width of the right section, but on the cross-section, it is relatively uniform). On the contrary, for a surface charge density of 10^{12} cm^{-2}, the electric current density is very high near the pore surface and decreases towards the wall center. The electric current thus moves largely on wall surface (figure 3.50 down).

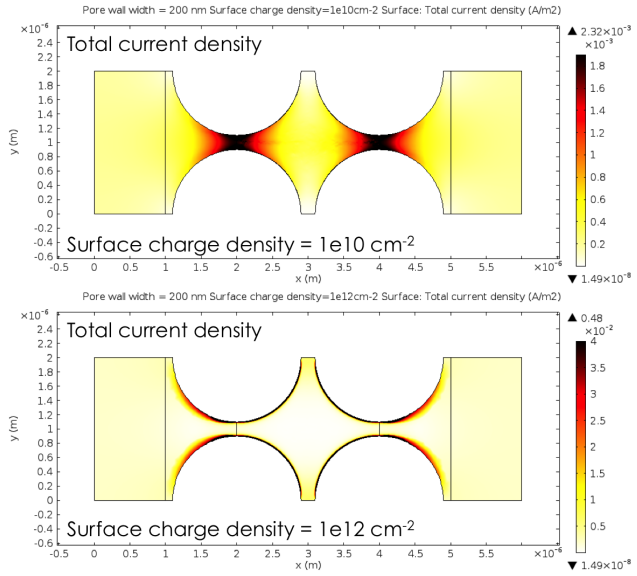


Figure 3.50: 2D simulation of total current density distribution for surface charge density, respectively (UP) 10^{10} and (DOWN) 10^{12} cm^{-2}. The width of pore wall is 200 nm.

The formation of a conduction channel at the semiconductor surface due to the presence of surface charges is a known phenomenon and is often parasite. In the case of macroporous silicon, crystallites are thin and they are oxidized on both sides which tends to accentuate the phenomenon of inversion of charge carriers. We assume that the width of the crystallites have an impact on the level of inversion.

We conducted the same simulations for wall thicknesses ranging from 25 nm to 400 nm (typically the dimensions obtained in our electrochemical etchings in the presence of metal electrodes). Graphs 3.51 and 3.52 show the distribution of the concentration of electrons in the walls for different densities of surface charges in the case of 25 nm walls (Figure 3.51) and 400 nm (Figure 3.52)

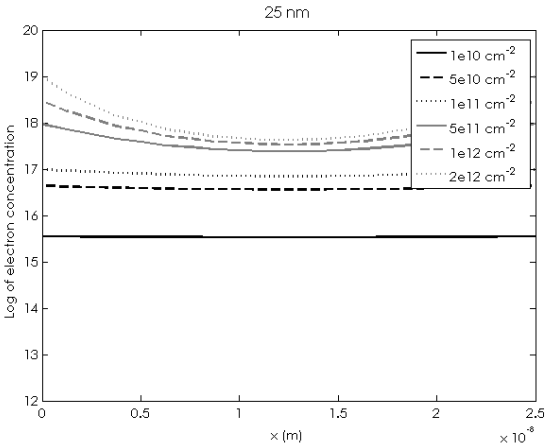


Figure 3.51: Graph of the distribution of the electron concentration in the pore walls for different surface charges densities. The pore wall width is 25 nm.

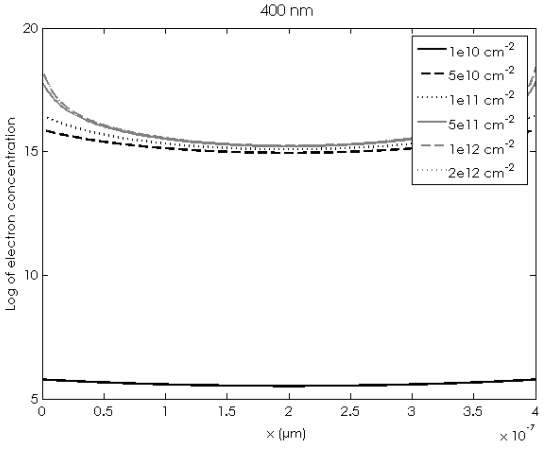


Figure 3.52: Graph of the distribution of the electron concentration in the pore walls for different surface charges densities. The pore wall width is 400 nm.

The thin walls of 25 nm-width are strongly inverted to all levels of surface charge density (from 10^{10} to 2×10^{12} cm^{-2}). The electron concentration levels reach the 10^{18}cm^{-2} and even 10^{19} cm^{-2} on the surface

for high surface charge densities. In the very thin walls, we assume that a strong inversion of charge carriers occurs with all the oxidation process listed in the table 3.6.

Conversely, for a surface charge density of 10^{10} cm^{-2}, the walls of 400 nm wide are not depleted of holes and no inversion of charge carriers happens. They remain still of p-type. For higher surface charge density, the inversion phenomenon occurs but the concentration levels are lower by several orders of magnitude relative to a wall of 25 nm wide.

Between different levels of surface charge densities, the charge carrier concentration in a thin pore wall (as 25 nm) varies more strongly than in a thick pore wall (as 400 nm). We assume that the thin walls will be more effective as the transducer in gas sensing application that thick walls.

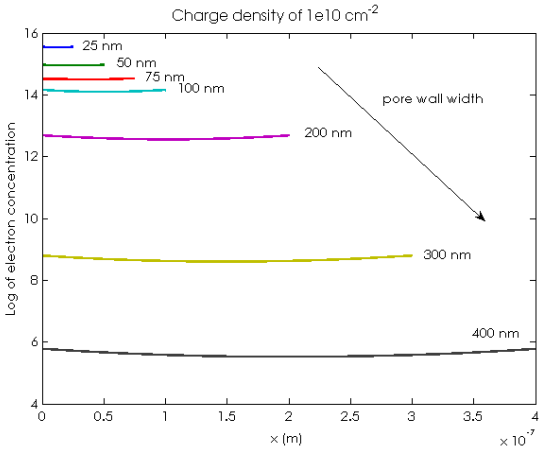


Figure 3.53: Distribution of the electrons concentration on the cross-section of the crystallites for various crystallites widths and for a surface charge density of 1e10 cm^{-2}.

Graphs 3.53 et 3.54 compare the distribution of the electron concentration on the cross-section of the crystallites for various crystallite widths and for a surface charge density of respectively 1e10 cm^{-2} and 2e12 cm^{-2}.

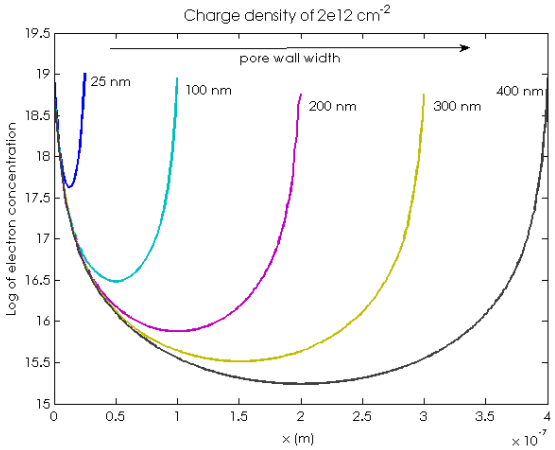
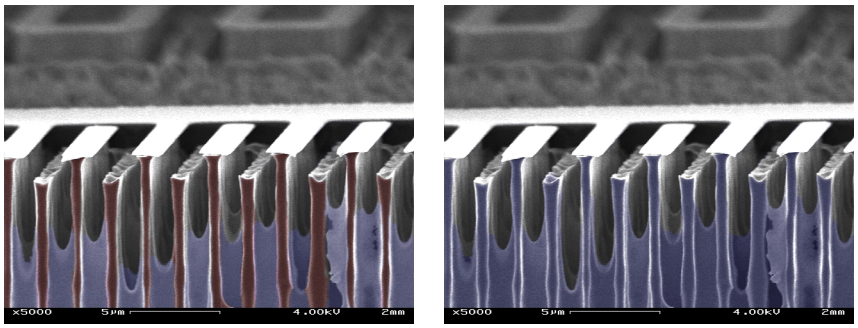


Figure 3.54: Distribution of the electrons concentration on the cross-section of the crystallites for various crystallites widths and for a surface charge density of 1e12 cm^{-2}.

For a low surface charge density of 1e10 cm^{-2}, crystallite width mainly influences the level of inversion charge carriers. A thickness of 400 nm does not cause the inversion of charge carriers. Lower thicknesses up to 200 nm causes a weak inversion. Strong inversion (electron concentration higher than initial doping level, 2×10^{14} cm^{-2}) appears for smaller widths. For a given width, the electron concentration is relatively constant over all the cross-section of the crystallites.

For a high surface charge density of 1e12 cm^{-2}, the width of the crystallite especially influences the level of concentration of the holes in the center of the cross section of the crystallites vary from $10^{17.6}$ cm^{-2} for crystallites of 25 nm wide to $10^{15.2}$ cm^{-2} for crystallites of 400 nm wide. More the crystallite is thin, the more electron attracting phenomena by surface charges on the two walls of the crystallites is increased. However, the level of electron concentration on the pore wall surface differs slightly depending on the crystallite width and is around of $10^{18.7}$ cm^{-2}.



a. b.

Figure 3.55: SEM pictures of a tilted view of metal patterned macroporous silicon layer. SEM images of a tilted view of macroporous silicon layer structured by metal. Zones were stained to represent the p-type silicon (red) and the n-type silicon (blue). (Left) The silicon beneath the electrodes does not undergo an inversion of the charge carriers and structure is PNP type. (Right) The silicon beneath the electrodes undergoes a (strong) inversion and the macroporous layer is fully n-type.

Two situations are possible (figure 3.55):

- The silicon under the electrodes remained p-type (red zones on figure 3.55a.): In this case, the structure is a PNP type with an n-region of several microns in length (blue zones on figure 3.55a.). One of the two junctions is in reverse mode and the direct current is blocked. Only a very small leakage current due to the photogeneration and recombination crosses the PNP junctions. In this situation, we assume that the electric current tends to pass below the porous layer and not by the walls of the pores. This will be likely to decrease the impact of the gas adsorption on the electric current and the measurement sensitivity will be degraded.

- Silicon under the electrodes is in inversion mode and all the macroporous layer has become n-type (blue zones on figure 3.55b.). The electrons can pass through the macroporous silicon from a metal/silcium to another, mainly by surface conduction. However, it is necessary that the Schottky contact formed by metal/silcium junctions are able to correctly collect the electrons.

3.5.3 Conclusions of simulations of electronic behavior in macroporous silicon

We conducted numerical simulations to understand the behavior of charge carriers in the pore walls. We have shown that the surface charges, typically caused by the silicon oxidation, has a decisive impact on the charge carrier concentrations. Indeed, for a sufficient surface charge density, the pore walls tend to be totally depleted of holes and an inversion of the charge carriers types occurs. For higher surface charge densities, a strong inversions with electron concentrations up to 10^{18} cm^{-3} takes place in pore walls.

The thickness of the pore walls has an impact on the behavior of the charge carriers. The thinner the wall is, the stronger the inversion of charge carrier is for lower surface charge densities. With a low surface charge density of 10^{10} cm^{-2}, an inversion occurs in walls with thickness less than 200 nm. The inversion is strong in walls whose thickness is less than 100 nm.

Conversely, no inversion occurs in thicker wall (over 300-400 nm) with low surface charge density of 10^{10} cm^{-2}. For a high density of surface charges (e.g. 10^{12} cm^{-2}), a strong inversion of charge carriers happens in all simulated thicknesses (25 to 400 nm) and pore walls become totally n-type.

To conclude this section, we propose to confront this numerical analysis with experimental measurements in a future work. An electrical characterization of the porous layer can enable to confirm or to refute whether an inversion of charge carrier occurs in pore walls and thus to infer the electric current path (by the pore walls, beneath the porous layer, or both).

This study allows us to recommend to use thinner walls as the transducer in gas sensing application. They should be more efficient than thick walls. The thin pore walls are obtained in proximity of the electrodes. A higher density of electrodes increases the density of thin walls. The current density also has control over the thickness of the pore walls. A higher electric current density decreases the thickness of the pore walls.

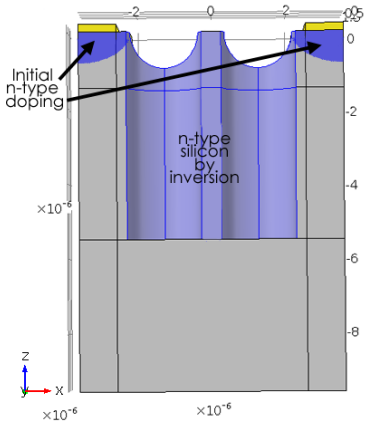


Figure 3.56: Schematic of 3D view of the cross section of a macroporous layer. The blue zones under the electrodes represent an initial n-type doping.

Finally, in perspective, we suggest two future works. The first is to dope the silcium under the electrode to make it n-type (figure 3.56). We assume that the electron channel formed by the inversion of the charge carriers in the pore walls will connect the two n-doped zones under the electrodes. This architecture facilitates the passage of electric current in the porous layer. By cons, it is likely that this initial doping has an impact on the growing of the pores, which will change the structure of the porous layer.

The second perspective is to invert the charge carriers in all the porous layer. The control of the surface charge density by oxidation control (chemical or thermal oxidation) or by a physico-chemical conformal deposition on the pore walls (by techniques as LPCVD, ALD ...) should create a surface conduction channel which joins the electrodes and passes in the pore walls.

3.6 Chapter conclusions and perspectives

We present a summary of the different conclusions drawn in this chapter:

First, we introduced a new method of integration of electrodes on the surface of the macroporous silicon. This method achieves dimensions for the metal pattern has not achieved with other integration techniques on macroporous silicon. Our original approach is based on the deposition of the metal electrodes before anodization and benefit from efficient patterning technique such as photolithography. The presence of a metal pattern on the silicon surface during electrochemical etching involves an electrode delamination. We have developed pretreatments before electrochemical etching to overcome this issue. Thick macroporous layers (50 to 70 μm) patterned by the metal electrodes are achieved. Compared to the commonly used techniques, our new method, based only on standard techniques, has the following advantages: (i) it enables a high flexibility in the design and (ii) micrometric dimensions of metal pattern to improve the quality of the chemiresistor sensing and (iii) increasing of miniaturization of pSi-based sensors.

Second, we report the results of a study on the selective anodization of patterned p-type silicon substrates to form thick macro-pSi layers. The mask presence can produce a large overetching caused by the capacitive attraction of the charge carriers providing by the external current. We have shown the over-etching is widely influenced by masking layer electrical properties, as well as by the etching parameters.

Third, the presence of metal electrodes during electrochemical etching affects the pore distribution and its morphology. The study of these phenomena is detailed. Pores grow faster in close proximity of the metal strip edges, leading to the formation of walls in the middle of the uncovered area for small electrodes spacing. For a wider electrode pitch, the pores adjacent to the electrodes have much thinner walls than the other pores. These alterations of the morphology of the porous layer should have a significant impact on the sensitivity of the porous layer as a transducer in gas sensing applications.

Fourth, computer simulation of the electrical behavior of the charge carriers suggests the presence of a surface-conduction layer in the pore walls. Indeed, the natural or forced oxidation of pore walls should generate a strong inversion layer in the surface of the walls. The surface conduction layer is largely influenced by the electrical charges in the pore wall surfaces. This phenomenon is exploited for the gas detection application. The simulations showed the influence of pore wall thickness on magnitude of the inversion of charge carriers in pore walls. Thus, by combining the results of the different studies, we assume that the finest pore walls will have more impact on the measurement sensitivity. Indeed, this pore walls are subject to higher amplitude of the variation of the charge carrier density depending on the surface charge density (due to the oxidation, but also to gas adsorption) than thick pore walls.

Recommended fabrication process

Through these studies, we propose a simple fabrication process of a miniaturized chemiresistor. To increase the density of the very thin pore walls, we recommend electrode width and pitch smaller than 5 μm (Details on the microsensors fabrication process are in Appendix I):

1. Wafer : p-type silicon wafer (10-20 Ω·cm, $\langle 100 \rangle$-orientation) cleaned in a piranha solution (at 110 °C), followed by a solution of HF (2 %) to etch the oxide layer.

2. Deposition of 250 nm thick silicon nitride by LPCVD technique.

3. (*If the porous layer is released as membrane*) Photoresist patterning on backside by standard photolithography.

4. Etching of the silicon nitride layer on the backside by RIE plasma etching.

5. (*If the porous layer is released as membrane*) Release of the membrane by TMAH etching.

6. Patterning and etching of the silicon nitride layer on the frontside by standard lithography and RIE plasma etching.

7. Cleaning of samples in a piranha solution (at 110 °C), followed by a solution of HF (2 %) to etch the oxide layer.

8. (*If the electrochemical etching is made in a simple bath cell*) Deposition of 200 nm-thick of Al on the wafers backside by e-beam evaporation following by an annealing at 432 °C in forming gas for 30 minutes to ensure good ohmic contact on the backside .

9. Etching of the native oxide on front-side by 2 % HF.

10. Growth of a room temperature plasma oxide in a barrel reactor for 1 min at 150 W.

11. Deposition, patterning and developing of the photoresist by spin coating, photolithography and immersion in a developper.

12. (*If the electrochemical etching is made in a simple bath cell*) Deposition of the metal layer by e-beam evaporation. The adhesion layer is 5 nm of Ti or Cr. The electrode is 30 to 150 nm of Pt or Ni and the sacrificial layer is 100 nm of Ti (For more information, see Appendix B).

13. Standard Lift-off in acetone or HNO_3 until all the excess metal is removed from the sample.

14. Silicon anodization occurs in a single cell with an electrolyte bath comprising HF:H_2O:DMF (1:1:8) prepared at least 20 days in advance to allow time for the DMF decomposition. The current density should be from 10 mA/cm^2 to 60 mA/cm^2 (below about 50 % of the electro-polishing current density). Fast delamination was observed for excessively high current density.

15. The anodizing time should not exceed 45 min. Depending on the electric current density, it is possible to obtain a macroporous silicon layer with a thickness higher than 70 microns.

16. (*If the electrochemical etching is made in a simple bath cell*) The samples are removed from the anodizing cell and briefly immersed in a 10 % HF solution to etch the aluminum on the backside.

17. The samples were then extensively rinsed in deionized water and dried in nitrogen.

18. To break the rectifier behavior of electrical contacts, the samples were annealed at 650 °C for 45 seconds by RTA technique in nitrogen atmosphere.

Reproducibility

The new technique of metal electrode integration in the macroporous silicon presented above exhibits good reproducibility. Indeed, independently of the dimensions of the electrodes, all metal electrodes adhered to the surface during the 45 min of anodization. This result has been observed on the 960 sensors on each of the ten anodized wafers.

Future work

The simulations presented in section 3.5 have shown that the walls of the macroporous silicon in vicinity of metal electrodes are totally depleted. In a resistance measurement in DC mode, the current does not cross these walls, which do not participate in the measurement. A measurement of the impedance of the porous layer in AC mode could overcome this issue. Indeed, the dielectric properties of these depleted walls influence the impedance of the porous layer. Assuming that the gas adsorption to the surface of pore walls alters their dielectric properties, it is possible to quantify the presence of gas by measuring the impedance change of the porous layer.

CHAPTER 4

Functionalization of metal-patterned macroporous Si for hydrogen sensing

4.1 Introduction

Porous silicon is a very promising material for the fabrication of efficient and cheap micro-scale gas sensors [204]. However, porous silicon lacks selectivity and sensitivity towards many gases such as hydrogen (see section 2.3 on page 41). In this chapter, palladium functionalization techniques are investigated as means to address sensitivity and selectivity issues of pSi-based hydrogen sensors.

The functionalization is the addition of one or more physico-chemical functions to a surface. In the application of gas sensing, sensor development commonly uses the functionalization to improve sensitivity and/or selectivity of sensitive layer to the target gas. The functionalization is achieved either by a functional material deposition on the sensitive layer, or by modification of the physico-chemical properties of the sensitive layer.

To increase its sensitivity to a target gas, pSi is commonly coated with a functional material [205]. Upon contact with the target gas, the functional surface undergoes a physicochemical modification. The porous silicon becomes a transducer, which transforms this physicochemical modification into a usable signal (usually electrical or optical).

The macroporous Si functionalization in metal electrode presence is a real challenge. Indeed, the presence of a metal layer can disrupt the deposition of the functional material. For example, the previous chapter has shown that the presence of metal electrodes disturbed the electric field distribution at the pSi surface, which can be problematic for an

electrochemical deposition technique. Also, metal electrodes may make inconsistent the deposition techniques of functional materials. For instance, a high-temperature process or use of corrosive products could significantly alter the metal electrodes and make them unusable.

In this chapter, we study the functionalization of macroporous silicon for hydrogen sensing. Two palladium nanoparticles deposition methods were implemented: An original two-step method for the deposition via precipitation and electroless plating, a common standard technique. In particular, the impact of the presence of the metal electrodes on these functionalization techniques is observed.

The first sections will provide the hydrogen concentration range for specific applications and we motivate the study about the macro-pSi functionalization for H_2-sensing applications.

Then, an overview on the hydrogen sensibility of the Pd/Si system is reported. In particular, the mechanism and kinetics of palladium-hydrogen interaction, the impact on silicon and the palladium nanostructuration are discussed.

Afterward, next sections are devoted to the study of the two techniques of palladium nanoparticles deposition on the pSi walls. A comparison between the two techniques reveals the advantages and disadvantages of both techniques.

Finally, the last section deals with the characterization of a proof-of-concept device, which consists of a hydrogen microsensor that combines the main results developed in this Thesis: (i) fabrication of miniaturized chemiresistor with the integration of micrometric size metal electrodes, and (ii) the functionalization with Pd nanoparticles of macroporous silicon.

The H_2 concentration ranges for specific applications

Table 4.1 lists the ranges of concentrations and pressures for some specific H_2 applications.

Table 4.1: Concentration and pressure ranges for some specific H_2 applications.

Applications	**H_2 Concentration**	**Pressure** MPa	**ref.**
Energie conversion (hydrogen to electricity)	100 %	0.8 up to 8	[206]
Hydrogen storage	100 %	35 - 70	[206, 207]
Hydrogen balloon	100 %	0.1	
Hydrogen-Cooled turbine generator	100 %	0.4 - 0.7	[208, 209]
Fossil fuels purification		0.1 - 10	[210]
Hydrogenation (Chemistry and agrifood)	100 %	0.1 - 10	[211]
Hydrogen transport pipelines	100 %	3.5 - 10	[210]
Medical applications (diagnostic of gastrointestinal disorders)	100 ppm	0.1	[210]
Safety/Area monitoring	1 - 40 000 ppm	1 atm 0.1 - 10 MPa	[210]

Motivations

In recent years, hydrogen emerged as an energy vector of the future. The growing number of applications is encouraging the development of materials and sensing platforms that allow the fast and selective detection of this gas. Indeed, hydrogen is a gas that can be dangerous and its use requires rapid and accurate measurement of its concentration.

The concentration window of explosive limit is 4 - 75 % v/v H_2 at room temperature, but hydrogen will burn at concentrations as low as 4 % in air [210]. Hydrogen is the lightest of elements and the smallest molecule. It, therefore, has the greatest tendency to leak. Thus, for a process safety application, a hydrogen leak can be more dangerous and its detection becomes more challenging than other gases. Although many applications listed in Table 4.1 using pure hydrogen (e.g. hydrogenation, energy conversion ...), it is critical for the hydrogen sensors to cover a wider measurement range (0 - 99 % v/v H_2) for the safety aspect of all hydrogen applications.

In Appendix G (on page 263), the state-of-the-art on hydrogen sensing technologies was presented. Some are already on the market, others are under development. At the end of this appendix, a table lists the most important specifications used to compare different techniques.

Due to the high surface to volume ratio, porous silicon is an ideal candidate for the detection of gases in general. The surface reactions as the physico-chemical adsorption are widely abundant in a restricted volume. Moreover, it has the advantages of being easily and unexpensively fabricated.

Macroporous silicon walls are nanoribbons-like. Indeed, their geometry is similar to that of nanoribbons: a thickness of tens to hundreds of nanometers and the other dimensions in the micrometer range.

Figures 4.1 shows SEM pictures of the top view of four different samples etched with an electric current density of 26 mA/cm^2 for 25 min. The figure in the bottom right was etched with an electric current density of 40 mA/cm^2 for 25 min. The perpendicular walls that connect the electrodes to the centrals walls are very thin and can be compared to nano-ribbons. Their thickness range between 25 and 200 nm. The mean linear density (number per unit length) of nano-ribbons-like is 12638.3 cm^{-1} with a maximum of 14109.3 cm^{-1} and a minimum of 10582 cm^{-1}.

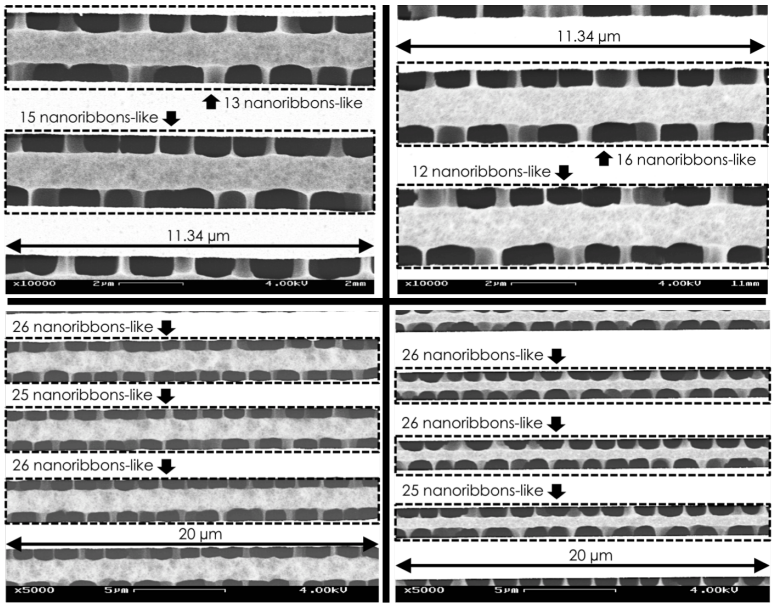


Figure 4.1: SEM images of the top view of macroporous layer patterned by the metal electrodes (white strips). On each picture, the number of nanoribbons-like is counted.

The distance between two rows of pores (d_p) is equal to the inter-electrode spacing ($d_i = 2\ \mu$m) and the width of the electrodes ($d_e = 2\ \mu$m for the finer) ($d_p = d_i + d_e = 4\ \mu$m). There are two rows of nanoribbons-like by inter-electrode spacing. The number of nanoribbons-like rows within a centimeter can be calculated:

$$2 \text{ nanoribbons-like } \frac{1 \text{ cm}}{d_p} = 2 \text{ nanoribbons-like } \frac{1 \text{ cm}}{4\,\mu\text{m}} = 5000 \text{ cm}^{-1} \tag{4.1}$$

By multiplying the mean linear density by the number of rows of nanoribbons-like within a centimeter, we obtain the mean surface density of nanoribbons-like:

$$12638.3 \text{ cm}^{-1} \times 5000 \text{ cm}^{-1} = 63\,191\,500 \text{ nanoribbons-like . cm}^{-2} \tag{4.2}$$

Equation 4.2 gives an idea of the number of nanoribbons-like placed in parallel in a surface of 1 cm^2. Total sensing surface area can be

estimated by assuming that a nanoribbon-like has a width of 1.5 μm and a length of 30 μm (the length depends on the thickness of the porous layer). Each nanoribbon-like features two sensing surfaces:

$$2 \times 63\,191\,500 \text{ nanoribbons-like . cm}^{-2} \times 1.5\mu m \times 30\mu m = 56.9 \frac{cm^2_{\text{specific surface area}}}{cm^2_{\text{apparent surface area}}} \quad (4.3)$$

Equation 4.3 shows that there is potentially about 57 cm^2 of sensing area per cm^2 of porosified area on the silicon wafer surface. This result is interesting potentially to improve the measurement sensitivity. Indeed, for a given volume, a larger specific surface area increases the number of interaction between the gas and the semiconductor.

These estimates allow to appreciate the benefits of porous silicon as sensing layer. Moreover, unlike nanoribbons which often requires costly fabrication techniques (e.g. electron-beam lithography), the porous silicon has an inexpensive fabrication.

As we present in the next section, pSi alone lacks of sensitivity and is not selective with respect to many gases other than hydrogen. It is thus necessary to functionalize its surface to improve both sensitivity and selectivity to hydrogen. The following section provides the functionalization of the porous silicon for H_2-sensing applications.

4.2 Functionalization of pSi: Overview

4.2.1 Hydrogen sensitivity of the porous silicon

pSi is naturally sensitive to the presence of H_2, its electrical properties are modified [99,136]. However, pSi is also sensitive to a large number of molecules (see section 2.3 on page 41). The sensing is not selective. The exact mechanisms related to the sensing of pSi towards various gases are still subjects of serious and diverse discussions.

In the previous chapter, we have presented proposals of Erson et al. [94], Ben-Chorin et al. [194] and the model of Stievenard and Deresmas [102]. In this model, the trapped charges at the interface SiO_2/pSi on pore walls form a space charge region by the action of the electric

field in the silicon crystallite. A central channel between the two space charge region in which the carriers can move appears when a potential is applied on the junction. However, they observed increment of conductivity with the exposure to molecules with non-zero dipolar moment, which they associated with the gas passivation on the dangling bonds and decreasing space charge region width, hence increasing the channel width for increased conductivity.

Ali et al. [136] observed the opposite behavior when the pSi is exposed to hydrogen. The electric current decreases with increasing H_2 concentration. They propose the following mechanism: H_2 gas is a source of electrons to pSi structure. Adsorbed hydrogen will form a definite density of electron donors bound to the surface of a semiconducting p-type pSi. They represent surface states which can exchange electrons with the interior of the pSi, thus forming a space-charge layer situated close to the surface [212], of length W. It follows that increasing H_2 concentration outside p-type pSi increases the SCR in the pSi due to electron exchange and hence reduces the central channel for hole conduction.

Currently, three main ways are accepted to explain the hydrogen influence on the electronic properties of pSi [213]:

1. Due to morphology, the electrical properties of pSi depend on the surface states. Hydrogen is one of the main surface species of pSi. The theoretical investigations reveal modification of surface trap distribution and energy structure of pSi covered by the H atoms versus unpassivated material [213]. The alteration of pSi bands induced by surface hydrogen coverage is manifested. It is mainly explained with modification of local electric fields and potential barriers induced by the potential of H atoms. However, a not significant influence of the Si-H bond length and the Si/H band line-ups on the energy structure of the material is obtained [213].

2. Passivation of dopant atoms in the bulk with hydrogen from the electrolyte was observed. During the pSi preparation process the H atoms from the electrolyte diffuse through pore walls into the bulk of Si. The depth of hydrogen propagation inside the lattice amounts to 0.1 μm. For example, the H atoms in p-type Si passivate boron dopants and form electrically neutral Si-H-B complexes. The effective amount of dopants decreases by two to three

orders. Hence, it contributes to the formation of depletion regions in pSi, which is accompanied by a decrease of conductivity in pSi.

3. Additional electronic states exist in the pSi gap due to the adsorbed hydrogen. Hence, more free charge carriers can be captured on the surface traps of pSi, which is an important factor of small conductivity.

4.2.2 Porous silicon selectivity to hydrogen

The bare pSi has a low sensitivity and almost no selectivity to hydrogen [136], which makes it useful in very limited applications of H_2 sensing. Functionalization of pSi is a technique that can simultaneously improve the sensitivity and selectivity to the target gas.

Functionalization by functional material coating depends mainly on two parameters: the deposited functional material and the deposition technique. This last parameter consists of two broad categories: continuous film coating and micro- or nanostructures deposition (wires, particles ...) which each bring their advantages and disadvantages.

In the context of the detection of hydrogen, several functional materials have been used. Gabouze *et al.* [214] use the coating hydrocarbon group (CH_x) by plasma technique. This functionalization has a fairly good sensitivity to H_2, but it is not selective with respect to other gases (carbon dioxide, ethylene, ethane, propane ...). Arakelyan [215], Aroutiounian [216] *et al.* functionalize the pSi surface with TiO_{2-x} and $ZnO\langle Al\rangle$. Depositions are made respectively by electron-beam evaporation and magnetron sputtering deposition. Then, a thin Pt catalytic layer is deposited by ion-beam sputtering. This type of structure has good selectivity with respect to propanebutane gas mixture environment [130].

Kanungo *et al.* [217] use functionalization by Pd, Ru and Pt on the pSi surface. Deposits are made by electroless on a MIS structure consisting of PdAg (contact)/pSi/p-Si/Al(contact). Pd has the highest sensitivity, the smallest response time and the smallest recovery time compared to the other two metals and the pSi surface unmodified.

Palladium is a metal widely used in hydrogen sensing. Appendix G presents a wide range (non-exhaustive) techniques of H_2 sensing. Several of them uses the interesting properties of Pd for this application.

The deposition of Pd nanostructures in pSi is the most widely used functionalization for H_2 sensing applications. The following two sections present the particular properties of Pd and interests using nanostructures for H_2 sensing.

4.2.3 The palladium-hydrogen system

Palladium demonstrates great selectivity towards hydrogen, then Pd is a widely used catalyst in the field of H_2 sensors [218]. Hydrogen is highly soluble in palladium [219], a reversible process where solubility is dependant on temperature and hydrogen partial pressure. The Pd-H system has been extensively studied because of its high sensitivity and selectivity to H_2 gas and its ability to absorb and release hydrogen at room temperature [220]. Palladium exposed to hydrogen, absorbs on its surface the molecule H_2, where it undergoes homolytic dissociation to atomic hydrogen [221]. In an inert atmosphere, hydrogen is able to diffuse into the bulk material (equation from [218]), where equilibrium is established between atomic hydrogen at the palladium surface (H_s), within the bulk material (H_b) and at the back interface (H_i).

$$H_2 \underset{c_s}{\overset{d_s}{\rightleftarrows}} 2H_s \underset{c_d}{\overset{d_d}{\rightleftarrows}} 2H_b \underset{c_i}{\overset{d_i}{\rightleftarrows}} 2H_i \tag{4.4}$$

where:

- d_s, c_s are the rate constants respectively for adsorption and desorption (typically 1.26×10^{-8} and 3.85×10^{-9} mol cm^{-2} s^{-1} [222])
- d_d, c_d are the the diffusion constants for diffusion respectively into and out of the bulk
- d_i, c_i are the rate constants for adsorption and desorption at the interface between Pd and Si.

The surface and interface of thin Pd layer are always in equilibrium, because diffusion of hydrogen through Pd is very fast and quoted between 1 and 5×10^{-7} cm^2 s^{-1} [221]. The transfer of hydrogen across 200 nm of Pd is estimated to occur within 0.15 ms at room temperature [223].

Based on the equilibrium reaction between hydrogen gas ($H_{2(g)}$) and hydrogen dissolved in the palladium (H_d),

$$H_{2(g)} \leftrightarrows 2H_d \tag{4.5}$$

the equilibrium constant can be written:

$$K_a = \frac{a_{H_d}^2}{a_{H_2}} \tag{4.6}$$

At low concentrations of H if it behaves ideally, the activity of monatomic hydrogen in the metal is equal to its concentration,

$$K_a = \frac{[H_d]^2}{p(H_{2(g)})} \tag{4.7}$$

The concentration of H atoms dissolved in palladium can then be written:

$$[H_d] = \sqrt{K_a}\sqrt{p(H_{2(g)})} \tag{4.8}$$

The equation 4.8 is known as the Sieverts's law and allows to predict the solubility of gases in metals [224, 225].

The diffusion of hydrogen in palladium is accompanied by a metal hydride. The following section briefly describes the metal hydride in general. Then we will explore it in particular palladium hydride.

4.2.3.1 Metal hydrides

Metal hydrides are chemical compounds formed of hydrogen atom(s) and of a metal or a metallic alloy. The bonding between the metal and the hydrogen is of metallic nature. The most common hydriding form is by direct dissociative chemisorption [226]:

$$Me + \frac{x}{2}H_2 \rightleftharpoons MeH_x \tag{4.9}$$

where Me represents a metal and MeH_x a metal hydride. Another rarer hydriding form is achieved by electrochemical splitting of water [226]:

$$Me + \frac{x}{2}H_2O + \frac{x}{2}e^- \rightleftharpoons MeH_x + \frac{x}{2}OH \tag{4.10}$$

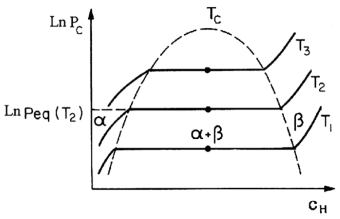


Figure 4.2: Ideal "p-c-T" diagram for the metalhydrogen system (adapted from [227]).

When the metal is exposed to hydrogen, it diffuses towards interstitial sites in the metal lattice accompanying α- or β-hydride phase transition [226] induced by increasing hydrogen concentration in the lattice. The α-phase corresponding to hydrogen atoms in solid solution in a metal and the β-phase, a fully formed hydride. For temperatures below critical temperature (T_c, depending on the metal), the MeH_x system has a region where the material exists in a homogeneous mixture of α- and β-phases [227] (figure 4.2).

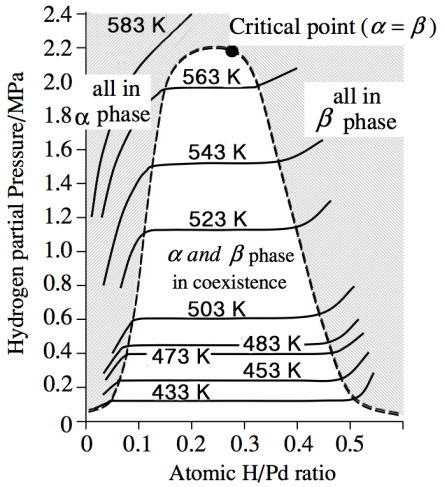


Figure 4.3: "p-c-T" diagram for the palladiumhydrogen system (adapted from [218]).

Palladium hydride: a reference system

The equilibrium "pressure-concentration-temperature" (p-c-T) diagram for the PdH system is shown in figure 4.3, which outlines the critical changes which occur to palladium as hydrogen diffuses in the lattice. The diagram is divided into three main zones. Each corresponds to a different phase of Pd-H system. The $\alpha-$phase, which has a low hydrogen content, and the $\beta-$phase, the hydrogen-rich phase. Those two phases are separated by a miscibility gap which narrows as temperature increases and eventually, the $\alpha-$phase and $\beta-$phase coalesce into an homogeneous solution at a critical point given by: T = 568 K, p = 19.87 atm and H/Pd = 0.27 [228]. Detailed studies have revealed significant hysteresis effects in the transition region where $\alpha-$ and $\beta-$phases coexist in equilibrium [218, 229].

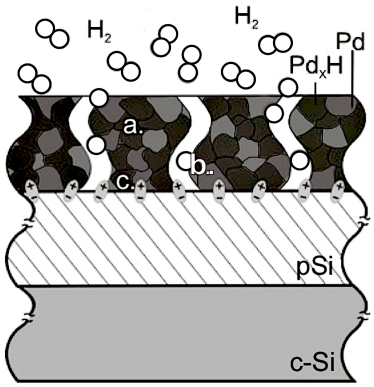


Figure 4.4: Schematic image for mechanisms of hydrogen adsorption. The H atoms occupy three different locations in palladium: (a.) octahedral interstitial sites in Pd lattice, (b.) In defects (dislocations ...), (c.) the Pd-Si interface where they form a series of dipoles [230, 231]. Inspired from reference [231].

When Pd is exposed to H_2, hydrogen molecules are adsorbed onto the Pd surface and dissociated into hydrogen atoms [221]. These hydrogen atoms diffuse until they occupy the interstitial sites of the Pd lattice to form palladium hydride [232]. Palladium exhibits a face-centered cubic (FCC) crystalline structure. Generally, there are three places for H atomes in Pd bulk [105] (figure 4.4):

I. H atoms occupy octahedral interstitial sites in the FCC lattice (figure 4.5). The $\alpha-$phase consists in a solid solution of PdH at low hydrogen pressures. This corresponds to an isotropically extended form of the FCC structure of pure Pd. At higher concentration of hydrogen in the Pd lattice, palladium-hydride is formed ($\beta-$phase). During the phase transitions ($\alpha \rightarrow \beta$) Pd lattice increases in volume [219, 233]. The isotropic expansion at $\beta-$phase can induce internal stresses being maintained in dislocation-free crystals of palladium [229, 234].

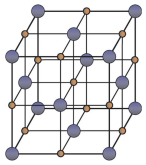


Figure 4.5: Unit cell of palladium metal showing octahedral sites that would be occupied by hydrogen in β-Pd hydride, for the limiting H:Pd ratio of 1. Note that the same sites are occupied by hydrogen in α-Pd hydride, at a considerably lower H:Pd ratio. Reproduced from [232].

In theory, there is a limitation in the concentration of H atoms in the Pd lattice. This limitation occurs when the H atoms occupy all octahedral interstitial sites. The lattice of system exhibit a "Rocksalt structure" and the limiting composition of the hydride would be PdH. However, experimentally, this is not the case because as the vacancies in the palladium lattice fill up, the lattice expands creating more absorption sites. The number of available absorption sites increases continuously with lattice expansion. At room temperature, the H/Pd atomic ratio is approximately 0.6 and never exceeds 0.8 under standard conditions [235].

An increase of the concentration of the H atoms when $\beta-$phase is alone to exist, creates defects such as vacancies and dislocations to maintain the expanded FCC structure of the palladium-hydride and also to release the strain produced by gradual volume expansion. A further increase in hydrogen concentration causes severe structural deformations which can only be partially recovered after hydrogen desorption [236].

In addition, these H atoms in octahedral interstitial sites increase the Pd electrical resistance [237]. Indeed, the presence of hydrogen atoms increases the frequency of scattering events of charge carriers. The magnitude of resistance increase is expected to be proportional to the atomic fraction of absorbed hydrogen atoms.

II. Trapping sites at defects (dislocations, vacancies, grooves, scratches ...) [238, 239]; this trapping decreases the hydrogen diffusion flux especially at room temperature [238].

III. After having diffused through the palladium layer, the H atoms are absorbed at the interface Pd-Si [230, 240, 241]. H atoms adsorbed at the interface are polarized and give rise to a dipole layer. The dipole layer at the interface change in the work function of the metal [128, 151, 217, 230, 233, 242–248].

Absorbed hydrogen impacts on Pd/Si junction

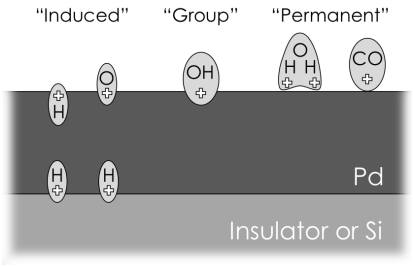


Figure 4.6: Origin of dipoles on a metal surface and at a catalytic metal-(insulator)-Si interface. The division into "Induced, group and permanent" dipoles is only schematic. Inspired from reference [230]

Many molecules and atoms adsorbed on a metal surface act as dipoles on the surface [230]. The origins of the dipoles are either that the adsorbed molecules or atoms have a permanent dipole moment and/or that they are polarized at the metal surface as illustrated in figure 4.6. H atoms are polarized at the interface from other polar molecules adsorbed on Pd surface and from surface effect. H atoms at the interface does not undergo the same interactions on Pd side than on the Si side. Its electron cloud becomes asymmetrical and an induced polarization appears.

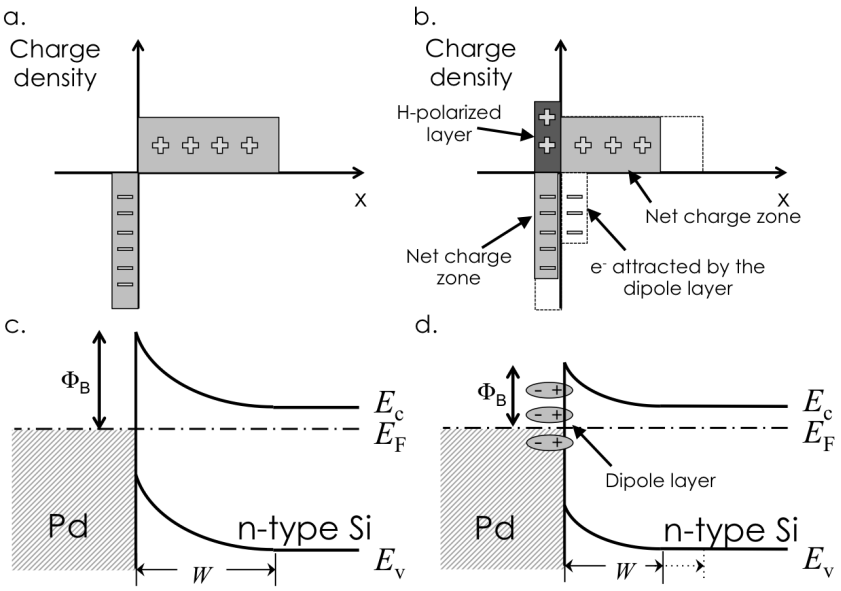


Figure 4.7: Charge density distribution (a. and b.) and band diagrams (c. and d.) of a Pd/n-type Si junction without (a. and c.) and with (b. and d.) dipole layer. The presence of hydrogen reduces both the SBH and the SCR width.

The effect of dipole layer on bands diagram of Schottky contacts with n-type and p-type semiconductor are shown respectively in figure 4.7 and figure 4.8. Figures 4.7a. and b. (resp. 4.8a. and b.) shows the charge density distributions with and without hydrogen adsorption, respectively for Pd/n-type Si (resp. Pd/p-type) junction. In a junction with an n-type semiconductor, the dipoles layer attracts electrons at the interface and the Schottky barrier height (SBH) decreases (decrease of the Pd work function). This results in increased thermionic current through the junction and a decrease in the space charge region (SCR) width (figures 4.7c. and d.). The reverse appears in a junction with a p-type semiconductor. The dipole layer repels holes in the p-type semiconductor. The SBH and the width of the space charge region increase (decrease of the Pd work function) (figures 4.8c. and d.). This results in a decrease in the thermionic current through the junction.

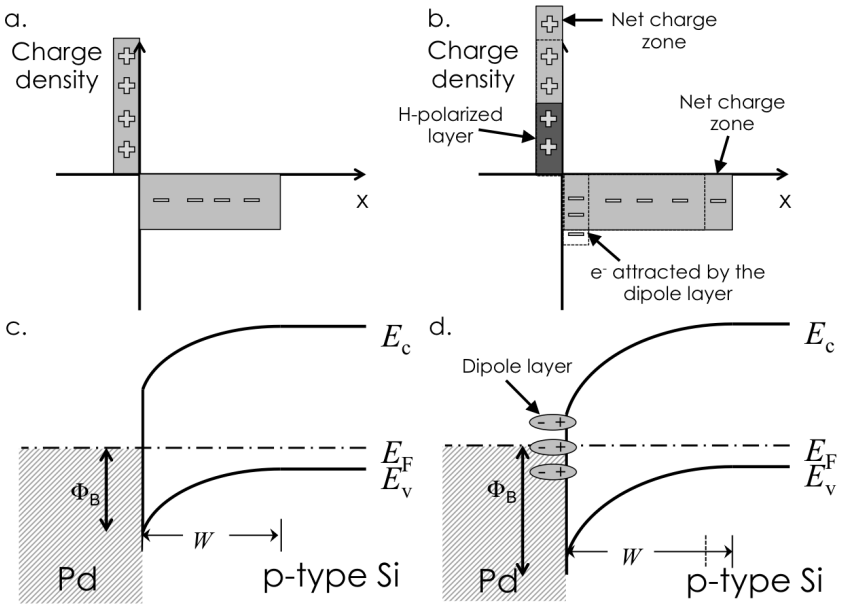


Figure 4.8: Charge density distribution (a. and b.) and band diagrams (c. and d.) of a Pd/p-type Si junction without (a. and c.) and with (b. and d.) dipole layer. The presence of hydrogen increases both the SBH and the SCR width.

In practice, a metal/semiconductor junction undergoes a small change due to the presence of the dipole at the interface. Indeed, for some semiconductors, such as Si, the barrier height at a metal/semiconductor junction is mainly determined by the surface states in the bandgap of the semiconductor. Many surface traps are concentrated at a energy level in semiconductor GAP. The quantity of charges required to equal the Fermi level of the metal may be provided by surface traps. Fermi-level is "pinned" at the trap energy level. In this situation, the SBH is the difference between the level of conduction (n-type) or valence (p-type) level and surface traps level and it is independent of the metal work function. One way to overcome this difficulty and get a barrier height, which varies with the metal work function, is to decrease the number of surface states by oxidation. In order that the dipole layer affects silicon, the oxide layer must be sufficiently thin [230, 247].

Three methods of hydrogen sensing based on the Pd work function modification by the presence of the induced dipole exist [247]:

1. **Schottky-type sensors:** This structure comprises a metal in contact with a semiconductor material (MS) or a metal in contact with a thin insulating (generally an oxide) layer on a semiconductor material (MIS/MOS) (figure 4.9a.). For hydrogen detection Pd or Pt are the metals most often used. The dipole from H atoms adsorbed at the interface changes the work function of the metal and hence the SBH. This change in the Schottky barrier height causes a shift in the current-voltage (I-V) characteristics and thus the response can be measured as the change in voltage when the diode is operated at constant bias current (figure 4.9d.).

2. **Metal-(insulator)-semiconductor transistor:** they use a field effect transistor (FET) to transform the change in the work function of a catalytic metal gate in the presence of hydrogen into an electrical signal related to the hydrogen concentration. Different configurations exist: MESFET (metal-semiconductor FET), MOSFET/MISFET (figure 4.9b.). But they all operate on the same principle: The dipole layer induced by the presence of the H atoms at M-(I)-S interface modulates the SCR in the semiconductor. This SCR modulation changes the section by which the electric current flows in the semiconductor, which changes its resistivity (figure 4.9e.). Many Hydrogen sensors based on a traditionnal MOSFET structure were reported in litterature. In this structure, a target gas sensitive metal is deposited on the insulating oxide layer to form the gate.

3. **Metal-insulator-semiconductor capacitor:** MIS-capacitors (or MOS-capacitors) are very similar in structure to the Schottky-type sensors however the insulating layer is thicker to prevent current conduction and to facilitate the build-up of charge on both sides (figure 4.9c.). The absorption of hydrogen and the chemical reactions at the metaloxide interface cause a change in the C-V plot and a shift of the flat band voltage proportional to the hydrogen gas concentration (figure 4.9f.).

For hydrogen in inert atmosphere such as argon, only the fundamental reaction (equation 4.5), takes place on the surface and kinetics developed above provides an explanation of the sensitivity of the Pd/Si junction at hydrogen.

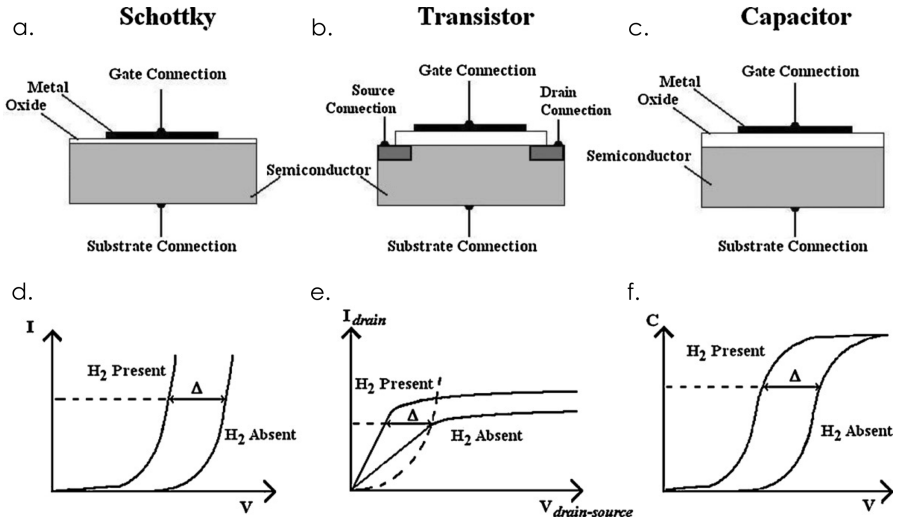


Figure 4.9: Cross-sectional view of a basic (a.) MOS-Schottky diode, (b.) MOS-transistor and (c.) MOS-capacitor sensor. The dipole layer formed by hydrogen adsorption at the metal/oxide interface creates a voltage change which can be measured by a shift in (d.) and (e.) the currentvoltage curve of a diode or transistor or (f.) the capacitancevoltage curve of a capacitor. Reproduced from reference [247]

When the H_2-sensing applications take place in air atmosphere, other chemical reactions take place on the Pd surface and disrupt the system. This is the case for the oxygen in the air [230]. Further two consecutive reactions occur:

I. Dioxygen adsorption

$$O_2 + 2H_a \longrightarrow 2(OH)_a \tag{4.11}$$

II. Water Formation

$$(OH)_a + H_a \longrightarrow H_2O \tag{4.12}$$

Two observations on the impact of the oxygen presence have been reported [239]: (i) The formation of a water molecule on the Pd surface consumes H ions that do not participate in the detection; (ii) adsorbed oxygen blocks hydrogen dissociation site. In both cases, the measurement sensitivity decreases.

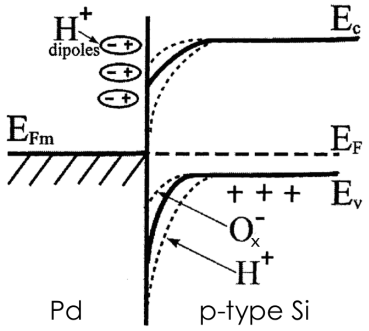


Figure 4.10: Schematic energy band diagrams for Pd/p-type Si-structure. The presence of dipoles generated by H atoms increases the SBH while the presence of negatively charged oxygen ions decreases SBH. Reproduced and modified from reference [249].

Another model of the oxygen impact on the Pd/p-type Si junction behavior has been proposed [249, 250]. The atmospheric oxygen on the metal surface can dissociate into oxygen atoms which may move through the Pd defects to the Pt/p-type Si interface and get polarized. These negatively charged ions can penetrate through eventual thin oxide layer between Pd and p-type Si, reach the SiO_2/p-type Si interface and decrease band bending of the junction. On exposure to the reducing gas (e.g. H_2), it interacts with oxygen atoms on the interfaces and decrease the concentration of negatively charged ions. The effect of oxygen ions decreases SBH and H atoms increases SBH for a junction with a p-type semiconductor (figure 4.10).

Initially, the palladium are covered by a thick oxygen layer [251] (figure 4.11a.). As the hydrogen is introduced, hydrogen tends to extract charged oxygen species from the surface (figure 4.11b.). However, the Pd surface are exposed to more oxygen compared to hydrogen because of higher oxygen partial pressure in the hydrogen-air mixture. So, the mechanism of sensing in air ambient is a competitive effect of forced oxygen removal by much lower percentage of hydrogen and more oxygen adsorption due to very high partial pressure of oxygen in the carrier gas (figure 4.11c.). The atmosphere of the measurement strongly impacts the phenomena involved.

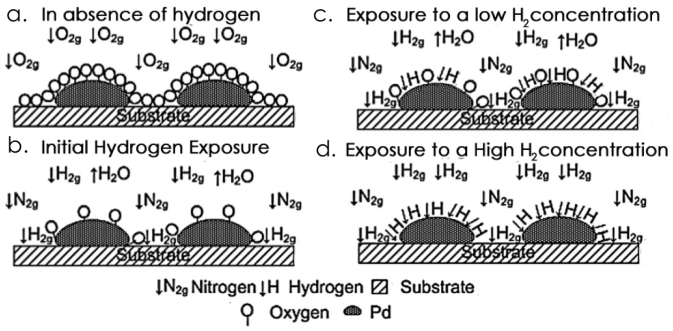


Figure 4.11: Schematic of cross-sectional view of Pd structures on a substrate. (a.) Initially, the palladium are covered by a thick oxygen layer. (b.) As the hydrogen is introduced, hydrogen tends to extract charged oxygen species from the surface. (c.) A competitive effect of forced oxygen removal by much lower percentage of hydrogen appears. (d.) At high H_2 concentration, adsorbed H atoms take the place of the oxygen at the surface. Reproduced and modified from reference [251].

4.2.4 Nanostructured palladium as sensing element

Hydrogen detection performances of a sensor are greatly enhanced when the metallic sensing element is nanostructured rather than used in its bulk form [236,246]. Nanostructures are objects of intermediate size between molecular structures and the microscopic scale which sometimes exhibit finite size effects. From a gas sensing perspective, nanostructuration has two benefits: first of all, thanks to a increased surface-to-volume ratio and higher hydrogen-accommodating sites density, metal nanostructures show increased absorption and dissociation rates. Second, nanostructures allow to suppress phase transition undergone by certain metals (such as the α-to-β transition palladium) impairing hydrogen sensing in a large H_2 concentration range [236]. Nanostructuration of metal sensing elements is a promising technique to improve the performances of existing sensors.

This section explores different low-dimensional Pd nanostructures used as sensing elements in hydrogen sensors. Several nanostructures are covered: 2D Pd thin films, 1D Pd nanowires and Pd nanoparticles. The relative strengths and weaknesses of the respective nanostructures

are discussed with emphasis on the fabrications techniques, sensor performances and means to further improve nanostructures efficiency.

Two-dimensional Pd thin films

Palladium thin films are the most basic form of Pd nanostructures. They are characterized by a thickness restricted to less than a hundred of nanometers. The film low aspect-ratio facilitates hydrogen absorption and desorption and play an important role in the sensing process [236]. Most palladium thin films are prepared by DC magnetron sputtering [252, 253], electroless plating [105, 254], electrodeposition [142, 255, 256], e-beam vapor deposition [160, 257] and very thin films by atomic layer deposition [258].

Palladium films behave like regular reversible sensors: hydrogen absorption in the metal causes a change in a physical property which is then measured. Thin films are often used as resistance-based sensors. Pd thin films presents a sensitivity[1] to hydrogen of 52 % for a concentration in H_2 of 2% [259]. The main issue with Pd film-based sensors is the phase transition occurring in metal hydrides. As the hydrogen concentration increases, the thin film enters a state of mixed phase $\alpha + \beta$. In this state, physical properties are more likely to be governed by the distribution and volume fraction of β-phase growing nuclei rather than the atomic fraction of hydrogen.

More importantly, the phase transition is accompanied by severe structural deformations in the thin film caused by the microstructure changes in the β-phase [259] (figures 4.12). The deformations can only be partially recovered after H_2 concentration has dropped. Indeed, dislocations created in β-phase cause irreversible plasticity onset. Pd thin films applications as sensing units are very limited because of the damages caused to the film, the subsequent risks of delamination [229] and the hysteresis phenomena all arising when hydrogen concentration increases past 2% [236]. The experimental evidence of hydrogen intake in α-phase palladium hydride suggests that palladium thin films obey the Sieverts' law (Eq. 4.8) [229].

[1] Sensitivity (S) is defined as the variation of the measured property (P) after H absorption divided by the initial value of the property: $S(\%) = \frac{P_{Hydrogen} - P_{pure}}{P_{Pure}} \times 100$.

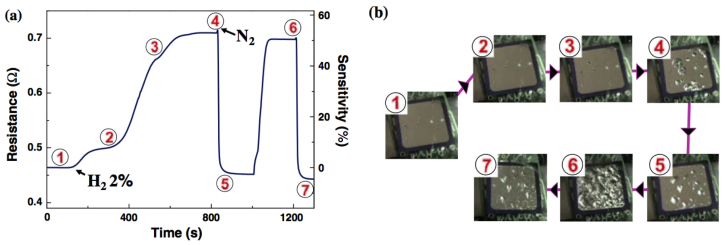


Figure 4.12: (a) Real-time evolution of sensitivity (or electrical resistance) of a Pd thin film resistance-based H_2 sensor. The device undergo cyclic exposure to 2% hydrogen gas at room temperature. Number 2 and 3 point to intermediate stages with decreased H_2 absorption rate. This denotes the occurrence of a new phase in the palladium thin film. (b) Evolution of the morphology of a 100 nm thick pure palladium film in response to cyclic exposure to 2% hydrogen gas at room temperature. Film damages can be observed, particularly on picture 4 and 6. Picture 7 shows an hysteresis effect. Reproduced from reference [259].

Four solutions have been explored to improve Pd thin films performances. Firstly, surface deformation is a thickness-dependent process. No hysteresis effects are observed in very thin films measuring less than 5 nm. With such small dimensions, the issue becomes to balance undesirable deformation effects with a low sensitivity and a bad control in the thickness during fabrication [236]. Secondly, alloyed thin films have been extensively studied. Palladium-nickel (Pd-Ni) thin films show good durability and fast response time. The addition of a small amount of nickel effectively enhance the structural stability of Pd films. However, such systems show low sensitivity to hydrogen [236, 260]. Nanoporous palladium films are currently investigated [261]. Porous films are less prone to delamination because of their relatively small thickness and they exhibit low detection limits thanks to the enlarged surface. Finally, a titanium buffer layer between the palladium film and the substrate allows to suppress the structural deformations in the Pd thin film [259]. The buffer layer properties can be tailored by varying its thickness from 0.5 to 80 nm. Titanium mediated improvement in adhesion strengthens a "clamping effect" from the substrate on the Pd film and thus restricts global volume expansion of the film. This limits the onset of the β-phase and related deformations. However, free volume restriction causes a lowering of the H_2 intake, reducing the sensor sensitivity [252, 259].

One-dimensional Pd nanowires

Nanowire design is based on the observation that increased sensing surface area can improve sensor response time and detection limit. Nanowires offer enhanced sensing characteristics but their fabrication present some challenges. Nanowire-based H_2 sensors are essentially metallic resistors: hydrogen concentration is related to a change of electrical resistivity through a metallic nanowire following hydrogen absorption [236]. In most cases, the electrical resistance of the nanowire-based sensor increases with hydrogen absorption because of the presence of H atoms in the interstitial sites impairing charge carriers flow through the wire [236]. However, the fabrication of arrays of mesowires in which hydrogen intake is related to a decrease in electrical resistance has been reported [262]. In these devices, the volume expansion subsequent to hydrogen absorption induce the creation of short-circuits between wires which leads to a decrease of resistance. There exists two main kinds of nanowires: lithographically patterned and bottom up grown.

Lithographically patterned Pd nanowires (LPN) are fabricated by a combination of e-beam lithography and lift-off processes. Sensing properties at room temperature are function of H_2 concentration and nanowire thickness. Thinner wires are less sensitive but have a faster response time. These characteristics are attributed to a strong clamping effect in thinner nanowires. Since every piece of matter in a narrow wire is closer to an interface, the clamping effect is stronger. The fabrication of very thin nanowires that can detect concentrations as low as 20 ppm has been reported. One drawback is that at very high H_2 concentrations, LPN face the risk of structural deformations since the nanowire body sticks to the substrate [236].

Bottom-up grown Pd nanowire (BUGN) arrays are created by palladium electrodeposition into nano-channels of anodic aluminum oxide templates. BUGN do not directly bond with the substrate and therefore are not subject to the clamping effect. Figure 4.13 shows a single BUGN palladium nanowire used for hydrogen sensing purposes. At room temperature, sensing properties of BUGN are function of H_2 concentration and nanowire diameter. Sensitivity is found to decrease with increasing nanowire diameter because of a higher surface-to-volume ratio and shorter diffusion paths for the narrower structures. In opposition to LPN, thinner BUGN exhibits larger sensitivity [263].

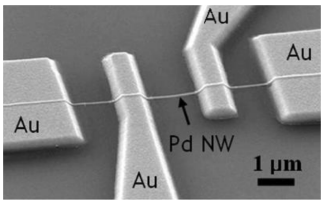


Figure 4.13: Sensing device made of an individual BUGN palladium nanowire (diameter of 20 nm) deposited on four gold terminals. Reproduced from reference [263].

Improving nanowires efficiency by inducing surface roughness (ion-milled nanowires), by tuning microstructure (grain-structured nanowires) [264] or by designing fracture resistant nanowire are currently being researched.

Pd nanoparticles

With a high surface-to-volume ratio and subsequent high hydrogen accommodating sites density, the hydrogen detection properties nanoparticles are optimal. A high surface-to-volume ratio ensure bigger interaction surface between the metal and hydrogen gas as well as enhanced hydridation kinetics. Hydrogen accommodating sites are active surface states that promote hydrogen diffusion by facilitating the adsorption and dissociation [246]. Nanoparticles exhibit higher sensitivity and decreased response time. In the following paragraphs, different techniques to incorporate nanoparticles on sensors are explored, including: continuous films of nanoparticles, grafting techniques, cluster beam deposition, electrodeposition and electroless deposition of particles.

Continuous films of palladium nanoparticles (CFN) are formed by potentiostatic electrodeposition of Pd particles on a conductive silicon substrate. Palladium nanoparticles with spherical shapes are electrochemically grown from a solution of palladium sulfate ($PdSO_4$) and sulfuric acid (H_2SO_4) [246]. CFN are made of nanoparticles with diameters ranging from 15 nm to 40 nm and more. A film is obtained when the deposits are dense enough to form a continuum where all the particles are electrically connected. Upon hydrogen absorption in palla-

dium, the electrical resistance of the film increases [246]. CFN exhibit higher sensitivity and lower response time than sputtered Pd thin films with the same thickness for all H_2 concentrations. The great sensing performances of CFN are attributed to a high surface-to-volume ratio and high hydrogen accommodating sites density which promotes large amount of H_2 intake and a fast hydrogen diffusion in the metal [236].

Palladium nanoparticles can be grafted onto different building blocks such as carbon nanotubes [236,265] or tin oxide nanostructures [266,267]. Grafting is a technique allowing the use of truly small nanoparticles, with an average diameter of 4 nm [236]. Hydrogen sensors based on single-walled carbon nanotubes (SWCNT) grafted with Pd nanoparticles exhibit a broad detection range (from 10 to 10000 ppm), a fast response time (as low as 3 s) and a high sensitivity [265]. SWCNT can be modified with dendrimers[2] acting as grafting mediators for palladium nanoparticles. Dendrimer layer may subsequently be removed by pyrolysis. The presence or absence of a dendrimer layer affects the response to H_2. Upon hydrogen absorption in palladium, dipole moment formation mediated by dendrimers is believed to change the sample electrical resistance, whereas direct electron transfer is possible in the case of Pd nanoparticles in contact with SWCNT. In both cases, the electrical resistance of the decorated SWCNT increases with H_2 concentration. However, each kind of detector exhibits different detection limits [265].

Palladium nanoparticles can be deposited on different substrates by cluster beam deposition (CBD). This technique involves three steps: first, palladium atoms are sputtered from a magnetron plasma aggregation source and particle clusters are formed. The formation of clusters is related to an aggregation process in a plasma of super-saturated metal vapor. Then, the clusters are swept by a gas stream out of the aggregation tube into a high vacuum chamber where cluster growth is stopped. Finally, the particle clusters pass through a diaphragm to form a beam of clusters ready to be deposited on a given substrate (see Fig. 4.14) [269, 270].

The detection mechanism of hydrogen sensors fabricated by CDB is either based on quantum conductance or on thin film percolation threshold. Quantum conductance refers to current transport across a

[2]Dendrimers are three-dimensional branched macromolecules.

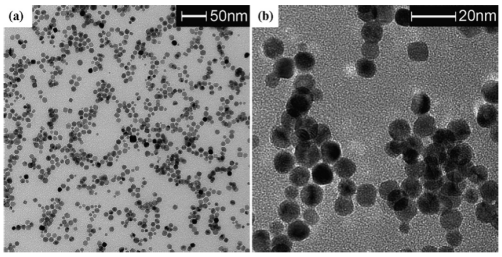


Figure 4.14: (a) TEM image of Pd particles arrays deposited by cluster beam deposition (deposition time of 300 s). Networks of randomly distributed closely spaced nanoparticles can be seen. (b) TEM image with a magnification on the clusters to show palladium nanoparticles. Reproduced from reference [268].

small gap separating neighboring nano-elements. In that case, electrons transport through the potential barrier is assured by thermally activated hopping [271] or by tunneling [272]. When hydrogen pressure increases, lattice expansion of Pd nanoparticles causes a decrease in gap size between sensing elements which results in a measurable change in electrical conductance for charge carriers hopping from one particle to another. Sensors based on percolation threshold use hydrogen-induced lattice expansion on discontinuous particles films to make them exceed the percolation threshold and then turn from non-conducting to conducting. Percolation can be seen as the formation of long-range connectivity in random systems. If a film made of palladium island-like structures is prepared just below the percolation threshold, hydrogen exposure lead to percolation and thus a change of the film conductance: this is known as the switching effect (see Fig. 4.15) [273].

Researches to improve cluster beam deposited nanoparticles characteristics allowed to address three main issues with important implications in the field of nanoparticles-based sensors: first, the use of nanoparticles allow to measure hydrogen in the range of the α-to-β phase transition. Second, it is known that the desorption of hydrogen from the Pd nanoparticles is a relatively slow process but no explanation about this phenomenon has been provided yet [274]. Finally, the use of nanoparticles as sensing element is compatible with substrate on which interdigitated metal electrodes have been deposited prior to nanoparticles functionalization [268, 271].

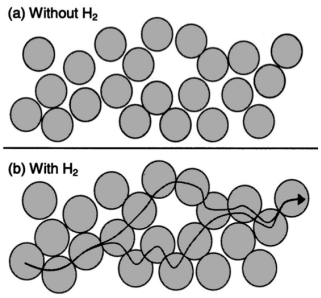


Figure 4.15: The concept of hydrogen-induced percolation and switching effect. (a) Non conduction palladium islands film. In absence of H_2, the islands do not make contact and the film is non-conducting. (b) Under H_2 exposure, the palladium islands expand and percolation is achieved. Note that the lattice expansion effect is strongly exaggerated for clarity purposes. Reproduced from reference [273].

Electrodeposition of palladium nanoparticles has been reported by various authors [246, 275, 276]. Potentiostatic electrodeposition in an electrolyte composed of palladium sulfate and sulfuric acid led to the formation of an nanoparticles and particle films. In the case of low applied voltages and small deposition times, spherical nanoparticles with an average size of 15 nm were obtained using this deposition technique. The surface coverage was fairly good and non-connected particles were obtained by applying a low voltage for a short deposition time [246]. In the presence of carbon nanotubes networks, site-specific electrodeposition can be performed. This deposition technique consists in a sequence of electrochemical potentials applied to single walled carbon nanotubes. This results in selective palladium deposition at defect sites [275]. Either acid or alkaline electrolytes can be used for electrodeposition plating of nanoparticles.

Metal nanoparticles can also be deposited by electroless. Electroless plating is an auto-catalytic chemical technique used to deposit a metal layer on a substrate. Unlike electroplating, electroless plating do not require an external electric current through the solution to form a deposit. The process relies on the presence of a reducing agent, which reacts with the metal ions to deposit metal. This method has attracted great inter-

est due to simplicity of operation, cost effectiveness and non-necessity to use complex equipment [256]. In a recent paper, Zhang *et al.* [277] reported electroless deposition of platinum nanoparticles on tungsten oxides films to create H_2 sensors. The platinum particles were deposited by an electroless plating technique based on the immersion of the samples in three deposition solutions. Particles with size in the range of 20 to 100 nm were obtained with a good coverage on the WO_3 surface [277]. The deposition of gold, platinum and palladium nanoparticles on germanium substrates from chloride solutions was also reported. By changing the deposition parameters, small particles or continuous films could be obtained [278].

Furthermore, Pd nanoparticles can be fabricated and deposited on various substrates by other techniques which are only mentioned. First, the fabrication of Pd-decorated ZnO-branched nanostructures was reported. A palladium metal layer is sputtered on branched ZnO nanowires and a subsequent annealing combined to the surface roughness of the shell of nanowires results in the formation of nanoparticles [267]. Secondly, the growth of Pd nanoparticles on a graphene substrate by thermal evaporation has been demonstrated. Nanoparticles are formed because cohesive bonds between metal atoms are stronger than adhesive bonds between the atoms and substrate [279, 280].

4.2.5 Functionalization of porous silicon by nanostructured palladium

The pSi functionalization by Pd nanostructures enables to benefit from the strengths of each sensing element being part of the sensor: (i.) Porous silicon provides a very large specific surface area for sensing as well as good compatibility with other silicon-based technologies. (ii.) Palladium as sensing element greatly improves the sensitivity and selectivity of the sensors towards the hydrogen. (iii.) Finally, the enhanced performances of nanostructured elements attributed to an increased surface-to-volume ratio and the suppression of phases transitions allow to further improve the sensor. In this section, we draw up a state of the art of functionalization of porous silicon by nanostructured palladium.

Deposition of Pd nanoparticles by electroless plating is the most common technique in the scientific literature [105,106,128,151,217,248,281–284]. Generally, the porous sample is immersed in an aqueous solution containing $PdCl_2$ and HCl to control the pH. The necessary electrons to chemical reduction of metal ions are provided by an reducing agent which may be a component of the electrolyte or the surface of the sample (porous silicon oxidation can provide electrons to metal ion).

The main disadvantage of electroless plating is the inhomogeneity of the nanoparticles density on sample surface [128, 284]. The deposit is mainly above the porous silicon. Traces of palladium are observable on the pore walls [105, 284]. Different techniques reduce this inhomogeneity: After the nanoparticles deposition, a thermal annealing at high temperature (900°C) enables nanoparticles to diffuse into the porous layer [283]; Increasing the pore diameter facilitates the penetration of the electrolyte into the pores before the nanoparticles growth at the pore entrance [128], but this may be insufficient (figure 4.16); Palladium acetate ($Pd(CH_3CO_2)_2$) as immersion solution, has a faster penetration rate into the porous layer [282], thereby functionalize a deeper thickness of the porous layer before the pore entrance being blocked by too rapid growth.

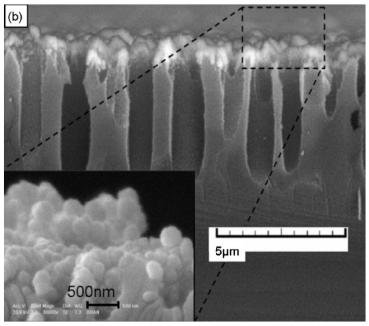


Figure 4.16: SEM picture from the cross-section of macroporous silicon samples after electroless deposition of palladium. Insets show the images with higher resolution. Reproduced from reference [105].

Another technique for Pd nanoparticles deposition is based on electroplating [142,143]. The deposition is carried out in an electrochemical cell comprising a reference electrode, a counter electrode and the sample,

which constitutes the working electrode. The electrolyte is an aqueous solution of $PdCl_2$ and HCl. Linear voltammetry technique was use to deposit Pd on porous silicon by reduction of Pd ions. The results were a semi-continuous layer of palladium and some dispersed clusters on top of the porous layer. The palladium deposits showed a poor penetration inside the pores [143].

The last technique is to dope the porous silicon by diffusion of palladium [127, 144, 285, 286]. A thin film of palladium (a few nanometers) is deposited on the silicon surface by evaporation or sputtering. Then the sample undergoes a long high temperature annealing (1h at 900°C) to allow the metal to diffuse into the porous layer. This technique tends to form a semi-continuous film of nanoparticles on the pore walls [285]. Oxidized palladium (PdO) and palladium silicide (Pd_xSi), poorly or no sensitive to hydrogen, was observed [127].

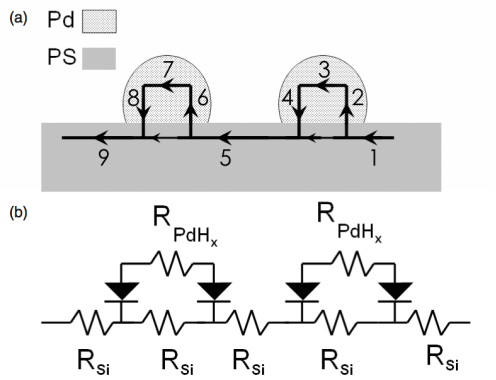


Figure 4.17: The model for the paths of current and the equivalent circuits. Reproduced from reference [151] and [281].

Rahimi *et al.* [281] observed porous Si resistivity decreases after Pd deposition. This decrease depends on the amount of deposited Pd. In their studies, they compare three different nanoparticle densities: Samples with dispersed Pd particles had highest resistance and have medium sensitivity to hydrogen; Samples with a large number of palladium clusters on the surface have medium resistance and highest sensitivity to hydrogen; Samples with a continuous Pd layer as a result of particle agglomeration has lowest resistance and lowest sensitivity to hydrogen.

They conclude that when the number of particles on the surface is low, the response is low. By increasing the number of palladium particles to a threshold, the response increases. However, if a continuous layer is formed on the surface, a negligible response would exist.

They proposed a model [281]: Near a Pd nanoparticle the electrical current could have two alternative paths (figure 4.17): one through the silicon skeleton and the other through Pd particles. As the resistivity of porous silicon is several orders higher than palladium, current mainly traverses the Schottky barrier between Si and palladium, passes through palladium and finally traverses another Schottky barrier reverse to the first one and then returns to the Si.

When hydrogen is introduced into the system, hydrogen molecules are dissociated into H atoms on the Pd surface and then diffuse into the lattice. At this time, three phenomena happen simultaneously:

1. Firstly, the electrical resistivity of palladium increases resulting from absorption of hydrogen. Therefore this happening increases the resistivity of some parts of the currents path (paths 3 and 7 in figure 4.17a.).

2. Secondly, H atoms form a dipole layer at the metal/Si interface and cause an additional increase in the energy barrier height at the metal/p-type Si interface. This phenomenon increases the resistivity of some other parts of currents path (paths 2, 4, 6 and 8 in figure 4.17a.). Decreased current flow is therefore seen both in the forward and in the reverse bias.

3. Finally, the lattice parameters of Pd showed a continuous gradual increase with increase in hydrogen content. It is known that the expansion of palladium specimens by about 3% in length and so about 10% in volume occurs. Thus if the palladium particles have sufficient close distance, after hydrogen absorption they join together and some paths of current is omitted (paths 4, 5 and 6 in figure 4.17a.). As the results of this elimination, the electrical current increases.

As the number of particles and consequently Schottky barrier increases, the change in electrical current and response to hydrogen increases. A sample containing a high density of nanoparticles is more sensitive. However, in the case of a continuous layer of palladium on the surface, the only effective mechanism of changing the current is the first mechanism. Since the order of this change is small the sensitivity of these samples are lowest [281].

4.2.6 Summary

This overview of the pSi functionalization shows the full force of Pd/Si system for H_2-sensing applications. The interactions between the palladium and hydrogen are rich and fast. Moreover, they are able to influence the electrical property of the porous silicon, which is exploited for sensing applications.

The interactions between catalytic metals and gases are greatly enhanced when the metallic sensing element is nanostructured rather than in its bulk form. Thanks to an increased surface-to-volume ratio and higher accommodating sites density, metal nanostructures show an increased catalytic activity. Moreover, nanostructures allow to suppress phase transitions undergone by certain metals. Those phase transitions can affect greatly sensing performances of a device over a wide concentration range.

A variety of techniques are available for the deposition of palladium nanoparticles into porous silicon, but some are incompatible with the presence of metal electrodes on the pSi surface.

In next sections, we study the functionalization of macroporous silicon by palladium nanoparticles using two deposition techniques: An original two-step method for the deposition via precipitation and electroless plating, a common standard technique. These techniques have the advantages of being fast, cheap and easily integrated into a standard microfabrication process. Their compatibility with the presence of metal electrodes has been considered.

Contrarily to electroless plating, the precipitation process does not involve any redox reaction. Briefly, a porous silicon sample is first immersed in a solution of palladium dichloride ($PdCl_2$) and then annealed

at high temperature. During the annealing step $PdCl_2$ is transformed into Pd. Under a chlorine atmosphere the dissociation temperature of $PdCl_2$ is 500°C while under inert atmosphere a temperature of 450°C is enough to obtain the precipitation of pure Pd nanostructures [287].

Control of the surface density of nanoparticles on the pore walls is an important parameter to master. Indeed, the model presented in the previous section shows that a high density of nanoparticles on the pore walls increases the measurement sensitivity. However, percolation between the nanoparticles must absolutely be avoided to prevent a significantly reduction of the measurement sensitivity.

Finally, the large majority of nanoparticles deposition techniques, described in the preceding section, results in a significant deposition on top of the porous silicon surface. Only traces of palladium nanoparticles were grown inside the porous matrix. Improving the homogeneity of the deposit in order to coat the pore walls on all the thickness of the porous layer is an interesting challenges to improve the measurement sensitivity.

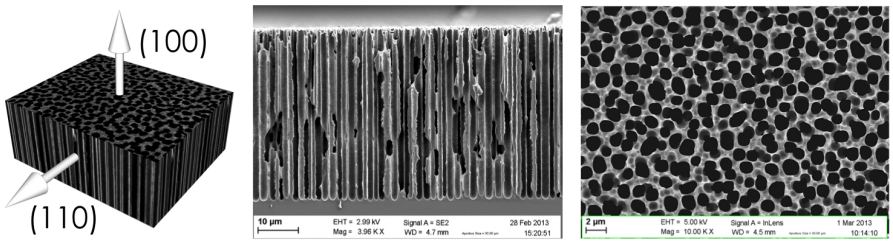
4.3 Materials and methods

Substrates

The samples were prepared starting from 3 inches p-type silicon wafers (<100>-orientation, 10-25 $\Omega\cdot$ cm, thickness 380 $\pm$ 10 μm, Siegert Wafer GmbH). All wafers were cleaned by immersion in Piranha solution (5:2 v/v 98% sulfuric acid: 30 % hydrogen peroxide, Chem-Lab) at 110 °C for 10 min followed by a triple rinse in deionized water. The wafers were then immersed in 2 % HF (Chem-Lab) solution for 30 seconds to etch the native oxide followed by another triple rinse with de-ionized water. A 200 nm-thick aluminum layer was evaporated (e-gun, Varian) on the wafers backside. The wafers were then annealed (Lindberg Tube furnace) in a H_2/Ar atmosphere at 432 °C to improve the electrical contact between the layer and the Si substrate.

Some of the wafers were patterned by metal electrodes using the method developed in the previous chapter. The presence impact of the metal electrodes on the quality of the deposits was observed on these samples.

Some of the wafers were anodized in a homemade Teflon single bath cell in order to obtain a macroporous layer. A platinum (Pt) grid was used as the cathode while the anode was the silicon substrate. The electrical contact was made with an aluminum (Al) plate placed in contact with the silicon wafer backside. The previously evaporated Al layer guaranteed the electrical contact between the plate and the wafer. The electrolyte was composed of HF and N,N-dimethylformamide (DMF) (HF(48%):DMF = 1:4, Chem-Lab). The macroporous silicon layer was formed keeping the etching current density J_{etch} constant at 32.5 mA/cm^2 for 25 min (Autolab PGSTAT302N, Metrohm). The macroporous layer so obtained is around 45 μm thick, with a mean pore diameter in between 1 and 2 μm (figure 4.18).



(a) (b) (c)

Figure 4.18: (a) Schematic diagram of a macroporous silicon samples with these crystalline directions representation. (b) SEM cross-section view and (c) top view of macroporous silicon layer made by anodisation in a HF(48%):DMF = 1:4 solution with a current density of 32.5 mA/cm^2 for 25 min.

All the wafers, porosified or not, were then diced in 20 $\times$ 20 mm rectangular shapes to obtain samples for the deposition experiments.

Some of the samples were furthermore etched with a solution of H_3PO_4 and isopropanol at 60 °C for 5 min, in order to remove the backside Al layer. All the samples were exposed after rinsing and drying to the ambient air for at least 1 hour before the deposition experiments.

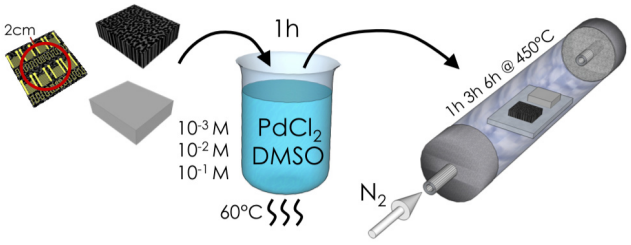


Figure 4.19: Schematic diagram of the deposition via precipitation experimental procedure.

Deposition via precipitation

The precipitation technique consists of two main steps (figure 4.19):

- Immersion of the sample in the deposition solution;
- Annealing at high temperature.

The *deposition solution* is composed of palladium dichloride ($Pd(II)Cl_2$, 60 % Pd, anhydrous, Sigma-Aldrich) dissolved in dimethyl sulfoxide (DMSO, 99.9 % A.C.S. reagent, Sigma-Aldrich). The critical point in this step is the penetration of the solution inside the pores so as to ensure a uniform coating on the entire pore walls. DMSO was chosen as solvent instead of water because of its lower surface tension (42.9 mJ/m^2 instead of 72.7 mJ/m^2). This allows for better penetration of the solution into the macropores.

Three different concentrations for the $PdCl_2$ were used: 1×10^{-3} M, 1×10^{-2} M, and 1×10^{-1} M (figure 4.20). The solubility at room temperature (RT) of the $PdCl_2$ in DMSO is lower than 1×10^{-1} M, thus the solution was heated at 60 °C during the experiments. The control of the temperature at 60 °C has two further advantages: the plating, depending on the temperature, is controlled and an higher temperature of the solution helps the solution diffusion into the pores. The substrates were immersed in the deposition solution for 1 h.

Immediately after the substrates were then annealed at 450 °C in an inert Ar atmosphere (MILA-5000, ULVAC Technologies, Inc.). The annealing transform deposited $PdCl_2$ particles into pure palladium.



Figure 4.20: Precipitation deposition solutions at room temperature. The solutions are composed of DMSO and $PdCl_2$. The color of the mixture varies with palladium salt concentration, from left to right: 10^{-3} M, 10^{-2} M, 10^{-1} M of $PdCl_2$.

The annealing temperature of 450 °C is enough to achieve the dissociation of $PdCl_2$ [287]. For too high annealing temperature (above 600 °C) risks of particles coalescence increase. Higher temperatures could also have adverse effects on the metal electrodes on top of macro-pSi. Indeed, during a long-time high temperature annealing, the metal diffuses into the silcium. At still higher temperatures, the metal may also evaporate. Three different annealing times were tested: 1, 3, and 6 h.

Electroless plating

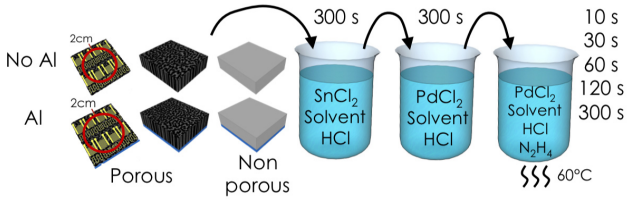


Figure 4.21: Schematic diagram of the deposition via precipitation experimental procedure.

Electroless plating is an autocatalytic nucleation and growth process, so a seed is needed to initiate the reaction. Since porous silicon has the ability to chemically reduce many substrates including metal ions as Pd(II) without the need of reducing agents in the solution, a simple method to obtain the nanoparticles on the pore walls, is the immersion of an oxide free porous samples in a solution containing Pd(II) ions. The Pd(II) reduction and the consequent deposition of Pd nanoparticles occur simultaneously with the oxidation of Si to SiO_2 [128]. However this method leads to a non uniform deposition and a low density of nanoparticles on the pore walls [288].

The uniformity of the deposition is improved by a pretreatment of the porous surface consisting of a sensitization and an activation step [289,290]. The sensitization of the surface is achieved by immersing the porous samples in a solution containing tin chloride ($SnCl_2$). Tin ions show a big affinity for oxide layers and are easily absorbed to form Sn^{2+} clusters. The Sn^{2+} clusters act as seeds for the formation of Pd nuclei, which initiates the deposition of larger structures.

The technique of electroless plating employed here consists in consecutive immersions in three different solutions (figure 4.21):

- A sensitization solution;
- An activation solution;
- And a plating solution.

The *sensitization solution* is composed of 3×10^{-2} M of tin chloride dihydrate ($Sn(II)Cl_2{\cdot}2H_2O$, high-purity reagent, Sigma-Aldrich), 6.77 ml/l of hydrochloric acid (HCl, 37%, fuming, A.C.S. reagent, Sigma-Aldrich) and a solvent; either de-ionized water (DI water) or dimethyl sulfoxide (DMSO, 99.9% A.C.S. reagent, Sigma-Aldrich). DI water is the standard solvent used in most electroless deposition processes since it is a very good polar solvent [256]. Also in this case DMSO was chosen instead of DI water as an alternative solvent because of its lower surface tension that allows a better infiltration into the porous layer. HCl is used to regulate the pH solution to 4 since tin(II) only precipitates under acidic conditions. The solution was stirred for 30 min after mixing the reagent. The substrates were immersed in the sensitization solution for 300 s at room temperature. The purpose of this step is to get Sn^{2+} ions absorbed on the Si walls.

The *activation solution* is composed of 2×10^{-3} M of palladium dichloride ($Pd(II)Cl_2$, 60% Pd, anhydrous, Sigma-Aldrich), 6 ml/l of fuming hydrochloric acid (37%) and a solvent; either DI water or DMSO. The presence of HCl ensure a good dissolution of $PdCl_2$ in water-based solutions and a better stability of the compound. The solution was stirred for 30 min after mixing the reagent. The substrates were immersed in the activation solution for 300 s at room temperature immediately after immersion in the sensitization solution.

During the activation, the Pd^{2+} ions are reduced on the surface by the Sn^{2+} absorbed ions leading to the formation of Pd^0 seeds (Eq. 4.13).

$$Pd^{2+} + Sn^{2+} \longrightarrow Sn^{4+} + Pd^0 \tag{4.13}$$

The *plating solution* is composed of $PdCl_2$ 2×10^{-3} M, 6 ml/l of fuming hydrochloric acid (37 %), hydrazine monohydrate 5×10^{-2} M ($N_2H_4 \cdot H_2O$, 64-65 % N_2H_4, reagent grade 98 %, Sigma-Aldrich), and a solvent. Two different solvents were used: DI water and DMSO. The solution was heated up to 60 °C. Hydrazine was used as reducing agent for the electroless experiments because this compound has the benefits of being suited to palladium deposition, is active in both acidic and alkaline solutions, and does not leave traces [291]. The solution was stirred for 30 min after mixing the reagents. The substrates were immersed in the plating solution for 10, 30, 60, 120 and 300 s at 60 °C immediately after immersion in the activation solution. All the samples were then quickly rinsed in DI water in order to stop the electroless reaction, and dried with nitrogen.

Characterization techniques

The functionalized samples were characterized by field emission gun scanning electron microscopy (or FEG-SEM, henceforth referred to as *SEM*) (Ultra 55, ZEISS), energy-dispersive X-ray spectroscopy (*EDX*) (EDS, BRUCKER), X-ray photoelectron spectrometry (*XPS*) (SSX 100/206 photoelectron spectrometer, Surface Science Instruments, USA) and optical microscopy. In porous samples SEM and XPS analysis were performed on the cross-section obtained by cleaving the sample after the Pd deposition. In non-porosified samples, to better simulate the conditions of a porous substrate, SEM and EDX analysis were performed on the (110) plane face along which the pores are normally grown (figure 4.18(a)).

SEM pictures were taken with an extra high tension (EHT) electron beam set to a voltage of 5 kV, unless stated otherwise. Most pictures were acquired by collecting secondary electrons using a mixing of signals from the InLens ("contrast" detection) and SE2 ("topography" detection) detectors in the following ratio: InLens:SE2 = 75:25. Aperture size was 30 μm and the distance to the sample always less than 2 mm. In general, the brightness and the contrast were adjusted respectively to 0 and to around 40% in order to keep the contrast levels consistent

between different pictures. These parameters enable to obtain clearly defined particles on the image with good contrast.

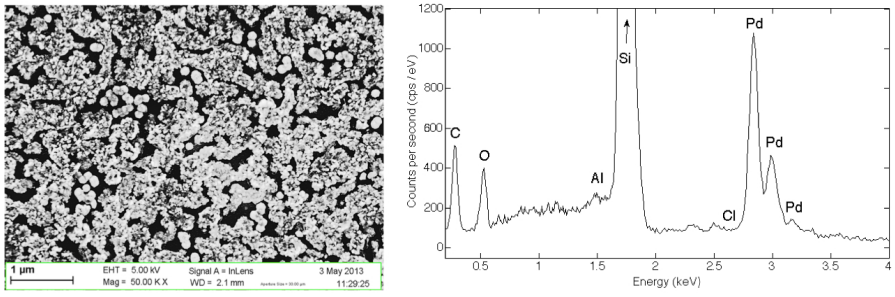
For the EDX acquisition, the SEM parameters were set to: EHT = 10 kV, aperture size = 30 mm, electron collector = SE2 and WD = 6 mm. In order to have enough resolution around palladium spectral lines, EHT value was set three times higher than the last significant palladium spectral line which is found at 3.171 eV ($\beta_{2,15}L_{III}N_{IV,V}$) [292]. The EDX software suite ESPRIT 1.9 (Bruker Nano GmbH, Germany) was used for a quantification of the spectra.

A code implemented in Matlab was used to determine the density and the diameter of the nanoparticles starting from SEM pictures. The code is presented in Appendix H. The measurement error is mostly determined by the limited resolution of the SEM images and by the determination of the grey threshold.

4.4 Results

4.4.1 Deposition via precipitation

Deposition on silicon



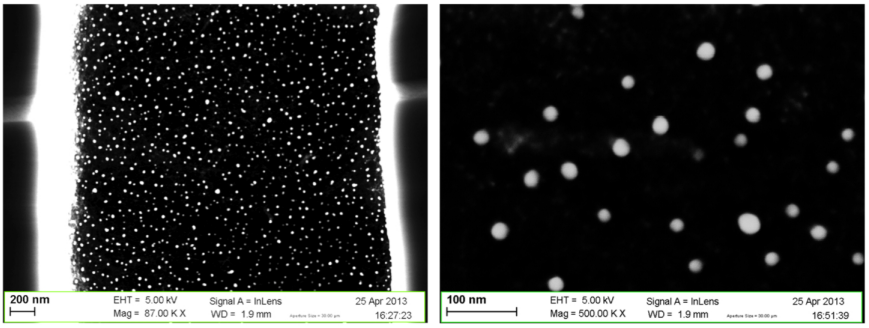
(a) (b)

Figure 4.22: (a) SEM top view and (b) EDX analysis of a silicon sample surface after Pd deposition by precipitation. The following parameters were used for the precipitation: 1×10^{-1} $PdCl_2$ in DMSO; 1 h immersion; 3 h annealing at 450 °C.

Figure 4.22(a) shows the SEM view of the cleaved face of a non-porosified silicon sample after the deposition via precipitation in a solution of 10^{-1} M of $PdCl_2$. A semi-continuous film composed of interconnected nanostructures covers the large majority of the surface. The agglomerates exhibit a round-like shape and are superposed on each other.

The EDX analysis shows that the elements at higher concentration are respectively Si and Pd (figure 4.22(b)). The Pd peak is due to the semi-continuous film while the Si peak is due to the substrate. The intensity of the Si peak is bigger than the Pd peaks because the depth of excitation necessary for the EDX analysis is larger than the semi-continuous Pd layer thickness. Peaks for carbon (0.2 keV) and oxygen (0.5 keV) are also noted. The peaks of C and O are attributed to the presence of contaminants on the sample due to the necessary handling. The presence of residual DMSO could also be an explanation. No peak appears around the spectral line of chlorine, suggesting that $PdCl_2$ is well-dissociated and gaseous dichlorine was evaporated.

Deposition via precipitation on macroporous silicon



(a) (b)

Figure 4.23: SEM picture of Pd nanoparticles deposited via precipitation into the pores. Cross sectional views of part of a pore with nanoparticles deposited on pore walls (magnitude 87 kx (a) and 500 kx (b)).

The deposition via this method on macroporous silicon gives rise to a quite different nanostructures morphology. In figure 4.23 are shown two different magnifications of the cross-section of a macroporous silicon

sample at the center of a macropore. In this case we obtained the deposition of well-spaced nanoparticles homogeneously distributed in terms of both dimension and density. This is most probably due to the smaller amount of reagent that can reach the surface of the pore walls with respect to the open surface of the non-porosified Si samples.

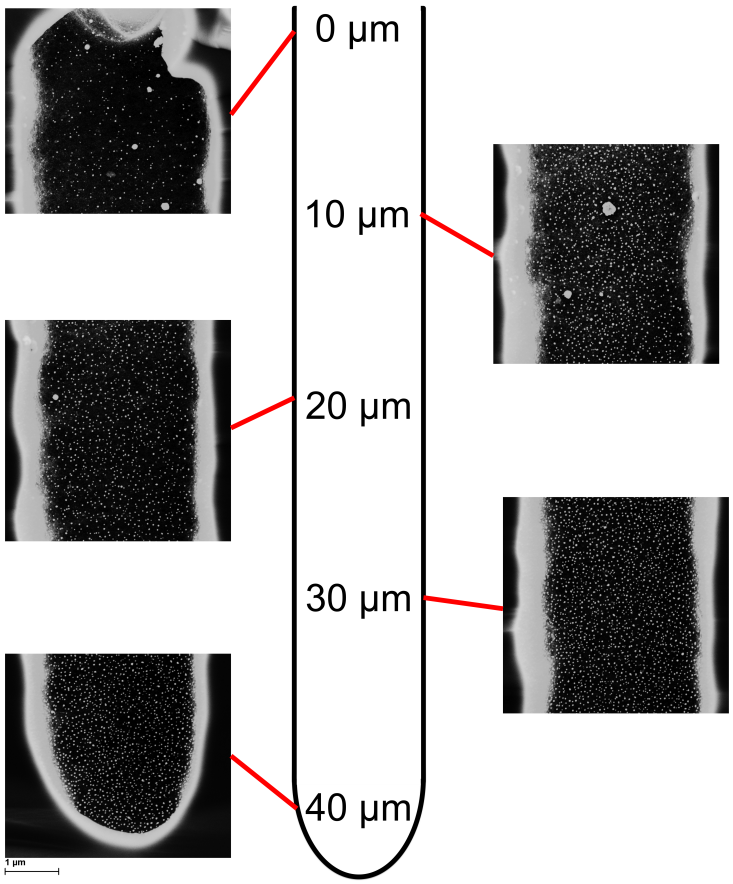


Figure 4.24: Particle coverage gradient along a single 40 μm pore. All the SEM pictures have been taken with the following settings: EHT= 5 kV, WD = 1.9 and Mag. = 50 kX.

The nanoparticles diameter ranges mostly in between 15 and 40 nm, rarely exceeding 45 nm. The density of nanoparticles is observed as homogeneous on a single pore wall (figure 4.24) and equally along the entire sample cross-section (figure 4.25).

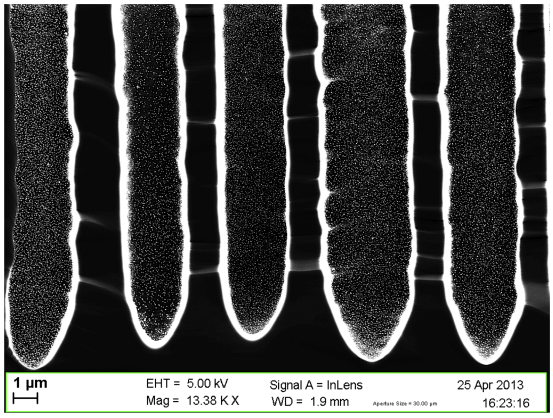


Figure 4.25: Particle coverage homogeneity across a few pores.

An increase of the density of nanoparticles with the $PdCl_2$ concentration in the deposition solution was observed (figure 4.26). The samples immersed in the solution with 10^{-3}, 10^{-2}, and 10^{-1} M exhibit a mean density of, respectively, 7, 32 and 118 particles/μm^2. While the shape of the particles does not change with the $PdCl_2$ concentration, a slight change in the size was observed: the average particle diameter increases by increasing the $PdCl_2$ concentration and the measured values are 18, 23, and 27 nm.

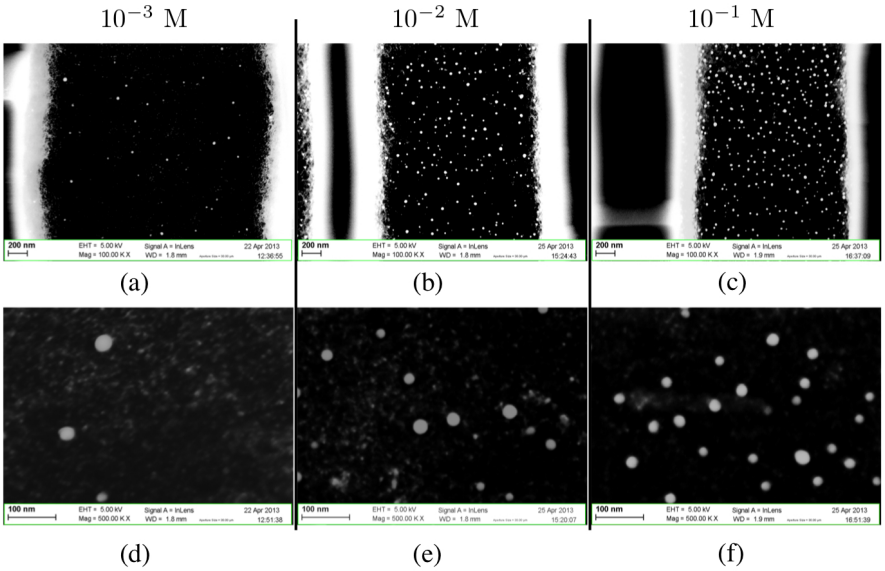


Figure 4.26: Impact of $PdCl_2$ concentration in deposition solution on the deposition via precipitation results. Cross sectional views with two different magnitude (up and down) of part of a pore with nanoparticles deposited on pore walls. The samples are immersed in the solution with respectively 10^{-3} M ((a) and (d)), 10^{-2} M ((b) and (e)) and 10^{-1} M ((c) and (f)).

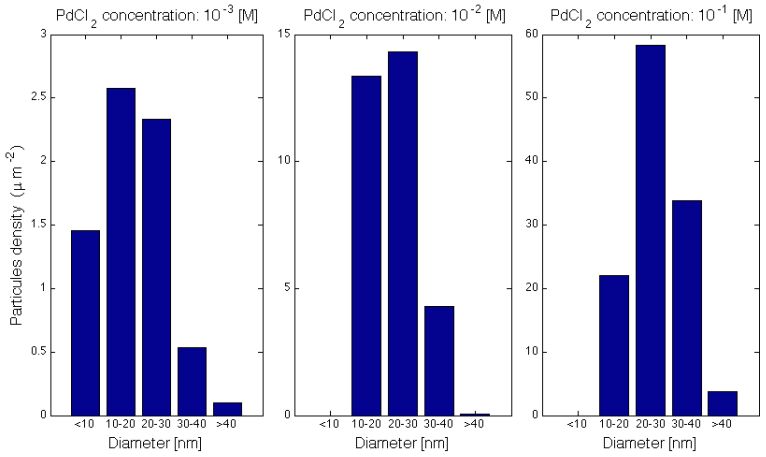


Figure 4.27: Particle diameter distribution in histogram form of Pd nanoparticles deposited via precipitation. The three histograms show the distribution into the pore walls obtained with deposition solution respectively (left to right) 10^{-3}, 10^{-2} and 10^{-1} M in $PdCl_2$.

Figure 4.27 shows the particle diameter distribution found on the pore walls of three samples immersed respectively in solution containing $PdCl_2$ 10^{-3}, 10^{-2}, and 10^{-1} M. In these histograms, it is clearly visible how the $PdCl_2$ concentration increase gives rise to the formation of a higher number and bigger size of Pd nanoparticles. Moreover, the concentration increase leads to a reduction of the spread out of the average particle diameter. The maximum value for the nanoparticles diameter remains stable around 45 nm and does not depend on the $PdCl_2$ concentration.

Another important parameter to take into account is the duration of the annealing at 450 °C. We analyzed samples after deposition via precipitation in a 10^{-2} M $PdCl_2$ solution and 1, 3, and 6 h annealing treatment as the only parameter that has been changing between the experiments. The particle shape was found to be independent on the annealing time, while the computed average particle diameters were 19, 23 and 18 nm respectively for 1, 3, and 6 h of annealing. The computed average particle density was found to be respectively 9, 32 and 18 particles/μm^2. No clear relation between the particle density and the annealing time could be highlighted. The homogeneity seems also to be independent on this parameter.

In the deposition via precipitation the formation of nanoparticles does not involve any charge transfer with the substrate. Pd nanoparticles deposited via precipitation are formed in a process of heterogeneous nucleation and growth of spherical $PdCl_2$ nanocrystals (colloid crystallization), followed by a thermally induced dissociation of fully-grown $PdCl_2$ nanoparticles into Pd nanoparticles.

The precipitation starts with the dissociation of the precursor $PdCl_2$.2DMSO. Nanoclusters of $PdCl_2$ can form through the agglomeration of sub-nuclei at a nucleation site. Sub-nuclei consist of aggregates of $PdCl_2$ of radius smaller than the threshold nucleation radius. Nanoclusters smaller than the threshold size are very unstable and tend to dissolve. Once a nanocluster reaches the threshold dimension, nucleation starts.

The reaction continues until the beginning of the actual growing process. The nanoparticle growth is the result of the competition between the addition of sub-nuclei to the nano-structure and the dissolution of the nanoclusters. As a consequence the increase of the $PdCl_2$ concentration leads to the formation of bigger and more densely distributed Pd nanoparticles. The growing rate tends to decrease with the particle size, until the process is stopped for a certain critical size of the nanoparticles, which is measured to be around 45 nm for the final Pd nanoparticle.

The XPS analysis performed on porous samples cross-section provide more information about the composition of the deposited nanoparticles (figure 4.28(a)). Overview XPS spectra of the porous films showed signals from oxygen (O), carbon (C), silicon (Si), aluminum (Al), and palladium (Pd). The presence of the Al signal is due to the presence of the Al layer on the backside of the Si wafer, while the large amount of carbon detected is attributed to the contamination due to the sample handling. The measurement window area of XPS equipment is 700 x 700 μm, which is bigger of the cross-section of the Si sample. Al on sample backside and also contaminants on the cross-section can be easily detected. Al is mainly detected in the oxidized state at 74.65 eV, with traces of metallic Al at 72.43 eV.

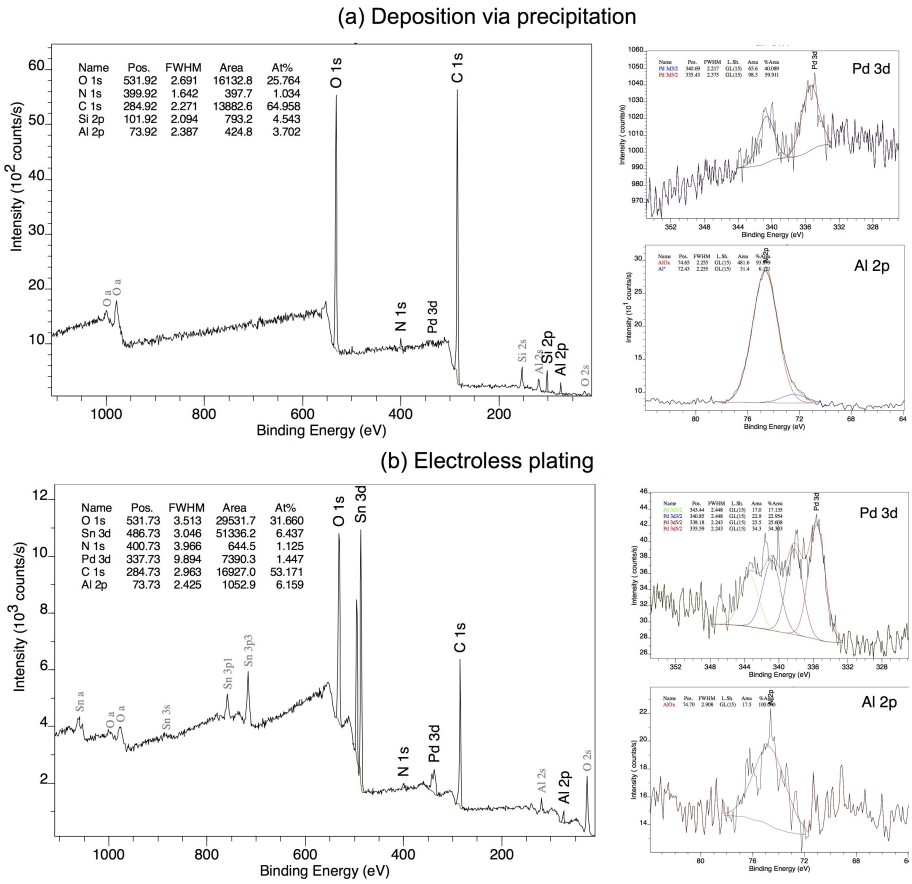


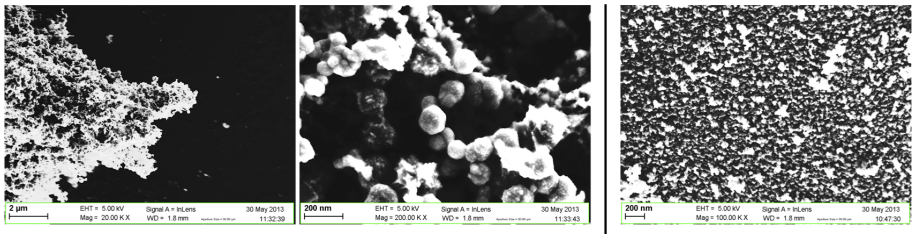
Figure 4.28: XPS spectra of pore walls after deposition via precipitation (a) and electroless plating (b) of Pd nanoparticles.

In the region corresponding to the detection of Pd two peaks are clearly visible at 335.43 eV, and 340.69 eV, both attributed to Pd in its Pd^0 state. In all samples no traces of chlorine were detected which together with the results of the EDX analysis performed on non porous samples, prove that $PdCl_2$ is completely dissociated during the thermal treatment. No difference between samples thermally annealed for different times were observed in the XPS analysis.

Electroless plating

In contrast to the deposition via precipitation, electroless plating is not only affected by experiment-related parameters, but also by the properties of the substrate. As we observed that the Al backside layer play an important role and strongly affects the deposition results, we conducted Pd electroless plating on samples with and without Al layer on the backside.

Pd electroless plating on bulk silicon



(a) (b) (c)

Figure 4.29: SEM pictures of deposits formed by electroless plating on flat silicon surface ((a) and (b)) without and (c) with aluminum on the wafer backside face. In the absence of aluminum on the backside face ((a) and (b)), the deposit is not a continuous layer. In the presence of aluminum in the backside face (c), the deposit is a compact and homogeneous film which covers the entire surface. Deposition parameters: Sensit. = 300 s / Activ. = 300 s / Plat. = 300 s.

In figure 4.29(a) and (b), two different magnifications of the cross-section of a non-porosified Si sample after Pd electroless plating are shown. No Al layer was on the backside of the analyzed sample. The result of the electroless plating is a non-continuous layer that leaves large portions of the silicon surface uncovered. The higher magnification SEM picture (figure 4.29(b)) shows that the layer is actually composed of round-shaped agglomerates grown one close to another. In figure 4.29(c) is shown a SEM view of the cross-section of a silicon sample with Al on the backside. As for samples without Al we obtained a layer composed of Pd round-shaped nanostructures agglomerates, but the layer is more homogeneous and covers the almost entire silicon surface.

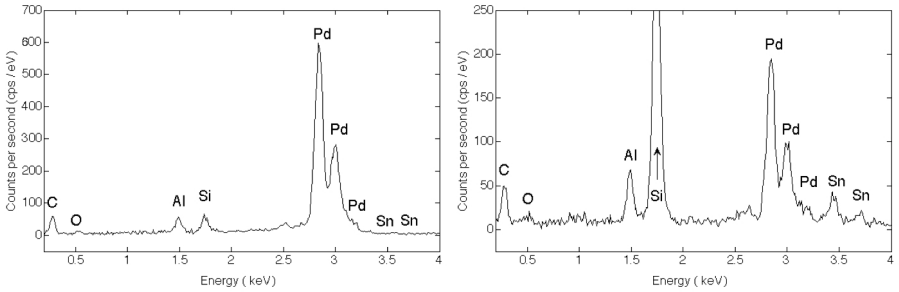


Figure 4.30: EDX analysis of a silicon sample surface after Pd deposition by electroless plating (a) without and (b) with aluminum on the wafer backside face.

We performed EDX analysis of both samples. In figure 4.30, the EDX spectra of samples (a) without and (b) with Al on the backside are shown. In both spectra, the peaks corresponding to carbon (0.277 keV), oxygen (0.525 keV), aluminum (1.486 keV), silicon (1.739 and 1.836 keV) and palladium (2.839 and 3.172 keV) are visible. The presence of O and C can be attributed to contamination due to the handling of the samples. The very low intensity of the Si peak in samples without Al layer on backside leads to the assumption that in these samples the Pd layer thickness is bigger than the penetration length of the EDX beam. The same assumption could explain why no trace of Sn was found on bare silicon samples while in samples with Al on the backside two small peaks close to the Sn spectral lines (3.443 and 3.662 keV) are visible in the spectra. The thickness of the Pd layer on samples with Al on the backside is probably smaller than the beam that can penetrate into the silicon substrate. Residual Sn was expected to be found when the beam goes through the Pd layer, which is not seen.

Pd electroless plating on macroporous silicon

Figure 4.31 showns two cross-sectional views of a macroporous sample (magnification of a single pore wall) on which the Al layer was removed before the Pd electroless plating. The two samples were immersed in a plating solution with DI water as solvent for 60 s (figure 4.31(a)) and 300 s (figure 4.31(b) and (c)).

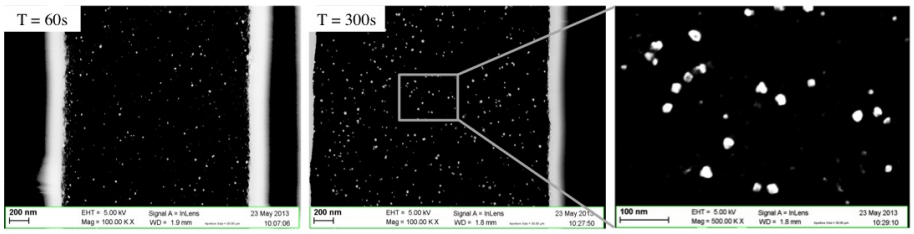


Figure 4.31: SEM pictures of cross sectional views of part of a pore with nanoparticles deposited on pore walls by electroless plating (sample without aluminum on backside face). Deposition parameters: Sensit. = 300 s / Activ. = 300 s / Plat. = 60 s (a) and 300 s (b). Magnification on nanoparticles (c).

Although the electroless plating resulted with the deposition of Pd nanoparticles, in contrast with the deposition via precipitation technique, the nanoparticles are distributed very unevenly on the pore walls. In certain areas of the pores, no particles could be found (figure 4.32).

As for the section of the pores exhibiting particles, the density is around 15 particles/μm^2 for the samples immersed in the plating solution for 60 s, and 37 particles/μm^2 for samples immersed for 300 s. Aggregates of 2-3 nanoparticles were also found.

Contrary to our expectations, the computed average diameter is of around 19 nm for both samples. The time in the plating solution should in fact determine the size of the nanoparticles: the reaction of Pd deposition is supposed to continue until the reactants are present in the solution, on the sites that have been activated in the previous step (the sensitization and activation times were 300 s each for both samples).

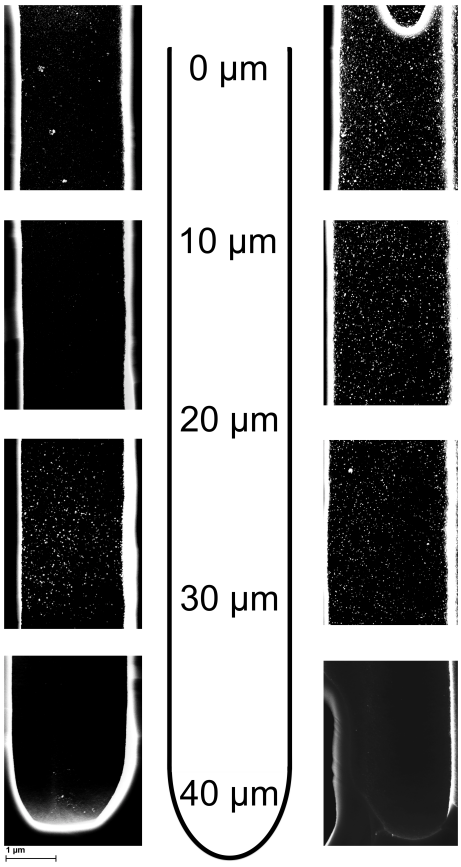
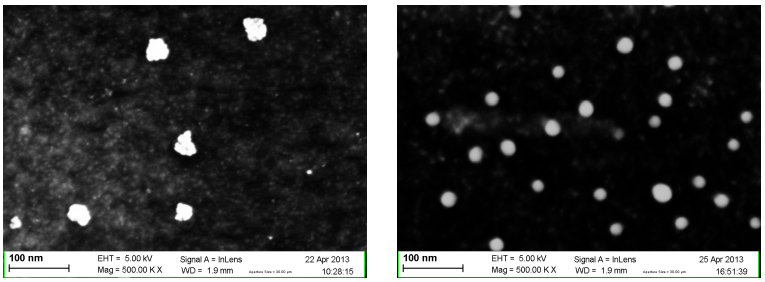


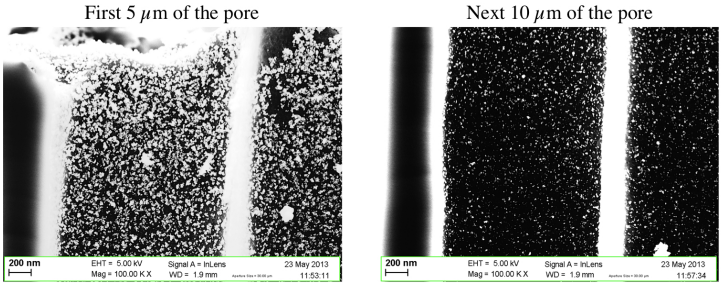
Figure 4.32: SEM pictures taken along two few microns-spaced pores. SEM pictures captured with the following settings: EHT= 5 kV, WD = 1.9 mm and Mag. = 50 kX.

In both samples the particle shape is variable (figure 4.33a.) compared to the results obtained with the precipitation process (figure 4.33b.). A number of round-shaped particles are observed, but most of them have irregular shapes, and other are the clear result of the overlap of different particles. The NPs density exhibits large variation along the pores depth. Same kind of inhomogeneity was observed between pores. In some of the pores no NPs were deposited.



a. b.

Figure 4.33: SEM pictures of the nanoparticle shapes deposited (a) by the electroless process and (b) by the precipitation process.



(a) (b)

Figure 4.34: SEM pictures of cross sectional views of part of a pore with nanoparticles deposited on pore walls by electroless plating (sample with aluminum on backside face). Views of (a) pores openings and (b) to 15 μm deep. Deposition parameters: Sensit. = 300 s / Activ. = 300 s / Plat. = 60 s.

The Al presence on the sample backside significantly affects the results of the electroless plating into the macropores. Figure 4.34 shows the cross section of a macroporous silicon sample in which the Al layer was still on the backside of the sample. Two portions of a macropore are shown, at the entrance (figure 4.34(a)) and at 15 μm in depth (figure 4.34(b)). In samples with Al on the backside a high density of nanoparticles is found at the entrance of the pore, in the first 5 μm in depth. Aggregates of particles that almost form a continuous layer are found in this area of the pores. The overall density (7 particles/μm^2) is

on the other hand comparable and even smaller than that computed for samples without Al. In fact, the density of particles decreases considerably with the pore depth and almost no particles can be found after 15 μm in depth.

The mean particle diameter was found to be 29 nm, with small variation around this value. Also in this case particles with different shapes can be found. Round-shaped particles can be rarely found. Tests carried out using DMSO instead of DI water did not give rise to significantly different results, just a slight better uniformity in the NPs distribution was observed.

The presence or not of the Al layer on the sample backside is the parameter that mostly affects the results of the electroless plating deposition experiments. We can say that we are in presence of Al-assisted Pd electroless deposition. The oxidation of the Al film proves that electrons are injected into the silicon substrate. These electrons reach the surface, and are then used for the reduction of Sn and Pd nuclei at the surface during the sensitization and activation steps. In other words, Al acts as a reducing agent promoting the deposition of active nuclei during the first two stages of the electroless deposition reaction.

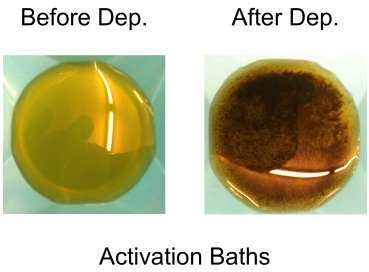


Figure 4.35: Activation baths before and after immersion of the substrates with Al layer on backside.

The Al layer was dissolved without formation of hydrogen bubbles while the sample was immersed in the deposition baths (figure 4.35). No gaseous hydrogen can be formed because the required electrons are instead injected in the bulk silicon. Moreover the higher density of the deposited film in bulk silicon samples, and at the entrance of macrop-

orous layers in samples with Al on the backside, could be explained by a change occurred in the first two steps of the deposition, because the Pd plating occurs only on pre-deposited and activated sites.

The results of the XPS measurements give more information about the composition of the deposited nanoparticles. In figure 4.28(b) are shown the spectra of a sample in which was present an Al layer on the backside that was etched during the electroless plating. The XPS spectrum shows the presence of O, C, Si, and of more interest Al, Sn and Pd. Although the Al layer on the backside was completely etched during the electroless plating, traces of Al are still present on the samples, it has to be noted that only the oxidized state of Al was found. Most probably, the Al^{3+} ions resulting from the dissolution of the Al layer in the electroless plating process, react and bond with the SiO_2 layer on the surface.

The presence of a large amount of Sn suggests that Pd does not substitute most of the Sn clusters. Assuming that the Sn cluster size is limited, it also suggests that the macropores walls are fully or partially covered with Sn clusters in the sensitization step. In next steps, these Sn clusters are not used for the following formation of Pd nanoparticles, which is limited to the entrance of the pores.

The decomposition of the XPS spectrum at binding energies corresponding to Pd shows the presence of two picks at 335.59 eV and 340.85 eV corresponding to Pd in its metallic state and other two picks at 338.18 eV and 343.44 eV attributed to Pd in its oxidized state (PdO_x or $PdCl_x$). The low amount of Cl detected, less than the 0.1 % lets suppose that PdO_x dominate.

4.5 Discussions

Morphology of the nanoparticles coverage

Table 4.2 summarizes the results obtained, for macroporous silicon samples processed with deposition via precipitation and electroless plating, using the image processing assisted analysis.

Table 4.2: Summary of the characterization of Pd nanoparticles deposited into the porous layer by deposition via precipitation and electroless plating. The symbols "+" and "-" are used to describe the shape quality of the deposited nanoparticles.

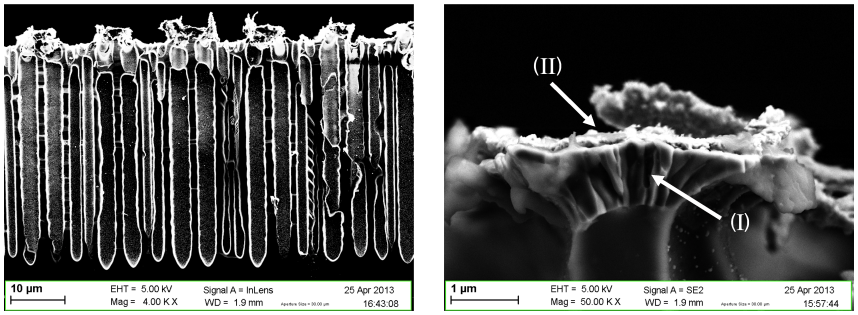
	Avg. NPs diameter (nm)	NPs shape (+/-)	Avg. NPs density (part./μm^2)	Density standard deviation (part./μm^2)
Dep. via Prec.				
10^{-3} M; 3h	18.4	+	7	7.7
10^{-2} M; 3h	23.4	+	32	3.7
10^{-1} M; 3h	27	+	118	46.8
10^{-2} M; 1h	19	+	9	5.2
10^{-2} M; 6h	18	+	18	7.1
Elec. plating				
without Al	19.9	-	25	22.9
with Al	29.3	-	7 (higher at the pore entrance)	87.6 (Excluding the first 5 μm)

In the deposition via precipitation, the $PdCl_2$ concentration plays an important role and affects many of the characteristics of the deposited nanoparticles: (i) the density of particles increases with the $PdCl_2$ concentration, (ii) the mean particle diameter increases with the $PdCl_2$ concentration, also the number of particles larger than the average size increases proportionally to the concentration, (iii) the maximum in diameter does not depend on the concentration and is stable around 45 nm, and (iv) in the range of concentration for $PdCl_2$ that we used, the deposition via precipitation allows to homogeneously cover the whole pore walls with Pd nanoparticles.

The results obtained by electroless plating are very different. Although the NPs average size is very similar to that obtained with the deposition via precipitation, their shapes is mostly not spherical and a large range of different shapes can be found. The nanoparticle density on the pore walls is very low and variable over the pore depth and in-between pores.

Interaction between particle deposition and metal electrodes.

Deposition via precipitation



a. b.

Figure 4.36: (a.) SEM picture of cross-section view of metal electrode patterned porous silicon layer after nanoparticles deposition by precipitation. (b.) Magnification on a metal electrode. Example of structure observed on top of some electrodes.

Figures 4.36 show a cross-section view of metal electrode patterned porous silicon layer after nanoparticles deposition by precipitation. Large nanoparticle clusters were developed on majority of the metal electrodes. Figure 4.36(b.) shows a magnification on an electrode. An interaction between the metal and the silicon has occurred. The region (identified by (I)) is probably the result of the metal diffusion in the silicon. Indeed, a long-time high temperature annealing promotes the interdiffusion of metal and silicon [293]. However, the oxide at the metal/Si interface could act as a diffusion barrier. However, the thickness and density of this plasma oxide is not very high. According to the diffusion constants of the metals constituting the metal electrodes found in literature [294, 295], the diffusion time through the oxide layer can be estimated. For example, the Ti adherence layer has a diffusion constant, D, in SiO_2 in the order of 1e-11 cm^2 s^{-1} [295]. Based on second Fick's law, the diffusion time, t_{diff}, through an 2 nm-thick oxide layer is:

$$t_{diff} = \frac{(\text{distance})^2}{2 \times D} = \frac{(2\text{ nm})^2}{2 \times \text{1e-11 cm2/s}} = 2\text{ ms} \tag{4.14}$$

Further analysis may reveal the nature of this region. However, we assume that this region is largely made up of silicide. Indeed, the metals constituting the electrodes, have sintering temperature[3] below 450 $°C$ used in the deposition by precipitation process [296–301].

The layer above the silicon crystallites (identified by (II)) may consist of: (i) the rest of the metallic multilayer, (ii) a nanoparticles layer and (iii) Si and O atoms which have diffused from the metal/SiO_2/Si interface towards the top of the metal layer. Again, further analysis would determine the nature of this region.

Figures 4.37 show the optical microscope pictures of the electrodes top view (before and after the deposition by precipitation). A high roughness appeared on metal patterned region. This suggests that a semi-continuous film of nanoparticles has grew on this region. This semi-continuous film is similar to one that has grew in the non-porosified samples previously presented (figure 4.22). We assume that when the reactants supply is not limited by the solution diffusion into the pores (as on the electrodes), the deposition by precipitation results in higher coverage density. However, the metallic nature of electrodes may also encourage the nanoparticles growth.

[3]Silicide formation temperature, but not necessarily in stable state.

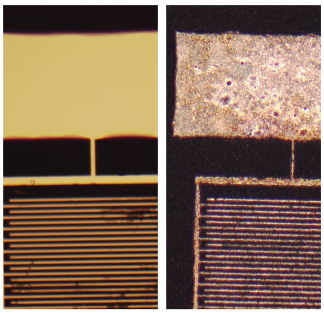
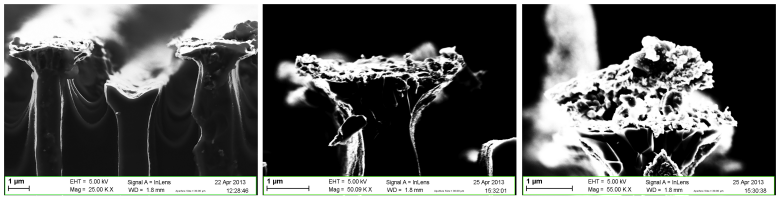


Figure 4.37: Optical microscope picture of top view of metal electrodes. The black background correspond to porous silicon and the yellow structures are the metal layer.

The presence of this semi-continuous film might be problematic in gas sensing applications. (i) Too large aggregates of nanoparticles could to create short-circuits between neighboring metal electrodes. However, it seems that aggregates observed in the SEM pictures have too limited sizes to that this problem occur. (ii) The Pd particles deposited on the electrodes are more rapidly exposed to the atmosphere and they consume the hydrogen instead of the nanoparticles on the pore walls. This might lead to a "screening effect" by the particles found on the metal electrodes. The difference in hydrogen sensitivity between the particules on electrodes and the particles on the pore walls is not determined. (iii) The Pd films are less hydrogen sensitive and are subject to the phase change and delamination problem (see section 4.2.4).

On the other hand, this semi-continuous film could improve the H_2-sensitivity of the device because its H_2-sensitivity "is added in series" to the H_2-sensitivity of the nanoparticles on the pore walls. Indeed, the external electric current passes through a electrode covered with a semi-continuous film, then it passes into the functionalized porous silicon layer and finally it passes through the second electrode also covered with the semi-continuous film. Each part is a transducer which converts the variation of the H_2-partial pressure in a resistivity modification of one part of the path traveled by the electric current. Provided that the different effects not result in resistivity modifications in opposite sign, the device sensitivity should be increased.



(a) (b) (c)

Figure 4.38: SEM pictures of cross-sectional view of metal electrodes after nanoparticles deposition by precipitation in solution of (a.) 10^{-3}, (b.) 10^{-2} and (c.) 10^{-1} M of $PdCl_2$. Sample dipped in a more concentrated solutions tend to exhibit more deposits on top of the metal layer.

The deposits and metal electrodes interact in the case of all $PdCl_2$ concentrations tested. Particles appear to have a greater affinity for metal electrodes and therefore, the metal layer is almost always covered with particles, no matter the deposition solution concentration. Figures 4.38 show a cross-section view of electrodes after deposition by precipitation in a solution of (a.) 10^{-3}, (b.) 10^{-2} and (c.) 10^{-1} M of $PdCl_2$. Sample dipped in a more concentrated solutions tend to exhibit more deposits on top of the metal layer. The deposit in the most concentrated solution resulting in aggregates of a few microns thick. However, all the electrodes do not undergo the deposit. Indeed, a small number of them have no deposit, while they can be located next to an electrode having a thick deposit.

Electroless plating

Figures 4.39 show the cross-section view of metal electrode after deposition of nanoparticles by electroless plating on substrate without Al layer on backside. Contrary to deposition by precipitation, this technique required no high temperature annealing, which does not result in a strong diffusion of metal in silicon. The metal electrodes appear completely covered by a small layer of particles. This suggest that deposition occurred preferentially on the metal electrodes rather than on the pore walls (figures 4.31).

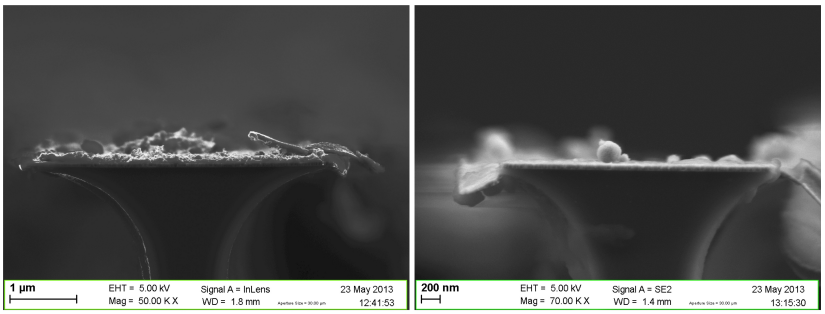


Figure 4.39: SEM pictures of bross-sectional view of metal electrodes after nanoparticles depostion by electroless plating. Samples without Al layer on backside. Deposition parameters: Solvent = DI-water / Sensit. = 300 s / Activ. = 300 s / Plat. = (a.) 60 s and (b.) 300 s. Electron collector = SE2.

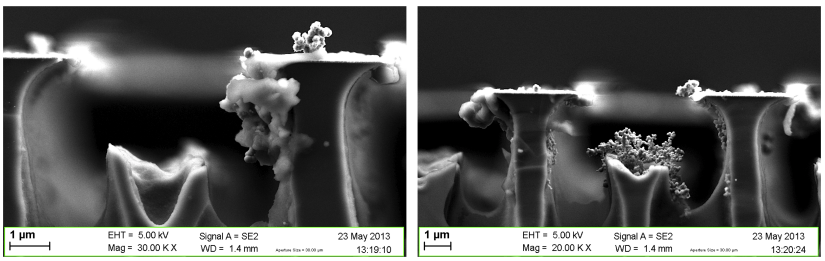


Figure 4.40: SEM pictures of bross-sectional view of metal electrodes after nanoparticles deposition by electroless plating. Samples with Al layer on backside. Deposition parameters: Solvent = DI-water / Sensit. = 300 s / Activ. = 300 s / Plat. = 300 s. Electron collector = SE2.

Figures 4.40 show the cross-section view of metal electrode after deposition of nanoparticles by electroless plating on substrate with Al layer on backside. The metal electrodes appear also completely covered by a small layer of nanoparticles. As on pore walls, in presence of Al layer, the deposition is larger. It is a phenomenon of Al-assisted Pd electroless deposition. Sometimes micrometric aggregates are present on or near the electrodes. (figure 4.40). However, these structures do not seem big enough to create a short circuit between the electrodes.

4.6 Conclusions on the comparison of functionalization methods

In conclusion, the original technique of deposition via precipitation proposed in this thesis was found to be an effective method to functionalize macroporous silicon with Pd nanoparticles. Round-shaped and uniformly distributed nanoparticles were deposited on the surface of the pore walls. Tunability of the number of nanoparticles on the surface can be achieved by changing the $PdCl_2$ concentration in the deposition solution. The EDX and XPS analysis showed the presence of metallic Pd in the pores, and no chlorine was detected.

The results are particularly encouraging in comparison to those obtained with one of the most standard techniques for the deposition of Pd nanoparticles, electroless plating. It was in fact shown that, with this technique, it is not possible to obtain a uniform coating of the pore walls with Pd nanoparticles. Moreover EDX and XPS analysis showed the presence of Sn and Al contamination on the deposited layer, and the presence of Pd in its oxidized state.

The deposition via precipitation not involving any redox reaction is compatible with a large variety of materials and could thus be used to functionalize different porous materials and sensing platforms.

Afterward, we observed the interaction between the two nanoparticle deposition techniques and metal electrodes. For both methods of deposition, the deposition of nanoparticles is enhanced on metal electrodes. For the deposition by precipitation, the metal electrodes are strongly altered due to the long-time high-temperature annealing. This produces a deep diffusion of the metal in the silicon crystallites and maybe silicide reactions. Due to the absence of annealing, the electroless plating technique does not affects the electrodes state. As on the pore walls and for the same reasons, the amount of deposited palladium is larger on samples with Al layer on backside compared to samples without Al layer.

4.7 Basic characterization of new miniaturized chemiresistor

In this section, we present a basic characterization of two sensors that combines all the results of this thesis (the new chemiresistor with the results of the previous chapter and the Pd nanoparticles deposition via precipitation described in this chapter). The fabrication process and design of this microsensor are described in Appendix I (page 285). The measurement was carried out only once on two differents microsensors: the first has not Pd nanoparticles and the second is coated with Pd nanoparticles deposited by precipitation in a solution of concentration 10^{-1} M $PdCl_2$ and annealed 3 h in N_2 atmosphere. Thermal annealing has an impact on the metal electrodes. To determine only the impact of Pd nanoparticles presence, the sensor without Pd nanoparticles has been annealed with the same parameters.

The measurement setup consists of a 10 cm diameter and 12 cm height cylindrical Teflon cell with a gas inlet and outlet (schematic view in Appendix F.5). The gas inlet is connected to a mixer-junction, which is plugged into the mass flow controllers. Air (50 %RH) and H_2 (in a concentration of 400 ppm in N_2) are used.

A N6705B DC Power Analyzer controlled by 14585A software (Agilent Technologies, USA) is used to monitor electric current evolution in time. An electrical voltage of 1 V is applied to each sensor.

Results and discussions

The measurements were carried out once on the both microsensors. They have the vocation to give an idea of the potential to combine the two important results of this thesis. However, more detailed measurements on a large number of microsensor are required to draw conclusions about the proof of concept.

Figure 4.41 shows the evolution of electrical current of microsensors without and with Pd nanoparticles deposited by precipitation in a solution of concentration 10^{-1} M $PdCl_2$ and annealed 3 h in N_2 atmosphere. The two microsensors were exposed to two different hydrogen concentrations (50 and 200 ppm) in humid air (50 %RH). The third graph shows the evolution of the H_2 concentration setpoint.

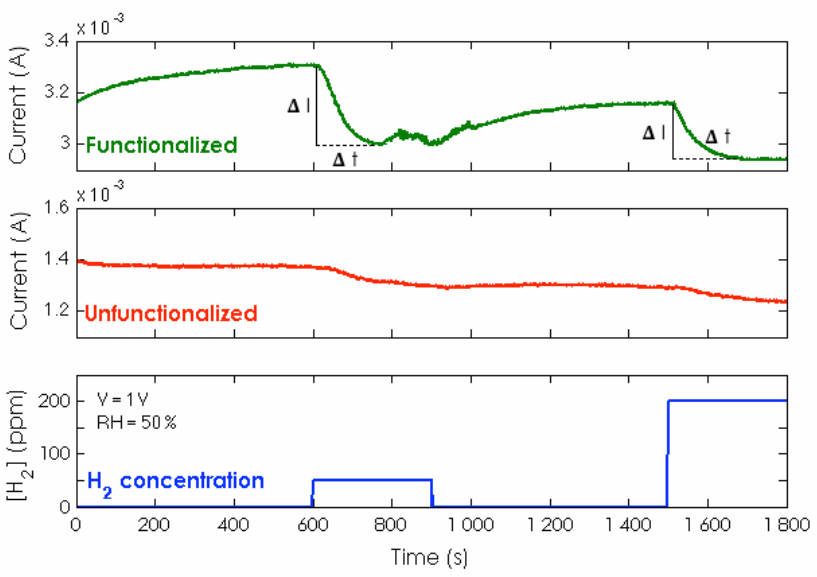


Figure 4.41: Evolution of electrical current versus time for (up) a functionalized (middle) and not functionalized sensors. The sensors were exposed to 50 and 200 ppm of hydrogen (in N_2) and humid air (50 %RH). A voltage of 1 V is applied to the sensors.

Both sensors exhibit a drift. Several reasons may be at the origin of this phenomenon: (i) The pressure of the air injected into the cell is higher than the atmospheric pressure at which the sensor was stored. The partial pressure of oxygen is higher. An amount of oxygen is absorbed and thus it modifies the Pd/Si system characteristics. (ii) Air is injected into the cell with 50 %RH humidity. Water molecules are absorbed on Si and/or Pd surfaces. Since they are polar, water molecules impact on the central channel in Si crystallites. (iii) The electric current produces a porous layer heating, which causes a continuous desorption and an electrical resistivity variation of Pd/Si system. Further analysis is necessary to determine the causes of the drift.

In the absence of hydrogen, the electrical resistivity of the sensor with Pd nanoparticles is approximately 2 to 3 times lower than the resistivity of the sensor without. Furthermore, for both sensors, the electrical resistivity increases when they are exposed to hydrogen. Both observations are consistent with the model presented in Section 4.2.5 (page 176). The electrical current near the palladium nanoparticles tends to cross the junction to transit through the nanoparticle, which has a much lower electrical resistivity. In the dipoles presence, the electrical resistivity of path that crosses the nanoparticle increases. At constant electrical potential, the electrical current decreases.

Both sensors have substantially different responses. The response of the sensor with Pd nanoparticles displays high current variation depending on change in H_2 concentration. Conversely, the response of sensor without Pd nanoparticles exhibits slight variations of the current.

Relative current variation

The sensor with Pd nanoparticles reacted more than the sensor without Pd nanoparticles to hydrogen variation. The measurement setup was not able to expose the sensors at lower H_2 concentration levels. However, by observing the response to 50 ppm of H_2, we assume that the detection limit should be well below 50 ppm.
The values considered to estimate the relative current variation of the measurement are schematized on figure 4.41. The relative current variation at the two hydrogen concentrations can be estimated by (C is the H_2 concentration):

$$\frac{\Delta I}{\Delta \mathrm{C}} = \frac{0.31\,\mathrm{mA}}{50\,\mathrm{ppm}} = 6.2\,\mathrm{uA/ppm} \tag{4.15}$$

$$\frac{\Delta I}{\Delta \mathrm{C}} = \frac{0.232\,\mathrm{mA}}{200\,\mathrm{ppm}} = 1.16\,\mathrm{uA/ppm} \tag{4.16}$$

One possible explanation is that the 50 ppm of concentration is beyond the upper limit of the sensing range of the sensor. In this case, the sensor is saturated and the differentiation between 50 ppm and 200 ppm is not possible. However, further analysis at lower hydrogen concentration are required.

Selectivity

Characterization of the selectivity has not been investigated. However, we assume that the humidity and air are at the origin of the initial drift. When the hydrogen is injected in much lower concentration that air and humidity, a significant response is detected. This result is encouraging for the measurement selectivity towards hydrogen.

Reversibility and hysteresis

The sensor seems partially reversible. The estimation of the hysteresis are difficult by the presence of drift. The hysteresis presence was observed. However, its origin could be made due to the fact that the sensor is exposed to concentration beyond the upper limit and that the nanoparticles have partially undergone a phase transition. Further analysis is necessary to determine these two parameters.

Miniaturization



Figure 4.42: Optical microscope picture of the microsensor compared to a piece of 1 euro cent. The sensitive layer is the black region.

The development of the microsize electrodes integration on macroporous silicon allowed us to significantly reduce the sensitive surface area of the chemiresistor. This first proof-of-concept has a sensitive area of less than 1 mm^2 (750 $\times$ 750 μm) (figure 4.42). The reduction of sensitive area is around 94 % compared to the smallest sensor in Table 2.1 in the "state of the art" section (page 55).

4.8 Chapter conclusions and perspectives

The porous silicon is an interesting transducer for implementation of the micro-scale gas sensors. Indeed, the surface area to volume ratio is very large, which concentrates the adsorption phenomena in a limited volume. However, porous silicon is poorly sensitive to hydrogen. We presented in this chapter various methods pSi functionalization to increase its sensitivity and selectivity to hydrogen. We discussed strengths and weaknesses of each method.

The Pd nanoparticles deposition inside porous silicon proved to be the most efficient functionalization method for hydrogen sensing by porous silicon because it presents several advantages: (i) Thanks to an increased surface-to-volume ratio and higher accommodating sites density, metal nanostructures show an increased catalytic activity. (ii) Nanostructures allow to suppress phase transitions undergone by certain metals, which can affect greatly sensing performances of a device over a wide concentration range. (iii) The discontinuous metal do not short-circuit the silicon.

Palladium is interesting because of the high solubility of hydrogen in it and fast diffusion to the Pd/pSi interface. These diffused H atoms form dipoles at the surface of the silicon, which affect the pSi electrical parameters. By these phenomena, the hydrogen partial pressure change is transduced in a readily usable electrical signal.

The original method of the deposition via precipitation proposed in this chapter, was found to be an effective method to functionalize macroporous silicon with Pd nanoparticles. A comparison with the most standard functionalization technique, electroless plating, shows that the deposition via precipitation gives some better results in term of density, coating quality, round-shape and chemical nature of the Pd nanoparticles. The deposition via precipitation enables a very homogeneous nanoparticles coating over the entire depth of the porous layer, unlike the electroless plating technique which forms an agglomerate of nanoparticles at the entrance of the pores and lets large non-coated surfaces.

The deposition via precipitation produces nanoparticles of Pd in the metal form and without contamination arising from the technique itself. Conversely, the electroless plating produces Pd nanoparticles in the oxidized form and contamination of Sn and Al were measured.

The impact of the two techniques of deposition on the metal electrodes was studied. The deposition by precipitation strongly alters the metal electrodes due to the long-time high-temperature annealing. By the absence of annealing, the electroless plating technique does not affects the electrodes state.

Finally, first basic measurement of one microsensor combining all results developed in this thesis has been characterized. By comparing the measurement of a microsensors with and without Pd nanoparticles, we have shown improving of hydrogen sensitivity of macroporous silicon with the presence of Pd nanoparticles on pore walls. The sensor response to the two hydrogen concentrations (50 and 200 ppm) are similar. We assume that the sensor is saturated. Further characterization is necessary to determine the measurement range of the sensor.

From this basic characterization, we obtain the competitive advantages of the new hydrogen sensor developed in this thesis:

- **Functionalization of the thick porous layer:** By combining macropores and the new technique of functionalization by precipitation, the thick layer of porous silicon is fully functionalized. This result is a technological improvement over the functionalization by electroless plating technique for the functionalization of micro- and mesoporous [217, 283] and macroporous [105] silicon.

- **Standard techniques:** The fabrication process and functionalization method of our sensor require only simple and standard techniques of microfabrication (e.g. The lift-off technique instead of the screen printing or the shadow mask technology).

- **Miniaturization:** The new fabrication process developed in this work allows to significantly reduce the dimensions of the sensor. For our first design, the sensitive area was reduced by 94 % compared to the state of the art (Table 2.1, page 55).

- **Low detection limit:** The basic characterization of the sensor suggests a detection limit of less than 50 ppm. This parameter is not mentioned in the articles concerning the detection of hydrogen by the porous silicon. A comparison of our results with the state of the art is not achivable. However, Huberta et al. [247]

identified the detection limits of the different technologies used in the detection of hydrogen: Thermoelectric (LOD of 10-25 ppm), Amperometric (LOD of 5 ppm), Metallic resistor (LOD of 10-25 ppm), Metalinsulatorsemiconductor transistor (LOD from 10 ppb to 300 ppm), quartz crystal microbalance (LOD of 8 ppm), Surface acoustic wave (LOD of 10 ppm). We assume that the LOD of our sensor is of the same order of magnitude.

However, the new sensor present several drawbacks such as poor relative current variation (at low hydrogen concentration), a drift of the electrical response and a poor reversibility. We assume these issues can be reduced by the treatment of the porous layer and/or Pd nanoparticles (e.g. [223], [136], [99], [111], [106], [217]).

Perspectives

As perspective to this work, further study is necessary to determine the best solution for Pd decoration, related to H sensing. We suggest to perform a large number of microsensors decorated by both Pd nanoparticles deposition techniques: precipitation and deposition via electroless plating. Each sensor must be electrically characterize under an atmosphere containing different hydrogen concentrations. A statistical analysis of the results should determine the most appropriate technique of functionalization for hydrogen sensing applications.

CHAPTER 5

Conclusions and outlook

This thesis details several technological developments leading to the fabrication of miniaturized chemiresistor based on macroporous silicon (for hydrogen sensing in particular).

In Chapter 1, we drew up an overview of the gas sensor operation and the main quality factors and we outlined the thesis objectives.

In Chapter 2, after the presentation of the fabrication and applications of porous silicon, we exposed the interests and obstacles of macroporous silicon as transducer in a gas sensor. First, the theory of mass transfer in porous media predicted that the diffusion of gases and liquids is faster in the macroporous silicon. This particularity is interesting to increase the kinetics of the gas sensor based on porous silicon and facilitate the functionalization of porous silicon by wet techniques. Then, we showed that the electrode miniaturization is required to improve the sensitivity and signal-to-noise ratio of the sensor response. However, the common techniques for metal electrodes integration on the macroporous silicon do not enable to reach these dimensions.

The Chapter 3 presents the technological development that have been necessary to propose the fabrication process of our miniaturized chemiresistor based on macroporous silicon:

▶ First, we investigated the origin of metal layer delimitation during electrochemical etching. We showed that the metal-assisted etching is the cause of the electrodes underetching. A detailed study has been conducted to understand the phenomenon and to propose several preprocesses to drastically reduce the electrodes delamination. The combination of these preprocesses thereby appeared as a new original way to obtain a one-step integration of micrometric interdigitated metal electrodes on thick macroporous silicon layers.

▶ Second, we reported a study on the selective anodization of patterned silicon substrates to form thick macroporous silicon layers. For a high current density, an overetching of the mask occurs. We showed that mask overetching is influenced by masking layer electrical properties, as well as by the etching parameters. 2D numerical simulations of the interface silicon/mask/electrolyte confirmed that carrier accumulation under the mask is the dominating phenomenon leading to the mask overetching for materials with higher permittivity and smaller thickness, due to a capacitive effect between silicon and the electrolyte separated by the mask. This study enabled us to determine the parameters of the electrochemical etching and the specifications of the masking layer to prevent mask overetching.

▶ Third, we studied the modification of pore distribution and morphology by the presence of the micrometric pattern. Pores grow faster in close proximity of the metal strip edges, leading to the formation of walls in the middle of the uncovered area for small electrodes spacing. An ordinary porosification grows between wider-spaced electrodes. Nevertheless, larger pores with very thin pore walls are developed in direct vicinity of the electrodes. The finite element simulations showed a current density distribution influenced by the enhanced electric field at the metal edges and promotes an electro-etching in this region.

▶ Finally, we simulated the electrical behavior of the charge carriers in pore walls. Considering the surface charge density induced by the oxidation of silicon, we have shown the existence of surface conduction in the pore walls. Indeed, the natural or forced oxidation of pore walls should generate a strong inversion layer in the surface of the walls. The surface conduction layer is largely influenced by the electrical charges on the pore wall surfaces. This phenomenon is exploited for the gas detection application. The simulations showed the influence of pore wall thickness on magnitude of the inversion of charge carriers in pore walls. We concluded that the finest pore walls will have more impact on the measurement sensitivity in gas sensing application. Indeed, this pore walls are subject to higher amplitude of the variation of the charge carrier density depending on the surface charge density (due to the oxidation, but also to gas adsorption) than thick pore walls.

Thus, by combining the results of the different studies, we recommended some design rules that should improve the performances of the chemiresistor in gas sensing application.

In the second part (chapter 4) of our work, we discussed on the functionalization of macroporous silicon for hydrogen sensing applications. Palladium has been found as the best functional material for H_2 sensing since it demonstrates great sensitivity and selectivity towards hydrogen. The Pd-H system has been detailed to show its strengths and weaknesses. A thorough review of the literature reveals that palladium nanostructuration is required to eliminate the harmful phase transition, increase the surface-to-volume ratio and thus the accommodating site density and increase catalytic activity.

Different Pd nanoparticules deposition techniques and the advantages and disadvantages of each has been reviewed. The electrode presence on the porous surface is a barrier to many of these deposition techniques. We presented an original, simple and cheap 2-step method to functionalize the macroporous silicon for hydrogen sensing application: deposition via precipitation. Compared with the most standard technique, electroless plating technique, we obtained better results in term of density, coating quality, round-shape and chemical nature of the Pd nanoparticles. The deposition via precipitation enables a very homogeneous metallic nanoparticles coating over the entire depth of the porous layer, unlike the electroless plating technique which forms an agglomerate of partially oxidized nanoparticles at the entrance of the pores and lets large non-coated surfaces.

Finally, we characterize basically a miniaturized chemiresistor combining all the results developed in this thesis. This novel architecture not only has exhibited some interesting results but it opened the door to the miniaturization of macroporous silicon-based devices, since we have reduced the area of the sensor surface by a factor of sixteen compared to the dimensions found in the literature. By comparing the response of miniaturized chemiresistor with and without Pd nanoparticles, we showed that the sensitivity of the chemiresistor is improved by Pd nanoparticle coating. However, further characterization is necessary to determine the real performances of the functionalized chemiresistor.

We hope that this small contribution to the large amount of publications in the field of porous silicon will improve the arguments to put forward the macroporous silicon as a serious candidate for the next generation of gas sensors.

Outlook

The new integration method of miniaturized electrodes is an innovation to fabricate new architectures for macroporous silicon-based microsensors. Future work must be focused on the study of the impact of the dimensions of the electrodes and their spacing on the measurement performances. This study will improve the microsensor design and its performances.

The deposition via precipitation technique offers the possibility to control the surface density of palladium nanoparticles on the pore walls of the macroporous silicon. Future work must determine the effect of this surface density on the sensitivity and selectivity of the sensor.

The basic characterization of functionalized miniaturized chemiresistor has shown promise in several quality factors of gas sensors. Further characterization must be done to measure its real performances. In particular, lower concentrations of hydrogen must be used to determine if the sensor is saturated in hydrogen concentrations higher or equal to 50 ppm. In this case, the detection limit and the measurement range must be determined.

The functionalization by the palladium is expected to increase the selectivity of the sensor for hydrogen sensing. This hypothesis has not been analyzed. Measurements of sensor exposed to other gases (such as NO_x, CO_x, ethanol, propanol, methane ...), but also to variations of temperature and humidity must be achieved to qualify the sensor selectivity.

Finally, in our study of metal-assisted etching, we have revealed the occurrence of macroporous silicon in the electroless etching process of the sample with aluminum as the adhesion layer. This phenomenon has never before been reported in the literature. We suggest that further analysis of this phenomenon could open an original way to fabricate a new morphology of porous silicon by metal-assisted etching.

APPENDIX A

Mass transfert theory

A.1 Expressions for Flux

Diffusion is the macroscopic result of random thermal motion on a microscopic scale. For example, on the figure A.1, species A and B molecules move in random directions, with kinetic energy on the order of kT.

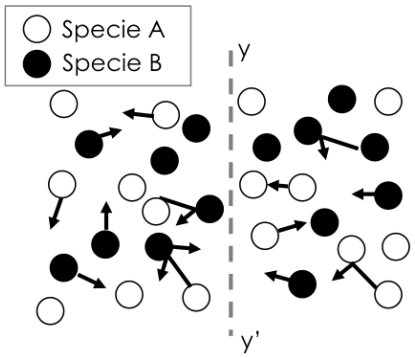


Figure A.1: Schematic representation of diffusion. The movement of the molecules is completely random.

If there are more A molecules on the left side of the plane y-y' than on the right, more molecules will cross to the right than to the left: there will be a net flux even though the motion of each individual molecule is completely random. If n is the concentration; the flux (J) is proportional to the gradient in the concentration (dn/dx) (Fick's Law):

$$J = -D\frac{dn}{dx} \tag{A.1}$$

where D is the diffusion constant and varies according to the diffusion regime.

A.2 The diffusion equation

Consider a volume from (x) to (x+dx) containing N molecules and a transport only by diffusion (figure A.2). The change in the number of molecules with time is the difference between the flux going in and the flux going out, assuming molecules are not generated or lost in the volume.

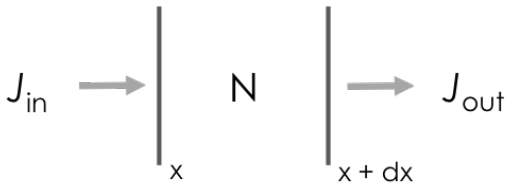


Figure A.2: The concentration variation in the volume [x, x+dx] is equal to the inflow (J_{in}) minus outflow (J_{out}).

By using the Fick's law expression for the flux (eq. A.1), we can relate the change in concentration to the derivatives at the edges of the region.

$$J_{net} = -D\left(\left[\frac{dn}{dx}\right]_x - \left[\frac{dn}{dx}\right]_{x-dx}\right) = \frac{\partial n}{\partial t} \tag{A.2}$$

By expanding the derivative at x+dx to first order in the derivative at x, we can derive the diffusion equation, which describes the relationship between the spatial and temporal behavior of concentration (second Fick's law):

$$\frac{\partial n}{\partial t} = D\frac{\partial^2 n}{\partial x^2} \tag{A.3}$$

A.3 The diffusion constants

A.3.1 Molecular diffusion coefficient

A.3.1.1 Theory [23]

In the simplest model of gas dynamics, the molecules are considered as rigid spheres and do not exert intermolecular forces. Collisions between rigid molecules are considered completely elastic. With these assumptions, a simplified model of an ideal gas mixture of specie A diffusing

through its A* isotope gives an equation for the self-diffusion coefficient, defined as:

$$D_{AA^*} = \frac{1}{3}\lambda u \tag{A.4}$$

where λ is the mean free path of length of species A, given by

$$\lambda = \frac{kT}{\sqrt{2}\pi\sigma_A^2 P} \tag{A.5}$$

and u is the mean speed of species A with respect to the molar-average velocity

$$u = \sqrt{\frac{8NkT}{\pi M_A}} \tag{A.6}$$

The self-diffusion coefficient becomes:

$$D_{AA^*} = \frac{2T^{3/2}}{3\pi^{3/2}\sigma_A^2 P}\left(\frac{k^3 N}{M_A}\right)^{1/2} \tag{A.7}$$

where M_A is the molecular weight (g/mol) of the diffusing species A, N is Avogadros number, P is the system pressure, T is the absolute temperature (K), k is the Boltzmann constant, and σ_A is the Lennard-Jones diameter of the spherical molecules.

Using a similar kinetic theory of gases approach for a binary mixture of species A and B composed of rigid spheres of unequal diameters, the gas-phase diffusion coefficient is shown to be

$$D_{AB} = \frac{2}{3}\left(\frac{k}{\pi}\right)^{3/2} N^{1/2} T^{3/2} \frac{\left(\frac{1}{2M_A} + \frac{1}{2M_B}\right)^{1/2}}{P\left(\frac{\sigma_A + \sigma_B}{2}\right)^2} \tag{A.8}$$

Modern versions of the kinetic theory have been attempted to account for forces of attraction and repulsion between the molecules. Hirschfelder *et al.* (1949) [302], using the Lennard-Jones potential to evaluate the influence of the molecular forces, presented an equation for the diffusion coefficient for gas pairs of nonpolar, nonreacting molecules:

$$D_{AB} = \frac{0.001858T^{3/2}\left[\frac{1}{M_A} + \frac{1}{M_B}\right]^{1/2}}{P\sigma_{AB}^2\Omega_D} \tag{A.9}$$

where D_{AB} is the mass diffusivity of A through B, in cm^2/s; T is the absolute temperature, in K; M_A, M_B are the molecular weights of A and B, respectively; P is the absolute pressure, in atmospheres; σ_{AB} is the *collision diameter*, a Lennard-Jones parameter, in $\mathring{A}$; and Ω_D is the *collision integral* for molecular diffusion, a dimensionless function of the temperature and of the intermolecular potential field for one molecule of A and one molecule of B.

Reference [23] lists Ω_D as a function of kT/ϵ_{AB}, k is the Boltzmann constant, and ϵ_{AB} is the energy of molecular interaction of the binary system A and B, a Lennard-Jones parameter.

For a binary system composed of nonpolar molecular pairs, the Lennard-Jones parameters of the pure component may be combined empirically by the following relations:

$$\sigma_{AB} = \frac{\sigma_A + \sigma_B}{2} \tag{A.10}$$

and

$$\epsilon_{AB} = \sqrt{\epsilon_A \epsilon_B} \tag{A.11}$$

A.3.1.2 Calculation

To evaluate the diffusion coefficient of hydrogen molecules in air at 20°C and atmospheric pressure.

	σ (in $\mathring{A}$)	ϵ/k (in K)
Air	3.617	97
H_2	2.968	33.3

Table A.1: The values of σ and ϵ/k from [23]

From [23], the values of σ and ϵ/k are listed in table A.1:

$$\sigma_{AB} = \frac{\sigma_{Air} + \sigma_{H_2}}{2} = \frac{3.617 + 2.968}{2} = 3.2925\mathring{A} \tag{A.12}$$

$$\frac{\epsilon_{AB}}{k} = \sqrt{\epsilon_{Air}\epsilon_{H_2}} = \sqrt{97 + 33.3} = 56.83 \tag{A.13}$$

$$T = 293K \qquad P = 1atm \tag{A.14}$$

$$\frac{kT}{\epsilon_{AB}} = 5.155 \tag{A.15}$$

From [23], the value of Ω_D is ~ 0.91.

$$M_{Air} = 29g/mol \qquad M_{H_2} = 2g/mol \tag{A.16}$$

Substituting these values into equation A.9, we obtain

$$D_{H_2/Air} = \frac{0.001858(293)^{3/2}(1/2 + 1/29)^{1/2}}{(1)(3,2925)^2(0.91)} = 0.69cm^2/s \tag{A.17}$$

A.3.2 Knudsen diffusion coefficient

A.3.2.1 Theory [23]

In Knudsen diffusion, the gas molecules will collide with the pore walls more frequently than with each other. Diffusion is reduced by the wall collisions. In this case, the free mean path length, λ is replaced by pore diameter, d_{pore} in equation A.4:

$$D_{KA} = \frac{d_{pore}}{3}u = \frac{d_{pore}}{3}\sqrt{\frac{8NkT}{\pi M_A}} \tag{A.18}$$

$$D_{KA} = \frac{d_{pore}}{3}\sqrt{\frac{8NkT}{\pi M_A}} \tag{A.19}$$

Applying the values of the constants, we find:

$$D_{KA} = 4850\, d_{pore}[cm]\sqrt{\frac{T}{M_A}} \tag{A.20}$$

Knudsen diffusion coefficient, D_{KA} is not a function of absolute pressure P and of the presence of species B in the binary gas mixture. It only depends on pore diameter, d_{pore}, temperature, T, and molecular weight, M_A.

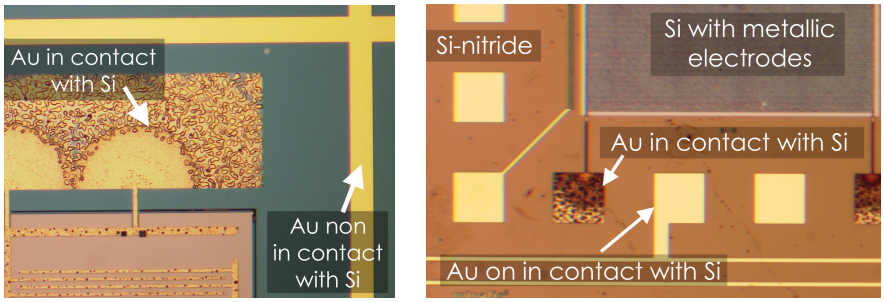
APPENDIX B

Metallisation

In section 3.2.2 (67), we mentioned that the nature of the metal in contact with the electrolyte did not significantly alter the behavior the MAE process. For cons, it has a large impact on the suppress by the RTA technique of the rectifying behavior of an MIS contact. The first experiments of silicon anodization of samples patterned by metallic electrodes were realized with a 150 nm-thick Au layer as an electrode. Gold is a common material in microfabrication wihich present an excellent electrical conductivity and an utter HF-resistance. Moreover, it is inert to the air, moisture and most of the corrosive agents, which makes it compatible with a wide range of sensing applications.

In the suite of the manufacturing process based sensors porous silicon, gold as the electrode material has been problematic. Indeed, the eutectic temperature of the system Au-Si is 370 °C [303] and 360 °C for the system Au-SiO_2 [304]. The contact between Au and Si and/or SiO_2 causes a reduction of the melting temperature. It is called *eutectic melting*. Figures B.1 shows the gold layer in contact with the SiO_2/Si after RTA process at 400°C and 470°C.

On figure B.1a., the metal pad appears to be aspirated on the silicon surface. This metal pad is on the silicon nitride mask and connected to the electrodes in direct contact with the silicon. A l'inverse, les parties mtalliques entirement isoles du silicium restent intacts. In the metal parts in contact with Si/SiO_2, a fast diffusion of Si/SiO_2 is expected along grain boundaries of the gold film on annealing below the eutectic temperature [293]. It is likely that diffusion takes place up to metal pads on top of the silicon nitride. It follows that the electrode and metal pads becomes a eutectic and their melting temperature is lowered to 360-370 °C. Above these temperatures, the formed eutectic melts. Because of the wide surface tension of the gold, the liquid film of Au-Si/SiO_2 contracts and form small clusters at the ends [304] [305].



a. b.

Figure B.1: Optical microscope images of the Au layer after RTA process (a.) at 470°C and (b.) at 400°C. The metal layer in contact with the silicon undergoes significant deteroration while the metal isolated of silicon remains intact.

However, annealing samples below the eutectic melting temperature of the system Au-Si/SiO_2 is not enough to destroy the rectifier behavior of MIS contact. Indeed, the diffusion of silicon through the silicon oxide to reach the metal (or vice versa) to form a silicide requires a RTA above 500°C (see Appendix I.1.6).

Finally, macroporous silicon functionalization requires a long annealing at 450 °C (see Chapter 4). Electrodes Au/Ti would not survive such a temperature.

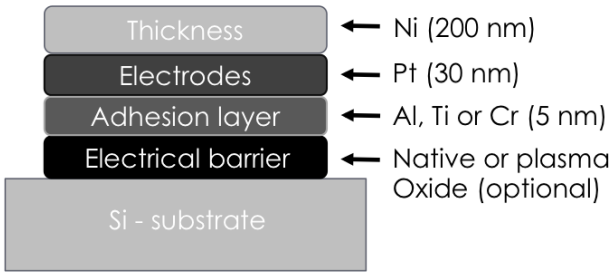


Figure B.2: Schematic representation of the electrode composed of a metal multilayer.

We opted for a metallic multilayer composed of a 5 nm thick adhesion layer (Al, Cr or Ti), a 30 nm thick Pt layer and a 200 nm thick Ni layer (figure B.2). This configuration is justified by:

- Al, Ti, and Cr are excellent adhesion layers on Si/SiO_2. However, they are weakly HF-resistant. In order to avoid a large contact with the HF-based electrolyte, their thickness should not be too large.
- The eutectic temperature of the system Pt-Si (980 °C) is well above the temperatures required for the formation of different platinum silicide (de 600 800°C) [306]and temperatures required for the metal diffuses through the oxide layer of the MIS contacts. Platinum silicide is the contact with the smallest potential barrier and therefore the lower resistivity.
- As cons the Pt is deposited by e-beam evaporation at high temperature (1492 °C at 10^{-6} Torr). Thick Pt layer would cause too much excessive heating of the standard resin used for lift-off process. We limit the thickness of the Pt layer to 30 nm.
- In sensing applications, the electrical current must be uniformly distributed in all IDE. For this, the linear resistance of metal electrodes must be extremely low. This linear resistance is inversely proportional to the metal paths thickness. We use a 200 nm thick Ni layer to thicken metal paths and reduce their linear resistance. The temperature of deposition of Ni is relatively lower than Pt (1072 °C at 10^{-6} Torr). Ni is a good HF-resistant.

APPENDIX C

Equivalent circuit of the microsensor

The macropSi-based microsensor is composed of two metal electrodes in contact with the p-type silicon. Each metal/p-type silicon contact have a rectifier behavior (Schottky contact). Porous silicon can be assimilated to a resistor.

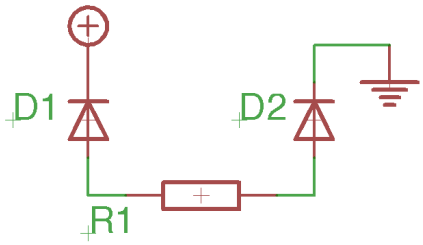


Figure C.1: Simplified equivalent circuit of the sensor. The diodes D1 and D2 schematize the metal/semiconductor contacts. Resistor R1 shows schematically the porous silicon layer.

Figure C.1 gives a simplified equivalent circuit of the sensor. The diodes D1 and D2 schematize the metal/semiconductor contacts. Resistor R1 shows schematically the porous silicon layer. The variation of the value of R1 which is the useful signal, since it will vary in the presence of analyte. The diodes D1 and D2 are in head to tail. When one is in the passing state, the other is in the blocking state.

Simulations of the simplified equivalent circuit were performed using Comsol Multiphysics© (COMSOL AB, Sweden) and its module "Electrical Circuit" to better understand the electrical behavior of the microsensor. The simulations are compared with the electrical measurements performed on microsensors.

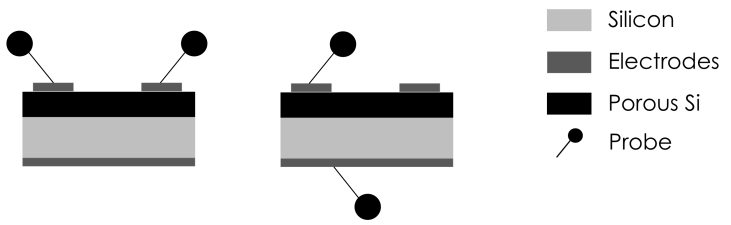


Figure C.2: Schema of (a.) an inter-electrodes measurement and (b.) a transverse measurement.

Two types of measurements and simulations were performed: an inter-measurement electrodes where the probes are placed on each of the electrodes of IDE (figure C.2a.) and a transverse measurement where a probe is placed on an electrode of IDE and the other on the backside of the wafer (figure C.2b.).

In a first step, the IV characteristic was measured between a metal electrode on the front and the aluminum electrode on the backside of the silicon wafer (figure C.3). This allows to isolate the rectifier behavior of a single electrode as the back contact has an ohmic behavior. The characteristic has a typical appearance of diode behavior. For positive potentials, the diode becomes conductive exponentially. For a negative electrical potential, the current is limited to the leakage current. The diode is not ideal, this leakage current increases with the electric potential. The IV characteristics were measured on porous and non-porous samples. The behavior is similar except that for the porous samples, the current increases less rapidly with the electric potential.

The equivalent circuit of this measurement is composed of a diode (D) in series with a resistor (R1) (figure C.3). The simulation parameters of the diode are shown in Table C.1. The difference in behavior between porous and non-porous samples can be simulated by a difference in resistance value R1 from 100 Ω for the nonporous sample to 1000 Ω for the porous sample.

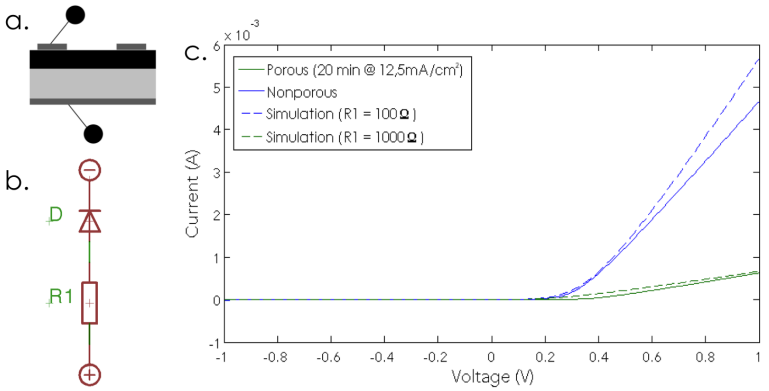


Figure C.3: (a.) Schematic view of the position of the probes on the sample. (b.) The equivalent circuit measurement. (c.) Results of the IV characteristic measurement (solid line) and the simulation of the equivalent circuit (dotted line).

In a second step, the IV characteristic was measured between two metal electrodes that form the IDE on the front side (figure C.4). The values of electric current is low and has two different slopes. Modeling of the equivalent system is shown in the same figure. This time the value of R1 is significantly higher for the samples nonporous. We have no explanation for this strange phenomenon. The simulations were performed with the parameters listed in Table diode C.1. Simulations show that the measured current is equal to the leakage current of each diode in blocking state.

The current is then limited by the leakage current of the diode in the blocking state. Indeed, when the diode D1 is conducting, the diode D2 is blocking and vice versa. Although the variation of R1 (and thus of the porous silicon) remains theoretically measurable, the magnitude of current flowing through the porous layer can be made very small by the problem of leakage current of contacts. A very low current requires special expensive equipment to be measured. To remedy this problem, the rectifier contact behavior must necessarily be reduced or removed. We do this by a high temperature annealing (see section I.1.6 on page 291).

Parameters	Values
Reverse breakdown voltage	1 V
Current at breakdown voltage	$1e^{-5}$ A
Corner for high-current roll-off	inf
Saturation current	$1e^{-10}$ A
Reverse saturation current	$1e^{-6}$ A
Grading coefficient	0.5
Ideality factor	1
Breakdown ideality factor	1
Reverse ideality factor	2
Series resistance	1 Ω
Parameter measurement temperature	293.15 K
Junction potential	1 V

Table C.1: Values of the parameters of the diode to simulate the equivalent circuit.

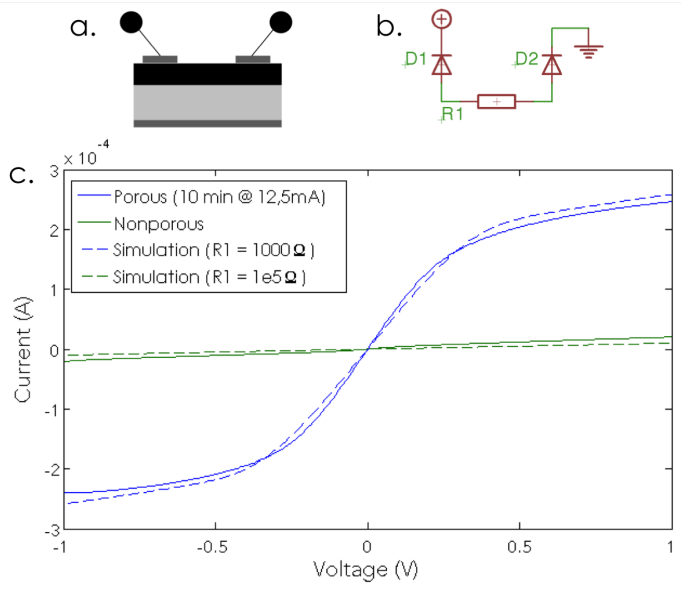


Figure C.4: (a.) Schematic view of the position of the probes on the sample. (b.) The equivalent circuit measurement. (c.) Results of the IV characteristic measurement (solid line) and the simulation of the equivalent circuit (dotted line).

APPENDIX D

Corrosion kinetics

D.1 Electrochemical corrosion [307]

Electrochemical corrosion is a reaction between a material, usually a metal, and its environment, which causes degradation of the material and its properties. Also called wet corrosion, it occurs when there is heterogeneity either in the metal or metal alloy or in the middle. There forming a voltaic cell with passage of a current. The system consists of two parts:

- Anode = the electrode where oxidation reaction(s) occurred, in which current flows from the metal to the solution.
- Cathode = the electrode where reduction reaction(s) occurs, in which the current flows from the metal to the solution.

The electrochemical reactions are redox reactions with electron transfer. Any redox reaction consists of two half-reactions:

- Oxidation reaction : $Red \longrightarrow Ox + ne^-$, anodic reaction with electrons loss,
- Reduction reaction : $Ox + ne^- \longrightarrow Red$, cathode reaction with electrons gain.

Both reactions occur simultaneously so that the total electric current (the current measured outside of the cell) is in appearance zero: it is nevertheless real. It is named *exchange current density* (i_0).

When an n-valent metal is immersed in a conductive medium, the M^{n+} ions pass into the solution while the negative charges appear in the metal.

$$M \rightleftarrows M^{z+} + ze^- \tag{D.1}$$

The passage of M^{n+} ions is limited in time as to leave the metal, ions must overcome the repulsion of ions that are already in the solution and the attraction of excess electrons which charge the metal negatively. The equilibrium is established and the metal reaction D.1 is reversible

as the rate of forward reaction is equal to the rate of reversible reaction. Macroscopically, the metal is not corroded. *Equilibrium potential* (E_{eq}) is the potential that takes a given metal (or a given alloy) over a given electrolyte. It is dependent on the experimental conditions and can be measured relative to a reference electrode.

D.2 Polarization diagram and Tafel plot

Polarization diagram are obtained by continuously varying the potential applied to the working electrode and recording for each potential value, the value of the corresponding current density (potentiostatic method) (figure D.1). The potential sweep speed must be slow enough to ensure the reversibility of the reactions. The shape of the curves information on the different electrochemical reactions involved for given potentials.

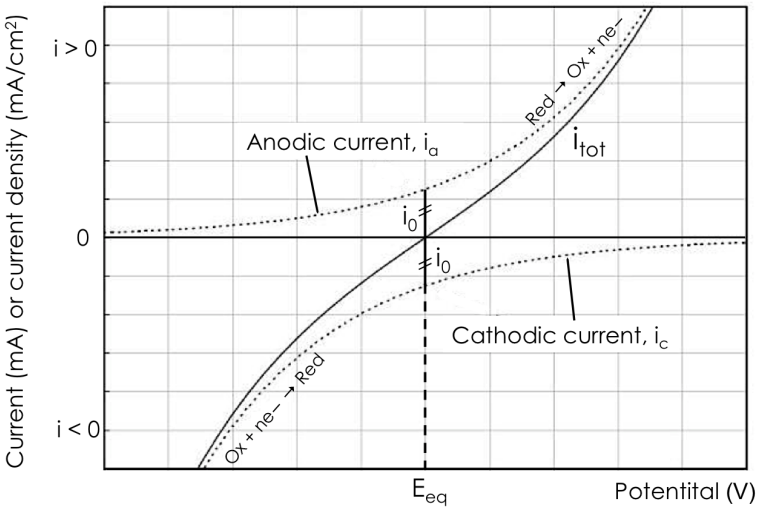


Figure D.1: Polarization diagram are obtained by continuously varying the potential applied to the working electrode and recording for each potential value, the value of the corresponding current density. The curve obtained experimentally is an addition of the anodic curve and the cathodic curve (dotted lines). Inspired from reference [163]

The curve passes through zero current between cathodic domain (on the left) and anodic domain (on the right). In the cathodic domain, the metal deposition (cathodic reaction) is widely favored over the metal dissolution (anodic reaction). The system requires an external supply of electrons because the metal dissolution is not sufficient to supply the electrons. In the anodic domain, the metal dissolution is greatly favored over the metal deposition. This time, the metal dissolution provides a substantial excess of electrons relative to those consumed by the metal deposition. The system needs getting rid of excess electrons on the outside to keep his balance. Measurement of i_{tot} therefore represents the difference between the anodic current (i_a) and the cathodic current (i_c) which are represented in dashed lines in figure D.1. The polarization curve reaches $i_{tot} = 0$ at the equilibrium potential, E_{eq}. At this point, the electrons released by the metal dissolution reaction are fully consumed by the metal deposition reaction. The cathodic current is equal to the anodic current (except for the sign) ($i_c = i_a = i_0$). i_0 is the exchange current between the anodic reaction and cathodic reaction when the system is isolated.

To determine experimentally i_0, logarithmic presentation of the current density is generally preferable. The Tafel plot is another graphic representation of D.1 [308]. The logarithm of the absolute value of current ($log(|i_{tot}|)$ is on the y-axis and the electrode potential (E) is on the x axis (Rem: it is common to see the x-axis and y-axis reversed) (figure D.2).

The corrosion current (i_0) is determined graphically from the Tafel plot. The tangents of the cathodic and anodic branches are plotted and are called *Tafel lines*. Tangent points are taken far from E_{eq} to avoid the effect of the anode current in the cathodic branch and vice versa. The intersection of two Tafel lines gives the value of $log(i_0)$ [308].

D.3 Galvanic corrosion [307, 309]

Galvanic corrosion is the preferential attack of the less noble phase of a alloy comprising two phases (mixed electrode) or corrosion that may exist between two metallic materials placed in the same environment. Galvanic corrosion also occurs when a metal piece is in contact with a

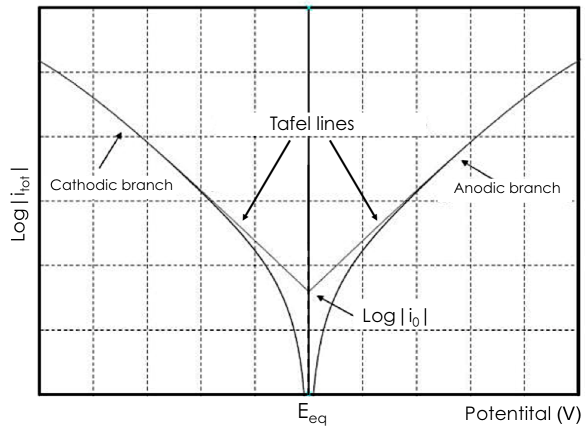


Figure D.2: Tafel plot is the graph of $\log(|i_{tot}|)$ vs. E. Inspired from reference [163]

heterogeneous environment (e.g. inhomogeneous concentration). There is formation of a galvanic cell. The less noble part is the anode and the cathode is the noblest. The ratio of anode/cathode surface area plays a very important role. More the anode is small, the more the dissolution rate is high.

For example, in deaerated acid solution, the anodic reaction remains the metal dissolution while the cathodic reaction is the hydrogen evolution:

- Anodic reaction : $M \rightarrow M^{n+} + ne^-$
- Cathodic reaction : $2H^+ + 2e^- \rightarrow H_2$

The electron exchange occurs between the two reactions and form the corrosion current (i_{corr}). The electrons released by the metal dissolution are consumed by hydrogen evolution. The metal is etched while the hydrogen is formed. The reaction continues to occur as one of the reactants is not fully consumed.

Figure D.3 show the polarization diagram of the two components (M and Red) of the galvanic cell measured separately. If $E_{eq,M} < E_{eq,Red}$, component X is the anode and the cathode is the component Y.

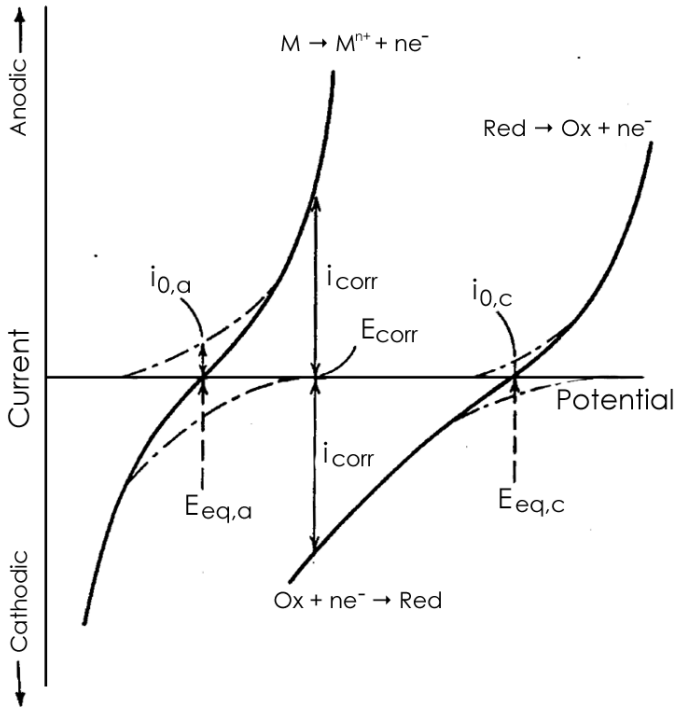


Figure D.3: Polarization diagrams of a metal dissolution/deposition and a accompanying redox showing how the two reactions couple together at corrosion potential (E_{corr}).

As in the case of a simple electrode, the corrosion current (i_{corr}) is determined graphically from the combination the Tafel curves for each component of the galvanic cell (figure D.4). This combination is called *Evans diagram.*

At the intersection of the two Tafel curves :

- the anodic and cathodic currents are equal in absolute value, the current value obtained gives the galvanic coupling current or galvanic corrosion current ($i_{a,M} = i_{c,Red} = i_{corr}$).
- the two composants are a common potential, called potential galvanic coupling or galvanic corrosion potential (E_{corr}).

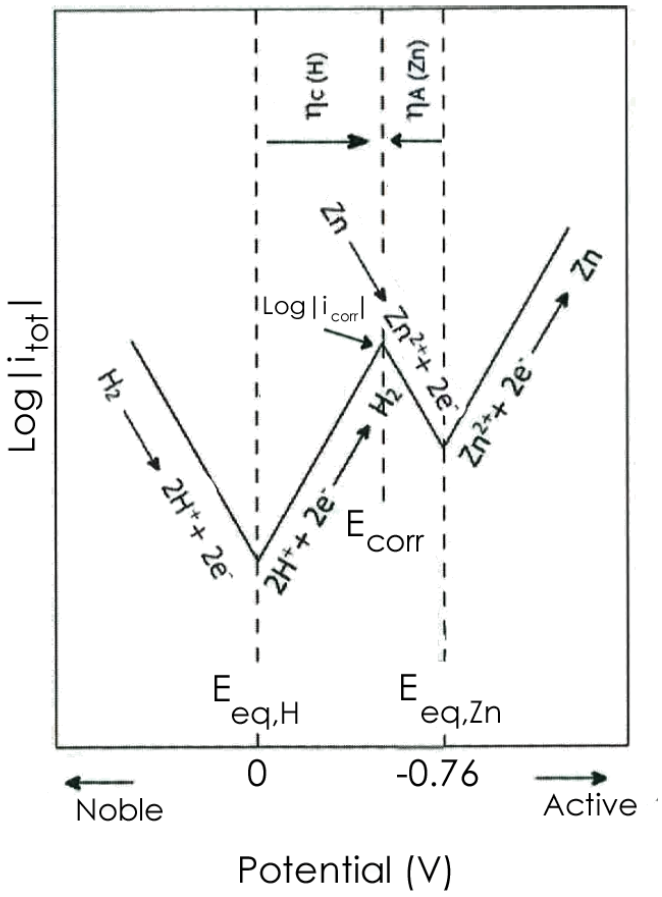
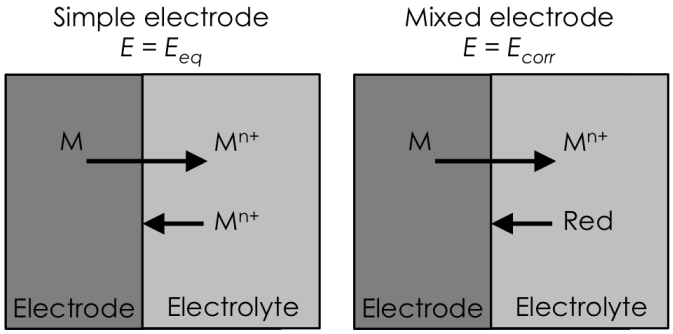


Figure D.4: Evans diagram of zinc placed in acidic solution. Reproduced and modified from reference [307].

Both of half cell reactions change the potential to an intermediate value E_{corr}. E_{corr} is a mixed potential between the anodic equilibrium potential $E_{eq,M}$ and the cathodic equilibrium potential $E_{eq,Red}$ ($E_{eq,M} < E_{corr} < E_{eq,Red}$) (figure D.5). E_{corr} takes its value where the anodic current is equal to the cathodic current (opposite in sign) ($i_c = i_a = i_{corr}$). No electrons are injected or absorbed from the outside of the system. The system is in equilibrium and in the same condition as when it was isolated from the outside or in open circuit state. The elec-



a. b.

Figure D.5: Metal electrode in contact with its ions (simple electrode) and in contact with any corrosive solution (mixed electrode). In the case of a simple electrode, an equilibrium potential (E_{eq}) is formed between the electrode and the solution. In the case of a mixed electrode, a corrosion potential (E_{corr}) is formed between the electrode and the solution. The corrosion potential is a mixed between of equilibrium potential of all anodic and cathodic reactions involved in the corrosion.

trical potential at the system terminals is open circuit potential. i_{corr} is the current flowing from the anode to the cathode in the system at equilibrium. At the corrosion potential, E_{corr}, rate of cathodic reaction (e.g. hydrogen evolution) is equal to rate of anodic reaction (e.g. metal corrosion) and the mass of the corroded metal dissolved in the electrolyte can be determined by applying the Faraday law to i_{corr}. The higher i_{corr}, the greater the rate of corrosion is high.

A corroding electrode constitutes a poly-electrode because a minimum of two electrode reactions, oxidation and reduction, occur simultaneously. Individual electrode parameters, such as current and individual electrode potentials, may be measured as a function of change in the external resistance. It is, however, impossible to measure the two parameters on the tiny anodic and cathodic areas of corroding metal. The difficulty in the measurement of individual current and potential is resolved by Evans diagram. By measuring Tafel plots of the various components of the redox reaction taken separately, the mixed potential and the corrosion current may be determined graphically by combining the two plots.

For example, consider a base metal, such as zinc, placed in acidic solution; the metal will dissolve at the same rate as hydrogen is evolved and the two reactions mutually polarize each other. This is shown in a very simple form by Evans diagram (figure D.4). A negligible resistance is assumed between the anode and cathode. Consider zinc corroding in dilute HCl. The following two reactions occur:

$$Zn \rightleftarrows Zn^{2+} + 2e^- \quad \text{(oxidation)} \tag{D.2}$$

$$2H^+ + 2e^- \rightleftarrows H_2 \quad \text{(reduction)} \tag{D.3}$$

$$E_{eq,Zn} = -0.76\ V_{(SHE)} \tag{D.4}$$

The Evans diagram shows four possible reactions:

For zinc :

$$Zn \longrightarrow Zn^{2+} + 2e^- \quad \text{(zinc oxidation)} \tag{D.5}$$

$$Zn^{2+} + 2e^- \longrightarrow Zn \quad \text{(zinc reduction)} \tag{D.6}$$

For hydrogen :

$$H_2 \longrightarrow 2Zn^+ + 2e^- \quad \text{(hydrogen oxidation)} \tag{D.7}$$

$$2H^+ + 2e^- \longrightarrow H_2 \quad \text{(hydrogen reduction)} \tag{D.8}$$

Of the four above reactions, only reactions D.5 and D.8 occur. Reaction D.7 hydrogen oxidation, and reaction D.6 zinc reduction, can be ignored because zinc can only be reduced at potentials more negative than -0.76 V and it continues to generate electrons with time. Hydrogen evolution can be clearly observed and it does not oxidize. The curves corresponding to the above reactions converge at a point of intersection, E_{corr} which is the mixed potential of the system and is lower than equilibrium potential of zinc, $|E_{corr}| < |E_{eq,Zn}|$ = -0.76 V. The corresponding current at the current axis is i_{corr}.

In the cases of corrosion considered so far, the corrosion is limited only by the charge transfer between one anode and one cathode. In a more complex system composed of alloy or complex electrolyte, the cathode and the anode may vary according to the potential.

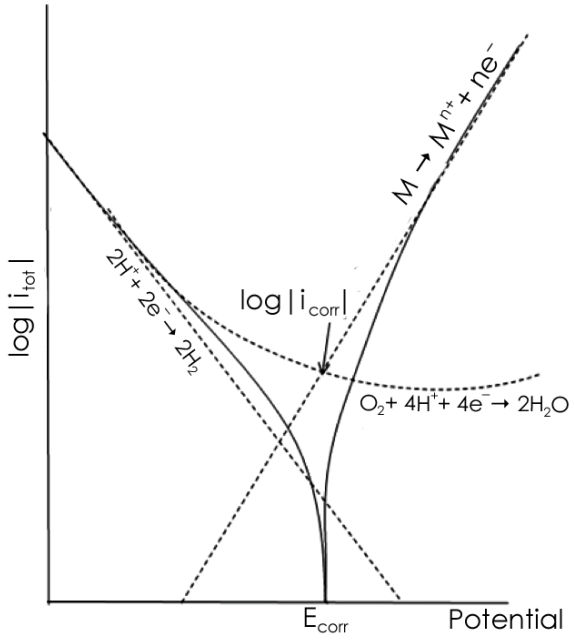


Figure D.6: Evans diagram for a complex electrolyte. Two cathodic reactions occur simultaneously. Reproduced from reference [309]

For example, a corrosion in an aerated acidic electrolyte is shown in figure D.6. Two oxidation reactions occur, but their rates depend on the corrosion potential. E_{corr} is a mixed potential between all anodic equilibrium potential and all cathodic equilibrium potential according to their importances in redox reactions. Total cathodic current corresponds to the sum of the currents for both hydrogen and oxygen reduction reactions and has to be balanced by the single anodic reaction current.

The presence of oxygen in the reaction has a direct impact on E_{corr} and i_{corr} changing respectively from -188 mV and 9.8×10^{-8} mA/cm^{-2} in a deoxygenated 5% HF solution to -158 mV and 7.55×10^{-7} mA/cm^{-2} in a oxygenated 5% HF solution [185].

D.4 Overpotential and polarization [163, 307]

The difference between the resultant potential (E_{corr}) and each individual reaction equilibrium potential (E_{eq}) is called polarization and quantified in terms of an overpotential (η) (figure D.4) as in equation [163]:

$$\eta_i = E - E_{eq,i} \tag{D.9}$$

where $i = a$ for anodic reaction and $i = c$ for cathodique reaction.

The polarization (η) is said to be either anodic, when the anodic processes on the electrode are accelerated by changing the specimen potential in the positive (noble) direction or cathodic when the cathodic processes are accelerated by moving the potential in the negative (active) direction. There are three distinct types of polarization (figure D.7) and these are additive, as expressed in equation [307]:

$$\eta_{tot} = \eta_{act} + \eta_{conc} + iR \tag{D.10}$$

where :

- η_{act} is the activation overpotential, a complex function describing the charge transfer kinetics of an electrochemical reaction (e.g. adsorption). Activation polarization is usually the controlling factor during corrosion in electrolyte concentrated in oxidizing agents (e. g. in a strong acid).

- η_{conc} is the concentration overpotential, a function describing the mass transport limitations associated with electrochemical processes. Concentration polarization usually predominates when the concentration of the active species is low; for example, in dilute acids or in aerated waters where the active component, dissolved oxygen, is only present at very low levels.

- iR is the ohmic drop. This function takes into account the resistivity of electrical path between the anodic and cathodic elements of a corrosion reaction when they are separated while still electrically coupled. The ohmic drop will become an extremely important factor when studying corrosion phenomena for which there is a clear separation of the anodic and cathodic corrosion sites.

Knowing the kind of polarization which is occurring can be very helpful, since it allows an assessment of the determining characteristics

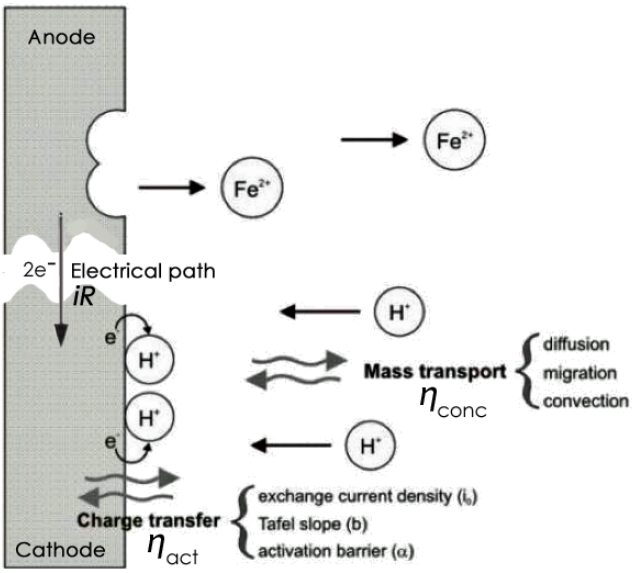


Figure D.7: Graphical representation of the processes occurring at an electrochemical interface. Inspired from reference [163, 309]

of a corroding system. For example, if corrosion is controlled by concentration polarization, then any change that increases the diffusion rate of the active species (e.g. oxygen) will also increase the corrosion rate. In such a system, it would therefore be expected that agitating the liquid or stirring it would tend to increase the corrosion rate of the metal. However, if a corrosion reaction is activation controlled then stirring or agitation will have no effect on the corrosion rate.

D.4.1 Activation Polarization [307, 309]

The term activation polarization makes reference to retarding factors that are an inherent part of the kinetics of all electrochemical reactions. For example, consider the evolution of hydrogen gas :

$$2H^+ + 2e^- \rightarrow H_2 \tag{D.11}$$

The reaction proceeds at a metal surface in three major steps. In the first step H^+ reacts with an electron from the metal to form an

Metal	**log(i_0)** (mA/cm^2)
Pb, Hg	-10
Zn	-11
Sn, Al, Be	-7
Ni, Ag, Cu, Cd	-4
Fe, Au, Mo	-3
W, Co, Ta	-2
Pd, Rh	-1
Pt	0

Table D.1: Approximate exchange current density (i_0) for the hydrogen oxidation reaction on different metals at 25 °C [163].

adsorbed hydrogen atom at the surface.

$$H^+ + e^- \rightarrow H_{ads} \tag{D.12}$$

In the second steps the reaction of two adsorbed hydrogen atoms forms a hydrogen molecule.

$$H_{ads} + H_{ads} \rightarrow H_{2,ads} \tag{D.13}$$

In the third step enough adsorbed hydrogen molecules combine and nucleate a hydrogen bubble on the surface. Any of these steps can be the rate limiting step and therefore cause the activation polarization. In fact, there is a wide variability in this transfer rate of electrons by various metals and, as a result, the rate of hydrogen evolution from different metal surfaces can vary greatly. Exchange current densities (i_0) reflect intrinsic rates of electron transfer between an analyte and the electrode. It is surely the single most important variable that explains the large differences in the rate of hydrogen on metallic surfaces. Table D.1 contains the approximate exchange current density for the reduction of hydrogen ions on a range of materials.

Note that the value for the exchange current density of hydrogen evolution on platinum is approximately 10^{-2} A/cm^2 whereas on mercury and lead it is 10^{-13} A/cm^2, eleven orders of magnitude for the rate of this particular reaction, or one hundred billion times easier on platinum than on mercury or lead.

The exchange current density for hydrogen reduction on silicon surface is in the range of 10^{-3} - 10^{-8} mA/cm^2 depending on the specific conditions of the silicon/electrolyte system [310]. Bertagna et *al.* [185] have shown that the type and amount of dopant in the silicon and the illumination of the electrolyte are important. For p-type Si (11 - 25 Ωcm), the exchange current for proton reduction at the equilibrium potential in 5% HF solution is 3×10^{-7} mA/cm^2 in dark and 3×10^{-3} mA/cm^2 under illumination (1400 lx, visible light). Pour un wafer moins rsistif (p-type Si, 1.85 - 3.6 Ωcm), the exchange current for proton reduction at the equilibrium potential in 5% HF solution is 2.8×10^{-8} mA/cm^2 in dark and 8×10^{-3} mA/cm^2 under illumination.

D.4.2 Concentration Polarization [163, 307, 309]

Up to now, the concentrations at the interface were considered similar to those in the middle of the solution. In practice, a slow diffusion of species in the electrolyte may limit the i_{corr}. Also, in the case of oxidation, the reaction products may form an insulating layer (for example the passivation) to the electrode and limit i_{corr}. In this case, the cathodic and anodic branches may pass through different regimes.

Concentration polarization is the polarization component that is caused by concentration changes in the environment adjacent to the surface as illustrated in the figure D.8. When a chemical species participating in a corrosion process is in short supply, the mass transport of that species to the corroding surface can become rate controlling. A frequent case of concentration polarization occurs when the cathodic processes depend on the reduction of dissolved oxygen since it is usually in low concentration.

Mass transport to a surface is governed by three forces : diffusion, migration and convection. In the absence of an electrical field, the migration term, that only affects charged ionic species, is negligible while the convection force disappears in stagnant conditions. Mass transport greatly depends on the temperature and the agitation of the electrolyte.

D.4.3 Ohmic Polarization [163, 307]

The ohmic overpotential appears as the simple product of a resistance and a current between the anodic and cathodic sites of a corrosion pro-

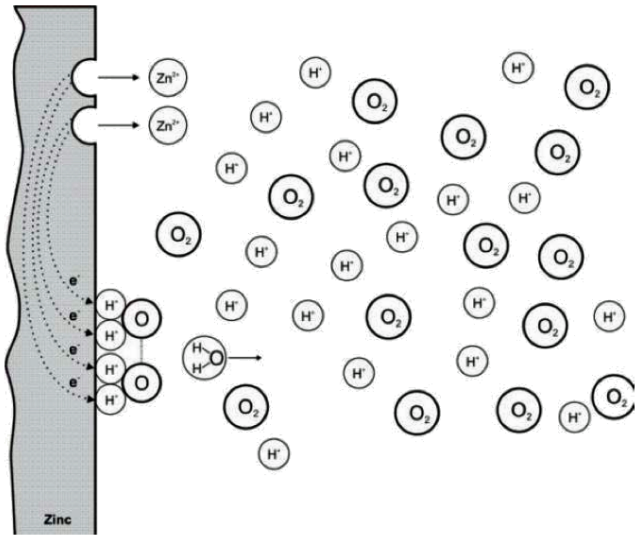


Figure D.8: Concentration changes in the vicinity of an electrode causing a concentration polarization effect. Reproduced from reference [163]

cess. For many corrosion situations these sites are adjacent to each other and the ohmic drop is negligible. However, there are special conditions where the separation of the anodic and cathodic sites can be an important factor in the corrosion progress (e.g. in galvanic corrosion). Corrosion is limited by the resistivity (or by the electrical behavior) of the electrons path between the anode and the cathode.

APPENDIX E

Redox potential

Reactions	**E^0 (volts)**
$F_2(g) + 2\ e^- \rightleftharpoons 2\ F^-$	2.890
$F_2O\ (g) + 2\ H^+ + 4\ e^- \rightleftharpoons 2\ F^- + H_2O$	2.168
$Au^+ + 1\ e^- \rightleftharpoons Au(s)$	1.69
$O_{2(g)} + 4\ H^+ + 4\ e^- \rightleftharpoons 2\ H_2O$	1.23
$Pt^{2+} + 2\ e^- \rightleftharpoons Pt(s)$	1.18
$PtO_2\ (s) + 4\ H^+ + 4\ e^- \rightleftharpoons Pt(s) + 2\ H_2O$	0.92
$Pd^{2+} + 2\ e^- \rightleftharpoons Pd(s)$	0.915
$Ag^+ + 1\ e^- \rightleftharpoons Ag(s)$	0.799
$PdO\ (s) + 2\ H^+ + 2\ e^- \rightleftharpoons Pd(s) + H_2O$	0.79
$Cu^+ + 1\ e^- \rightleftharpoons Cu(s)$	0.518
$Cu^{2+} + 2\ e^- \rightleftharpoons Cu(s)$	0.339
$CoOH^+ + H^+ + 2\ e^- \rightleftharpoons Co(s) + H_2O$	0.003
$2\ H^+ + 2\ e^- \rightleftharpoons H_2(g)$	0.000
$HCOOH_{(aq)} + 2\ H^+ + 2\ e^- \rightleftharpoons HCHO_{(aq)} + H_2O$	-0.03
$Sn^{2+} + 2\ e^- \rightleftharpoons Sn(s)$	-0.141
$Ni^{2+} + 2\ e^- \rightleftharpoons Ni(s)$	-0.236
$SnF_6^{2-} + 4\ e^- \rightleftharpoons Sn(s) + 6\ F^-$	-0.25
$Co^{2+} + 2\ e^- \rightleftharpoons Co(s)$	-0.282
$Cr^{3+} + 3\ e^- \rightleftharpoons Cr(s)$	-0.74
$2\ H_2O + 2\ e^- \rightleftharpoons H_2(g) + OH^-$	-0.828
$Cr^{2+} + 2\ e^- \rightleftharpoons Cr(s)$	-0.89
$\mathbf{SiO_2\ (s) + 4\ H^+ + 4\ e^- \rightleftharpoons Si(s) + 2\ H_20}$	**-0.99**
$TiO_2(s) + 4\ H^+ + 4\ e^- \rightleftharpoons Ti(s) + 2\ H_2O$	-1.076
$TiF_6^{2-} + 4\ e^- \rightleftharpoons Ti(s) + 6\ F^-$	-1.191
$\mathbf{SiF_6^{2-} + 4\ e^- \rightleftharpoons Si(s)} + 6\ F^-$	**-1.24**
$Ti^{2+} + 2\ e^- \rightleftharpoons Ti(s)$	-1.60
$Al^{3+} + 3\ e^- \rightleftharpoons Al(s)$	-1.677
$AlF_6^{3-} + 3\ e^- \rightleftharpoons Al(s) + 6\ F^-$	-2.069

Table E.1: Redox potential of the possible reactions in the electrolyte in contact with metals commonly used in microfabrication.

APPENDIX F

Finite element simulations

F.1 Simulation of the electrode spacing impact on penetration depth of the electric current lines.

The simulation was performed by Electric currents module of finite element software COMSOL Multiphysics© (COMSOL AB, Stockholm, Sweden).

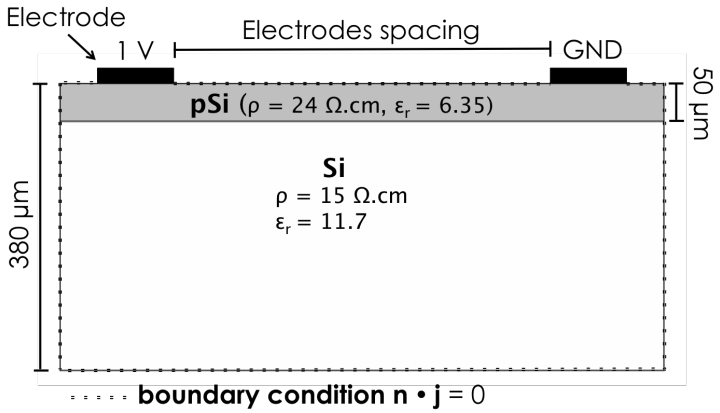
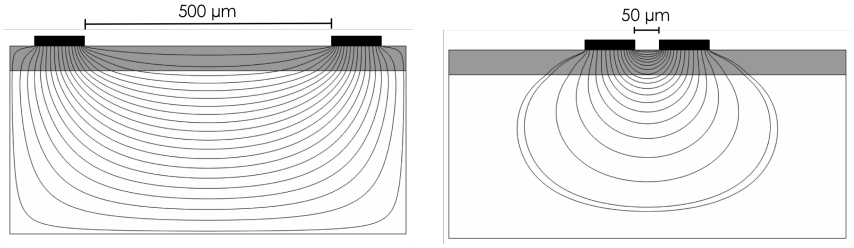


Figure F.1: Geometry used to perform the simulation of the electric current lines distribution in the sample. The gray area represents the porous layer.

Figure F.1 the model of a 2D cross-section of 380 μm-thick wafer with a 50 μm-thick porous layer and two metal electrodes placed on the porous silicon. Electrodes are placed on the porous layer and a difference of electric potential of 1 V is applied thereto. The spacing between the electrodes is a variable of the simulation and takes following values : 50 and 500 μm for the first simulation, 10, 30, 60, 100, 150 μm for the second, 10, 30, 60, 100, 150, 250, 500 μm for the last. The resistivity and the relative permittivity of the bulk silicon are respectively 15 Ω.cm and 11.7 . The resistivity of the porous layer is much larger than that

of bulk silicon, which promotes the flow of current in the bulk silicon. Depending morphology of macroporous layer, its resistivity exceeds the resistivity of the initial silicon by 1.6-15 times [311]. We adopted as the simplified hypothesis that the resistivity of the porous layer is 1.6 times that of bulk silicon. The second hypothesis is to apply an average relative permittivity of 6.35 to the porous layer which is constituted of 50% air ($\varepsilon_r = 1$) and 50% silicon ($\varepsilon_r = 11.7$).



a. b.

Figure F.2: Distribution of the electric current lines for electrodes spacing of (a.) 500 μm et (b.) 50 μm.

Figures F.2 show the distribution of electric current in the sample for 2 electrodes distances (500 μm and 50 μm). The distance of 500 μm is chosen to simulate the smallest inter-electrodes distance shown in the literature (see state-of-the-art, table 2.1 on page 55). In this case, a large amount of electric current are distributed in the bulk silicon. This part is not used because it does not participate in the sensing application. In the case of a small electrodes spacing, the electric current is more concentrated in the porous layer.

The graph in figure F.3 shows the evolution of the electric current intensity as a function of depth in the substrate for different electrode spacings (10, 30, 60, 100 and 150 μm). Values were taken on the vertical dashed line in figure F.1.

Figure F.4 shows the evolution of the percentage of the electric current intensity concentrated in the porous layer to the total electric current intensity for different electrode spacing (10, 30, 60, 100, 150, 250, 500 μm). This percentage varies from 37 % for a electrodes spacing of 10 μm and 20 % for a electrodes spacing of 500 μm. The calculation

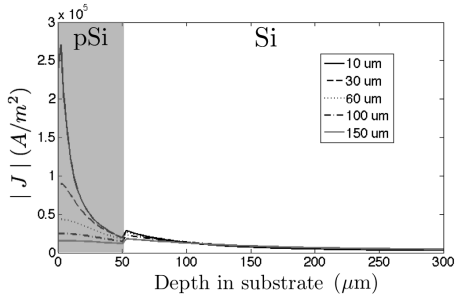


Figure F.3: Electric current intensity in a function of depth into the substrate to different electrode spacing. Values were taken on the vertical dashed line in figure F.1.

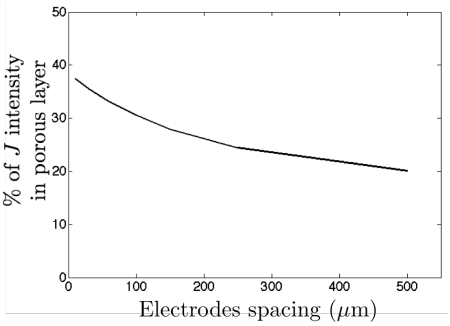


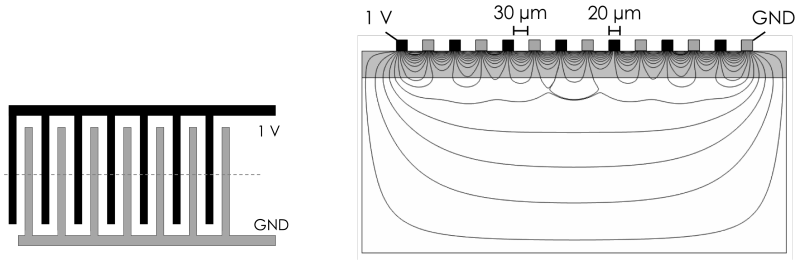
Figure F.4: Evolution of the percentage of the electric current intensity concentrated in the 50 μm-thick porous layer depending on the electrode spacing. The calculation was performed by calculating the integral of the electric current intensity into the porous layer on the integral of the electric current intensity across the substrate.

was performed by calculating the integral of the electric current intensity into the porous layer on the integral of the electric current intensity across the substrate.

When the electrodes are spaced by a distance equal to or greater than the porous layer thickness, more than two thirds of the electric current intensity is located in the bulk silicon and does not participate in the measurement of physico-chemical reactions happening in the porous layer. It is therefore more interesting to reduce the electrodes spacing

to concentrate the electric current lines in the porous layer and to probe mainly the porous layer. The sensitivity of the measurement increases.

The width of the electrodes also affects the distribution of electric current lines. Indeed, wide electrodes will act as spaced electrodes. The main part of the electric current will be located in the bulk silicon. Only by using very fine closely spaced electrodes, the probed volume of the porous silicon is limited. We use interdigitated electrodes (IDE, figure F.5) with small width to repeat many times this small volume and thus probe the porous silicon over a large area without increasing the penetration depth of the electric current lines. Thus, the measurement is mostly concentrated in the porous layer.



a. b.

Figure F.5: (a.) Schematic image of top view of the interdigitated electrodes with a potential difference of 1 V (b.) Distribution of the electric current lines between IDE of 20 μm wide and spaced from 30 μm.

Figure F.5a. shows a schematic top view of interdigitated electrodes. This form allows for probing a large area with narrow electrodes. One of the electrodes is set at a potential (here 1V) while the other is grounded. Figure F.5b. shows the distribution of the electric current lines in the substrate. These are mainly concentrated in the porous layer through the IDE, 63% of the electric current intensity is located in the porous layer.

F.2 Simulation of the distribution of hole concentration and the hole curent density in Si crystallites

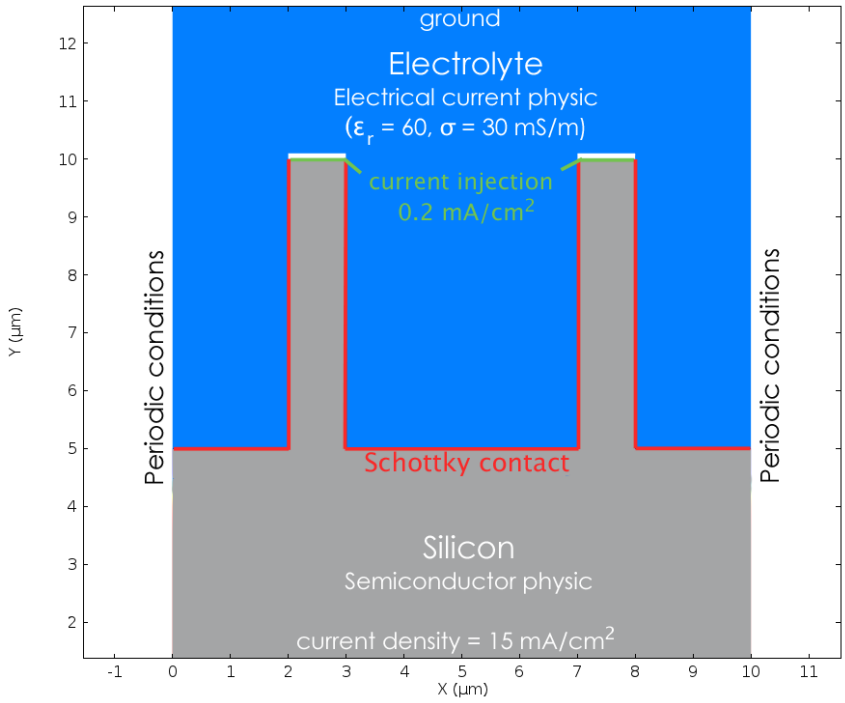


Figure F.6: Simulation geometry and volume and boundaries conditions.

To achieve this simulation, we used a coupling between the semiconductor module (for silicon) and the electric current module (for the electrolyte) of COMSOL Multiphysics©. Figure F.6 shows the geometry of the simulation and the main parameters. A current injection of 0.2 mA/cm^2 is used under the electrodes (green boundary) to simulate the corrosion current arising from the reduction reaction at the metal / electrolyte interface. Silicon / electrolyte interface is set as a Schottky contact (red border). The parameter values used in the simulations are shown in the table F.1.

Notations	**Values**
n_i	1.46×10^{10} cm^{-3} (T = 300K)
N	4e14 at./cm^3
ϵ_r (Si)	11.7
ϵ_r (Electrolyte)	60
σ (Electrolyte)	30 mS/m
μ_n	1450 cm^2/Vs
μ_p	500 cm^2/Vs
χ	4.05 V
τ_n	0.1μs
τ_p	0.1μs
Barrier height (Si/electrolyte)	0.67 V

Table F.1: Materials properties used in the model.

F.3 Simulation of the hole current density and the hole concentration under the mask

(based on model provided by Erik Danielsson, Royal Institute of Technology, Stockholm (Model ID: 114 on www.comsol.com).

For this simulation, the electrolyte is considered as a metal. Two different physical were coupled: Electrostatic physics is applied to three domains (eletrolyte, mask and silicon, variable : Ψ); The physics of the charge transport by diffusion and migration in an electric field is applied only to silicon domain (variables: n and p). Figure F.7 shows simulation geometry and its volume and boundaries conditions.

This simulation is based on the three basic semiconductor equations :

$$-\nabla \cdot (\epsilon \nabla \Psi) = q(N + p - n) \tag{F.1}$$

$$-\nabla \cdot \overrightarrow{J_n} = -qR_{SRH} \tag{F.2}$$

$$-\nabla \cdot \overrightarrow{J_p} = qR_{SRH} \tag{F.3}$$

where Ψ indicates electrostatic potential, q equals the elementary charge, p and n are the hole and electron concentrations, respectively and N represents the fixed charge associated with doping.

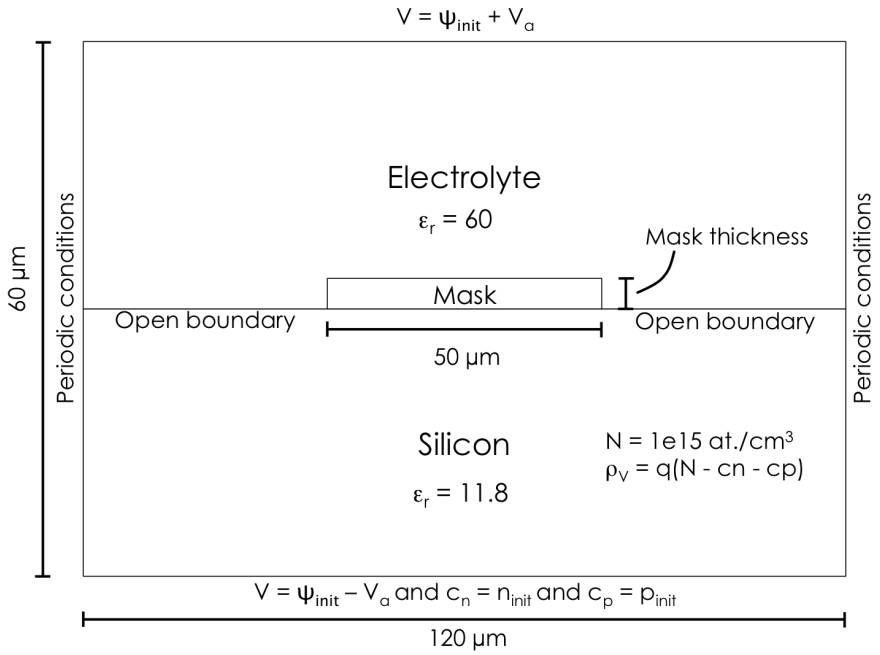


Figure F.7: Simulation geometry and volume and boundaries conditions.

The electron and hole current densities, $\overrightarrow{J_n}$ and $\overrightarrow{J_p}$ can be expressed in terms of Ψ, n and p :

$$\overrightarrow{J_n} = -qn\mu_n\nabla\Psi + qD_n\nabla n \tag{F.4}$$

$$\overrightarrow{J_p} = -qp\mu_p\nabla\Psi - qD_p\nabla p \tag{F.5}$$

where μ_n and μ_p are the carrier mobilities, and D_n and D_p are the carrier diffusivities.

The term R_{SRH} represents the *Shockley-Read-Hall recombination*, which is a general recombination process using traps in the forbidden band gap of the semiconductor.

$$R_{SRH} = \frac{np - n_i^2}{\tau_p(n + n_1) + \tau_n(p + p_1)} \tag{F.6}$$

Here n_i is the intrinsic carrier concentration, τ_n and τ_p are the carrier lifetimes, and n_1 and p_1 are parameters related to the trap energy level.

If the trap level is located at the middle of the band gap (which the model assumes), then n_1 and p_1 equal n_i.

Boundary conditions of silicon

The boundaries of the right and left are far from the area under the action of the mask. We apply periodic conditions (the electric field and carrier currents have zero normal component).

At boundaries in contact with a metal and electrolyte (considered as metal), the electrostatic potential is fixed. If you assume infinite recombination velocity at the contact, the mass action law is valid:

$$n_i^2 = np \tag{F.7}$$

It is now possible to calculate the carrier concentrations using this law along with the dopant concentration N and the assumption that there is no charge at the contact. The applied voltage equals the Fermi level in the semiconductor at the contact, so the electrostatic potential at the contact is the applied voltage plus the energy difference between the Fermi level and the reference level used for the electrostatic potential. The energy difference has a logarithmic dependence of the carrier concentrations.

The boundary conditions are

$$\Psi = Va + \frac{kT}{q} \ln \left(\frac{\frac{N}{2} + \sqrt{\left(\frac{N}{2}\right)^2 + n_i^2}}{n_i} \right) \tag{F.8}$$

$$n = \frac{N}{2} + \sqrt{\left(\frac{N}{2}\right)^2 + n_i^2} \tag{F.9}$$

$$n = -\frac{N}{2} + \sqrt{\left(\frac{N}{2}\right)^2 + n_i^2} \tag{F.10}$$

where V_a is the applied voltage.

Initial conditions

As the majority carriers are holes, $p = N$ and $n = \frac{n_i^2}{N}$ in the bulk silicon. At the boundaries with the contacts, the initial conditions are :

$$\psi_{init} = \frac{kT}{q} + \log \frac{n_{init}}{n_i} \tag{F.11}$$

$$p_{init} = \frac{N}{2} + \sqrt{\frac{N^2}{4} + n_i^2} \tag{F.12}$$

$$n_{init} = \frac{\frac{ni^2}{N}}{2} + \sqrt{\frac{N^2}{4} + n_i^2} \tag{F.13}$$

Materials properties

The parameter values used in the simulations are shown in the table F.2.

Notations	Values
n_i	1.46×10^{10} cm^{-3} (T = 300K)
N	1e15 at./cm^3
ϵ_r (Si)	11.8
ϵ_r (Electrolyte)	60
μ_n	800 cm^2/Vs
μ_p	200 cm^2/Vs
D_n	20.7 cm^2/s
D_p	5.17 cm^2/s
τ_n	0.1μs
τ_p	0.1μs
V_a	- 1 V

Table F.2: Materials properties used in the model.

F.4 Simulation of the impact of surface charge on the concentration of charge carriers in the pore walls

We conducted numerical simulations to characterize the impact of surface charge on the concentration of charge carriers in the pore walls. Numerical simulations were performed using the Atlas software (Silvaco, inc., USA) and Comsol.

F.5 Simulation of the response time of the measuring cell at H_2 diffusion

An important parameter of gas sensors performances is the response time. Indeed, higher it is, the faster the sensor detects a change in the concentration of the analyte. The measuring cell has too a response time, which is the time required for the analyte concentration is at the desired value (or a percentage thereof):

- If the response time of the cell is longer than the response time of the sensor, the sensor measurement is limited by the response time of the cell. The measure does not reflect the kinetics of the sensor but that of the cell.
- If the measured response time is (very) longer than the response time of the cell, the measurement reflects the response time of the sensor.

Know the response time of the cell is essential. The response time of the cell can be determined either experimentally or by either simulation. The latter method gives an approximation of the response time of the cell, but is easier to implement.

Geometry

The cell geometry is composed of a 5 cm-radius and 12cm-height cylinder, which is the internal volume of the measuring cell. A first tube of inner radius of 5 mm is positioned below the cell for gas inlet. A second tube of inner radius of 1 mm is positioned on the side of the cell for the gas outlet. The cell is considered hermetic (which is not the case in practice). Finally, only half geometry is simulated to take advantage of the cell symmetry.

Conditions for fluid dynamics

Domain conditions

- Laminar flow ($Re < 2000$)
- Compressive flow ($Ma < 0.3$)

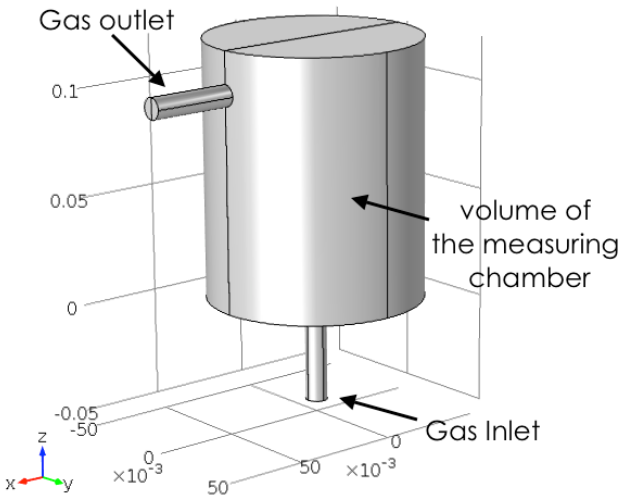


Figure F.8: Geometry of the measuring cell.

- Volume air (density = 2.4 kg/m^3 and dynamic viscosity = 1.8 × 10^{-5} Pa.s varies with pressure)

Boundary conditions

- Walls: flow without slip
- Inlet tube: laminar flow with a flow rate of 0.5 l/min (to simulate 1 l/min in the half geometry)
- Outlet tube: 1 atm pressure
- Symmetry face : symmetry conditions.

Conditions for transport of diluted species

Domain conditions

- Diffusive and convective transports
- Diffusion coefficient : 7 × 10^{-5} m^2/s (diffusion of H_2 in air)

Boundary conditions

- Walls: no flow
- Inlet tube: constant concentration of 0.00892857142 mol/m^3 (which should correspond to 200 ppm)
- Outlet tube: outflow condition
- Symmetry face : symmetry conditions.

Results

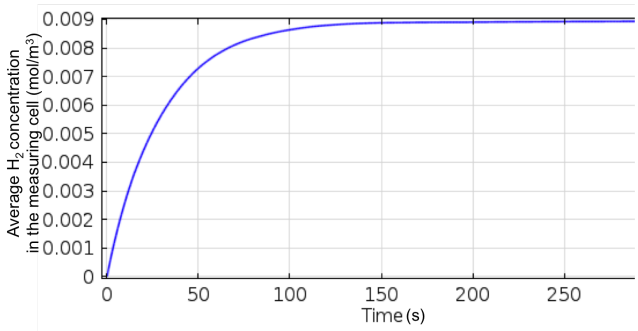


Figure F.9: Evolution of the average hydrogen concentration over time in the measuring cell when hydrogen is injected.

Figure F.9 shows the evolution of the average H_2 concentration over time in the measuring cell when H_2 is injected. The response time of the cell is of the order of one or two minutes. However, the central column of the cell more quickly reached the final concentration. The sensors are usually placed there, will be exposed more quickly to the desired concentration.

APPENDIX G

Hydrogen sensors and their applications

G.1 What is Hydrogen? And its safety issues.

Hydrogen (symbol : H) is the simplest element known to exist. An atom of hydrogen consists of one proton and one electron. Hydrogen is the first element in the periodic table with the atomic number 1. It is the lightest and most abundant element in the universe representing 75 mass% or 90 vol% of all matter. It is above all in the chemical compounds. Hydrogen exists also as a free element in the atmosphere, but only to the extent of less than 1 ppm (by volume). Hydrogen has the highest energy content of any common fuel by weight (atomic weight of 1.00794 u), but the lowest energy content by volume.

Hydrogen can be considered an ideal gas over a wide temperature range and even at high pressures. At standard temperature and pressure conditions, it is a colourless, odourless, tasteless, non-toxic, non-corrosive, non-metallic diatomic gas, which is in principle physiologically not dangerous.

By cons, hydrogen gas is highly flammable and will burn in air at a very wide range of concentrations between 4% and 75% by volume. Hydrogen gas has the ability to spread very quickly. At a leakage it rapidly mixes with the ambient air. Leakage rates are by a factor of 50 higher than for water and by a factor of 10 compared to nitrogen. The rapid mixing of hydrogen with air is a safety issue, because it leads very quickly to flammable mixtures, which on the other hand, for the same reason, will also quickly dilute the non-flammable range.

Because of its small size, its small molecular weight and its low viscosity, hydrogen gas is able to diffuse through certain materials (in particular organic materials).

Another safety issue is due to the volume increase by a factor of

845, when liquid hydrogen is heated up to ambient conditions, the local atmosphere may change drastically.

G.1.1 How is hydrogen made?

Hydrogen gas was first artificially produced in the early 16th century, via the mixing of metals with acids. In the 18th century, Henry Cavendish was the first to recognize that hydrogen gas was a discrete substance, he called inflammable air [312]. He discovered that hydrogen produces water when burned, which will later give his name: hydrogen comes of "water-former" in Greek.

The hydrogen in gaseous form exists in very small quantities in admosphre (less than 1 ppm by volume) then it is so abundant in compound form: Combined with oxygen, it is water (H_2O). Combined with carbon, it forms organic compounds such as methane (CH_4), coal, and petroleum.

Different methods to produce hydrogen exist. The two most important are:

1. **Steam reforming :** High-temperature steam separates hydrogen from the carbon atoms in methane (CH_4). The hydrogen produced by this method is not used as a fuel, but for industrial processes. This is the most cost-effective way to produce hydrogen today, but it uses fossil fuels both in the manufacturing process and as the heat source.

2. **Electrolysis :** splitting water into its basic elements: hydrogen and oxygen. Electrolysis involves passing an electric current through water to separate the atoms (2 H_2O + electricity $\longrightarrow$ 2 H_2 + O_2). Hydrogen collects at the cathode and oxygen at the anode. Hydrogen produced by electrolysis is extremely pure, and electricity from renewable sources can power the process, but it is very expensive at this time. Today, hydrogen from electrolysis is ten times more costly than natural gas and three times more costly than gasoline per Btu. On the other hand, water is abundant and renewable, and technological advances in renewable electricity could make electrolysis a more attractive way to produce hydrogen in the future.

Other methods to produce hydrogen are still at the experimental stage. For example, photoelectrolysis uses sunlight to split water molecules into its components [313]. A semiconductor absorbs the energy from the sun and acts as an electrode to separate the water molecules. In biomass gasification, wood chips and agricultural wastes are superheated until they turn into hydrogen and other gases [314, 315]. Biomass can also be used to provide the heat. Some algae [316] and bacteria [317, 318] produce hydrogen under certain conditions. But now, these methods of hydrogen production are not efficiently.

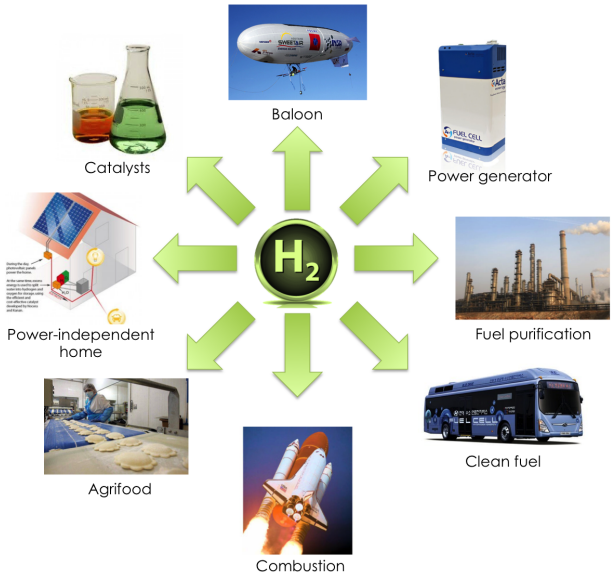


Figure G.1: Hydrogen is useful in many current and future applications.

G.1.2 Hydrogen applications

1. Combustion : The mass density of energy contained in hydrogen is very high: 1 kg of hydrogen contains 132.5 MJ, which is approximately 2.5 times more energy than is contained in 1 kg of natural gas and 3 times more energy than is contained in 1 kg of gasoline. From the beginning of the space industry, hydrogen immediately played an important role as a rocket fuel. A criterion of primary importance when you consider that a space launcher must be as light as possible. Hydrogen's main use as a fuel is in space program of all space agencies in the

world. Liquid hydrogen is the fuel that has propelled the space shuttle and other rockets since the 1970s.

The use of hydrogen as a fuel for zero-emissions vehicles is also under development. Currently, there is this type of vehicle in test phase (mainly USA) [319]. As for electric vehicles, the main current drawback is the absence of charging stations.

The first widespread use of hydrogen will probably be as an additive to transportation fuels. Hydrogen can be combined with compressed natural gas to increase performance and reduce pollution. Adding 20% hydrogen to compressed natural gas can reduce nitrogen oxide (NO_x) emissions by 50% in todays engines. An engine converted to burn pure hydrogen produces only water and minor amounts of NO_x as exhaust.

Hydrogen can also be used to heat homes and offices. But currently, cost is the major obstacle for use as fuel in everyday.

2. Energy carriers : Our model of organization in the field of energy is largely based on three steps. A first source of energy (mainly fossil fuels: coal, natural gas, nuclear ...) are consumed to produce electricity. Electricity is a secondary source of energy. Secondary sources of energy are used to store, move, and deliver energy in an easily usable form. We convert energy to electricity because it is easier for us to transport and use. Electricity is a energy carriers. In the future, however, hydrogen will join electricity as an important energy carrier, since it can be made safely from renewable energy sources and is virtually non-polluting [320].

Currently, full-electric cars are in their infancy. They already offer power performance (acceleration and speed) compared to conventional fuel car. However, a major obstacle to this technology is the lack of batteries with sufficiently large capacity. Their autonomy can not currently exceed 200 km per charge. Also, they are quite fragile and have problem of breakdown which makes them suddenly unusable.

The use of hydrogen as an energy carrier is a very interesting alternative. As far as the hydrogen is produced by renewable energy, cars using hydrogen as a fuel do not reject either of pollutant (only water vapor). There are two types of vehicles that use hydrogen as fuel. First, vehicles with an engine similar to vehicles running on petrol whose fuel

is hydrogen. Second, vehicles equiped with fuel cell. Hydrogen is used in a cell as combustible to generate electricity, which is then used by the vehicle engine.

3. Electricity generation : The space shuttle used hydrogen fuel cells (batteries) to run its computer systems. The fuel cells basically reverse electrolysis : hydrogen and oxygen are combined to produce electricity. Hydrogen fuel cells are very efficient and produce only water as a by-product, but they are expensive to build.

4. Energy Storage: Hydrogen is a very interesting way to store energy especially renewable energies that are usually fluctuating. The electricity excess generated at some time (for example the day mainly for photovoltaic panel) is used in hydrogen production. When electricity demand becomes more important, the hydrogen is consumed to generate electricity. The efficiency of this conversion/reconversion is very good (60 % in 2010 [**?**]) (http://energy.gov/eere/fuelcells/national-hydrogen-storage-project, September 1, 2014).

5. Hydrogen balloon: The first hydrogen-filled balloon was invented by Jacques Charles in 1783. Hydrogen provided the lift for the first reliable form of air-travel following the 1852 invention of the first hydrogen-lifted airship by Henri Giffard. Because H_2 is lighter than air, having a little more than 1/14 of the density of air, it was once widely used as a lifting gas in balloons and airships. However, hydrogen has been replaced by helium, a inflammable gas, especially after the disaster of the Zeppelin airship LZ 129 Hindenburg which was destroyed by fire in 34 seconds in his landing, causing 36 deaths [321].

The weather balloons are balloons that are attached meteorological instruments. These balloons are released into the air and allow locally probing meteorological parameters. They sometimes use of hydrogen instead of helium which is a more expensive gas.

6. Cooling system : Hydrogen turns into a liquid when it is cooled to a temperature below ~ 20 K. It has the highest thermal conductivity of any gas. Liquid H_2 is used in cryogenic research, including super- and supraconductivity studies. It is also used as a cooling system in super computers and in equipment of special measures (Nuclear magnetic resonance scanners ...)

7. Fossil fuels purification : Hydrodealkylation, Hydrodesulfurization are examples of methods used in the petrochemical industry to remove various pollutants in fossil fuels. These methods employ hydrogen [210]. The hydrocracking is another method used in petrochemistry to break a long-chain of hydrocarbons into short ones.

8. Synthesis of chemical compounds : Hydrogen is involved in several processes of synthesis of chemical compounds. Probably, the production of ammonia and methanol are methods which uses larger amount of hydrogen in the synthesis industry.

9. Agrifood : Hydrogen is an authorized food additive (E 949), which allows leak testing in package food and other anti-oxidant properties [210]. It is also used in the modification of fatty acids.

G.2 Operating principles of H_2 sensors

It is possible to classify hydrogen sensors into eight different operating principles [247] : catalytic, thermal conductivity, electrochemical, resistance based, work function based, mechanical, optical and acoustic hydrogen sensors.

• **Catalytic H_2-sensors** operate on the principle that reaction of a combustible gas with oxygen on the catalytic sensor surface releases heat. In the case of detection of hydrogen, the most widely used catalysts are platinum and palladium. Catalytic sensors may further be divided into pellistor type and thermoelectric type [247].

Pellistor element hydrogen gas sensors consist of a platinum wire coil embedded within a bead containing the catalytic material. The platinum coil has two functions; it act as a heater as well as being a resistance thermometer. In general, the sensor consists of two pellistors mounted in parallel in a Wheatstone bridge circuit. The second pellistor, called the compensator, is similar except that the bead does not contain catalytic material and as a consequence is inert to hydrogen (figure G.2). In this way, changes in environmental parameters such as relative humidity, temperature or thermal conductivity of the ambient gas influence in the same manner both pellistors and have little influence

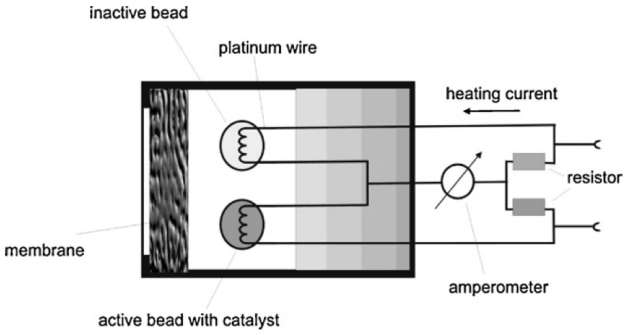


Figure G.2: The active and inactive beads are connected in a Wheatstone bridge circuit. In presence of catalyst, hydrogen molecules are oxidised with oxygen molecules. This exothermic reaction raises the temperature of the activate bead which results in a change in its electrical resistance. The Wheatstone bridge circuit is unbalanced. Reproduced from reference [247].

on the output signal of Wheatstone bridge circuit. For the hydrogen oxidation reaction goes place, the catalyst is heated up to temperatures typically above $300°C$ by applying a current through the the platinum coils. Hydrogen molecules are oxidised with oxygen molecules in the presence of the catalyst to form water. The exothermic reaction raises the temperature of the activated pellistor which results in a change in its electrical resistance. Recourse to microfabrication has significantly reduced power consumption and faster response time [322] [323] [324].

In the case of thermoelectric sensors, the measurement is always made from the temperature rise due of exothermic oxidation reaction of hydrogen, but the thermoelectric effect (or Seebeck effect) is used to generate the electrical signal [325] [326]. The thermoelectric effect arises when there is a temperature difference between two points of a conductor or semiconductor material which results in a voltage difference between these points. The main advantage of thermoelectric sensors is the lowest operating temperature (typically $100°C$ instead of 300 $°C$).

Catalytic-type hydrogen sensors have a number of disadvantages. Firstly they are not selective for hydrogen and will respond to other combustible gases such as hydrocarbons and carbon monoxide. Sec-

ond, by their operating principle, a high power consumption is required to heat the catalyst. Third, the need for oxygen in the gas mixture to allow the oxidation reaction limits possible measures environments [247].

• **Thermal conductivity H_2-sensors** operates on the basis of the measurement of heat loss from a hot body to the surrounding gas. Hydrogen possesses the highest thermal conductivity of all gases [327]. As for catalytic-type hydrogen sensors, thermal conductivity sensors are composed of two platinum coils used as heat resistance placed in parallel in a Wheatstone bridge circuit . Each resistor is placed in a separate chamber. The detecting resistor is exposed to the gas being measured while the reference resistor is sealed in a chamber containing a reference gas. When the two resistors are exposed to the same gas, they lose heat at the same rate. When the detecting resistor is exposed to the measured gas mixture, it loses more or less heat depending on the thermal conductivity of the measured gas relative to the reference gas. This then leads to a modification the detecting resistor temperature and therefore its resistance change is measured by the Wheatstone bridge. Thermal conductivity sensors have a wide detection range and they do not chemically interact with the surrounding gases [328]. However, these devices are not accurate for very low hydrogen concentrations [329].

• **Electrochemical H_2-sensors** detect changes in charge transport or electrical properties due to electrochemical reactions involving H_2- gas and occurring at sensing electrodes. Electrochemical sensors are generally constituted by two electrodes (the working-electrode and counter-electrode) immersed in an electrolyte (solid or liquid) allowing ions transport and a gas permeable layer allowing to control the sensor sensitivity [330] [331]. Surface reactions at the electrode cause a polarization and limit the concentration of reactant gas. Regularly a third electrode (reference electrode) is used that maintains the thermodynamic potential of the working electrode constant during sensing. Electrochemical sensors are devices that extract information about sample from measurement of some electrical parameter. Depending on the measured electrical parameter, electrochemical sensors are classified into three different categories [331] : amperometric [332], potentiometric [333] and conductometric sensors. The two greatest advantages of electrochemical sensors are low power consumption and room temperature operation which do them the well-established commercially.

Amperometric gas sensor is operated under an externally constant

applied voltage, which drives the electrode reaction in one direction. Hydrogen gas diffuses through gas permeable layer and electrolyte and is oxidised at the sensing electrode. This results in a change of the sensing electrode potential. At the counter electrode the reduction of oxygen takes place. The flow of electrons from the anode to the cathode constitutes an electric current. If the rate of reaction at the surface is high enough, the reaction rate is limited only by the diffusion of the H_2 to the electrode surface. The sensor signal is a diffusion limited current proportional to the concentration of the analyte in the surrounding gas [331]. Amperometric gas sensors are the are the most common because of their linear response [332] and good accuracy [247].

Potentiometric gas sensor operate at zero current (or quasi zero current) and the measured quantity is the potential difference or electromotive force between the two electrodes. All reactions must be in equilibrium to observe the themodynamic potential that can be related to the hydrogen gas concentration by the Nernst equation [333] :

$$E = E^0 + \left[\frac{RT}{zF}\right] \ln\left(\frac{a}{a_0}\right) \tag{G.1}$$

where E is electrode potential, E^0 is standard electrode potential, R is universal gas constant, T is absolute temperature, F is Faraday constant, z is number of electrons taking part in the reaction, a is chemical activity of the analytes (proportional to hydrogen concentration), a_o is the activity of the reference. The electrical signal is proportional to the logarithm of the hydrogen concentration which can result in lower accuracy at high concentrations. The measured signal from a potentiometric sensor is nearly independent of sensor size and geometry but the redox potential of the electrolyte components. This is an advantage from the point of view of sensor miniaturisation [247].

Conductometric gas sensor uses the change in electrolyte conductance to measure the hydrogen concentration. The measurement can be done in DC or AC signal [330]. The change in the conductance of the electrolyte is not intrinsic to hydrogen which can make this type of sensor non-selective. As hydrogen have a large conductivity of the proton as compared to other ions, a good choice of the electrolyte and the design can nevertheless be selective [331].

- **Resistance based H_2-sensors** operate on the measurement of

the resistance variation of a semiconducting metal-oxide or a metal. Semiconducting metaloxide sensor use the principle that the electrical properties of metal oxides change when they are exposed to reducing gases [334] (figure G.3). Although, the sensing mechanism of metal-oxide sensors remains uncertain, it is generally acknowledged that the reaction of hydrogen with oxygen adsorbed provides surface electrons and induces a decrease in the resistance of the metal oxide [247] :

$$H_2 + O^-_{ads} \longrightarrow H_2O + e^- \tag{G.2}$$

To promote the reaction between hydrogen and oxygen but also for evaporating the water, the reaction product, the metal oxide is generally heated between $180°C$ and $450°C$ depending on the metal oxide used. One significant shortcoming of semiconductor gas sensors is their low selectivity. The most efficient semiconducting metaloxide sensors are based on SnO_2 (undoped, doped with Sn, In, Cu, Pt, Pd, and different metal oxides, the Schottky diode), ZnO, WO_3 , Ga_2O_3 , TiO_2 , Fe_2O_3, etc. [334]. Semiconducting metaloxide sensors have the disadvantages of having to O_2 in the gas mixture to operate, a high operating temperature (may lead to high power consumption) and a low sensitivity to H_2.

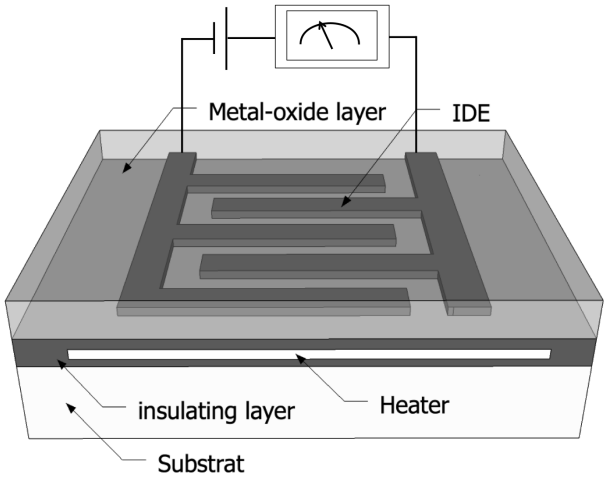
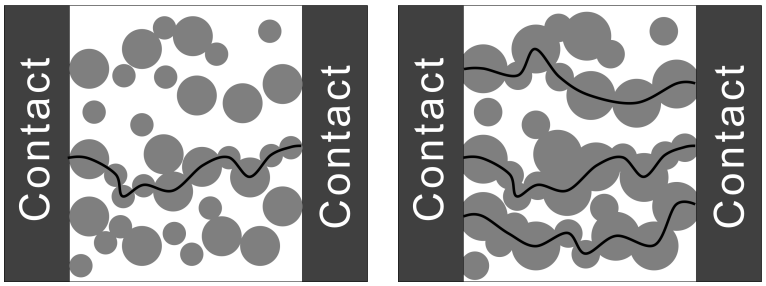


Figure G.3: Schematic of a metaloxide sensor.

Metallic resistors are the second type of resistance based gas sen-

sors. Two mechanisms are known for describing the resistance of metals in contact with hydrogen [264]. First, the presence of hydrogen atoms in solid solution in the host lattice increases the frequency of charge carriers scattering events (higher resistivity of the PdHx relative to pure Pd). This is reflected by an increase of electrical resistance of the device ($\Delta R_{H_2} > 0$) [246]. The main disavantage this sensors is that they are especially subject to poisoning [335].

The second mechanism is the volume change associated with the α to β phase transition. This sensors generally show decreased resistance in the presence of hydrogen ($\Delta R_{H_2} < 0$). The volume change causes the expansion of the metal structures leading to the creation of new electrical connections between them. As the number of short-circuits increases, electrical resistance of the whole device decreases. These metal structures are typically palladium meso- or nanowires [262] or on palladium nanoparticles [235] [271] (figure G.4). Resistance-based hydrogen sensors have many benefits such as overall high performances, simplicity of fabrication and compatibility with the current integrated circuit process lines [236].



a. b.

Figure G.4: Schema corresponding to sensors based on the volume changes of nanoparticles (represented by gray discs) (a) before and (b) during exposure to H_2 gas. The volume change causes the expansion of the metal structures leading to the creation of new electrical connections between them.

• **Work function based H_2-sensors** have a structure comparable to the metal-oxide-semiconductor technology (MOS). The work function is the minimum energy, measured in electron volts, needed to remove

an electron from the Fermi level of a metal to a point at infinity besides metal (vacuum level). Depending on the polarization applied to to the metal layer (called *gate*), a layer of accumulation or depletion of charge carriers is created in the interface oxide/semiconductor leading to a variation of the resistance of the device. In the case of hydrogen sensing, the gate is composed of a hydrogen sensitive catalytic metal (mainly Pd or Pt [336]). Hydrogen atoms diffuse through the metal and adsorb at the metal/oxide interface. This interface is electrically perturbed by the presence of hydrogen, changing the work function of the metal and shifting the energy levels at the metal/insulator interface. This results in a change in the electrical potential applied to the semiconductor. The cause of the disruption of metal/oxide interface by hydrogen atoms is subjet to discution [337]. The first model is based on the formation of a dipole layer of polarized H atoms affecting energy levels at the metal/semiconductor interface. The second model states that an excess of charges at the metal/semiconductor interface is created in the presence of hydrogen and cause a reduction of the Schottky barrier height. Several structures used to measure the change in the work function. Three categories are presented in this work: metal-(insulator)-semiconductor (MS/MIS) Schottky diodes, metal-oxide-semiconductor field effect transistors (MOSFET) and metal-oxide-semiconductor capacitors [247] (figure G.5).

Metal-semiconductor (Schottky) diode can be made in two different structures : metal-semiconductor (MS) or a metal-insulator-semiconductor (MIS). A Schottky diode is formed by contacting a metal and a semiconductor. The electrical contact is nonlinear. The Fermi level of the semiconductor is curved to align with the Fermi level of the metal forming a potential barrier for a quantity equal to the difference between work functions of the two materials (the Schottky barrier height). The presence of a thin insulating layer at the interface increases the height of the potential barrier. Using a metal such as Pt or Pd, the potential barrier depends on the hydrogen concentration in the gas mixing. Indeed, hydrogen molecules adsorbed on the surface of the catalytic metal are dissociated into hydrogen atoms. Then some of the atoms diffuse through the metal film to the metal/insulator interface. At the interface, the H atoms form a dipole layer, which changes the work function of the metal, and thus the height of the Schottky barrier [98]. This change in the barrier height is proportional to the amount of H atoms that diffuse into the metal, and thus is proportional to the concentration of H2 gas.

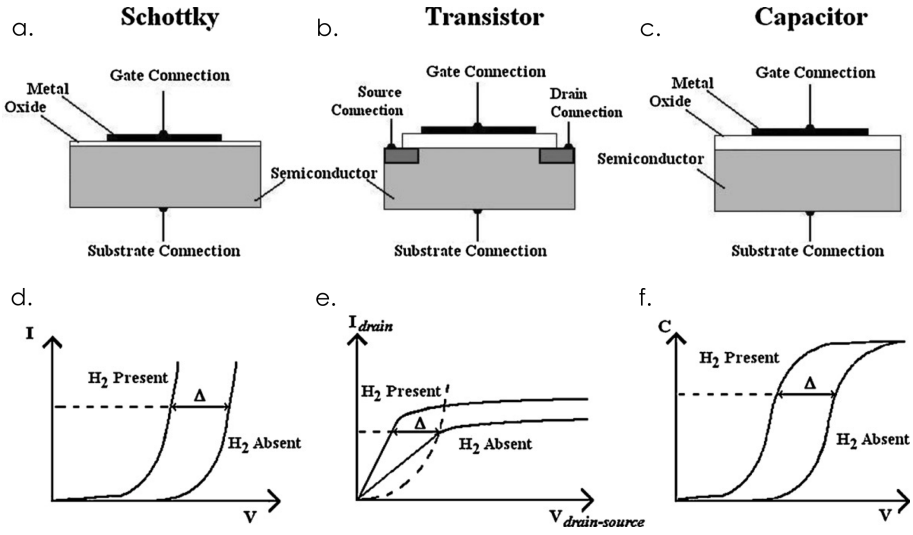


Figure G.5: Cross-sectional view of a basic MOS-Schottky diode, MOS-transistor and MOS-capacitor sensor. The dipole layer formed by hydrogen adsorption at the metal/oxide interface creates a voltage change which can be measured by a shift in (a) the currentvoltage curve of a diode or transistor or (b) the capacitancevoltage curve of a capacitor. Reproduced from reference [247].

This change in the height of the Schottky barrier causes a change in the current-voltage characteristics (IV). Applying a constant bias current, the voltage varies depending on the hydrogen concentration [247].The presence of a thin oxide layer between the metal and the semiconductor has resulted in better performance in terms of sensitivity. This can be explained by the elimination of the Fermi-level pinning effect by the insulating oxide layer which otherwise decreases hydrogen detection.

Metal-insulator-semiconductor transistor uses a field effect transistor (FET). The metal catalyst is used as the gate. As for the Schottky diode of the absorbed H atoms diffuse to the metal/insulator interface altering the work function of the metal layer. The change in the work function of the metal modifies its electrical potential which influences the conductivity between the source and the drain [338] [339]. Some hydrogen sensors based on MOSFET technology has been commercialized. Because the manufacturing process is similar to those of the standard

microelectronics, this technology should thrive in the years to come.

Metal-oxide-semiconductor capacitors utilizes a shift in the capacitance that occurs between the metal and the semiconductor, spaced by the insulator [340]. Generally, the insulating layer is thicker than in the MOSFET structure to avoid leakage currents. The absorption of hydrogen and its diffusion to the metal/insulator interface cause a change in the capacitance-voltage plot (C-V) and a shift of the flat band voltage proportional to the hydrogen gas concentration. Although little commercialized, this technology is currently the only one which covers a very large range from low ppm to 100% and has response time of some seconds [247].

• **Mechanical H_2-sensors** use the volume change of the metal by the hydrogen absorption. Absorbed hydrogen atoms in a metal occupy interstitial sites in the host lattice causing volume expansion and related internal stresses [257]. The simplest mechanical gas sensors consists in a bilayer beam with one layer is a metal catalyst and the other is a inert layer [260]. In contact with hydrogen, the catalyst layer increases in volume, but it is constrained by the inert layer, that transduced into the mechanical bending or curvature of the beam (figure G.6). The curvature is proportional to the hydrogen concentration and can be measured optically or capacitively. More sophisticated mechanical sensors are based on non-amplified lattice expansions as detection principle [341]. MEMS technology is particularly suitable for miniaturization of this kind of sensor. By their operating principle, mechanical sensor suffers regularly problem of delamination between the layers of the beam. The great advantage of mechanical sensors is their very low power consumption (a few picowatts). They are also effective for the measurement of low concentrations of hydrogen [342]. By cons, their response time is often long compared to other technologies [247].

• **Optical H_2-sensors** use the change of the optical properties of certain materials when they interact with hydrogen. The optical properties can vary are reflectivity, refractive index ... There are various devices for measuring changes in the optical properties [247]. The most widely used are based either on thin films of palladium and/or chemochromic oxides coated onto the tip or along the length of an optical fibre [343]. Such fibre optic sensors are known as optrodes or optodes. Surface plasmon resonance (SPR) [344] and measurement of evanescent field

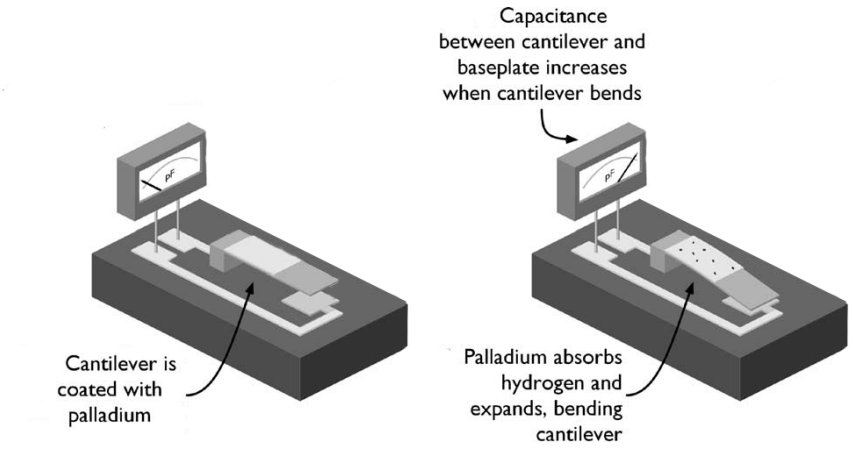


Figure G.6: Diagram illustrating the microcantilever hydrogen sensor concept : (a.) In the absence of hydrogen, the palladium layer contains no particular constraint. The cantilever is in its initial position. (b.) In the presence of hydrogen, the volume of palladium increases resulting of the curvature of the cantilever. The capacitance between the cantilever and baseplate decreases. Reproduced and modified from reference [260]

interaction [345] are techniques often give promising results. Surface plasmons are surface electromagnetic waves that propagate parallel to a metal/dielectric interface and that are therefore sensitive to changes in the structure of the metal surface exposed to hydrogen. When a wave propagates in a delimited by a second material with a different refractive index material, the waves arriving in some incidences are totally reflected. However, the light crosses the interface and penetrate partly in the low-index material. This part of the electromagnetic field is called evanescent field and has the particularity to decrease exponentially. The interaction of hydrogen with the interface of this two material causes a change in its refractive index, which in turn causes a change in the attenuation in the evanescent field. This can be detected as a change in transmittance. Optical sensors still need to be improved because they tend to interfere with the light or are resorting to expensive lighting systems (laser ...). By cons, they offer three advantages over other detection technologies: detection without running the risk of inflammation, the ability to detect distributed along an optical fiber and a low sensi-

tivity to electromagnetic noise [247] [343].

• **Acoustic H_2-sensors** detect changes in the properties of elastic waves in the mat- ter thanks to adsorbent or absorbent materials sensitive to hydrogen placed on a piezoelectric element. Several different systems have been studied using tranduscer techniques such as quartz crystal microbalance (QCM) or surface acoustic wave (SAW). A quartz crystal microbalance is basically composed of a crystal sandwiched between two electodes on which a frequency electrical signal is imposed. The electrical signal is used to deform the crystal and put it in resonance. The resonance frequency is sensitive to the change in mass of the system and more specifically to the accumulation of mass of the measured analyte on a functionalizated surface of crystal. This accumulation is proportionnal to the concentration of the analyte in the ambient environment. This type of device has overall good sensing properties and low power consumption. In addition, they have the potential to detect hydrogen over a wide concentration range extending from the ppm level to 100%, with rapid response time. However, improvements are required in terms of stability of the sensor [247].

Table G.2 provides a summary of the performance of hydrogen sensors according to their operating principle.

Sensor type	Principle/Device	Performance					
		Measuring range [Vol%]	Accuracy [% of ind.]	Response time (t_{90}) [s]	Power cons. [mW]	Gas environment	Lifetime [years]
Catalytic	Pellistor	Up to 4	$< \pm 5$	< 30	1000	-20 to 70°C $5 - 95\%$ RH $70 - 130$ kPa	5
Thermal conductivity	Calorimetric	$1 - 100$	± 0.2	< 10	< 500	0 to 50°C $0 - 95\%$ RH $80 - 120$ kPa	5
Electrochemical	Amperometric	Up to 4	$\leq \pm 4$	< 90	$2 - 700$	-20 to 55°C $5 - 95\%$ RH $80 - 120$ kPa	2
Resistance based	Semiconducting metal-oxide	Up to 2	$< \pm 10 - 30$	< 20	800	-20 to 70°C $10 - 95\%$ RH $80 - 120$ kPa	> 2
	Metallic resistor metal-oxide	$0.1 - 100$	$< \pm 5$	< 15	> 25	0 to 45°C $0 - 95\%$ RH Up to 700 kPa	< 10
Work function based	Capacitor	Up to 5	$\leq \pm 7$	< 60	4000	-20 to 40°C $0 - 95\%$ RH $80 - 120$ kPa	10
	MOS field effect transistor	Up to 4.4	$\leq \pm 7$	< 2	700	-40 to 110°C $5 - 95\%$ RH $70 - 130$ kPa	10
Optical	Optrode	$0.1 - 100$	± 0.1	< 60	1000	-15 to 50°C $0 - 95\%$ RH $75 - 175$ kPa	> 2

Table G.1: Comparison of performance specifications of commercially available sensors. Based on typical data collected from datasheets provided by sensor supplier. Reproduced from reference [247].

APPENDIX H

Matlab code for SEM pictures processing

The Matlab code for the processing of SEM images on which deposited nanoparticles on pore wall appear is presented in this Appendix. The code is an expanded version by Antoine Douchamps of an original picture processing Matlab routine developed by Jonathan Rasson.

```
%%%%%%%%%%%%%%%%%%%%%%%%%%%%%%%%%%%%%%%%%%%%%%%%%%%%%%%%%%%%%%%%
% Image processing of SEM pictures of nanoparticles %
% by Antoine Douchamps                                %
% - based on a code provided by Jonathan Rasson      %
%%%%%%%%%%%%%%%%%%%%%%%%%%%%%%%%%%%%%%%%%%%%%%%%%%%%%%%%%%%%%%%%

%%% ------- picture_analysis
% @pre : path to the SEM picture and conversion index
% @returns: number of particules on the picture
%           and data matrix
%%%
function [number,surface,data]= picture_analysis(
    file_name,conv)

  %% Image Processing
  I = imread(file_name);     % Import
  Gray = rgb2gray(I);        % Grayscale Conversion
  level = graythresh(Gray); % Otsu Method. Possible
      loss
  BW = im2bw(Gray,level);    % Creation of a binary
      image
  Fill = imfill(BW,'holes');% Filling of defects in
      structures

  sedisk = strel('disk',1,0);
  Erode = imerode(Fill, sedisk);
  Dil = imdilate(Erode, sedisk);
  EDF = imfill(Dil,'holes');% Erode, Dilation and Fill

  Final = imclearborder(EDF);% Borders processing

  %% Analysis
```

```
29    F_size = size(Final);       % Surface of the picture
30    surface = (F_size(1,1) * conv) * (F_size(1,2) * conv
          );
31
32    % Single out connected elements and number them
33    [Label,number] = bwlabel(Final,4);
34
35    % Data matrix
36    % Col 1 : paricle identification number
37    % Col 2 : surface area
38    % Col 3 : perimeter
39    data = zeros(number,3);
40    for i = 1:number
41        data(i,1) = i;
42        pix = find(Label == i);
43        data(i,2) = (length(pix)* (conv)^2);
44    end
45    perim = bwperim(Label);
46    inside = find(perim == 0);
47    contour = Label;
48    contour(inside) = 0;
49    for i = 1:number
50        pix = find(contour == i);
51        data(i,3) = length(pix)* conv;
52    end
53 end
54
55 %%% ---------- conversion
56 % @pre : path to the scale and real distance(in nm)
57 % @returns : conversion index(nm/pixel)
58 %%%
59 function [conv] = conversion(file_name,scale_nano)
60
61     %% Image processing
62     I = imread(file_name);
63     Gray = rgb2gray(I);
64     level = graythresh(Gray);
65     BW = im2bw(Gray,level);
66
67     %% Isolation of the scale line
68     compl = imcomplement(BW);
69     seline = strel('line',4,0);
70     get_line = imerode(compl, seline);
71
72     %% Line length
```

```
73      inc = 0;
74      lsize = size(get_line);
75      for i= 1:lsize(1,1)
76          if (inc ~= 0), save = inc; end
77          inc = 0;
78          for j= 1:lsize(1,2)
79            if (get_line(i,j) == 1), inc = inc + 1; end
80          end
81      end
82      conv = scale_nano / save;
83  end
84
85  %%% ---------- Additional lines
86  %%%%% Import
87  conv_D6 = conversion('D6/D6_scale.png',1000);
88  [number_D6_a, surface_D6_a, data_D6_a]=
        picture_analysis('D6/D6_9.png' ,conv_D6);
89  % Other imports not shown
90
91  %%%%% Particles coverage
92  coverage_D6_a = number_D6_a / surface_D6_a;
93  coverage_D6   = [coverage_D6_c coverage_D6_b
        coverage_D6_a];
94  mean_coverage_D6 = mean(coverage_D6);
95
96  %%%%% Particles diameter and diameter repartition
97  diam_D6_a = (data_D6_a(:,2).^(1/2) ./ sqrt(pi)) .*2;
98  diam_D6   = [diam_D6_a ; diam_D6_b ; diam_D6_c];
99  edge_D6 = [ 0 10 20 30 40 5000];
100 n_D6 = histc(diam_D6,edge_D6);
101 mean_diam_D6 = mean(diam_D6);
102
103 %%%%% Circularity
104 spher_D6_a =   ((2 * sqrt(pi)) .* data_D6_a(:,2)
        .^(1/2)) ./ (data_D6_a(:,3));
105 spher_D6   = [spher_D6_a ; spher_D6_b ; spher_D6_c];
106 mean_spher_D6 = mean(spher_D6);
107 %%%%% Singling out outliers
108 muD = mean(spher_D6);
109 sigmaD = std(spher_D6);
110 outliersD = (spher_D6 - muD) > 2*sigmaD;
111 nnzD = find(outliersD);
112 spher_D6m = spher_D6;
113 spher_D6m(nnzD) = NaN;
114 mean_spher_D6m = nanmean(spher_D6m);
```

APPENDIX I

Microsensor fabrication process

In this Appendix, the fabrication process of macroporous silicon-based hydrogen microsensor are described, using the integration method of micrometric size metal electrodes.

I.1 Fabrication process

Figure I.1 shows the schematic view of the fabrication process flow of the microsensor. The flow process is composed of six steps of only standard microfabrication and CMOS-compatible techniques thereby to accelerate the transfer of the sensors to the industrial valorisation.

The fabrication process is composed by 5 steps: A standard cleaning of silicon wafer (figure I.1a.), deposition and patterning of the masking layer (figure I.1b. et c.), deposition and patterning of metal electrodes (figure I.1d.) and silicon electroetching (figure I.1e.).

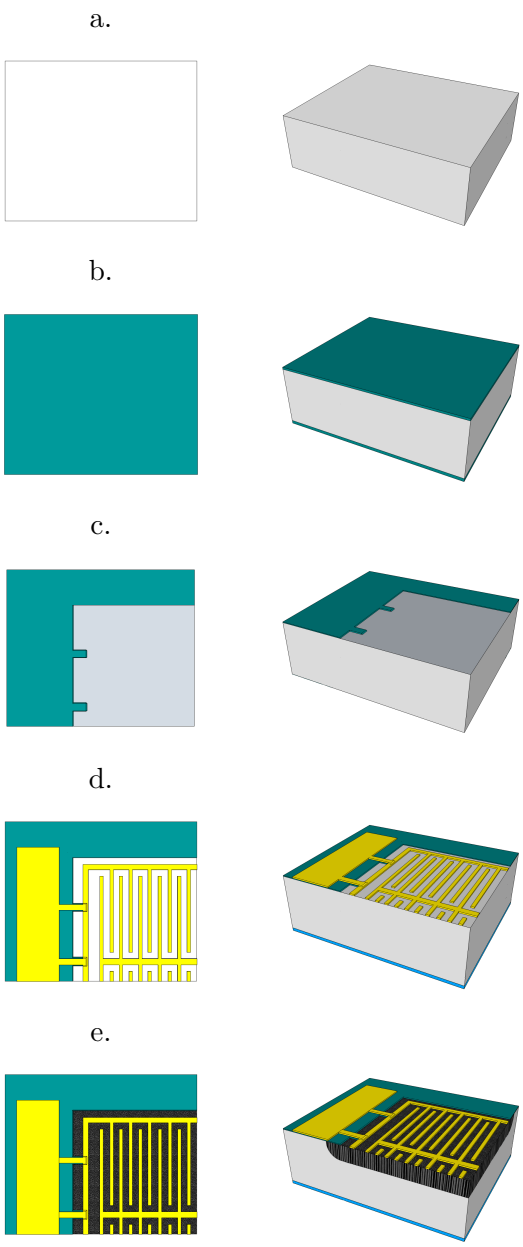


Figure I.1: Process flow of macroporous silicion-based microsensor. The first and second columns show respectively a top view and a 3D view the different steps of fabrication.

I.1.1 Substrate and cleaning

p-type silicon wafer (10-20 Ω·cm, ⟨100⟩-orientation) are cleaned in a piranha solution (H_2SO_4:H_2O_2 5:2) followed by rinsing with DI water eliminates all organic contaminants that may be present on the wafers. Then, wafers are immersed in a solution of HF (2%) to etch the oxide layer. After rinsing and drying under nitrogen flow, the sample is placed quickly in the following deposition equipment to prevent the growth of a native oxide on the silicon surface.

I.1.2 Silicon nitride deposition

A uniform deposition of rigid material on whole surface of the wafer is performed. The material enhance the anchoring of the macroporous membranes and the substrate. In addition, it plays role of the electric insulation between the connection pads and the substrate. Finally, it must be chemical resistant at HF-based electrolyte during porosification. In the current microfabrication materials, silicon nitride (Si_3N_4) is a solution to the three criteria listed above. Silicon nitride is commonly deposited by PECVD or LPCVD techniques. Si_3N_4-LPCVD is more HF-resistant [346] compared to a Si_3N_4-PECVD. In the HF/DMF/H_2O mixture it is etched at an approximative rate of 0.4 nm/min, allowing etching 250 min long with a 100 nm thick masking layer.

A 200 nm thick Si_3N_4 layers is deposited on the wafer surface at the temperature of 750 °C and the pressure of 35 Pa by LPCVD in a vertical furnace (Koyo, Japan).

I.1.3 Mask patterning

Standard photolithography is used to pattern the surface. After the lithography the LPCVD-Si_3N_4 layer is etched by Reactive Ion Etching (RIE). The technique plasma etching presents a good resolution, selectivity and anisotropy. The plasma etching is a dry etching which involves ions (such as oxygen, chlorine, fluorine) generated in an excited gas and submitted to an electric field directed toward the sample. These ions are accelerated before colliding with the sample. They are physically and chemically react with the surface and etch it. A "more chemical" etching improves the selectivity of the etched materials, but will be relatively

Parameter	Values
CHF_3	50 sccm
O_2	10 sccm
Pressure	20 mTorr
Power	100 W
Si_3N_4 rate etching	100 nm/min
Si rate etching	5 nm/min
PR selectivity	1:1

Table I.1: RIE parameters for Si_3N_4 etching.

isotropic (figure I.2a.). It is not possible to obtain patterns with high aspect ratios. Conversely, a "more physical" etching reduces selectivity but has particularly directional (figure I.2b.) or anisotropic profiles (figure I.2c.).



a. b. c.

Figure I.2: Different profiles for (a.) isotropic, (b.) directional and (c.) anisotropic etching.

The etching parameters are shown in the table I.1. Etching with CHF_3 gives a good selectivity for Si_3N_4 etching relative to Si etching. The addition of oxygen in the plasma increases slightly the lateral etching. As a result, the sides of the Si_3N_4 layer are a oblique and not a vertical orientation. The step is not steep to ensure the electrical connection between the connection pads on the nitride layer and the metallic IDE on the silicon surface (figure I.3). Backside patterning is identically.

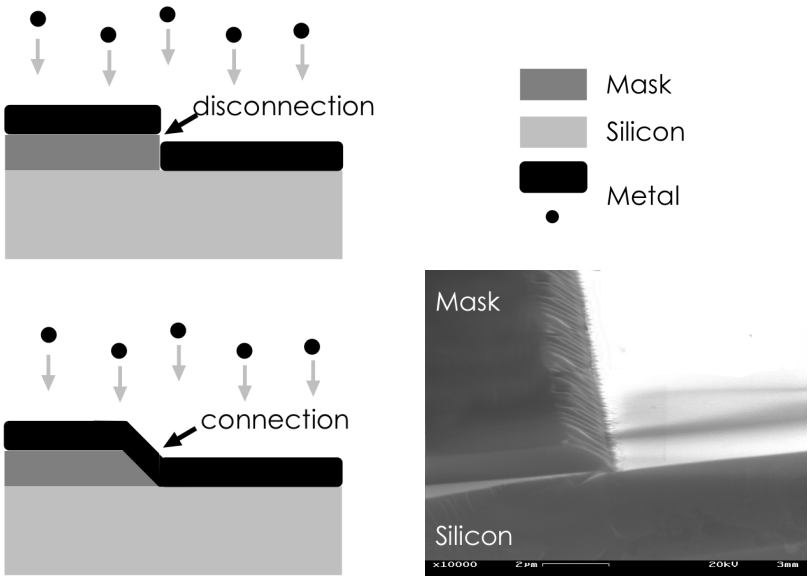


Figure I.3: (Left) Representation of the step between the connection pads above Si_3N_4 layer and interdigitated electrodes on the silicon surface. (Right) SEM picture of the Si nitride step.

I.1.4 Metallization

Backside metallization

A 200-nm thick aluminum layer was evaporated on the wafer back side for contact with the aluminum electrode of the anodizing cell (single baths cell, see section 2.1). A annealing of wafers in a tubular furnace at 432°C in a reducing atmosphere (forming gas) for 30 minutes is used to ensure a good electrical contact. Aluminium diffuses in silicon and reduces contact resistivity.

Front side metallization

In section 3.2, we have shown the importance of the interface between the metal electrodes and the silicon to prevent delamination of the electrodes during the porosification. Before performing photolithography to pattern the metal electrodes, the native oxide is etched by HF etching. Then, the wafer is placed quickly (to prevent further oxidation not con-

trolled) in a plasma Barrel (Tepla 300E) to 150W for 1 minute to create a thin plasma oxide on the silicon surface.

The metallization is carried out in an e-beam evaporator (e-gun Vacotec) in a vacuum of 4×10^{-7} Torr. The choice of deposited metals and their thicknesses has been described in Appendix B (page 227). The lift-off is performed by immersing the sample in a bath of aceton to 65°C during 2h. Figure I.4 shows a microsensor after the metallization step.

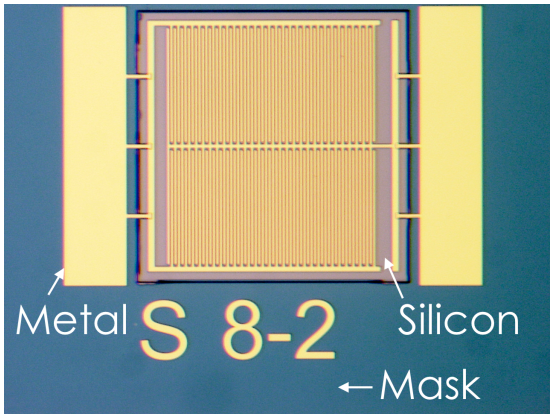


Figure I.4: Optical microscope picture of microsensor after the metallization step.

I.1.5 Electrochemical etching of silicon

The sample were electrochemically etched to form a macroporous silicon layer at room temperature, and the solution was stirred with a rotating propeller to avoid inhomogeneities due to the gas accumulation on the surface. A platinum grid placed at 5 cm from the sample was used as cathode, while the anode was the silicon substrate. An electrical contact was made by placing an aluminum plate in direct contact with aluminium on sample backside. The macroporous silicon layer was formed by setting the etching current density J_{etch} at 17.5 mA/cm^2 with a potentiostat (Princeton Applied Research, Ametek, VersaSTAT 3) during 30 minutes in ODS-type electrolyte (see Section 3.2). No reference electrode was used to perform the anodization.

I.1.6 Rapid thermal annealing

In Section 3.2, rectifier behavior of metal / silicon junction had been strengthened to prevent delamination of the metal electrodes. For the use of sensors in gas detection application, rectifier behavior must be broken to become an ohmic contact. A high-temperature annealing is required to allow chemical reactions to take place between the electrodes and the semiconductor (eg silicidation). These chemical reactions usually need several hundred degrees to occur.

The method used is the *rapid thermal annealing* (RTA) technique. A sample is annealed at high temperature (several hundred degrees Celsius) in a short period of time. Heating and cooling times are of the order of some ten seconds.

These chemical reactions usually need several hundred degrees to occur. However, when these reactions take place in a traditional oven, heating and cooling times are very long. The metal have the time to diffuse into the semiconductor and electrode is deteriorated. Other undesired phenomenon is that silicon atoms diffuse to the top of the electrodes and are oxidized. A thin insulating layer appears on the electrode. RTA technique, with a very rapid heating and a very rapid cooling, strongly limits the interdiffusion phenomena.

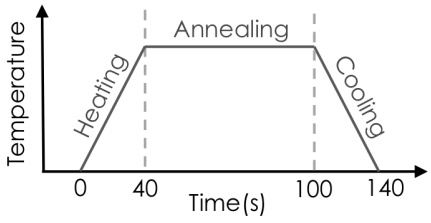
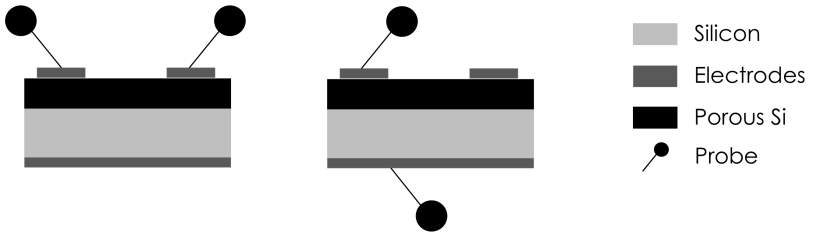


Figure I.5: Schematic representation of the temperature evolution over time in a RTA process.

RTA is realized at different temperatures on samples with and without the porous layer. The annealing is performed under a nitrogen atmosphere to prevent oxidation by the presence of oxygen. Before raised in temperature, a constant step of 10 minutes at room temperature is used

to avoid the presence of oxygen in the annealing chamber. The heating and cooling times are set at 40 seconds. The annealing time is set to 1 minute (figure I.5). The different temperatures of annealing are 450 °C, 550 °C and 650 °C. Below these temperatures, the electrical contacts undergo very little change. Above these temperatures, the appearance of metal is very altered.



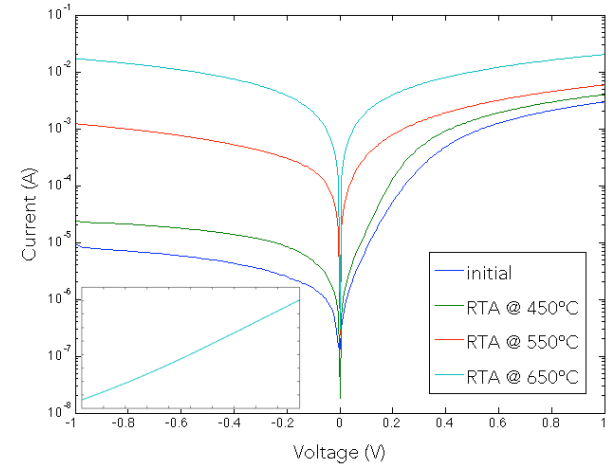
a. b.

Figure I.6: Schema of (a.) an inter-electrodes measurement and (b.) a transverse measurement.

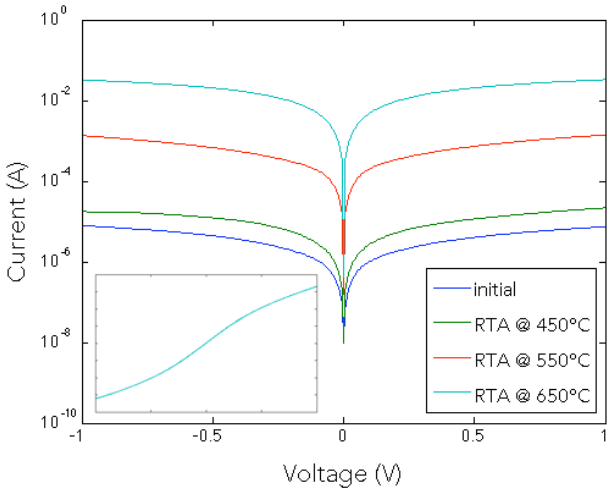
Electrical characterization is carried out in a prober using a Keithley 2636 SourceMeter. An electrical potential difference is imposed with a ramp from -1V to 1V across the IDE (figure I.6a.) as well as a front electrode and the aluminum electrode on the backside (figure I.6b.). This last measurement can isolate the behavior of a single electrode of IDE. For clarity, we will call the first measurement *inter-electrodes measurement* and the second measurement, *transverse measurement*.

The graphs in Figure I.7 show IV measurements before and after RTA annealing at 450 °C, 550 °C and 650 °C on non-porosified sample. Graph I.7a. is a transverse measurement and graph I.7b. is a inter-electrodes measurement. In Inset, IV measurements after RTA at 650 °C in linear scale are shown.

Without annealing, the contact between the metal and the silicon has a good rectifier behavior, the curve is asymmetric and the leakage current (current for negative potential) is limited (figure I.7a.). The inter-current electrodes (figure I.7b.) is symmetrical and is identical to the leakage current measured in the previous graph. This behavior is



a.



b.

Figure I.7: IV measurements before and after RTA annealing of a sample without porous layer at different temperatures (a.) a transverse measurement and (b.) an inter-electrodes measurement. Inset : IV measurement after RTA at 650 °C in linear scale.

logical since when the inter-electrode measurement, the two contacts are connected in opposite direction diodes (head to tail). When one is in passing mode, the other is in blocking mode and vice versa. The diode

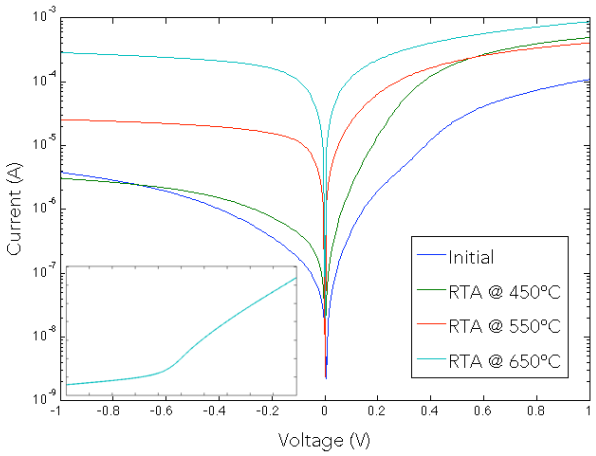
in blocking mode imposes electrical current value. The equivalent circuit for this behavior was simulated in Appendix C (page 231).

Annealing at 450 °C maintains a rectifying behavior. Forward and reverse currents increase slightly. Annealing 550 °C decreases the rectifier behavior. The asymmetry of the curve is less pronounced. The leakage current is gaining two orders of magnitude. Annealing at 650 °C totally destroyed the rectifier contact behavior. The curve is quasi symmetrical. The leakage current gets three orders of magnitude. Contact became ohmic.

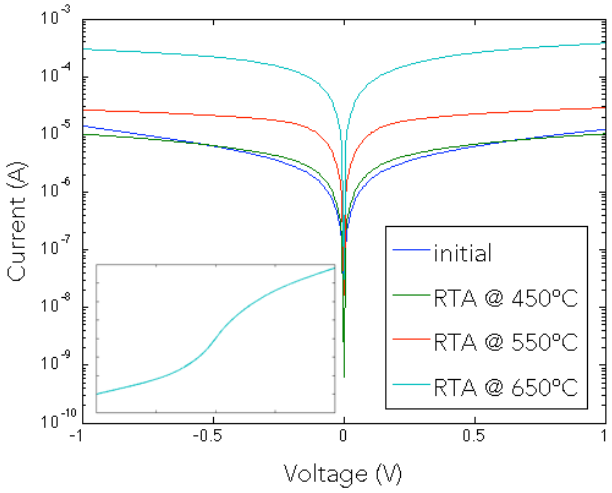
The graphs in Figure I.8 show IV measurements before and after RTA annealing at 450 °C, 550 °C and 650 °C on porosified sample. Graph I.8a. is a transverse measurement and graph I.8b. is a inter-electrodes measurement. In Inset, IV measurements after RTA at 650 °C in linear scale are shown.

Similar behaviors to non-porosified sample are observed. Before RTA annealing, the leakage current is similar to the leakage current of the non-porosified sample. However, there is an order of magnitude to the current in direct bias between the two samples. As for the non-sample porosified, the higher the annealing temperature is, the more the rectifying behavior is reduced. Annealing at 650 °C destroyed the rectifier contact behavior. But the curve is non-symmetrical. The leakage current gets two orders of magnitude, which is less than in the case of the non-sample porosified.

The porous silicon acts as a series resistor between the two electrical contacts. When the current is limited by the diode effect of the contacts, the series resistance is substantially "transparent". As leakage current increases with the annealing temperature, the influence of the series resistor increase and porous layer becomes the current-limiting element. We assume that the current limitation by the resistivity of the porous layer is at the origin of the difference between IV measurements of two kinds of samples. The non-symmetry of the IV curve after a RTA annealing at 650 °C can be caused from the not completely removed rectifier behavior. As a higher temperature affects the condition of the metal, we assume that a longer annealing could more reduce or eliminate the rectifier behavior of metal/silicon junction in porous samples.



a.



b.

Figure I.8: IV measurements before and after RTA annealing a porosified sample at different temperatures (a.) a transverse measurement and (b.) an inter-electrodes measurement. Inset : IV measurement after RTA at 650 °C in linear scale.

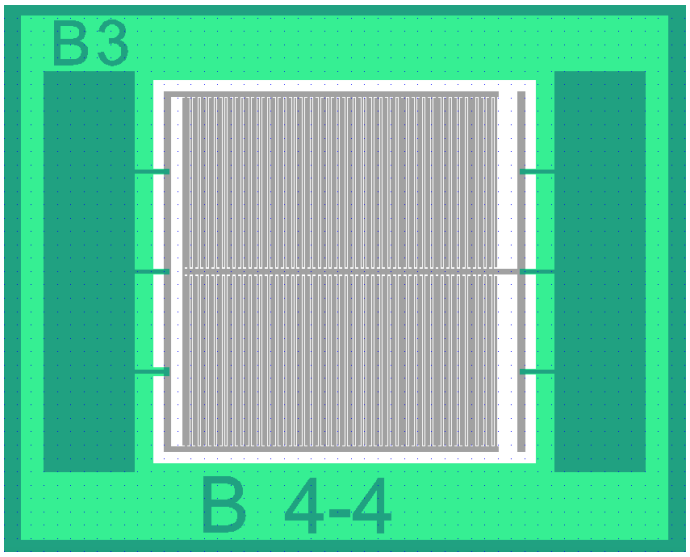


Figure I.9: The two masking levels for electodes geometry 4 μm width and spaced of 4 μm.

I.2 Gas sensor design

Figure I.9 shows the microsensor design. The electrodes width and the electrodes spacing are fixed to 4 μm. The dimensions of the openings in the nitride layer are to 750 x 750 μm.

The flow process is composed of two masking levels. The first mask level is the openings pattern in silicon nitride (figure I.10a.). The second level is the metal electrodes pattern (figure I.10b.).

The first masking level consists in squares of 750 $\times$ 750 μm (figure I.11a.). At under the metal electrodes, strips of Si_3N_4 over a distance of 50 μm were kept to avoid a short circuit between the metal and the bulk silicon at the place of Si_3N_4 step (figure I.12).

The metal pattern are two interdigitated electrodes as in figure I.11b..The shape of the electrodes was designed to promote a homogeneous distribution of electric current throughout the porous layer.

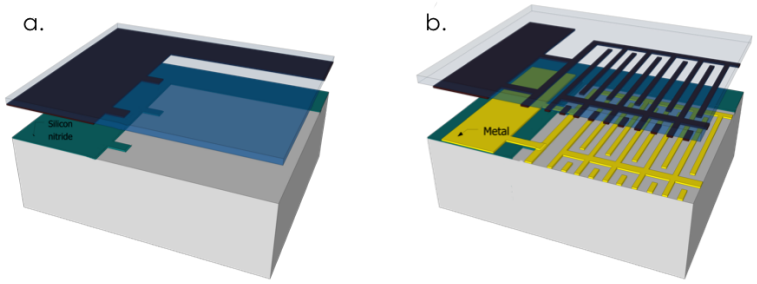
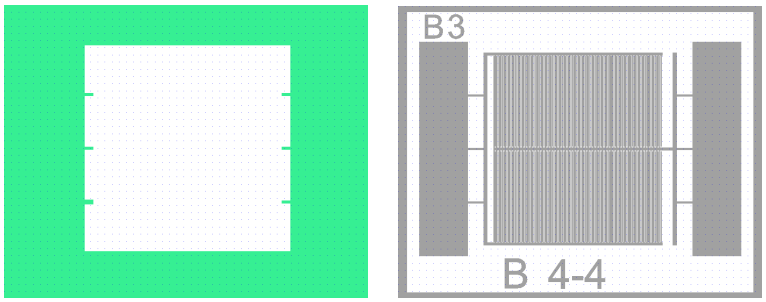


Figure I.10: Schematic drawing of the two masking levels.



a. b.

Figure I.11: (a.) First masking level: patterning of the porous silicon areas. The mask is positive. (b.) Second masking level: patterning of metal electrodes. The mask is negative.

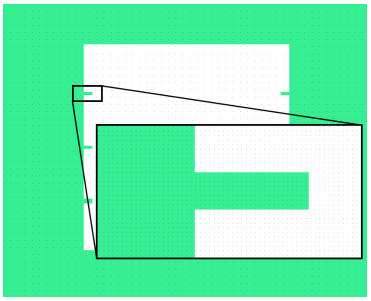


Figure I.12: Zoom on a strip. Silicon nitride extend onto the membrane to prevent a short circuit between metal and bulk substrate at the place of Si_3N_4 step.

Bibliography

[1] Peter Gründler. *Chemical Sensors.* An Introduction for Scientists and Engineers. Springer, January 2007.

[2] S Roy Morrison. Selectivity in semiconductor gas sensors. *Sensors and Actuators*, 12(4):425–440, 1987.

[3] A Uhlir. Electrolytic Shaping of Germanium and Silicon. *Bell Syst. Technol. J.*, 35:333–347, 1956.

[4] L T Canham. Silicon quantum wire array fabrication by electrochemical and chemical dissolution of wafers. *Appl. Phys. Lett.*, 57(10):1046–1048, September 1990.

[5] Nobuyoshi Koshida and Hideki Koyama. Visible electroluminescence from porous silicon. *Appl. Phys. Lett.*, 60(3):347–349, 1992.

[6] Z C Feng and R Tsu. *Porous Silicon.* World Scientific, 1994.

[7] Volker Lehmann. *The electrochemistry of silicon.* instrumentation, science, materials and applications. Vch Verlagsgesellschaft Mbh, December 2010.

[8] Sebastian P Scheeler, Simon Ullrich, Stefan Kudera, and Claudia Pacholski. Fabrication of porous silicon by metal-assisted etching using highly ordered gold nanoparticle arrays. *Nanoscale Res Lett*, 7(1):450, 2012.

[9] M Hajj-Hassan, M C Cheung, and V P Chodavarapu. Ultra-thin porous silicon membranes fabricated using dry etching. *Micro Nano Lett.*, 6(4):226, 2011.

[10] M Mehran, Z Sanaee, M Abdolahad, and S Mohajerzadeh. Controllable silicon nano-grass formation using a hydrogenation assisted deep reactive ion etching. *Materials Science in Semiconductor Processing*, 14(3-4):199–206, September 2011.

[11] T Ripenbein, D Golodnitsky, M Nathan, and E Peled. Novel porous-silicon structures for 3D-interlaced microbatteries. *Electrochim Acta*, 56(1):37–41, December 2010.

[12] R L Smith and S D Collins. Porous silicon formation mechanisms. *J. Appl Phys.*, 71(8):R1–R22, 1992.

[13] V LEHMANN and U G osele. POROUS SILICON FORMATION - A QUANTUM WIRE EFFECT. *Appl. Phys. Lett.*, 58(8):856–858, 1991.

[14] M J Sailor. *Porous Silicon in Practice*. Preparation, Characterization and Applications. John Wiley & Sons, January 2012.

[15] GregoryX Zhang. Porous Silicon: Morphology and Formation Mechanisms. In C G Vayenas, RalphE White, and MariaE Gamboa-Adelco, editors, *Modern Aspects of Electrochemistry*, pages 65–133. Springer US, 2006.

[16] J Carstensen S Ottow Silke Rönnebeck and H Föll. Crystal Orientation Dependence of Macropore Growth in n-Type Silicon. pages 1–3, October 1999.

[17] M Christophersen, J Carstensen, A Feuerhake, and H F oll. Crystal orientation and electrolyte dependence for macropore nucleation and stable growth on p-type Si. *Materials Science and Engineering: B*, 69-70:194–198, December 1999.

[18] M Christophersen, J Carstensen, S Ronnebeck, C Jäger, W Jäger, and H Foll. Crystal orientation dependence and anisotropic properties of macropore formation of p-and n-type silicon. *J Electrochem Soc*, 148(6):E267–E275, 2001.

[19] Emeline Méry. Intégration du silicium poreux dans des microsystèmes fluidiques. INSA de Lyon, 2006.

[20] S Matthias, F M uller, J Schilling, and U G osele. Pushing the limits of macroporous silicon etching. *Appl. Phys. A*, 80(7):1391–1396, January 2005.

[21] Dimitrios N Pagonis and Androula G Nassiopoulou. Free-standing macroporous silicon membranes over a large cavity for filtering and lab-on-chip applications. *Microelectron Eng*, 83(4-9):1421–1425, 2006.

[22] Guillaume de Souza. *Purification des gaz par le procede PSA*. Ed. Techniques Ingénieur, September 2009.

[23] James R Welty, Charles E Wicks, Robert E Wilson, and Gregory L Rorrer. *Fundamentals of momentum, heat, and mass transfer; 5th ed.* Wiley, Hoboken, NJ, 2008.

[24] Xiayan Wang, Chang Cheng, Shili Wang, and Shaorong Liu. Electroosmotic pumps and their applications in microfluidic systems. *Microfluid Nanofluid*, 2009.

[25] M J Sailor. *Porous Silicon in Practice*. Preparation, Characterization and Applications. John Wiley & Sons, January 2012.

[26] A Wolf and R Brendel. Thermal conductivity of sintered porous silicon films. *Thin Solid Films*, 513(1-2):385–390, August 2006.

[27] G Gesele, J Linsmeier, V Drach, J Fricke, and R Arens-Fischer. Temperature-dependent thermal conductivity of porous silicon. *J Phys D Appl Phys*, 30(21):2911–2916, January 1999.

[28] G Kaltsas and AG Nassiopoulou. Novel C-MOS compatible monolithic silicon gas flow sensor with porous silicon thermal isolation. *Sensor Actuat A-Phys*, 76(1-3):133–138, 1999.

[29] C Tsamis, A G Nassiopoulou, and A Tserepi. Thermal properties of suspended porous silicon micro-hotplates for sensor applications, 2003.

[30] Walter Lang. Silicon microstructuring technology. *Mat Sci Eng R*, 17(1):1–55, September 1996.

[31] P STEINER and W Lang. Micromachining applications of porous silicon. *Thin Solid Films*, 255(1-2):52–58, January 1995.

[32] Th Bischoff, G Müller, W Welser, and F Koch. Frontside micromachining using purous-silicon sacrificial-layer technologies. *Sensor Actuat A-Phys*, 60(1-3):228–234, May 1997.

[33] Hans Artmann and Wilhelm Frey. Porous silicon technique for realization of surface micromachined silicon structures with large gaps. *Sensor Actuat A-Phys*, 74(1-3):104–108, April 1999.

[34] G Kaltsas and A G Nassiopoulos. Bulk silicon micromachining using porous silicon sacrificial layers. *Microelectron Eng*, 35(1-4):397–400, February 1997.

[35] P M Fauchet, L Tsybeskov, S P Duttagupta, and K D Hirschman. Stable photoluminescence and electroluminescence from porous silicon. *Thin Solid Films*, 297(1-2):254–260, April 1997.

[36] Qing-lan Ma, Rui Xiong, and Yuan Ming Huang. Tunable photoluminescence of porous silicon by liquid crystal infiltration. *J. Lumin.*, 131(10):2053–2057, October 2011.

[37] Michael J Sailor and Elizabeth C Wu. Photoluminescence-Based Sensing With Porous Silicon Films, Microparticles, and Nanoparticles. *Adv. Funct. Mater.*, 19(20):3195–3208, October 2009.

[38] Serdar Ozdemir and James L Gole. The potential of porous silicon gas sensors. *Curr Opin Solid St M*, 11(5-6):92–100, 2007.

[39] Bayram Unal. Quenching influence of cell culture medium on photoluminescence and morphological structure of porous silicon. *Appl Surf Sci*, 258(1):207–211, October 2011.

[40] Ilaria Rea, Emanuele Orabona, Ivo Rendina, and Luca De Stefano. Porous silicon integrated photonic devices for biochemical optical sensing. *A VOIR DANS LA PUBLI!!!*

[41] D C Tessier, S Boughaba, M Arbour, P Roos, and G Pan. Improved surface sensing of DNA on gas-etched porous silicon. *Sensor Actuat B-Chem*, 120(1):220–230, December 2006.

[42] Andrew Jane, Roman Dronov, Alastair Hodges, and Nicolas H Voelcker. Porous silicon biosensors on the advance. *Trends in Biotechnology*, 27(4):230–239, 2009.

[43] T V Semikina and A N Shmyryeva. Porous silicon in solar cells technology. *Renewable Energy*, 15(1):479–482, 1998.

[44] E Osorio, R Urteaga, L N Acquaroli, G García-Salgado, H Juaréz, and R R Koropecki. Optimization of porous silicon multilayer as antireflection coatings for solar cells. *Solar Energy Materials and Solar Cells*, 95(11):3069–3073, November 2011.

[45] Maïlys Grau, Nhat-Tai Nguyen, Alain Straboni, and Mustapha Lemiti. Structural and Optical Properties of Annealed Porous Silicon Bragg Reflector for Thin-Film Crystalline Silicon Solar Cells. *Energy Procedia*, 10:8–13, January 2011.

[46] D Hunkel, M Marso, R Butz, R Arens-Fischer, and H Luth. Integrated photometer with porous silicon interference filters. *Materials Science and Engineering: B*, 69-70:100–103, January 2000.

[47] Luca De Stefano, Ivo Rendina, Luigi Moretti, and Andrea Mario Rossi. Optical sensing of flammable substances using porous silicon microcavities. *Materials Science and Engineering: B*, 100(3):271–274, July 2003.

[48] P Ferrand. Le silicium nanoporeux : microstructuration diélectrique et application aux structures photoniques avancées. *Ann. Phys. Fr.*, 27(2):1–121, 2002.

[49] P Ferrand, R Romestain, and J Vial. Photonic band-gap properties of a porous silicon periodic planar waveguide. *Phys Rev B*, 63(11):115106, February 2001.

[50] Didac Vega, Jordi Reina, and Angel Rodríguez. Macroporous silicon photonic crystals for gas sensing. In *2013 Spanish Conference on Electron Devices (CDE)*, pages 143–146. IEEE.

[51] S Rowson, A Chelnokov, and J M Lourtioz. Two-Dimensional Photonic Crystals in Macroporous Silicon: From Mid-Infrared (10 m) to Telecommunication Wavelengths (1.3-1.5 m). *Journal of Lightwave Technology*, 17(11):1989–1989, November 1999.

[52] F M uller, A Birner, U G osele, V LEHMANN, S Ottow, and H F oll. Structuring of macroporous silicon for applications as photonic crystals. *J. of Porous Mat.*, 7:201–104, 2000.

[53] S Desplobain, G Gautier, J Semai, L Ventura, and M Roy. Investigations on porous silicon as electrode material in electrochemical capacitors. *physica status solidi (c)*, 4(6):2180–2184, May 2007.

[54] Madhuri Thakur, Mark Isaacson, Steven L Sinsabaugh, Michael S Wong, and Sibani Lisa Biswal. Gold-coated porous silicon films as anodes for lithium ion batteries. *J Power Sources*, 205:426–432, May 2012.

[55] Heon-Cheol Shin, James A Corno, James L Gole, and Meilin Liu. Porous silicon negative electrodes for rechargeable lithium batteries. *J Power Sources*, 139(1-2):314–320, January 2005.

[56] Dae-Keun Kang, James A Corno, James L Gole, and Heon-Cheol Shin. Microstructured Nanopore-Walled Porous Silicon as an Anode Material for Rechargeable Lithium Batteries. *J Electrochem Soc*, 155(4):A276, 2008.

[57] Zhong He, Shiunchin Wang, Xianqin Wang, and Zafar Iqbal. Hydrogen storage in hierarchical nanoporous silicon-carbon nanotube architectures. *Int. J. Energy Res.*, 37(7):754–760, November 2012.

[58] Tayyar Dzhafarov and Sureyya Aydin Yuksel. Nano-porous silicon-based mini hydrogen fuel cells. *Alternative fuel, Intech, Rijeka, Croatia*, page 309, 2011.

[59] Kuan-Lun Chu, Mark A Shannon, and Richard I Masel. Porous silicon fuel cells for micro power generation. *J. Micromech. Microeng.*, 17(9):243, September 2007.

[60] T Pichonat, B Gauthier-Manuel, and D Hauden. A new proton-conducting porous silicon membrane for small fuel cells. *Chem Eng J*, 101(1-3):107–111, 2004.

[61] K Grigoras, S Franssila, T Sikanen, T Kotiaho, and R Kostiainen. Fabrication of porous membrane filter from p-type silicon. *Phys Status Solidi A*, 202(8):1624–1628, 2005.

[62] A Kovacs and U Mescheder. Transport in Nanostructured Porous Silicon Layers. *Procedia Engineering*, 25:1569–1572, January 2011.

[63] Milagros Wong-Sifuentes, Makoto Nanko, and Joaquín Lira-Olivares. Synthesis and Characterization of a Porous Silicon Filter with Si_3N_4 Whiskers. *DDF*, 289-292:185–194, April 2009.

[64] A A Agrawal, B J Nehilla, K V Reisig, T R Gaborski, D Z Fang, C C Striemer, P M Fauchet, and J L McGrath. Porous nanocrystalline silicon membranes as highly permeable and molecularly thin substrates for cell culture. *Biomaterials*, 31(20):5408–5417, July 2010.

[65] Christopher C Striemer, Thomas R Gaborski, James L McGrath, and Philippe M Fauchet. Charge- and size-based separation of macromolecules using ultrathin silicon membranes. *Nature*, 445(7129):749–753, February 2007.

[66] Alexandra Splinter, Jörg Stürmann, Olaf Bartels, and Wolfgang Benecke. Micro membrane reactor: a flow-through membrane for gas pre-combustion. *Sensor Actuat B-Chem*, 83(1):169–174, 2002.

[67] Margherita Bassu, Salvatore Surdo, Lucanos Marsilio Strambini, and Giuseppe Barillaro. Electrochemical Micromachining as an

Enabling Technology for Advanced Silicon Microstructuring. *Adv. Funct. Mater.*, 22(6):1222–1228, January 2012.

[68] Margherita Bassu, Lucanos M Strambini, and Giuseppe Barillaro. Advances in Electrochemical Micromachining of Silicon: Towards MEMS Fabrication. *Procedia Engineering*, 25:1653–1656, January 2011.

[69] C Pramanik, T Islam, and H Saha. Temperature compensation of piezoresistive micro-machined porous silicon pressure sensor by ANN. *Microelectronics Reliability*, 46(2-4):343–351, February 2006.

[70] T Toriyama and S Sugiyama. Single crystal silicon piezoresistive nano-wire bridge. *Sensor Actuat A-Phys*, 108(1-3):244–249, November 2003.

[71] K Kolokolov, A Savin, S Beneslavski, N Minina, and O Hansen. Energy spectrum and topology evolution of the Fermi surface of two-dimensional holes in GaAs/Al0.5Ga0.5As heterostructures under uniaxial compression: Theory and experiment. *Phys Rev B*, 59(11):7537–7545, March 1999.

[72] T Hadjersi and N Gabouze. Photodetectors based on porous silicon produced by Ag-assisted electroless etching. *Optical Materials*, 30(6):865–869, February 2008.

[73] V Torres-Costa, R J Martín-Palma, and J M Martínez-Duart. All-silicon color-sensitive photodetectors in the visible. *Materials Science and Engineering: C*, 27(5-8):954–956, September 2007.

[74] L A Balagurov, S C Bayliss, S Ya Andrushin, A F Orlov, B Unal, D G Yarkin, and E A Petrova. Metal/PS/c-Si photodetectors based on unoxidized and oxidized porous silicon. *Solid State Electronics*, 45(9):1607–1611, September 2001.

[75] Hernandez, Martinez, Diaz, Juarez, Rosendo, Galeazzi, Garcia, and Juarez. Fabrication, characterization, and analysis of photodetectors metal-porous silicon with different geometry and thickness of the porous silicon layer. *Microelectronics Journal*, 39(3-4):5–5, February 2008.

[76] A F Abd Rahim, M R Hashim, and N K Ali. High sensitivity of palladium on porous silicon MSM photodetector. *Physica B*, 406(4):1034–1037, February 2011.

[77] Saakshi Dhanekar and Swati Jain. Porous silicon biosensor: Current status. *Biosens Bioelectron*, 41(C):54–64, March 2013.

[78] Vicky Vamvakaki and Nikos A Chaniotakis. DNA Stabilization and Hybridization Detection on Porous Silicon Surface by EIS and Total Reflection FT-IR Spectroscopy. *Electroanalysis*, 20(17):1845–1850, September 2008.

[79] Mariusz Tichoniuk, Marta Ligaj, and Marian Filipiak. Application of DNA Hybridization Biosensor as a Screening Method for the Detection of Genetically Modified Food Components. *Sensors*, 8(4):2118–2135, March 2008.

[80] M M Archer, M M Christophersen, and P M PM Fauchet. Macroporous Silicon Electrical Sensor for DNA Hybridization Detection. *Biomedical Microdevices*, 6(3):203–211, August 2004.

[81] Deng Zhang and Evangelyn C Alocilja. Characterization of nanoporous silicon-based DNA biosensor for the detection of Salmonella Enteritidis. *Ieee Sens J*, 8(5-6):775–780, 2008.

[82] G A Melikjanyan and Kh S Martirosyan. POSSIBILITY OF APPLICATION OF POROUS SILICON AS GLUCOSE BIOSENSOR . *ajp.asj-oa.am*, January 2012.

[83] G Recio-Sanchez, G Dominguez-Canizares, M Manso, I Preda, V Torres-Costa, A Gutierrez, L Soriano, and R J Martin-Palma. Surface Functionalization of Nanostructured Porous Silicon by APTS: Toward the Fabrication of Electrical Biosensors of Bacterium Escherichia coli. *CNANO*, 7(2):178–182, April 2011.

[84] Gonzalo Recio-Sánchez, Vicente Torres-Costa, Miguel Manso, Darío Gallach, Juan López-García, and Raúl J Martín-Palma. Towards the Development of Electrical Biosensors Based on Nanostructured Porous Silicon. *MATERIALS*, 3:755–763, January 2010.

[85] R Dev Das, C RoyChaudhuri, S Maji, S Das, and H Saha. Macroporous silicon based simple and efficient trapping platform for electrical detection of Salmonella typhimurium pathogens. *Biosens Bioelectron*, 24(11):3215–3222, 2009.

[86] Andrea M Rossi, Lili Wang, Vytas Reipa, and Thomas E Murphy. Porous silicon biosensor for detection of viruses. *Biosens Bioelectron*, 23(5):741–745, December 2007.

[87] Sanket Tembe, Prajakta S Chaudhari, S V Bhoraskar, S F D'Souza, and Meena S Karve. Conductivity-Based Catechol Sensor Using Tyrosinase Immobilized in Porous Silicon. *Sensors Journal, IEEE*, 8(9):1593–1597.

[88] R Ravi Kumar Reddy, Indranil Basu, Enakshi Bhattacharya, and Anju Chadha. Estimation of triglycerides by a porous silicon based potentiometric biosensor. *Curr Appl Phys*, 3(2-3):155–161, April 2003.

[89] Marion Thust, M J Schöning, S Frohnhoff, R Arens-Fischer, P Kordos, and H Luth. Porous silicon as a substrate material for potentiometric biosensors. *Meas. Sci Technol.*, 7(1):26–29, January 1999.

[90] Giuseppe Barillaro. Porous Silicon Gas Sensing. In *link.springer.com*, pages 1–12. Springer International Publishing, Cham, May 2014.

[91] Mikko Björkqvist, Jarno Salonen, Jaani Tuura, Tero Jalkanen, and Vesa-Pekka Lehto. Detecting amine vapours with thermally carbonized porous silicon gas sensor. *physica status solidi (c)*, 6(7):1769–1772, July 2009.

[92] Mikko Björkqvist, Jarno Salonen, Jaani Paski, and Ensio Laine. Characterization of thermally carbonized porous silicon humidity sensor. *Sensor Actuat A-Phys*, 112(2-3):244–247, May 2004.

[93] Z M Rittersma, A Splinter, A Bödecker, and W Benecke. A novel surface-micromachined capacitive porous silicon humidity sensor. *Sensor Actuat B-Chem*, 68(1-3):210–217, August 2000.

[94] Rolfe C Erson, Richard S Muller, and Charles W Tobias. Investigations of porous silicon for vapor sensing. *Sensor Actuat A-Phys*, 23(1-3):835–839, April 2001.

[95] S Belhousse, H Cheraga, N Gabouze, and R Outamzabet. Fabrication and characterisation of a new sensing device based on hydrocarbon groups (CHx) coated porous silicon. *Sensor Actuat B-Chem*, 100(1-2):250–255, June 2004.

[96] A Foucaran, B Sorli, M Garcia, F Pascal-Delannoy, A Giani, and A Boyer. Porous silicon layer coupled with thermoelectric cooler: a humidity sensor. *Sensor Actuat A-Phys*, 79(3):189–193, December 1999.

[97] M Archer, M Christophersen, and P M Fauchet. Electrical porous silicon chemical sensor for detection of organic solvents. *Sensor Actuat B-Chem*, 106(1):347–357, February 2004.

[98] Y K Fang, S B Hwang, C Y Lin, and C C Lee. Trench Pd/Si metal-oxide-semiconductor Schottky barrier diode for a high sensitivity hydrogen gas sensor. *Applied Physics Letters (ISSN 0003-6951)*, 57:2686–2688, December 1990.

[99] N Naderi, M R Hashim, and T S T Amran. Enhanced physical properties of porous silicon for improved hydrogen gas sensing. *Superlattice Microst*, 51(5):626–634, May 2012.

[100] Zeno Gaburro, Claudio J Oton, Lorenzo Pavesi, and Lucio Pancheri. Opposite effects of NO2 on electrical injection in porous silicon gas sensors. *Appl. Phys. Lett.*, 84(2):4388, May 2004.

[101] J Mares. Influence of humidity on transport in porous silicon. *Thin Solid Films*, 255:272–275, January 1995.

[102] D Stievenard and D Deresmes. Are electrical properties of an aluminum–porous silicon junction governed by dangling bonds? *Appl. Phys. Lett.*, 67(11):1570–1572, 1995.

[103] A Foucaran. Porous silicon layers used for gas sensor applications. *Thin Solid Films*, 297(1-2):317–320, April 1997.

[104] L Pancheri, C J Oton, Z Gaburro, G Soncini, and L Pavesi. Very sensitive porous silicon NO2 sensor. *Sensor Actuat B-Chem*, 89(3):237–239, April 2003.

[105] F Razi, A Iraji zad, and F Rahimi. Investigation of hydrogen sensing properties and aging effects of Schottky like Pd/porous Si. *Sensor Actuat B-Chem*, 146(1):53–60, April 2010.

[106] J Kanungo, H Saha, and S Basu. Pd sensitized porous silicon hydrogen sensor-Influence of ZnO thin film. *Sensor Actuat B-Chem*, 147(1):128–136, 2010.

[107] D Bilenko, O Belobrovaya, E Jarkova, O Coldobanova, I Mysenko, and E Khasina. Sensors on low-dimensional silicon structures. *Sensor Actuat A-Phys*, 62(1-3):621–623, July 1997.

[108] Giuseppe Barillaro, A Nannini, and F Pieri. APSFET: a new, porous silicon-based gas sensing device. *Sensor Actuat B-Chem*, 93(1-3):263–270, 2003.

[109] Giuseppe Barillaro, A Nannini, F Pieri, and LM Strambini. Temperature behavior of the APSFET - a porous silicon-based FET gas sensor. *Sensor Actuat B-Chem*, 100(1-2):185–189, 2004.

[110] Giuseppe Barillaro, A Diligenti, G Marola, and LM Strambini. A silicon crystalline resistor with an adsorbing porous layer as gas sensor. *Sensor Actuat B-Chem*, 105(2):278–282, 2005.

[111] Giuseppe Barillaro, A Diligenti, A Nannini, LM Strambini, E Comini, and G Sberveglieri. Low-concentration NO2 detection with an adsorption porous silicon FET. *Ieee Sens J*, 6(1):19–23, 2006.

[112] Giuseppe Barillaro, G M Lazzerini, and L M Strambini. Modeling of porous silicon junction field effect transistor gas sensors: Insight into NO2 interaction. *App. Phys. Lett.*, 96(16):162105, 2010.

[113] Giuseppe Barillaro, P Bruschi, G M Lazzerini, and L M Strambini. Validation of the Compatibility Between a Porous Silicon-Based Gas Sensor Technology and Standard Microelectronic Process. *Ieee Sens J*, 10(4):893–899, 2010.

[114] G M Lazzerini, L M Strambini, and G Barillaro. Addressing Reliability and Degradation of Chemitransistor Sensors by Electrical Tuning of the Sensitivity. *Sci. Rep.*, 3, 2013.

[115] Giuseppe Barillaro, A Difigenti, and L M Strambini. p(+)-n diodes with a lateral porous layer as gas sensors. *Phys Status Solidi A*, 204(5):1399–1403, 2007.

[116] Giuseppe Barillaro, A Diligenti, LM Strambini, E Comini, and G Faglia. NO2 adsorption effects on p+–n silicon junctions surrounded by a porous layer. *Sensor Actuat B-Chem*, 134(2):922–927, September 2008.

[117] R Prabakaran, H Aguas, E Fortunato, R Martins, and I Ferreira. n-PS/a-Si:H heterojunction for device application. *J Non-Cryst Solids*, 354:2632–2636, May 2008.

[118] L Boarino, C Baratto, F Geobaldo, and G Amato. NO 2 monitoring at room temperature by a porous silicon gas sensor. *Materials Science and ...*, pages 1–5, 2000.

[119] R Angelucci, A Poggi, L Dori amd G C Cardinali, A Parisinia, A Tagliania, M Mariasaldi, and F Cavani. Permeated porous silicon for hydrocarbon sensor fabrication. *Sensor Actuat A-Phys*, 74(1-3):95–99, January 2000.

[120] R ANGELUCCI, A POGGI, L DORI, A TAGLIANI, G C CARDINALI, F CORTICELLI, and M MARISALDI. Permeated Porous Silicon Suspended Membrane as Sub-ppm Benzene Sensor for Air Quality Monitoring. *Journal of Porous Materials*, 7:197–200, July 2000.

[121] C Baratto, E Comini, G Faglia, G Sberveglieri, G Di Francia, F De Filippo, V La Ferrara, L Quercia, and L Lancellotti. Gas detection with a porous silicon based sensor. *Sensor Actuat B-Chem*, 65(1-3):257–259, 2000.

[122] G Di Francia, V La Ferrara, L Quercia, and G Faglia. Sensitivity of Porous Silicon Photoluminescence to Low Concentrations of CH4 and CO - Springer. *Journal of Porous Materials*, 7(1/3):287–290, 2000.

[123] A Šetkus, A Galdikas, A Mironas, V Strazdien, I Šimkien, I Ancutien, V Janickis, S Kačiulis, G Mattogno, and G M Ingo. The room temperature ammonia sensor based on improved CuxS-micro-porous-Si structure. *Sensor Actuat B-Chem*, 78(1-3):208–215, August 2001.

[124] Sanjay Chakane, Anisha Gokarna, and S V Bhoraskar. Metallophthalocyanine coated porous silicon gas sensor selective to NO2. *Sensor Actuat B-Chem*, 92(1-2):1–5, July 2003.

[125] Zeno Gaburro, Paolo Bettotti, Massimo Saiani, Lorenzo Pavesi, Lucio Pancheri, Claudio J Oton, and Nestor Capuj. Role of microstructure in porous silicon gas sensors for NO2. *Appl. Phys. Lett.*, 85(4):555, July 2004.

[126] Stephen E Lewis, John R DeBoer, James L Gole, and Peter J Hesketh. Sensitive, selective, and analytical improvements to a porous silicon gas sensor. *Sensor Actuat B-Chem*, 110(1):54–65, September 2005.

[127] Kevin Luongo, Altagrace Sine, and Shekhar Bhansali. Development of a highly sensitive porous Si-based hydrogen sensor using Pd nano-structures. *Sensor Actuat B-Chem*, 111-112:125–129, 2005.

[128] F Rahimi and A Iraji zad. Characterization of Pd nanoparticle dispersed over porous silicon as a hydrogen sensor. *J Phys D Appl Phys*, 40(23):7201–7209, November 2007.

[129] N Sankara Subramanian, R Vivek Sabaapathy, P Vickraman, G Vimal Kumar, R Sriram, and B Santhi. Investigations on Pd:SnO2/porous silicon structures for sensing LPG and NO2 gas. *Ionics*, 13(5):323–328, August 2007.

[130] V E Galstyan, Kh S Martirosyan, V M Aroutiounian, V M Arakelyan, A H Arakelyan, and P G Soukiassian. Investigations of hydrogen sensors made of porous silicon. *Thin Solid Films*, 517(1):239–241, November 2008.

[131] Kui-Qing Peng, Xin Wang, and Shuit-Tong Lee. Gas sensing properties of single crystalline porous silicon nanowires. *Appl. Phys. Lett.*, 95(24):243112–243112, 2009.

[132] Peng SUN, Ming HU, Mingda Li, and Shuangyun Ma. Nano-WO 3film modified macro-porous silicon (MPS) gas sensor. *J. Semicond.*, 33(5):054012, May 2012.

[133] Serdar Ozdemir and James L Gole. A phosphine detection matrix using nanostructure modified porous silicon gas sensors. *Sensor Actuat B-Chem*, 151(1):274–280, November 2010.

[134] C J Oton, L Pancheri, Z Gaburro, L Pavesi, C Baratto, G Faglia, and G Sberveglieri. Multiparametric porous silicon gas sensors with improved quality and sensitivity. *Phys. Stat. Sol. a*, 197(2):523–527, 2003.

[135] Andras Kovacs, Dirk Meister, and Ulrich Mescheder. Investigation of humidity adsorption in porous silicon layers. *Phys. Stat. Sol. a*, 206(6):1343–1347, June 2009.

[136] N Ali, M Hashim, and A Aziz. Effects of surface passivation in porous silicon as H2 gas sensor. *Solid State Electronics*, 52:1071–1074, July 2008.

[137] Galeazzo, Peres, Santos, and Peixoto. Gas sensitive porous silicon devices: responses to organic vapors. *Sensor Actuat B-Chem*, 93(1-3):7–7, July 2003.

[138] N Gabouze, S Belhousse, and H Cheraga. CHx - porous silicon structures for gas sensing applications. *physica status solidi (c)*, 2(9):3449–3452, June 2005.

[139] C Baratto, G Faglia, E Comini, G Sberveglieri, A Taroni, V La Ferrara, L Quercia, and G Di Francia. A novel porous silicon sensor for detection of sub-ppm NO2 concentrations. *Sensor Actuat B-Chem*, 77(1-2):62–66, 2001.

[140] E Massera, I Nasti, L Quercia, I Rea, and G Di Francia. Improvement of stability and recovery time in porous-silicon-based NO2 sensor. *Sensor Actuat B-Chem*, 102(2):195–197, September 2004.

[141] C RoyChaudhuri, S Gangopadhyay, R DevDas, S K Datta, and H Saha. High Performance Macroporous Silicon Chemical Sensor With Improved Phase Detection Electronics. *INTERNATIONAL JOURNAL ON SMART SENSING AND INTELLIGENT SYSTEMS*, 1(3):638.

[142] F Razia and A Iraji zad. Annealing effect on hydrogen sensitivity of electrodeposited Pd/Pororus Si. pages 1–2, November 2012.

[143] F Razi Astaraie, A Iraji zad, N S Taghavi, D Abbaszadeh, A Dolati, and S S Mahshid. Morphology and hydrogen sensing studies of the electrodeposited nanostructure palladium on porous silicon. *International Journal of Nanotechnology*, 6:892, 2009.

[144] Kang-San Kim and Gwiy-Sang Chung. Characterization of porous cubic silicon carbide deposited with Pd and Pt nanoparticles as a hydrogen sensor. *Sensor Actuat B-Chem*, 157(2):482–487, October 2011.

[145] A IRAJIZAD, F Rahimi, M CHAVOSHI, and M AHADIAN. Characterization of porous poly-silicon as a gas sensor. *Sensor Actuat B-Chem*, 100(3):341–346, May 2004.

[146] S Green and P Kathirgamanathan. Effect of oxygen on the surface conductance of porous silicon: towards room temperature sensor applications. *Mater Lett*, 52(1-2):106–113, January 2002.

[147] N Mendoza-Agüero, Y Kumar, S F Olive-Méndez, J Campos-Alvarez, and V Agarwal. Optimization of tungsten oxide films electro-deposited on macroporous silicon for gas sensing applications: Effect of annealing temperature. *Ceramics International*, August 2014.

[148] Mingda Li, Ming HU, Wenjun Yan, Shuangyun Ma, Peng Zeng, and Yuxiang Qin. NO2 sensing performance of p-type intermediate size porous silicon by a galvanostatic electrochemical etching method. *Electrochim Acta*, 113:354–360, December 2013.

[149] M Li, M Hu, P Zeng, S Ma, W Yan, and Y Qin. Effect of etching current density on microstructure and NH 3-sensing properties of porous silicon with intermediate-sized pores. *Electrochim Acta*, 2013.

[150] R Dev Das, C RoyChaudhuri, and S Das. Macroporous silicon as an interdigitated electrode-less platform for impedance based bacteria detection. In *2010 International Conference on Systems in Medicine and Biology (ICSMB)*, pages 121–125. IEEE.

[151] F Rahimi, A Iraji zad, and F Razi. Characterization of porous poly-silicon impregnated with Pd as a hydrogen sensor. *J Phys D Appl Phys*, 38(1):36–40, December 2004.

[152] Yun Wang, Seungwoo Park, John T W Yeow, Andreas Langner, and Frank Müller. A capacitive humidity sensor based on ordered macroporous silicon with thin film surface coating. *Sensor Actuat B-Chem*, 149(1):136–142, 2010.

[153] Yaqiao Wu, Ming HU, Yuxiang Qin, Xiaoying Wei, Shuangyun Ma, and Dali Yan. Enhanced response characteristics of p-porous silicon (substrate)/p-TeO2 (nanowires) sensor for NO2 detection. *Sensor Actuat B-Chem*, 195:181–188, May 2014.

[154] H Saha. Porous Silicon Sensors-Elusive and Erudite. *Int. J. on Smart Sensing and Intelligen Systems*, 1(1):34–56, 2008.

[155] S Maji, R Dev Das, M Jana, C RoyChaudhuri, N Mondal, S K Dutta, N R Bandopadhyay, and H Saha. Formation of ohmic contact by pre-annealing of shallow nanopores in macroporous silicon and its characterization. *Solid State Electronics*, 54(5):568–574, April 2010.

[156] P N Vinod. The ohmic properties and current–voltage characteristics of the screen-printed silicon solar cells with porous silicon surface. *Solid State Communications*, 149(23-24):957–961, June 2009.

[157] T D Dzhafarov, S S Aslanov, S H Ragimov, M S Sadigov, and S Aydin Yuksel. Effect of nanoporous silicon coating on silicon solar cell performance. *Vacuum*, 86(12):1875–1879, July 2012.

[158] Be Mahmoudi, N Gabouze, M Haddadi, Br Mahmoudi, H Cheraga, K Beldjilali, and D Dahmane. The effect of annealing on the sensing properties of porous silicon gas sensor: Use of screen-printed contacts. *Sensor Actuat B-Chem*, 123(2):680–684, May 2007.

[159] The Gwent Group, Leaders in paste manufacturing, sensor/ biosensor development and Instrumentation .

[160] Sami Franssila. *Introduction to Microfabrication*. John Wiley & Sons, October 2010.

[161] Zhipeng Huang, Nadine Geyer, Peter Werner, Johannes de Boor, and Ulrich Gösele. Metal-Assisted Chemical Etching of Silicon: A Review. *Adv Mater*, 23(2):285–308, September 2010.

[162] Formation of porous silicon on patterned substrates. pages 1–4, August 2011.

[163] Pierre Roberge. *Corrosion Engineering*. Principles and Practice. McGraw Hill Professional, March 2008.

[164] C L Eberling. *Dimethylformamide. In: Kirk RE, Othmer DF, Grayson M, Eckroth DV, eds. Kirk-Othmer encyclopedia of chemical technology, 3rd ed.*, volume 11. John Wiley & Sons, New York, NY, 1980.

[165] JEAN Juillard. Dimethylformamide: purification tests for purity and physical properties. *Pure Appl Chem*, 49(16):885–892, 1977.

[166] Raymond T Tung. Recent advances in Schottky barrier concepts. *Mat Sci Eng R*, 35(1):1–138, December 2000.

[167] B J Baliga. *Advanced Power Rectifier Concepts*. Springer, 2009.

[168] Bart Van Zeghbroeck. Principles of semiconductor devices. *Colorado University*, 2004.

[169] B Smith. Schottky barriers on p-type silicon. *Solid State Electronics*, 14:71–75, January 1971.

[170] M Turner. Metal-silicon Schottky barriers. *Solid State Electronics*, 11:291–300, March 1968.

[171] H C Card and E H Rhoderick. Studies of tunnel MOS diodes I. Interface effects in silicon Schottky diodes. *J Phys D Appl Phys*, 4(10):1589, 1971.

[172] Cetin, Sahin, Ayyildiz, and Turut. Ti/p-Si Schottky barrier diodes with interfacial layer prepared by thermal oxidation. *Physica B*, 364(1-4):9–9, July 2005.

[173] T Yamaguchi, H Kato, N Fujimura, and T Ito. Annealing behavior of electrical properties in plasma-exposed Ti/p-Si interfaces. *Thin Solid Films*, 396(1-2):119–125, September 2001.

[174] Subhash Chand and Saroj Bala. Simulation studies of current transport in metal–insulator–semiconductor Schottky barrier diodes. *Physica B*, 390(1-2):179–184, March 2007.

[175] P S Lee, D Mangelinck, K L Pey, J Ding, J Y Dai, C S Ho, and A See. On the Ni–Si phase transformation with/without native oxide. *Microelectron Eng*, 51:583–594, 2000.

[176] Dana Skácelová, Vladimir Danilov, Jan Schäfer, Antje Quade, Pavel Sťahel, Mirko Černák, and Jürgen Meichsner. Room temperature plasma oxidation in DCSBD: A new method for preparation of silicon dioxide films at atmospheric pressure. *Materials Science and Engineering: B*, 178(9):651–655, May 2013.

[177] H Kakiuchi, H Ohmi, M Harada, H Watanabe, and K Yasutake. Formation of silicon dioxide layers at low temperatures (150–400 °C) by atmospheric pressure plasma oxidation of silicon. *Sci Technol Adv Mat*, 8(3):137–141, July 2008.

[178] T Majamaa, O Kilpelä, and S Novikov. Fabrication of ultrathin silicon dioxide layers in room temperature by ultrahigh vacuum plasma oxidation. *Appl Surf Sci*, 136(1-2):17–21, October 1998.

[179] J C Tinoco, M Estrada, H Baez, and A Cerdeira. Room temperature plasma oxidation: A new process for preparation of ultrathin layers of silicon oxide, and high dielectric constant materials. *Thin Solid Films*, 496(2):546–554, February 2006.

[180] Modification of Al/Si interface and Schottky barrier height with chemical treatment. pages 1–4, July 2012.

[181] J C Yeoh, P W Green, T J Thornton, S Kaya, K Fobelets, and J M Fernández. MOS gated Si:SiGe quantum wells formed by anodic oxidation. *Semicond. Sci. Technol.*, 13(1):1442–1445, December 1998.

[182] Masashi Kato, Masaya Kimura, and Masaya Ichimura. Leakage Current Suppression by Passivation of Defects by Anodic Oxidation of 4H-SiC Schottky Contacts. *Jpn J Appl Phys*, 52(4S):04CP02, December 2013.

[183] S R Forrest. Organic-on-inorganic semiconductor contact barrier devices. *Appl. Phys. Lett.*, 41(1):1–5, 1982.

[184] Yunfei Liu, Jing Xie, Mingliang Zhang, Jinling Yang, and Fuhua Yang. An Effective Approach for Restraining Galvanic Corrosion of Polycrystalline Silicon by Hydrofluoric-Acid-Based Solutions. *J Microelectromech S*, 20(2):460–465.

[185] Valerie Bertagna. p- and n-Type Silicon Electrochemical Properties in Dilute Hydrofluoric Acid Solutions. *J Electrochem Soc*, 143(11):3532, 1996.

[186] E H Nicollian. Electrical properties of the Si–SiO2 interface and its influence on device performance and stability. *J Vac Sci Technol*, 14(5):1112, September 1977.

[187] MO Aboelfotoh. Influence of thin interfacial silicon oxide layers on the Schottky-barrier behavior of Ti on Si(100). *Phys. Rev., B Condens. Matter*, 39(8):5070–5078, March 1989.

[188] P L Hanselaer, W H Laflere, R L Van Meirhaeghe, and Felix Cardon. The influence of a HF and an annealing treatment on the

barrier height of p-and n-type Si MIS structures. *Appl Phys A-Mater*, 39(2):129–133, 1986.

[189] P Chattopadhyay and K Das. The origin of aging in Al–SiO2–Si tunnel diodes. *J. Appl Phys.*, 80(7):4229, 1996.

[190] L J Zeng, T Greibe, S Nik, P Delsing, and E Olsson. Interdiffusion at the Al/SiO2 interface in Al/AlOx/Al Josephson junctions. *European Microscopy Congress, Manchester Central, United Kingdom, 16th - 21st September 2012*.

[191] G Lammel, S Schweizer, and Ph Renaud. Microspectrometer based on a tunable optical filter of porous silicon. *Sensors and Actuators A*, 92:52–59, 2001.

[192] A G Nassiopoulou and G Kaltsas. Porous Silicon as an Effective Material for Thermal Isolation on Bulk Crystalline Silicon. *Phys Status Solidi A*, 182:307, 2000.

[193] M Hejjo Al Rifai, M Christophersen, S Ottow, J Carstensen, and H Foll. Potential, temperature and doping dependence for macropore formation on n-Si with backside-illumination. *Journal of Porous Materials*, 7(1-3):33–36, 2000.

[194] Moshe Ben-Chorin, Andreas Kux, and Israel Schechter. Adsorbate effects on photoluminescence and electrical conductivity of porous silicon. *Appl. Phys. Lett.*, 64(4):481, 1994.

[195] John Bardeen. Surface States and Rectification at a Metal Semi-Conductor Contact. *Physical Review*, 71(1):717–727, May 1947.

[196] R H Kingston. Water Vapor and the "Channel" Effect in n-p-n Junction Transistors. *Physical Review*, 93(2):346–347, January 1954.

[197] F Roozeboom. *Advanced Gate Stack, Source/drain, and Channel Engineering for Si-based CMOS 2: New Materials, Processes and Equipment*. ECS transactions. Electrochemical Society, 2006.

[198] J R Schrieffer. Effective Carrier Mobility in Surface-Space Charge Layers. *Physical Review*, 97(3):641–646, February 1955.

[199] W L Brown. n-Type Surface Conductivity on p-Type Germanium. *Physical Review*, 91(3):518–527, August 1953.

[200] Bruce E Deal, Maija Sklar, A S Grove, and E H Snow. Characteristics of the SurfaceState Charge (Qss) of Thermally Oxidized Silicon. *J Electrochem Soc*, 114(3):266–274, 1967.

[201] W Henrion, M Rebien, H Angermann, and A Röseler. Spectroscopic investigations of hydrogen termination, oxide coverage, roughness, and surface state density of silicon during native oxidation in air. *Appl Surf Sci*, 202(3):199–205, December 2001.

[202] H Angermann, W Henrion, M Rebien, and A Röseler. Wetchemical preparation and spectroscopic characterization of Si interfaces. *Appl Surf Sci*, 235(3):322–339, 2004.

[203] Oleksandr Malik and F Javier De la Hidalga-W. Physical and Technological Aspects of Solar Cells Based on Metal Oxide-Silicon Contacts with Induced Surface Inversion Layer. InTech, February 2013.

[204] Giuseppe Barillaro. Porous Silicon Gas Sensing. In Leigh Canham, editor, *Handbook of Porous Silicon*, pages 1–12–12. Springer International Publishing, Cham, 2014.

[205] Frèderique Cunin. Functional Coatings of Porous Silicon. In Leigh Canham, editor, *Handbook of Porous Silicon*, pages 1–16–16. Springer International Publishing, Cham, 2014.

[206] Ulrich Eberle, Bernd Müller, and Rittmar von Helmolt. Fuel cell electric vehicles and hydrogen infrastructure: status 2012. *Energy Environ. Sci.*, 5(10):8780, 2012.

[207] Honda Worldwide - FCX Clarity.

[208] S Nagano, T Kitajima, K Yoshida, Y Kazao, Y Kabata, D Murata, and K Nagakura. Development of world's largest hydrogen-cooled turbine generator. *Audio, Transactions of the IRE Professional Group on*, 2:657–652, July 2002.

[209] Ansaldo Energia HYDROGEN COOLED AND HYDROGEN AND STATOR WATER TURBOGENERATORS.

[210] Prabhu Soundarrajan and Frank Schweighardt. Hydrogen sensing and detection. *Hydrogen Fuel*, pages 495–534, 2009.

[211] Domenico Sanfilippo and Paul N Rylander. *Hydrogenation and Dehydrogenation*. Wiley-VCH Verlag GmbH & Co. KGaA, Weinheim, Germany, June 2000.

[212] Sukharev VY. *Handbook of Sensors and Actuators*, volume 4 of *Semiconductor Sensors in Physico-Chemical Studies*. Elsevier.

[213] A I Manilov and V A Skryshevsky. Hydrogen in porous silicon — A review. *Materials Science and Engineering: B*, 178(15):942–955, September 2013.

[214] N Gabouze, S Belhousse, H Cheraga, N Ghellai, Y Ouadah, Y Belkacem, and A Keffous. CO2 and H2 detection with a CHx/-porous silicon-based sensor. *Vacuum*, 80(9):986–989, June 2006.

[215] V M Arakelyan, V E Galstyan, Kh S Martirosyan, G E Shahnazaryan, V M Aroutiounian, and P G Soukiassian. Hydrogen sensitive gas sensor based on porous silicon/TiO"2"-"x structure. *Physica E*, 38(1-2):219–221, March 2007.

[216] V Aroutiounian, V Arakelyan, V Galstyan, K Martirosyan, and P Soukiassian. Hydrogen Sensor Made of Porous Silicon and Covered by TiO or ZnOAl Thin Film. *Sensors Journal, IEEE*, 9(1):9–12, December 2008.

[217] J Kanungo, H Saha, and S Basu. Room temperature metal–insulator–semiconductor (MIS) hydrogen sensors based on chemically surface modified porous silicon. *Sensor Actuat B-Chem*, 140(1):65–72, June 2009.

[218] R R J Maier, J S Barton, J D C Jones, S McCulloch, B J S Jones, and G Burnell. Palladium-based hydrogen sensing for monitoring of ageing materials. *Meas. Sci Technol.*, 17(5):1118–1123, April 2006.

[219] F A Lewis. *The palladium hydrogen system*. Academic Press, 1967.

[220] F D Manchester, A San-Martin, and J M Pitre. The H-Pd (hydrogen-palladium) system. *JPE*, 15(1):62–83, 1994.

[221] Constantinos Christofides and Andreas Mandelis. Solid-state sensors for trace hydrogen gas detection. *J. Appl Phys.*, 68(6):R1–R30, 1990.

[222] Su-Il Pyun, Chan Lim, and Kwang Bum Kim. An investigation of the electrochemical kinetics of deuterium insertion into a Pd membrane electrode in 0.1 M LiOD solution by the a.c. impedance technique. *J Alloy Compd*, 203:149–156, January 1994.

[223] V Polishchuk, E Souteyrand, J-R Martin, V I Strikha, and V A Skryshevsky. A study of hydrogen detection with palladium modified porous silicon. *Anal Chim Acta*, 375(3):205–210, November 1998.

[224] J H Scaff and E E Schumacher. Some Theoretical and Practical Aspects of Gases in Metals*. *Bell System Technical Journal*, 12(2):178–196, 1933.

[225] Martin Dornheim. Thermodynamics of Metal Hydrides: Tailoring Reaction Enthalpies of Hydrogen Storage Materials. InTech, November 2011.

[226] Sakintuna and Hirscher. Metal hydride materials for solid hydrogen storage: A review. *Int J Hydrogen Energ*, 32(9):20–20, May 2007.

[227] Gondor. Analysis of hydride formation for hydrogen storage: Pressure-composition isotherm curves modeling. *Intermetallic*, 15(7):11–11, June 2007.

[228] M Hansen, K P Anderko, and R P Elliott. Constitution of Binary Alloys. New York, McGraw-Hill, 1958.

[229] Lee, Lee, Koo, Lee, and Lee. Hysteresis behavior of electrical resistance in Pd thin films during the process of absorption and desorption of hydrogen gas. *Int J Hydrogen Energ*, 35(13):8–8, June 2010.

[230] Ingemar Lundström. Hydrogen sensitive MOS-structures: part 1: principles and applications. *Sensors and Actuators*, 1:403–426, 1981.

[231] V Solntsev, V Litovchenko, T Gorbanyuk, and A Evtukh. Influence of H2S and H2 adsorption on characteristics of MIS structures with Si porous layers. *Semiconductor Physics, Quantum Electronics & Optoelectronics*, 11(4):381–384, 2008.

[232] Jewell and Davis. Review of absorption and adsorption in the hydrogen-palladium system. *Applied Catalysis A: General*, 310:15–15, August 2006.

[233] G Kaltenpoth, P Schnabel, E Menke, E C Walter, M Grunze, and R M Penner. Multimode Detection of Hydrogen Gas Using Palladium-Covered Silicon μ-Channels. *Anal Chem*, 75(18):4756–4765, September 2003.

[234] Wu-Shou Zhang, Zhong-Liang Zhang, and Xin-Wei Zhang. Effects of self-stress on the hydrogen absorption into palladium hydride electrodes of plate form under galvanostatic conditions. *J Electroanal Chem*, 474(2):130–137, September 1999.

[235] T Xu, M P Zach, Z L Xiao, D Rosenmann, U Welp, W K Kwok, and G W Crabtree. Self-assembled monolayer-enhanced hydrogen sensing with ultrathin palladium films. *Appl. Phys. Lett.*, 86(2):3104, May 2005.

[236] Jin-Seo Noh, Jun Min Lee, and Wooyoung Lee. Low-dimensional palladium nanostructures for fast and reliable hydrogen gas detection. *Sensors*, 11(12):825–851, December 2010.

[237] F LEWIS. Hydrogen in palladium and palladium alloys. *Int J Hydrogen Energ*, 21(6):461–464, June 1996.

[238] R V Bucur. Effect of trapping on the solubility and diffusivity of hydrogen in palladium (α-phase). *J Mater Sci*, 22(9):3402–3406, 1987.

[239] JWill Medlin, Andrew E Lutz, Robert Bastasz, and Anthony H McDaniel. The response of palladium metal-insulator-semiconductor devices to hydrogen–oxygen mixtures: comparisons between kinetic models and experiment. *Sensor Actuat B-Chem*, 96(1):290–297, December 2002.

[240] Alireza Salehi, Alireza Nikfarjam, and Dara Jamshidi Kalantari. Pd/porous-GaAs Schottky contact for hydrogen sensing application. *Sensor Actuat B-Chem*, 113(1):419–427, January 2006.

[241] Ingemar Lundström and Dennis Söderberg. Hydrogen sensitive mos-structures part 2: characterization. *Sensors and Actuators*, 2:105–138, January 1981.

[242] Huey-Ing Chen, Yen-I Chou, and Chin-Yi Chu. A novel high-sensitive Pd/InP hydrogen sensor fabricated by electroless plating. *Sensor Actuat B-Chem*, 85(1-2):10–18, June 2002.

[243] Cuicui Ling, Qingzhong Xue, Zhide Han, Zhongyang Zhang, Yonggang Du, Yanmin Liu, and Zifeng Yan. High hydrogen response of Pd/TiO2/SiO2/Si multilayers at room temperature. *Sensor Actuat B-Chem*, September 2014.

[244] Skucha, Fan, Jeon, Javey, and Boser. Palladium/silicon nanowire Schottky barrier-based hydrogen sensors. *Sensor Actuat B-Chem*, 145(1):7–7, March 2010.

[245] P F Ruths, S Ashok, S J Fonash, and J M Ruths. A study of Pd/Si MIS Schottky barrier diode hydrogen detector. *Electron Devices, IEEE Transactions on*, 28(9):1003–1009, September 2003.

[246] Rakesh K Joshi, Subramanian Krishnan, Mashamichi Yoshimura, and Ashok Kumar. Pd Nanoparticles and Thin Films for Room Temperature Hydrogen Sensor. *Nanoscale Res Lett*, 4(10):1191–1196, July 2009.

[247] T Huberta, L Boon-Brettb, G Blackb, and U Banacha. Hydrogen sensors – A review. *Sensor Actuat B-Chem*, 157(2):329–352, October 2011.

[248] J Kanungo, H Saha, and S Basu. Effect of porosity on the performance of surface modified porous silicon hydrogen sensors. *Sensor Actuat B-Chem*, 147(1):145–151, 2010.

[249] V G Litovchenko, T I Gorbanyuk, V S Solntsev, and A A Evtukh. Mechanism of hydrogen, oxygen and humidity sensing by Cu/Pd-porous silicon–silicon structures. *Appl Surf Sci*, 234(1-4):262–267, July 2004.

[250] Vinod Kumar, Sunny, Ishpal Rawal, V N Mishra, R Dwivedi, and R R Das. Fabrication and characterization of gridded Pt/SiO2/Si MOS structure for hydrogen and hydrogen sulphide sensing. *Mater Chem Phys*, 146(3):418–424, August 2014.

[251] D Gupta, D Dutta, M Kumar, P B Barman, C K Sarkar, S Basu, and S K Hazra. A low temperature hydrogen sensor based on palladium nanoparticles. *Sensor Actuat B-Chem*, 196:215–222, June 2014.

[252] Pivak, Schreuders, Slaman, Griessen, and Dam. Thermodynamics, stress release and hysteresis behavior in highly adhesive Pd-H films. *Int J Hydrogen Energ*, 36(6):12–12, February 2011.

[253] B McCool, G Xomeritakis, and Y S Lin. Composition control and hydrogen permeation characteristics of sputter deposited palladium–silver membranes. *J Membrane Sci*, 1999.

[254] Mostafa Zahedi, Boshra Afra, Mostafa Dehghani-Mobarake, and Majid Bahmani. Preparation of a Pd membrane on a WO3 modified Porous Stainless Steel for hydrogen separation. *J Membrane Sci*, 333(1-2):45–49, 2009.

[255] Yanping He, Dongyan Ding, Xiang Gao, Zhi Chen, Ming Li, and Dali Mao. Electrodeposition of palladium films on Ni-Co coatings. pages 1–5, 2008.

[256] Mordechay Schlesinger and Milan Paunovic. *Modern Electroplating*. The ECS Series of Texts and Monographs. John Wiley & Sons, February 2011.

[257] R Delmelle, G Bamba, and J Proost. In-situ monitoring of hydride formation in Pd thin film systems. *Int J Hydrogen Energ*, 35(18):9888–9892, September 2010.

[258] Jay J Senkevich, Fu Tang, Diana Rogers, Jason T Drotar, Christopher Jezewski, William A Lanford, G C Wang, and T M Lu. SubstrateIndependent Palladium Atomic Layer Deposition. *Chemical Vapor Deposition*, 9(5):258–264, 2003.

[259] Kyung Rae Kim, Jin-Seo Noh, Jun Min Lee, Youn Joo Kim, and Wooyoung Lee. Suppression of phase transitions in Pd thin films by insertion of a Ti buffer layer. *J Mater Sci*, 46:1597–1601, March 2011.

[260] D R Baselt, B Fruhberger, E Klaassen, S Cemalovic, C L Britton, Jr., S V Patel, T E Mlsna, D McCorkle, and B Warmack. Design and performance of a microcantilever-based hydrogen sensor. *Sensor Actuat B-Chem*, 88(2):120–131, January 2003.

[261] Dongyan Ding, Zhi Chen, and Chi Lu. Hydrogen sensing of nanoporous palladium films supported by anodic aluminum oxides. *Sensor Actuat B-Chem*, 120(1):182–186, 2006.

[262] Frederic Favier, Erich C Walter, Michael P Zach, Thorsten Benter, and Reginald M Penner. Hydrogen sensors and switches from electrodeposited palladium mesowire arrays. *Science*, 293(5538):2227–2231, 2001.

[263] Kye Jin KJ Jeon, Minhong M Jeun, Eunsongyi E Lee, Jun Min JM Lee, Kyoung-Il KI Lee, Paul P von Allmen, and Wooyoung W Lee. Finite size effect on hydrogen gas sensing performance in single Pd nanowires. *Nanotechnology*, 19(49):495501–495501, December 2008.

[264] Fan Yang, David K Taggart, and Reginald M Penner. Fast, sensitive hydrogen gas detection using single palladium nanowires that resist fracture. *Nano Lett*, 9(5):2177–2182, April 2009.

[265] Ju, Lee, Jung, Lee, Lee, and Kim. Highly sensitive hydrogen gas sensors using single-walled carbon nanotubes grafted with Pd nanoparticles. *Sensor Actuat B-Chem*, 146(1):7–7, April 2010.

[266] Zhi-Min Cui, Ahmed Mechai, Lin Guo, and Wei-Guo Song. Palladium nanoparticles on the inner wall of tin oxide hollow nanospheres with enhanced hydrogen sensing properties. *RSC Adv.*, 3(35):14979–14982, 2013.

[267] Sang Sub Kim, Han Gil Na, Sun-Woo Choi, Dong Sub Kwak, and Hyoun Woo Kim. Decoration of Pd nanoparticles on ZnO-branched nanowires and their application to chemical sensors. *Microelectron Eng*, 105, May 2013.

[268] Bo Xie, SiShi Zhang, Fei Liu, Xing Peng, Fengqi Song, Guanghou Wang, and Min Han. Response behavior of a palladium nanoparticle array based hydrogen sensor in hydrogen–nitrogen mixture. *Sensor Actuat A-Phys*, 181:20–24, July 2012.

[269] J B Chen, J F Zhou, A Häfele, C R Yin, W Kronmüller, M Han, and H Haberland. Morphological studies of nanostructures from directed cluster beam deposition. *The European Physical Journal D*, 34(1):251–254, July 2005.

[270] M Han, C Xu, D Zhu, L Yang, J Zhang, Y Chen, K Ding, F Song, and G Wang. Controllable Synthesis of Two- Dimensional Metal Nanoparticle Arrays with Oriented Size and Number Density Gradients. *Adv Mater*, 19(19):2979–2983, October 2007.

[271] Bo Xie, Linlin Liu, Xing Peng, Yue Zhang, Qian Xu, Mengyang Zheng, Toshio Takiya, and Min Han. Optimizing Hydrogen Sensing Behavior by Controlling the Coverage in Pd Nanoparticle Films. *J. Phys. Chem. C*, 115(32):16161–16166, August 2011.

[272] J van Lith, A Lassesson, S A Brown, M Schulze, J G Partridge, and A Ayesh. A hydrogen sensor based on tunneling between palladium clusters. *Appl. Phys. Lett.*, 91(1):1910, October 2007.

[273] Olof Dankert and Astrid Pundt. Hydrogen-induced percolation in discontinuous films. *Appl. Phys. Lett.*, 81(9):1618, August 2002.

[274] Christoph Langhammer, Vladimir P Zhdanov, Igor Zorić, and Bengt Kasemo. Size-dependent kinetics of hydriding and dehydriding of Pd nanoparticles. *Phys. Rev. Lett.*, 104(13):135502–135502, April 2010.

[275] Syed Mubeen, Ting Zhang, Bongyoung Yoo, Marc A Deshusses, and Nosang V Myung. Palladium Nanoparticles Decorated Single-Walled Carbon Nanotube Hydrogen Sensor. *J. Phys. Chem. C*, 111(17):6321–6327, April 2007.

[276] D Bera, S C Kuiry, S Patil, and S Seal. Palladium nanoparticle arrays using template-assisted electrodeposition. *Appl. Phys. Lett.*, 82(1):3089, May 2003.

[277] Chao Zhang, Abdoul-Fatah Kanta, Hong Yin, Abdelhamid Boudiba, Jan D'haen, Marie-Georges Olivier, and Marc Debliquy. H 2 sensors based on WO 3 thin films activated by platinum nanoparticles synthesized by electroless process. *Int J Hydrogen Energ*, 38(6):2929–2935, 2013.

[278] Lon A. Porter, Hee Cheul Choi, Alexander E. Ribbe, and Jillian M. Buriak. Controlled Electroless Deposition of Noble Metal Nanoparticle Films on Germanium Surfaces. *Nano Lett*, 2:1067–1071, October 2002.

[279] M G Chung, D H Kim, D K Seo, T Kim, and H U Im. Flexible hydrogen sensors using graphene with palladium nanoparticle decoration. *Sensors and Actuators B*, 2012.

[280] Wu, Liu, Jauregui, Yu, Pillai, Cao, Bao, Chen, and Pei. Wafer-scale synthesis of graphene by chemical vapor deposition and its

application in hydrogen sensing. *Sensor Actuat B-Chem*, 150(1):5–5, September 2010.

[281] F Rahimi and A Iraji zad. Effective factors on Pd growth on porous silicon by electroless-plating: Response to hydrogen. *Sensor Actuat B-Chem*, 115(1):164–169, May 2006.

[282] A I Manilov, S A Alekseev, V Skryshevsky, S V Litvinenko, G V Kuznetsov, and V Lysenko. Influence of palladium particles impregnation on hydrogen behavior in meso-porous silicon. *J Alloy Compd*, 492(1-2):466–472, March 2010.

[283] C Tsamis, L Tsoura, A G Nassiopoulou, A Travlos, C E Salmas, K S Hatzilyberis, and G P Androutsopoulos. Hydrogen catalytic oxidation reaction on Pd-doped porous silicon. *Sensors Journal, IEEE*, 2(2):89–95, April 2002.

[284] Haohao Lin, Ting Gao, Joshua Fantini, and Michael J Sailor. A Porous SiliconPalladium Composite Film for Optical Interferometric Sensing of Hydrogen. *Langmuir*, 20(12):5104–5108, June 2004.

[285] Sekhar, Sine, and Bhansali. Effect of varying the nanostructured porous-Si process parameters on the performance of Pd-doped hydrogen sensor. *Sensor Actuat B-Chem*, 127(1):8–8, October 2007.

[286] K Luongo and S Bhansali. Hydrogen sensor. US Patent Office, 2011.

[287] Robert C Weast. Handbook of chemistry and physics. CRC Press, 1975.

[288] Yae, Nasu, Matsumoto, Hagihara, Fukumuro, and Matsuda. Nucleation behavior in electroless displacement deposition of metals on silicon from hydrofluoric acid solutions. *Electrochim Acta*, 53(1):7–7, November 2007.

[289] Richard Sard. The nucleation, growth, and structure of electroless copper deposits. *J Electrochem Soc*, 117(7):864–870, 1970.

[290] J P Marton and M Schlesinger. The Nucleation, Growth, and Structure of Thin Ni-P Films. *J Electrochem Soc*, 115(1):16, 1968.

[291] Volpe, Inguanta, Piazza, and Sunseri. Optimized bath for electroless deposition of palladium on amorphous alumina membranes. *Surface and Coatings Technology*, 200(20-21):7–7, May 2006.

[292] J A Bearden. X-RAY WAVELENGTHS. *Rev Mod Phys*, 39:78–124, 1967.

[293] M A Nicolet. Diffusion barriers in thin films. *Thin Solid Films*, 52(3):415–443, 1978.

[294] Bo Cao, Yan-Hui Jia, Gong-Ping Li, and Xi-Meng Chen. Atomic diffusion in annealed CU/SiO2/Si (100) system prepared by magnetron sputtering. *Chinese Physics B*, 19(2):6601, February 2010.

[295] J D McBrayer. Diffusion of Metals in Silicon Dioxide. *J Electrochem Soc*, 133(6):1242, 1986.

[296] M Wittmer, D L Smith, P W Lew, and M A Nicolet. Electrical characteristics of palladium silicide. *Solid State Electronics*, 21(3):573–580, 1978.

[297] C J Kircher. Metallurgical properties and electrical characteristics of palladium silicide-silicon contacts. *Solid State Electronics*, 14(6):507–513, 1971.

[298] D Lévy, A Grob, J J Grob, and J P Ponpon. Formation of palladium silicide by rapid thermal annealing. *Applied Physics A Solids and Surfaces*, 35(3):141–144, November 1984.

[299] François Léonard and A Alec Talin. Electrical contacts to one- and two-dimensionalnanomaterials. *Nature Nanotech*, 6(12):773–783, November 2011.

[300] John Foggiato, Woo Sik Yoo, Michel Ouaknine, Tomomi Murakami, and Takahashi Fukada. Optimizing the formation of nickel silicide. *Materials Science and Engineering: B*, 114:56–60, December 2003.

[301] H Bentmann, Alexander Demkov, R Gregory, and S Zollner. Electronic, optical, and surface properties of PtSi thin films. *Phys Rev B*, 78(20):205302, November 2008.

[302] J Benitez. *Principles and Modern Applications of Mass Transfer Operations*. Wiley, 2011.

[303] W Gerlach and B Goel. Gold silicon phase diagram. *Solid State Electronics*, 10(6):589–592, 1967.

[304] De Los Santos, V Luis, Dongwook Lee, Jiwon Seo, F Lizbet Leon, D Angel Bustamante, Seiichi Suzuki, Yutaka Majima, Thanos Mitrelias, and Adrian Ionescu. Crystallization and surface morphology of Au/SiO 2 thin films following furnace and flame annealing. *Surf Sci*, 603(19):2978–2985, 2009.

[305] J F Chang, T F Young, Y L Yang, H Y Ueng, and T C Chang. Silicide formation of Au thin films on (100) Si during annealing. *Mater Chem Phys*, 83(2-3):199–203, February 2004.

[306] Erik C Garnett, Wenjie Liang, and Peidong Yang. Growth and Electrical Characteristics of PlatinumNanoparticleCatalyzed Silicon Nanowires. *Adv Mater*, 19(19):2946–2950, 2007.

[307] Zaki Ahmad. *Principles of Corrosion Engineering and Corrosion Control*. Butterworth-Heinemann, September 2006.

[308] D Landolt. *Corrosion et chimie de surfaces des métaux*. Traité des matériaux. Presses polytechniques et universitaires romandes, 1993.

[309] K A Natarajan. Advances in Corrosion Engineering. In *nptel.ac.in*. IISc Bangalore.

[310] Xiaoge Gregory Zhang. *Electrochemistry of Silicon and Its Oxide*. Springer, September 2001.

[311] E V Buzaneva and P Scharff. *Frontiers of Multifunctional Nanosystems*. NATO science series: Mathematics, physics, and chemistry. Springer Netherlands, 2002.

[312] Henry Cavendish. Three Papers, Containing Experiments on Factitious Air, by the Hon. Henry Cavendish, F. R. S. *Philosophical Transactions (1683-1775)*, 56:141–184, January 1766.

[313] Craig A Grimes, Oomman K Varghese, and Sudhir Ranjan, editors. *Light, Water, Hydrogen*. Springer US, Boston, MA, 2008.

[314] Suresh P Babu. Biomass gasification for hydrogen production–process description and research needs. *Revised draft (Oct. 29, 2002). IEA, Gas Technology Institute, IL, USA*, 2002.

[315] National Renewable Energy Laboratory (Nr. *Hydrogen Production Cost Estimate Using Biomass Gasification*. Independent Review. BiblioGov, July 2012.

[316] A Melis and T Happe. Hydrogen Production. Green Algae as a Source of Energy. *PLANT PHYSIOLOGY*, 127(3):740–748, November 2001.

[317] Y Kim and B E Logan. Hydrogen production from inexhaustible supplies of fresh and salt water using microbial reverse-electrodialysis electrolysis cells. *Proceedings of the National Academy of Sciences*, 108(39):16176–16181, September 2011.

[318] Suellen A Van Ooteghem, Stephen K Beer, and Paul C Yue. Hydrogen production by the thermophilic bacterium Thermotoga neapolitana. *Appl Biochem Biotechnol*, 98-100:177–189, March 2002.

[319] California Fuel Cell Partnership. A California Road Map : The Commercialization of Hydrogen Fuel Cell Vehicles , July 2014.

[320] Introducing Hydrogen as an Energy Carrier. European Commission, 2006.

[321] B Waibel. *The Zeppelin airship LZ 129 Hindenburg*. Bilder der Luftfahrt. Sutton Verlag GmbH, 2013.

[322] Eui-Bok Lee, In-Sung Hwang, Jung-Ho Cha, Ho-Jun Lee, Won-Bae Lee, James Jungho Pak, Jong-Heun Lee, and Byeong-Kwon Ju. Micromachined catalytic combustible hydrogen gas sensor. *Sensor Actuat B-Chem*, 153(2):392–397, April 2011.

[323] Han, Hong, Kim, Gwak, Han, and Singh. Synthesis of Pd or Pt/titanate nanotube and its application to catalytic type hydrogen gas sensor. *Sensor Actuat B-Chem*, 128(1):6–6, December 2007.

[324] E Brauns, E Morsbach, G Schnurpfeil, M Bäumer, and W Lang. A miniaturized catalytic gas sensor for hydrogen detection based on stabilized nanoparticles as catalytic layer. *Sensor Actuat B-Chem*, January 2013.

[325] Maiko NISHIBORI, Woosuck Shin, Noriya Izu, Toshio ITOH, Ichiro Matsubara, Nobuyuki WATANABE, and Toshihiro KASUGA. Thermoelectric hydrogen sensors using Si and SiGe thin films with a catalytic combustor. *J. Ceram. Soc. Japan*, 118(1375):188–192, 2010.

[326] Tajima, Qiu, Shin, Izu, Matsubara, and Murayama. Micromechanical fabrication of low-power thermoelectric hydrogen sensor. *Sensor Actuat B-Chem*, 108(1-2):6–6, July 2005.

[327] I Simon and M Arndt. Thermal and gas-sensing properties of a micromachined thermal conductivity sensor for the detection of hydrogen in automotive applications. *Sensor Actuat A-Phys*, 2002.

[328] William J Buttner, Matthew B Post, Robert Burgess, and Carl Rivkin. An overview of hydrogen safety sensors and requirements. *Int J Hydrogen Energ*, 36(3):2462–2470, February 2011.

[329] L BOONBRETT, J Bousek, and P Moretto. Reliability of commercially available hydrogen sensors for detection of hydrogen at critical concentrations: Part II – selected sensor test results. *Int J Hydrogen Energ*, 34(1):562–571, January 2009.

[330] Jiri Janata. *Principles of Chemical Sensors*. Springer, July 2009.

[331] Ghenadii Korotcenkov, Sang Do Han, and Joseph R Stetter. Review of electrochemical hydrogen sensors. *Chem. Rev*, 109(3):1402–1433, March 2009.

[332] Lu, Wu, Wang, and Su. Solid-state amperometric hydrogen sensor based on polymer electrolyte membrane fuel cell. *Sensor Actuat B-Chem*, 107(2):6–6, June 2005.

[333] Okuyama, Kurita, Yamada, Takami, Ohshima, Katahira, and Fukatsu. A new type of hydrogen sensor for molten metals usable up to 1600K. *Electrochim Acta*, 55(2):5–5, December 2009.

[334] Aroutiounian. Metal oxide hydrogen, oxygen, and carbon monoxide sensors for hydrogen setups and cells. *Int J Hydrogen Energ*, 32(9):14–14, May 2007.

[335] RaviPrakash, McDaniel, Horn, Pilione, Sunal, Messier, McGrath, and Schweighardt. Hydrogen sensors: Role of palladium thin film morphology. *Sensor Actuat B-Chem*, 120(2):8–8, January 2007.

[336] Anette Salomonsson, Mats Eriksson, and Helen Dannetun. Hydrogen interaction with platinum and palladium metalinsulatorsemiconductor devices. *J. Appl Phys.*, 98(1):014505, July 2005.

[337] Karin K Potje-Kamloth. Semiconductor junction gas sensors. *Chem. Rev*, 108(2):367–399, January 2008.

[338] Chin-Chuan Cheng, Yan-Ying Tsai, Kun-Wei Lin, Huey-Ing Chen, Wei-Hsi Hsu, Ching-Wen Hong, and Wen-Chau Liu. Characteristics of a Pd–oxide–In0.49Ga0.51P high electron mobility transistor (HEMT)-based hydrogen sensor. *Sensor Actuat B-Chem*, 113(1):29–35, January 2006.

[339] Hung, Lin, Chen, Tsai, Lai, Fu, Chuang, and Liu. Comprehensive study of a Pd-GaAs high electron mobility transistor (HEMT)-based hydrogen sensor. *Sensor Actuat B-Chem*, 122(1):8–8, March 2007.

[340] Mats Eriksson, Anette Salomonsson, Ingemar Lundström, Danick Briand, and A Elisabeth A Bom. The influence of the insulator surface properties on the hydrogen response of field-effect gas sensors. *J. Appl Phys.*, 98(3):4903, August 2005.

[341] Kirby, Chang, Stratton, and Zinck. A differential capacitive thin film hydrogen sensor. *Sensor Actuat B-Chem*, 141(2):7–7, September 2009.

[342] Chou, Chiang, and Wang. Study on Pd functionalization of microcantilever for hydrogen detection promotion. *Sensor Actuat B-Chem*, 129(1):7–7, January 2008.

[343] Masanori Ando. Recent advances in optochemical sensors for the detection of H2, O2, O3, CO, CO2 and H2O in air. *TrAC Trends in Analytical Chemistry*, 25(10):937–948, November 2006.

[344] Morjan, Zuchner, and Cammann. Contributions to a reliable hydrogen sensor based on surface plasmon surface resonance spectroscopy. *Surf Sci*, 603(10-12):7–7, May 2009.

[345] Villatoro and Badenes. Optical fiber hydrogen sensor based on core diameter mismatch and annealed Pd-Au thin films. *Sensor Actuat B-Chem*, 125(1):6–6, July 2007.

[346] K R Williams, K Gupta, and M Wasilik. Etch rates for micromachining processing-Part II. *Microelectromechanical Systems, Journal of*, 12(6):761–778, 2003.